Nanoscale Mechanical and Transport Properties of Multilayers and Energy Materials



León-Manuel Pablo Romano Brandt

St Hugh's College

Supervised by

Professor Alexander M. Korsunsky

A thesis submitted for the degree of

Doctor of Philosophy

Hilary Term 2021

Abstract

Thermal and mechanical properties of thin films and nano-multilayer coatings are governed by a multitude of interlinked material properties that arise as a consequence of deposition technique and parameters. Understanding the origin of these properties including residual stress, fracture toughness, thermal diffusivity and thermal degradation activation temperature enables the careful design and control of material properties, tailored to technological applications.

The key objective of this thesis is to expand the current knowledge of the origins and controllability of thin film properties, by understanding the link between deposition parameters, film microstructure, mechanical properties and thermal properties. Starting with the mechanical properties, advanced residual stress measurement techniques are used to show how magnetron chamber pressure variation can be used to control residual stress distributions within thin films, and how this stress is linked to microstructural properties. To develop further mechanical insights directly applicable to technological applications of thin films on polymer substrates, a model for the mechanical degradation under uniaxial tension is presented, in addition to a new method for the determination of the Mode I fracture toughness.

Based on the obtained findings, thermal properties including thermal diffusivity and thermal degradation onset temperature are linked to deposition-induced microstructural properties. A model for the residual-stress driven thermal diffusion activation is presented, combining insights gained from both mechanical and thermal property analysis.

To apply the findings to cutting-edge technology, interlinked diffusion and mechanical degradation phenomena in next-generation Li-ion battery cathode material are analysed. Based on the identified mechanisms and using novel experimental techniques, a deep understanding of the relation between Li-ion transport, stress and microstructural degradation in thin film, solid state multilayer batteries is developed.

The investigations presented in this thesis open new perspectives for the precise optimisation of high-technology thin film and nano-multilayer properties and performance.

Acknowledgements

This DPhil thesis is the result of extensive international academic collaboration - I would therefore like to thank a number of people for their support throughout my time in Oxford.

First and foremost, I would like to thank my supervisor Prof. Alexander M. Korsunsky, who gave me this unique opportunity following an internship at MBLEM in 2016. Starting from the first synchrotron experiment at Diamond Light Source, I was extremely excited about his cutting-edge experimental work and knew that I wanted to become a member of his research group to learn from his understanding of the mechanics of materials. His support and brilliant ideas guided me throughout my time as researcher in Oxford and allowed me to push the work presented in this thesis significantly beyond what I had expected to achieve.

I would further like to express my gratitude to my family: my parents Natalia and Rüdiger, who raised me to be curious and always gave me the freedom and support to pursue my goals, as well as my sisters Yannick and Luna, and my grandparents Renate, Paul, Karin and Manuel. Words can hardly describe my gratitude for what you all have given me, including the continual belief in my potential. I am dedicating this thesis to you. A special thanks to Faez – you have made the past years in Oxford the best of my life so far, with many more adventures to follow.

My thanks must also go to the numerous colleagues who have helped me and my work over the past five years and made my time in Oxford so enjoyable – be it during sleepless nights at the synchrotron or during formal halls in college. Thanks to all the former and current members of the AMK group who I had the pleasure to work with: Enrico Salvati, Chryssa Papadaki, Ricky Ying, Tom Moxham, Hongjia Zhang, Joris Everaerts and Fatih Uzun. Furthermore, I would like to thank Eric Le Bourhis for the great collaboration on Cu/W nano-multilayers and for welcoming me at the Institut P' in Poitiers. Thanks to James T

Coates for introducing me to the fun side of Oxford life. Also many thanks to Taro Hitosugi and Kazunori Nishio at the Tokyo Institute of Technology for providing world-leading thin film battery samples and welcoming me to their lab in Tokyo. My special thanks goes to researchers at the Diamond Light Source and the European Synchrotron Radiation Facility (ESRF) – in particular Igor Dolbnya (DLS, B16) and Didier Wermeille (ESRF, XMaS) enabling my experiments, without which this thesis wouldn't have been possible. I would further like to thank Kalin Dragnevski and Marzena Tkaczyk (LIMA Oxford) for their experimental support.

I would like to send my thanks to St Hugh's College, my home for the past four years, where I have had the pleasure of living, studying and working. I have made some amazing friends, met some incredible people and have been provided with some exceptional opportunities during my time in Oxford. I feel very privileged to have been awarded my role as Junior Dean and would like to thank the entire decanal team for the great working experience.

Finally, many thanks to my examiners for taking the time to read my thesis. I am looking forward to discussing my work with you.

Selected Publications

1. **L. Romano Brandt**, K. Nishio, K. Simon, C. Papadaki, T. Hitosugi, A. M. Korsunsky, Strain Accommodation in Solid State Thin Film Li-NMC Batteries Observed by in situ Lamella Charging. (Under review, Advanced Energy Materials)

2. **L. Romano Brandt**, E. Salvati, D. Wermeille, C. Papadaki, E. Le Bourhis, A.M. Korsunsky, Stress-assisted thermal diffusion barrier breakdown in Cu/W nano-multilayers on Si substrate observed by in situ GISAXS and transmission EDX. ACS Applied Materials & Interfaces (2021), 13, 5, 6795-6804.

3. **L. Romano Brandt**, A. M. Korsunsky, The Effect of Deposition Parameters on the Mechanical and Transport Properties in Nanostructured Cu/W Multilayer Coatings, Functional Thin Films (Book Chapter). Taylor & Francis (2021), 380687.

4. **L. Romano Brandt**, E. Salvati, E. Le Bourhis, A.M. Korsunsky, Mode I fracture toughness determination in Cu/W nano-multilayers on polymer substrate by SEM - Digital Image Correlation, Journal of the Mechanics and Physics of Solids 145 (2020) 104145.

5. **L. Romano Brandt**, J.-J. Marie, T. Moxham, D.P. Förstermann, E. Salvati, C. Besnard, C. Papadaki, Z. Wang, P.G. Bruce, A.M. Korsunsky, Synchrotron X-ray quantitative evaluation of transient deformation and damage phenomena in a single nickel-rich cathode particle. RSC Energy & Environmental Science (2020) 3556–3566.

6. **L. Romano Brandt**, E. Salvati, E. Le Bourhis, T. Moxham, I.P. Dolbnya, A.M. Korsunsky, Nano-scale residual stress depth profiling in Cu/W nano-multilayers as a function of magnetron sputtering pressure. Surface & Coatings Technology 381 (2020) 125142.

7. **L. Romano Brandt**, E. Salvati, C. Papadaki, H. Zhang, S. Ying, E. Le Bourhis, I. Dolbnya, T. Sui, A.M. Korsunsky, Probing the deformation and fracture properties of Cu/W nano-multilayers by in situ SEM and synchrotron XRD strain microscopy. Surface & Coatings Technology 320 (2017) 158–167.

Table of Contents

1 Introduction 5

1.1 General background 5

1.2 Aim and scope of current research 11

1.3 Thesis overview 14

2 Experimental Methods 17

2.1 Thin Film Deposition 17

2.1.1 Magnetron Sputter Deposition 18

2.1.2 Ion Beam Deposition 20

2.1.3 Pulsed Laser Deposition 21

2.2 Electron and Ion Based Techniques 22

2.2.1 Scanning Electron Microscopy 23

2.2.2 Focused Ion Beam Imaging, Milling and Platinum Deposition 23

2.2.3 Transmission Electron Microscopy 25

2.2.4 Scanning Transmission Electron Microscopy 25

2.2.5 (Transmission) Energy-Dispersive X-Ray Spectroscopy (EDX) 25

2.2.6 (Transmission) Electron Backscatter Diffraction (EBSD) 27

2.3 Synchrotron X-Ray Based Techniques 28

2.3.1 X-Ray Powder Diffraction 29

2.3.2 Grazing-Incidence Small-Angle X-Ray Scattering (GISAXS) 33

2.3.3 Coherent Ptycho-Tomography 36

2.3.4 $Sin^2(\Psi)$ technique 37

2.3.5 X-Ray Reflectivity 39

2.4 Microscale Mechanical Characterisation 40

2.4.1 Focused Ion Beam – Digital Image Correlation 42

2.4.2 Micro-Cantilever Deflection Analysis 46

3 The effect of energetic deposition conditions on the mechanical properties of thin films 47

3.1 Nano-scale residual stress depth profiling in Cu/W nano-multilayers as a function of magnetron sputtering pressure 47

3.1.1 Introduction and Literature Review 47

3.1.2 Material and methods 51

3.1.3 Micro-Cantilever Deflection 55

3.1.4 Calculation 56

3.1.5 Results 70

3.1.6 Discussion 71

3.1.7 Conclusions 73

3.2 Probing the deformation and fracture properties of Cu/W nano-multilayers by in situ SEM and synchrotron XRD strain microscopy 73

3.2.1 Introduction and Literature Review 73

3.2.2 Materials and methods 76

3.2.3 Results 78

3.2.4 Discussion of existing models 92

3.2.5 An improved model 93

3.2.6 Model discussion and experimental validation 95

3.2.7 Conclusions 96

3.3 Determining the Mode I fracture toughness of Cu/W nano-multilayers on compliant substrate using Digital Image Correlation 98
3.3.1 Introduction and Literature Review 98
3.3.2 Materials and Methods 100
3.3.3 Results and Discussion 106
3.3.4 Conclusion 113

4 The effect of energetic deposition conditions on the thermal and diffusion properties of nanostructured coatings 115

4.1 Controlling Thermal Diffusivity, Residual Stress and Texture in W/Cu Nano-Multilayers by Magnetron Chamber Pressure Variation 115
4.1.1 Introduction and Literature Review 115
4.1.2 Materials and Methods 116
4.1.3 Results and Discussion 118
4.1.4 Conclusion 122

4.2 Stress-Assisted Thermal Diffusion Barrier Breakdown in Ion Beam Deposited Cu/W Nano-Multilayers on Si Substrate Observed by in situ GISAXS and Transmission EDX .. 123
4.2.1 Introduction and Literature Review 123
4.2.2 Materials and Methods 125
4.2.3 Results and Discussion 129
4.2.4 Conclusion 146

5 Advanced energy materials in technological applications: interaction of diffusion, stress and degradation in cathode particles and multilayer thin film batteries 147

5.1 Synchrotron X-ray quantitative evaluation of transient deformation and damage phenomena in a single Nickel-rich cathode particle 147
5.1.1 Introduction and Literature Review 147
5.1.2 Materials and Methods 149
5.1.3 Results and Discussion 154
5.1.4 Conclusion 174

5.2 Improving Ultra-Fast Charging Performance and Durability of All Solid State Thin Film Li-NMC Battery-On-Chip Systems by in situ TEM Lamella Analysis 175
5.2.1 Introduction and Literature Review 175
5.2.2 Materials and Methods 177
5.2.3 Results and Discussion 181
5.2.4 Modelling and Simulation 190
5.2.5 Discussion 193
5.2.6 Conclusion 194

6 Conclusions 195

6.1 Evaluation and origin of mechanical properties of Cu/W nano-multilayers 195

6.2 Origins of thermal and diffusion properties in Cu/W nano-multilayers 196

6.3 Diffusion and transport properties in a single NMC811 cathode particle and thin film solid state batteries 198

6.4 Future Work 198

References 201

Acronyms

A-MEMS	Autonomous Microelectro-Mechanical Systems
AC	Alternating Current
AFM	Atomic Force Microscopy
APD	Avalanche PhotoDiode
BCC	Body-Centred-Cubic
BSE	Backscattered Electron
CCD	Charge-Coupled Device
CVD	Chemical Vapour Deposition
DC	Direct Current
DIC	Digital Image Correlation
EBSD	Electron Backscatter Diffraction
EDX	Energy-Dispersive X-Ray Spectroscopy
ESRF	European Synchrotron Radiation Facility
EV	Electric Vehicles
FCC	Face-centred-cubic
FEM	Finite Element Method
FWHM	Full Width at Half Maximum
GB	Grain Boundary
GIS	Gas Injection System
GISAXS	Grazing-Incidence Small-Angle X-Ray Scattering
IBD	Ion Beam Deposition
IBD	Ion Beam Deposition
IoT	Internet of Things
KB	Kirkpatrick-Baez
LEFM	Linear Elastic Fracture Mechanics
MBLEM	Multi-Beam Laboratory for Engineering Microscopy
MEMS	Micro Electromechanical Systems
MLM	Multi-layer Monochromator
MSD	Magnetron Sputter Deposition
MSD	Magnetron Sputter Deposition
NML	Nano-multilayer

PLD	Pulsed Laser Deposition
PVD	Physical Vapour Deposition
RF	Radio Frequency
RoI	Region of Interest
RT	Room Temperature
sccm	Standard cubic centimetre per minute
SE	Secondary Electron
SEI	Solid-Electrolyte Interface
SEM	Scanning Electron Microscopy
SIF	Stress Intensity Factor
SoC	State of Charge
STEM	Scanning Transmission Electron Microscopy
t-EBSD	Transmission Electron Backscatter Diffraction
t-EDX	Transmission Energy-Dispersive X-Ray Spectroscopy
TEM	Transmission Electron Microscopy
TGS	Transient Grating Spectroscopy
WAXS	Wide-Angle X-Ray Scattering
XRD	X-Ray Diffraction
XRR	X-ray Reflectometry

1 Introduction

1.1 General background

Thin films and multilayer coatings are omnipresent in advanced technological applications, where they enable system miniaturisation and improve a wide range of substrate properties such as transmissivity, reflectivity, absorption, hardness, as well as corrosion and thermal properties, amongst others [1]. Examples of advanced thin films applications include, but are by no means not limited to, flexible electronics deposited on polymer substrates, e.g. for on-skin vital sign monitoring (Figure 1a), advanced optical multilayer coatings for X-Ray optics (Figure 1b), as well as flexible thin film Li-ion batteries used in cutting-edge electronics applications (Figure 1c). While the manufacturing route and type of loading applied is different for each of the three sample systems, there are common requirements of reliability and high resistance to thermal, mechanical and mass-transport induced degradation. To unlock this reliability, in-depth understanding needs to be sought of both the coating properties and the interaction between coating and substrate.

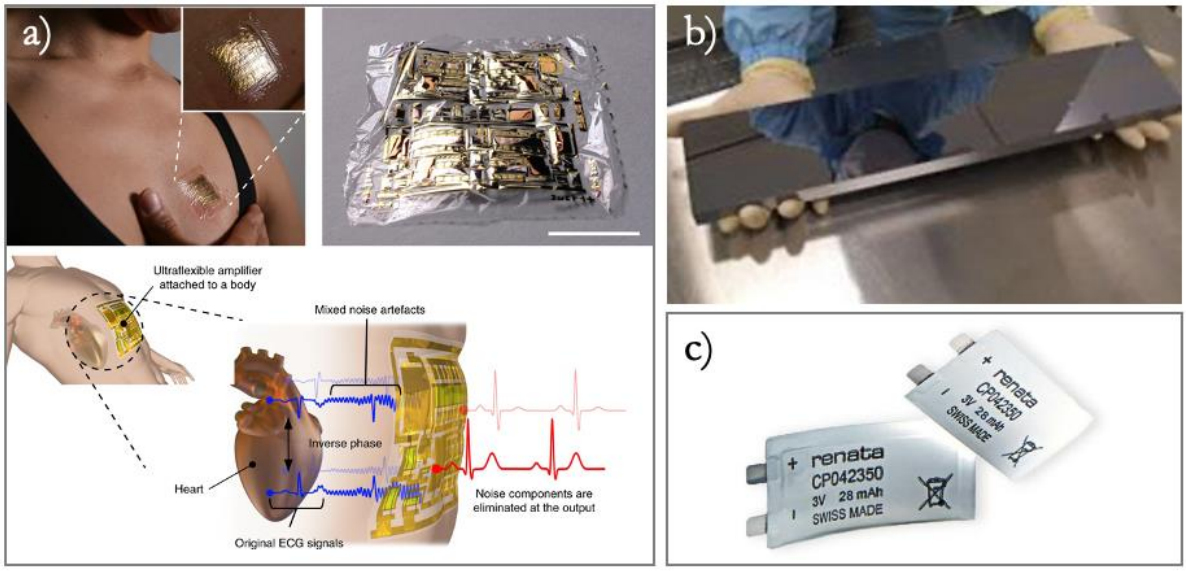


Figure 1a. Thin film amplifier on flexible substrate used for the on-skin recording of electrocardiograms, adapted from [2]. b. W/C nano-multilayer mirror for Kirkpatrick-Baez (K-B) mirror X-Ray focusing system, adapted from [3]. c. Flexible thin film Li-ion battery for use in flexible electronics, adapted from [4].

Nanostructured coatings and thin films are commonly classified according to their layer thickness: while thin layers of material with a total thickness between atomic mono-layer (~0.4 nm) and several micrometre can be referred to as thin films, the expression 'ultrathin film' is frequently referring to film thicknesses up to around 100 nm. Significant differences are, however, present in the literature due to a lack of standardised definitions. In this context, multilayers describe a periodic arrangement of stacked thin films or ultrathin films deposited upon each other. The terms thin films, ultra-thin films and multilayers have been employed in this thesis.

Historically, substrates have been coated with thin metallic films for the manufacture of optical mirrors for many centuries, by spreading tin-mercury amalgam on transparent glass and subsequently evaporating the mercury by heating the mirror [5]. While this technique permitted the creation of thin films with a thickness of few hundred microns, controlling the film properties was hardly possible. This significantly changed with the rise of automated deposition techniques towards the end of the 19th century, when Magnetron Sputter Deposition (MSD) gained wide popularity [6], enabling a significant reduction in film thickness and precise control of microstructural and functional properties. Since then, a wide range of other specialised deposition techniques, such as Ion Beam Deposition (IBD) and Pulsed Laser Deposition (PLD, 1960s), have been developed. The simultaneous rise of nano-scale characterisation techniques such as Transmission Electron Microscopy (TEM, 1940s) and Scanning Electron Microscopy (SEM, 1950s) allowed establishing the correlation between thin film deposition parameters, microstructure and functional properties, and marked the beginning of the rise of micro- and nano technology. The X-Ray diffraction method for the characterisation of polycrystals built on the achievements of Max von Laue (Nobel Prize Physics 1914) and William Henry Bragg (Nobel Prize Physics 1915) formed the theoretical foundation for the use of synchrotron radiation in engineering, the advent of which

represented a significant leap in experimental characterisation techniques that was achieved in the 1950s with the commissioning of the first large-scale synchrotron radiation facility (Bevatron, Lawrence Berkeley Laboratory), ultimately enabling *in situ* and *operando* studies of the deformation and transformation of materials.

In addition to rapid developments in manufacturing and characterisation techniques, the theoretical understanding of the relationship between material properties, applied forces and observed degradation advanced significantly with the rise of fracture mechanics (Griffith's Criterion, 1921 [7] and Irwin's Modification, 1957 [8]). Rapidly expanding research and theoretical models in the fields of Materials Engineering, Solid Mechanics and Fracture Mechanics were soon complemented by the Eigenstrain Theory, which describes the internal deformation of materials that is not caused by external mechanical stress [9]. While the examples above cover only a small proportion of the developments enabling today's cutting-edge thin film and multilayer applications, they represent the key pillars on which their reliability is built: (i) carefully controlled deposition techniques, (ii) advanced material and mechanical characterisation down to the atomic level, and (iii) in-depth theoretical understanding of the relation between material properties, external influences and degradation.

To map the current state of knowledge in thin film and multilayer research, three material properties will be considered for the scope of this thesis: microstructure, mechanical properties and thermal properties, all of which are controlled by the selected material and deposition parameters. Microstructural properties depend on the film growth kinetics during deposition, as well as post-deposition treatments such as thermal annealing or ion irradiation. When a substrate is exposed to atom flux during deposition, three distinct growth phases can be identified: nucleation, coalescence, and thickness growth. During the nucleation phase, condensation of adatoms at the substrate surface can lead to three different growth modes,

depending on the interaction energies of substrate atoms and incoming sputtered atoms [10]: if the bonding forces between substrate and film atoms are larger than the bonding forces between individual film atoms, layer growth, also known as Frank-van der Merwe-growth can be observed (Figure 2a). If the bonding forces between film atoms are greater than the bonding forces between film and substrate atoms, island growth, also known as Volmer-Weber growth can be observed (Figure 2b). Finally, a mixed growth mode is possible, starting with uniform layer growth, which is then followed by island growth. This growth mode is known as the Island-Layer or Stranski-Krastanov growth (Figure 2c).

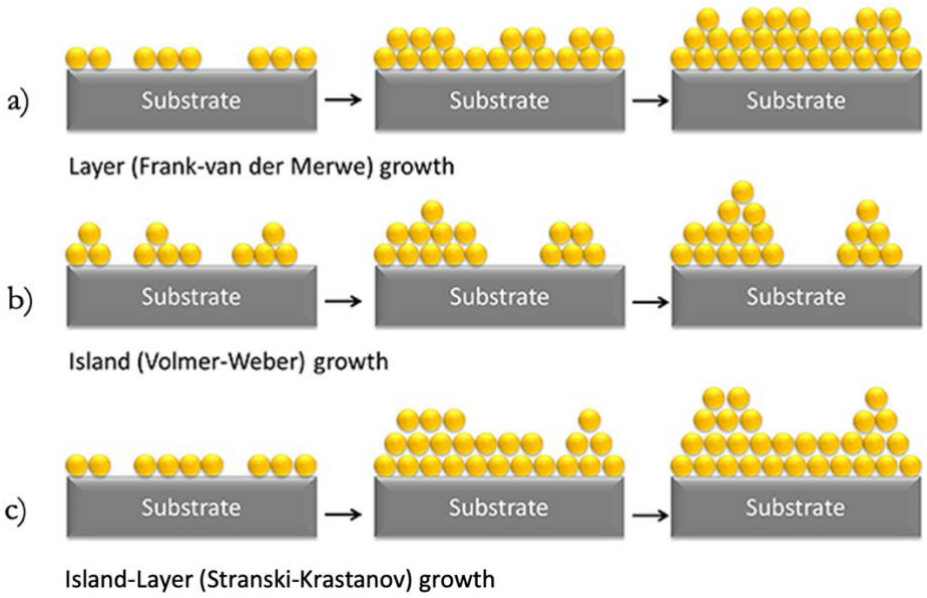


Figure 2. Thin film growth modes. a. Layer by layer growth. b. Island growth. c. Island-Layer growth. Adapted from [11]

After initial island formation, coalescence results in the formation of a continuous film. Depending on the surface energies and diffusion parameters, island coalescence can either result in grain boundary formation in between islands, or in their fusion into single crystal. As a result, the substrate temperature during deposition alongside the impurity content determine the final film microstructure, as illustrated in Figure 3 [12].

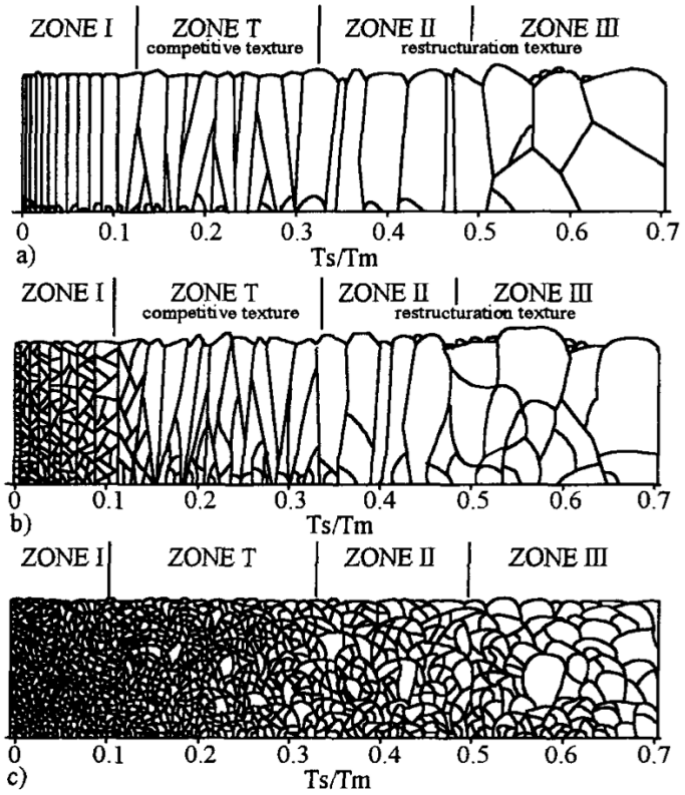


Figure 3. Illustration of thin film microstructure depending on substrate temperature as fraction of melting temperature as well as the impurity content (a. low, b. medium, c. high). Adapted from [12].

Depending on the microstructural growth dynamics, significant variations in thermal properties such as thermal diffusivity and thermal conductivity can be observed [13–15]. Phonon transport in thin film lattices can vary significantly due to the differences in crystal imperfections such as dislocations, vacancies, self-interstitials and grain boundaries. This applies in particular to systems containing a large number of interfaces such as nano-multilayers. While some of these aspects have been previously discussed in the literature [16], significant gaps remain in the understanding of the relationship between deposition parameters, microstructure and thermal properties in ultrathin films and nano-multilayers.

In addition to thermal properties, the mechanical properties including residual stress are controlled by thin film deposition parameters. A wide range of measurement methods are available for the quantification of residual stress in thin films, including the well-established

$\sin^2(\Psi)$ technique [17], cross-sectional synchrotron nano-diffraction [18], as well as micro-cantilever deflection analysis [19]. While most of these methods are only able to provide the average residual stress within thin films, micro-cantilever deflection analysis can be used for the reconstruction of local stress gradients. The significant amount of sample preparation and surface modification required for this analysis, however, raises questions regarding focused ion beam induced sample modification. Consequently, improved methods for the determination of local residual stresses in thin films and multilayers are required, which can then be employed for an in-depth understanding of the relation between deposition parameters and arising residual stress depth profiles.

Further to deposition-induced residual stress, the knowledge of other mechanical parameters such as the fracture toughness are of crucial importance for applications involving thin films and multilayers on compliant substrates. While nano-indentation techniques are well-established for the determination of thin film fracture toughness [20], this technique can be applied to thin films with sub-micron thickness only with some limitations and caveats. As newly emerging, cutting edge applications for thin films on compliant polymer substrates require nanometre thin coatings with well-known fracture properties, new methods for the determination of the fracture toughness are required. In addition, detailed models of the degradation mechanisms of these systems under mechanical load are required for improving reliability.

In this regard, Cu/W nano-multilayer coatings are of significant relevance due to their potential use in high-technology applications such as nuclear fusion and fission reactors, as well as micro-electronics, all of which require superior mechanical and thermal stability. In addition, Cu/W nano-multilayers make for ideal model systems for the study and characterisation of the microstructural properties in advanced mutually immiscible bi-metallic coatings, combining two well-understood metals which together show unique

properties and dynamic behaviour. For this reason, the fundamental characterisation of thermal and mechanical properties in this thesis was executed using Cu/W nano-multilayer samples on polymer and Silicon substrate.

Another range of challengingly complex, cutting-edge applications of nano-multilayer systems arises in the context of energy systems, such as fuel cells, supercapacitors, and all solid state thin film batteries. Achieving optimal combination of mechanical and functional properties of thin layers in these systems requires in-depth knowledge of the relation between film fabrication, microstructure, ion diffusion pathways, and resulting internal strains. Previously, these systems were optimised mainly from electro-chemistry perspectives on the parameters such as energy and power density, enhanced charge rate, etc. However, the insights sought in the present project illustrate that the microstructural and mechanistic aspects of charging and discharging processes can reduce battery capacity fade and unlock optimised combinations of charging performance and durability.

1.2 Aim and scope of current research

As outlined in the previous section (§1.1), thermo-mechanical properties of thin films and nano-multilayers are determined to an overwhelming extent by their microstructure, which in turn is controlled by the deposition parameters. In addition to the properties of the coating itself, the interaction between substrate and coating is of fundamental importance for system integrity. This interdependence, illustrated in Figure 4, highlights the key topics required to bridge knowledge gaps in the literature that have been analysed in this thesis.

To develop an in-depth understanding of the key parameters underlying thin film and multilayer coating properties, mechanical aspects are initially analysed independently. Further, thermal aspects are considered so that the background of microstructural-mechanical mechanisms can be identified, thus resulting in the development of a combined theory for the

origins of residual stress and thermal diffusivity in thin films. This section aims to provide an overview of the nature and significance of the results presented in Chapters §3-5, as well as to amplify and make explicit the links between these different research aspects.

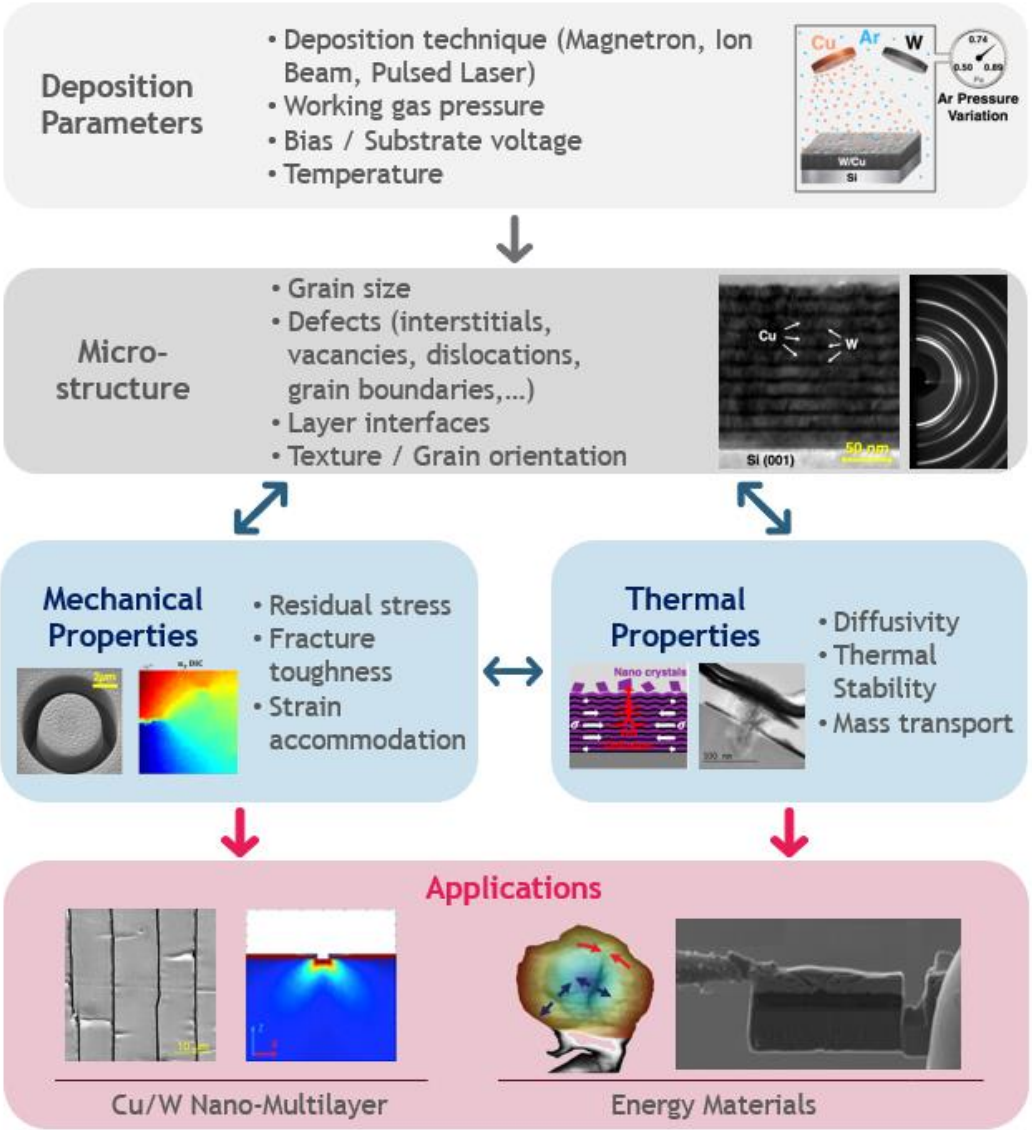


Figure 4. The interdependence between the deposition parameters, microstructure, thermal and mechanical properties of thin films and nano-multilayers.

As far as the mechanical properties are concerned in Chapter 3, the main aim is to develop applicable strategies for the control of thin film and nano-multilayer microstructure and residual stress by achieving an in-depth theoretical understanding of the effect of deposition parameters. In addition to the microstructural causes of the residual stress, an understanding

of the application-related mechanisms and properties is presented, such as strain transfer between substrate and coating, as well as the determination of the Mode I fracture toughness of nano-multilayers on polymer substrate. New experimental techniques for the determination of these key mechanical parameters are further introduced.

Building on the identified microstructural properties, Chapter 4, describing the thermal properties of thin films and multilayer coatings, aims to develop insights into the origins of thermal diffusivity variation in nano-multilayers deposited under different conditions. One important aim is to link the separate independent findings regarding the thermal and mechanical properties of the thin film to common microstructural origins. In addition, in order to understand the degradation in Cu/W nano-multilayer coatings at elevated temperatures driven by both thermal diffusion and residual stress, a new combination of experimental techniques is developed and presented.

Based on the fundamental understanding of the origins of thermal and mechanical properties in thin films and multilayer coatings, the final task set for this thesis was to apply the findings to several selected challenges in cutting-edge technology in Chapter 5. For this purpose solid state, nano-multilayer Li-ion batteries were chosen. The ultimate goal of this Chapter was the understanding of cathode material degradation driven by Li intercalation and de-intercalation. However, in the field of thin film batteries there is a severe lack of quantitative literature data for key parameters. This situation called for an initial assessment of the properties of a Li-ion battery cathode material in a more conventional form of secondary micro-particle(s). Starting with spheroidal nano-crystalline Li-ion battery particles, a link between Li-ion diffusion and mechanical degradation is established. Based on these findings, fundamental insights into the degradation of thin film batteries are unlocked. These findings conclude the scope of this thesis.

1.3 Thesis overview

In terms of its layout this thesis can be divided into three blocks of Chapters: Introductory, Analytical, and Concluding.

The problem identification and setting are covered in Chapter 1. The description of the deposition and characterisation methods is presented in Chapter 2.

For the purpose of clarity and cohesive integration, a full comprehensive literature review of the current state of research by topic is presented in each respective topic chapter.

The first Chapter devoted to specific problem analysis (§3) focuses on the mechanical properties of thin films and nano-multilayers. In §3.1 that deals with the nano-resolution determination of residual stress distributions within Cu/W nano-multilayers deposited at varying magnetron chamber pressures, a strong correlation between the deposition parameters, microstructure, and mechanical properties is presented. The method of FIB-DIC micro-ring-core depth profiling used in this chapter was applied to nano-multilayer systems for the first time. This required cross-validation of the obtained results with commonly used experimental techniques, such as the $\sin^2(\Psi)$ method and micro-cantilever deflection analysis.

Based on the developed in-depth understanding of the residual stress state in multilayer coatings, §3.2 focuses on the mechanical interaction between metallic coatings and compliant polymer substrates under external load. To understand the deformation and fracture properties of thin films on compliant polymer substrates under uniaxial tension, a combination of experimental insights and mechanical modelling were used. The experimentally observed regular arrangement of coating cracks was explained using a newly developed version of the popular shear lag model. The findings were confirmed experimentally by combining Synchrotron X-Ray Diffraction (XRD) and *in situ* in-SEM Digital Image Correlation (DIC).

The final part of the mechanical characterisation of Cu/W nano-multilayers presented in §3.3 provides further insights into the interaction between polymer substrates and metallic coatings by showcasing a new experimental method for the determination of the critical stress intensity factor for thin and ultra-thin films on polymer substrate. Finite Element Method (FEM) simulations were carried out to confirm the experimental findings, which enabled the determination of the Mode I fracture toughness (critical stress intensity factor) of Cu/W nano-multilayers coatings as a key mechanical parameter for advanced technological applications.

The next chapter, §4, focuses on the thermal and diffusion properties of Cu/W nano-multilayer coatings. Starting with the quantification of the thermal diffusivity as a function of varying the magnetron deposition pressure, a link between microstructure, residual stress and thermal diffusivity is established in §4.1, demonstrating that mechanical and thermal properties can be considered as design parameters in thin films synthesis.

In the following section (§4.2) a novel combination of *in situ* experimental methods is used to understand the structural degradation in Cu/W nano-multilayers at elevated temperatures. A theoretical model combining the influence of residual stress and thermal diffusion is presented in order to explain the observed microstructural changes. This study concludes the combined analysis of microstructure, residual stress and thermal diffusion in Cu/W nano-multilayers.

To apply the obtained findings and insights to a cutting-edge technological application, solid state-thin film batteries deposited by magnetron sputter deposition were analysed. As these systems have been developed very recently, only very limited understanding of their microstructural and mechanical properties is available in the literature. In order to develop more a fundamental understanding of the mechanical processes related to Li-ion battery charging and discharging, more traditional Li-ion battery cathode particles with currently widely studied material composition were first analysed in §5.1. A new combination

of *operando* diffraction, *in situ* tomography and FEM simulations was used to identify the drivers underlying battery cathode particle degradation at the sub-micron level. A fundamental understanding of the interaction between local crystal orientation, directional strain and mechanical degradation was established.

Based on these insights, ultra-fast charging thin film, solid state batteries deposited by Physical Vapour Deposition (PVD) with carefully designed grain orientation and interfaces were characterised *in situ*, to identify the mechanical implications of extremely high charging rates. This experimental study was combined with microstructural characterisation to explain the observed performance and capacity.

The final, concluding part of the thesis, §6, presents an overall discussion and evaluation of the findings, as well as a brief outlook for possible future work.

2 Experimental Methods

In this chapter, an overview over the thin film deposition and analysis techniques employed across this investigation is provided. Three different energetic deposition techniques used for sample manufacture are presented in §2.1, followed by an overview over the different electron- and ion-based characterisation techniques in §2.2 and X-ray based techniques in §2.3. Finally, complex experimental techniques for the microscale mechanical characterisation based on SEM imaging, which require post-experimental data analysis and processing are presented in §2.4. This includes FIB-DIC residual stress reconstruction and micro-cantilever deflection analysis.

2.1 Thin Film Deposition

A broad variety of deposition techniques is available, which permit the deposition of thin and ultrathin films and coatings onto substrates with Ångström precision thickness. Common deposition techniques can be subdivided into two main categories: Physical Vapour Deposition (PVD) and Chemical Vapour Deposition (CVD). Throughout this thesis, samples produced by three different PVD methods, namely, Magnetron Sputter Deposition (MSD), Ion Beam Deposition (IBD), and Pulsed Laser Deposition (PLD), have been used. All three methods rely on in-vacuum deposition and share the common manufacturing process characteristics of PVD: the material to be deposited onto the substrate, commonly referred to as target, experiences an influx of either charged particles or highly energetic photons, resulting in the kinetic energy-driven release of surface atoms. Depending on the deposition technique, the released metal atoms and atom clusters in their gas phase either travel through ultra-high vacuum or a low pressure inert gas atmosphere before reaching the substrate, which

strongly affects their kinetic energy and thus growth dynamics. A comparison of the different kinetic particle energies and growth rates by deposition technique is provided in Figure 5. It can be seen that PLD, MSD, and IBD all cover a distinctively different energy and growth rate range, the impact of which on the thin film properties will be thoroughly described and discussed in this thesis. Individual deposition techniques will be discussed in the following sub-sections.

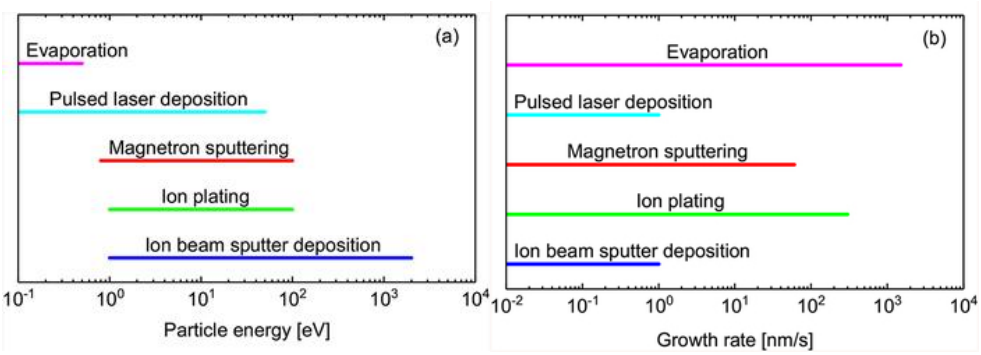


Figure 5a. Kinetic particle energy ranges and b. growth rates of thin films deposited by different methods [21].

2.1.1 Magnetron Sputter Deposition

MSD is a widespread, low cost technology for the deposition of conductive, semi-conductive or insulating thin films and coatings. It is relatively easy to use and control and enables large substrate areas to be coated at relatively high growth rate (Figure 5b) with a broad variety of parameters available to fine-tune the final coating properties. The fundamental mechanism of MSD relies on the ionisation of inert Argon at low chamber pressure. For this purpose, the magnetron chamber is pumped down to high vacuum and Argon is leaked into the chamber at constant rate to create a low pressure Argon atmosphere. While it is possible to introduce other gases such as Oxygen and Nitrogen into the chamber to create Oxide or Nitride coatings, only pure metal thin films created in a low pressure Argon atmosphere have been used for samples presented in this thesis. By applying a high negative voltage to the target, naturally

existing, positively charged Ar+ ions are accelerated towards the target surface. Due to the high kinetic Ar+ energy, target atoms are knocked out from the target surface in gas phase and accelerated towards the opposite substrate. As a by-product of this sublimation process, secondary electrons are emitted from the sample surface, which are trapped near the target surface by a magnetic field generated by permanent magnets, as shown in Figure 6. If the magnetic field strength is uniform across all three magnets, the configuration is called balanced magnetron configuration, while a decreased magnetic strength of the centre magnet results in the unbalanced magnetron configuration. Balanced magnetron deposition results in electron entrapment and plasma formation exclusively near the target surface, while unbalanced magnetron deposition results in the plasma reaching the substrate surface, thus significantly increasing the sputtering yield. In both cases, the entrapped electrons ionise the Ar atmosphere in a stable chain reaction, resulting in a self-sustaining sputtering cycle and high level of target material emission.

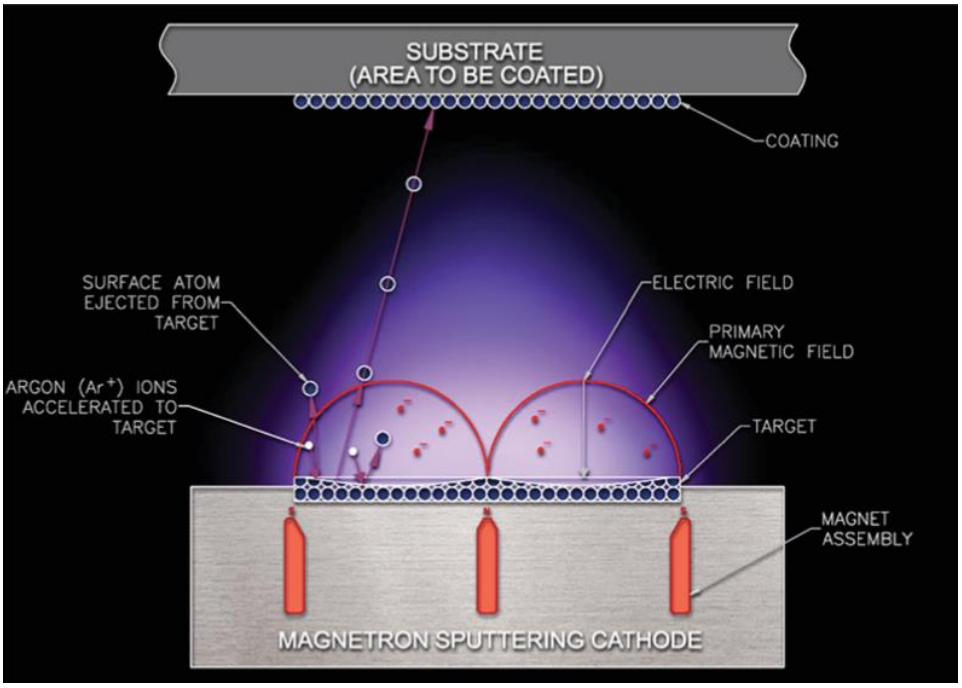


Figure 6. Schematic overview over the MSD process (adapted from *Angstrom Science, 2009*). The target is shown at the bottom of the figure, with the substrate located opposite at the top.

The target can be charged either by direct current (DC) or alternating current (AC). Radio frequency (RF) AC magnetron sputtering is commonly used for the deposition of non-conductive materials, as it prevents charge build-up on the target surface, which would decrease the sputtering process efficiency. Various parameters can be modified during deposition, depending on the thin film requirements. The broad range of parameter modifications includes, but is not limited to the substrate bias, substrate temperature, Ar chamber pressure, DC/RF power, and target-substrate distance.

For the manufacture of samples in this study, the PUMA magnetron (Institut P', CNRS, Université de Poitiers, France) was employed, enabling the use of up to 3 targets in confocal geometry. The Cu/W nano-multilayer samples produced across a range of magnetron chamber pressures were used for the studies presented and discussed in §3.1 and §4.1.

2.1.2 Ion Beam Deposition

Similar to MSD, IBD relies on the kinetic energy transfer from Ar+ ions onto a target for material sublimation and deposition onto a substrate. The mechanism underlying Ar+ ion generation, however, is fundamentally different: Ar+ ions are generated in a RF deposition gun and directed towards the target, where their kinetic energy leads to atom emission towards the substrate. Additional oxygen and nitrogen atoms can contribute to the deposition process by employing an assist gun, as shown in Figure 7. This permits the operation of IBD at lower chamber pressures as compared to MSD, resulting in higher particle energies and lower growth rates, as shown in Figure 5. For the samples presented in §3.2, §3.3 and §4.2 of this study, a Nordiko-3000 deposition system (Institut P', CNRS, Université de Poitiers, France) with Ar+ RF source was employed. As only pure metals were deposited, the assist gun was not used.

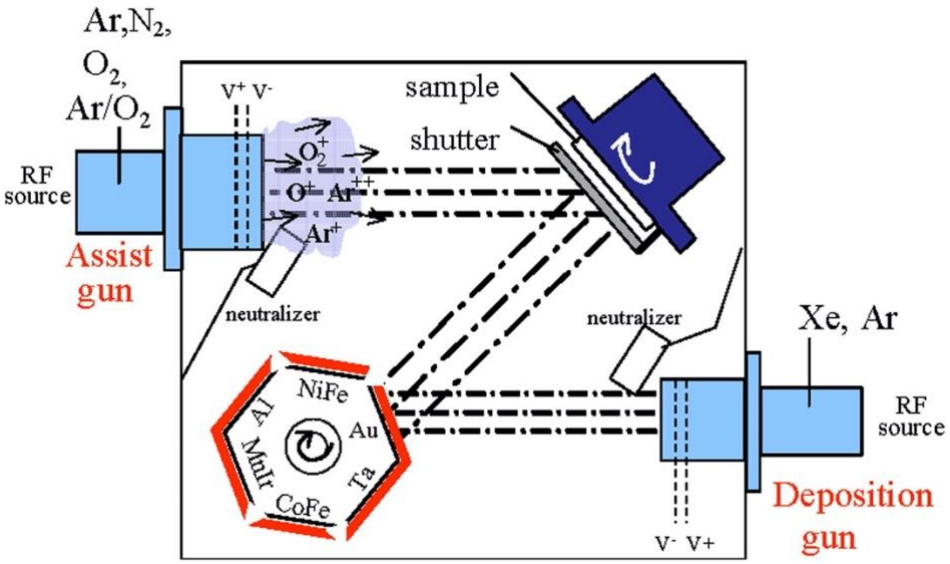


Figure 7. Schematic of the ion beam deposition process [23]

2.1.3 Pulsed Laser Deposition

High power pulsed laser photon irradiation is used in PLD to evaporate the target material, as shown in Figure 8. As this deposition technique does not require any ionised atmosphere, it can be carried out under ultra-high vacuum conditions. While the detailed mechanisms of interaction between photons and target material are highly complex and involve electronic excitation followed by energy conversion into thermal, chemical and mechanical energy, the overall mechanism leading to the formation and growth of thin films is similar to MSD and IBD. A so called plasma plume is formed upon interaction between laser pulse and target surface, resulting in the evaporation and re-deposition of target materials onto the substrate. Tuneable parameters include the laser pulse energy and rate, the substrate temperature, as well as the optional gas inlet, which can be used to crease oxide and nitride coatings. PLD was used for the deposition of individual layers of the sample presented in §5.2.

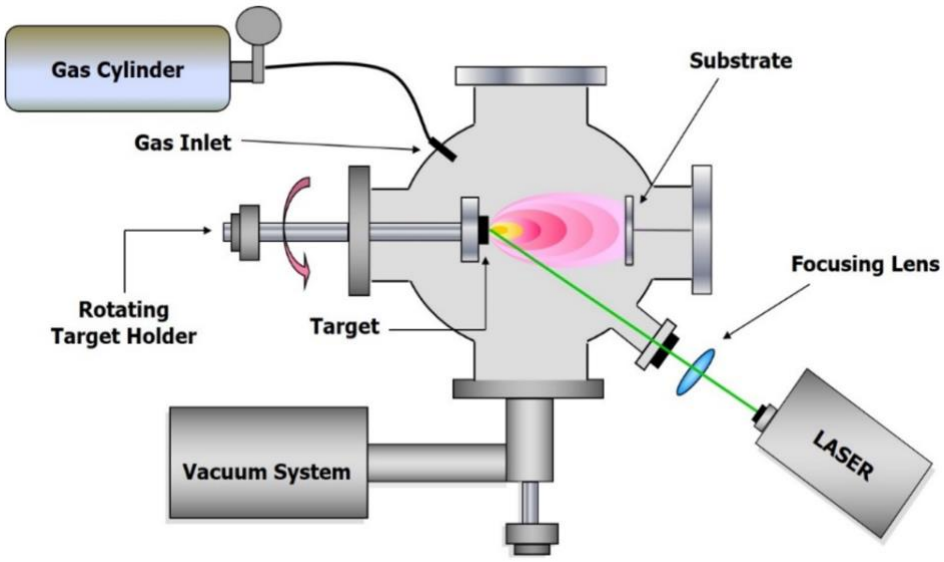


Figure 8. Overview over the pulsed laser deposition process [24].

2.2 Electron and Ion Based Techniques

Electron and ion based imaging and milling techniques are most commonly used for the micro- and nano-scale imaging, characterisation and manipulation of conductive materials. All techniques are based on the acceleration and electromagnetic focusing of charged species such as electrons and ions onto a nanometre-sized spot at a desired position on the sample. For SEM and FIB imaging, the interaction between sample and beam is measured in reflection geometry, while TEM and Scanning Transmission Electron Microscopy (STEM) rely on analysis of transmitted electrons. An overview of the different geometries is provided in Figure 9.

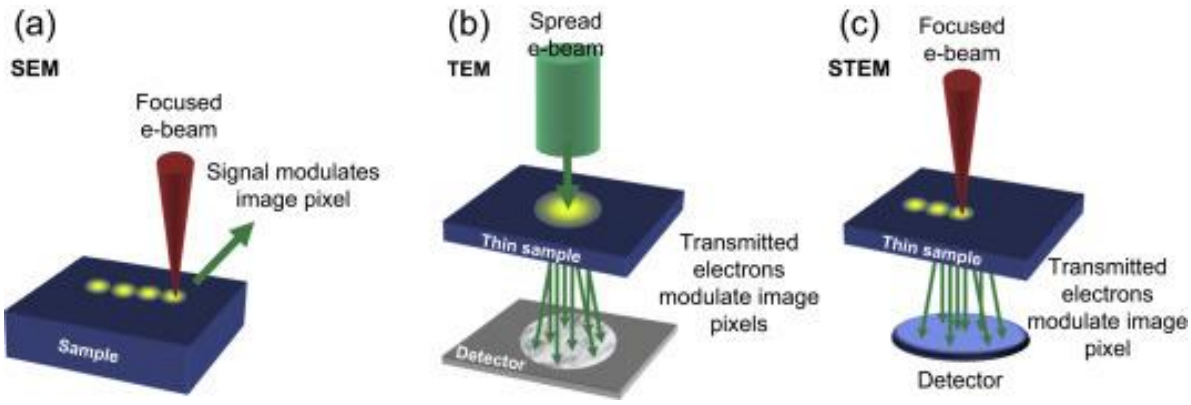


Figure 9. Geometric configurations of electron-based analysis techniques: a. Scanning Electron Microscopy (same geometry for Focused Ion Beam) b. Transmission Electron Microscopy c. Scanning Transmission Electron Microscopy [25].

2.2.1 Scanning Electron Microscopy

SEM imaging relies on the counting of emitted electrons from the interaction volume between nano-focused electron beam and conductive sample. The beam is deflected across the sample surface using a scanning coil, resulting in a raster scan as shown in Figure 9a. Depending on the desired sample information, different electron counting detectors are available and placed inside the SEM chamber, which assign a grey scale value to either Secondary Electron (SE) or Backscattered Electron (BSE) counts. For the purpose of the present analysis, the SE detector of a LYRA 3XM FIB-SEM instrument at the Multi-Beam Laboratory for Engineering Microscopy (MBLEM) Oxford was used for imaging.

2.2.2 Focused Ion Beam Imaging, Milling and Platinum Deposition

Similar to raster scanning in SEM imaging, Ga+ ions as charged species can be extracted from an ion source as shown in Figure 10, and accelerated and focused onto the sample surface for FIB imaging and milling. Depending on the FIB emission current and duration of

interaction, the sample can either be imaged or material removed. FIB imaging always inflicts a certain degree of surface amorphisation, which is why the interaction between FIB and sample should be kept as brief as possible for imaging purposes. FIB imaging is sensitive to the material grain orientation, resulting channelling contrast, which was exploited for grain orientation sensitive imaging in §5.1. The main use of the FIB in this work, however, was the nano precision removal of material at calibrated rates. It permits cutting and notching material, which was employed for the purpose of this thesis in §3.1, §3.3, §5.1 and §5.2.

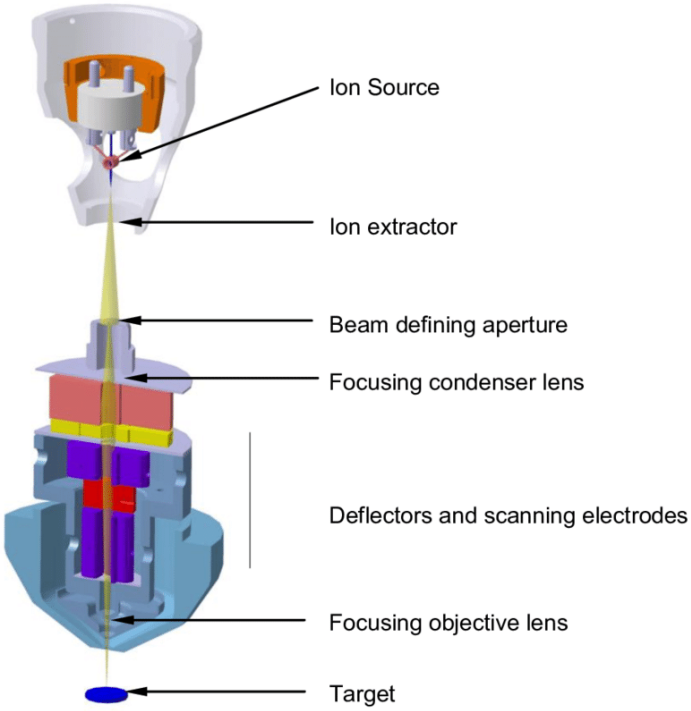


Figure 10. Schematic representation of the Focused Ion Beam column [26]

Finally, at low emission current, the FIB can be used to deposit Pt droplets on the sample surface. For this purpose, a nozzle at the tip of the Pt Gas Injection System (GIS) is brought in close proximity to the sample surface and negatively charged Pt vapour is released into the vacuum chamber. Due to the interaction with the oppositely charged Ga+ ions, the Pt gas

attaches to the FIB ions, which transport the Pt atoms to the sample surface. The use of this Pt droplet deposition will be discussed in further in §2.4.

2.2.3 Transmission Electron Microscopy

In order to achieve atomic lattice resolution, TEM is required. As the sample is imaged in transmission geometry (Figure 9b), complex sample preparation requiring the FIB sectioning of a thin lamella with a thickness of around 50 nm is required. The sample is illuminated with a broad beam spot, resulting in no raster scanning being required. In this study, the JEOL JEM-2100 TEM at the Research Complex in Harwell (Oxfordshire, UK) was employed for the imaging presented in §4.2 and §5.2.

2.2.4 Scanning Transmission Electron Microscopy

STEM combines characteristics of SEM and TEM by relying on SEM beam raster scans in transmission geometry across a thin lamella, as shown in Figure 9c. One key benefit of this setup is the combination of high resolution capabilities with a raster probe, which enables the local detection of sample properties that would otherwise be averaged in conventional large beam TEM analysis. For the purpose of this study, the STEM detector inside the TESCAN Lyra 3XM instrument was employed in §4.2, §5.1 and §5.2. Atomic lattice resolution STEM was further employed using the JEOL ARM200F microscope at the E01 beamline at the Diamond Light Source (Harwell, UK). The obtained data is presented and discussed in §5.2.

2.2.5 (Transmission) Energy-Dispersive X-Ray Spectroscopy (EDX)

When highly energetic electrons from the SEM beam interact with atoms at or near the sample surface, electrons from the inner atomic shell get removed. When these get replaced by

electrons from the outer atomic shell, the difference in potential energy is emitted as photon with characteristic wavelength. The emitted element-specific X-ray photons can then be counted by an EDX detector synchronously during the SEM raster-scan. With the obtained counts it is possible to generate high resolution material maps, permitting the analysis and processing of local X-ray spectra. The size of the droplet shaped interaction volume between beam and sample depends significantly on the beam energy and sample material, but is normally within a range of 1-5 µm depth. This volume contributing to the EDX signal is shown in Figure 11a, while the chamber geometry with detector position is shown in Figure 11b.

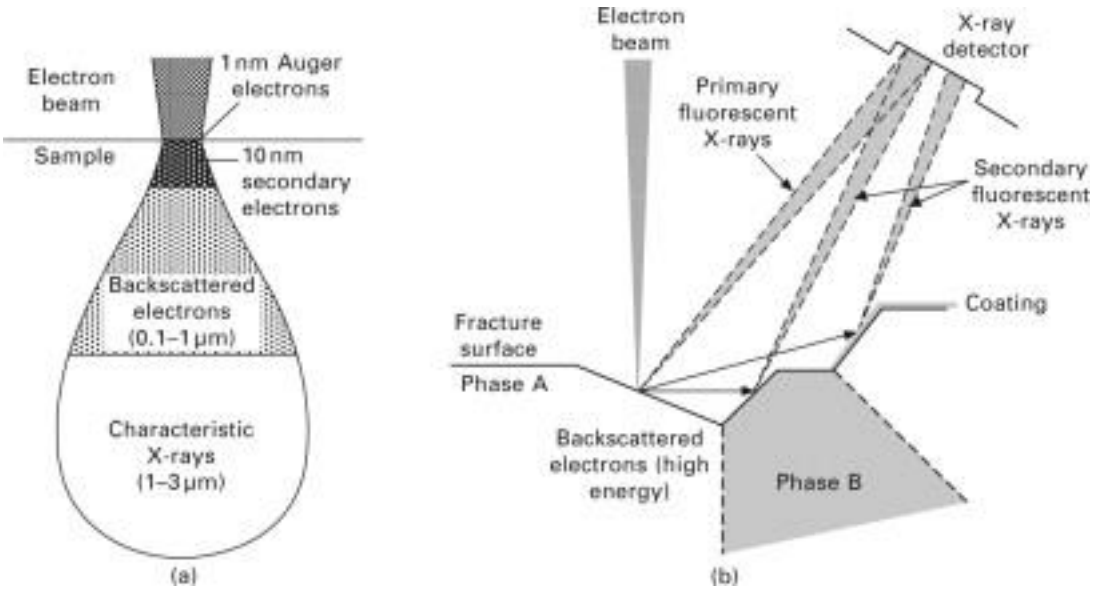


Figure 11a. Interaction volume between SEM beam and sample showing the region of characteristic X-ray generation. b. EDX geometry within the microscope chamber [27].

For the analysis of nanocrystalline materials presented in §4.1, §4.2, §5.1 and §5.2 of this thesis, however, an interaction volume of several µm diameter is not sufficiently accurate. In order to increase the EDX resolution, analysis can be carried out in transmission geometry on a TEM lamella, thus reducing the interaction volume between beam and sample to a lamella thickness of around 50-100 nm. Transmission EDX (t-EDX) has been used in this thesis for enhanced material mapping resolution.

2.2.6 (Transmission) Electron Backscatter Diffraction (EBSD)

EBSD is an highly automated and popular technique for the crystallographic characterisation of crystalline materials. While it is most frequently employed for the grain orientation analysis, it can be used for the study of defects and plastic strain. To obtain the so called Kikuchi electron diffraction patterns, the sample is mounted at an angle of 70° with respect to the EBSD detector surface normal. As the SEM beam interacts with the sample, electrons in Bragg condition with the local crystal lattice diffract from the sample surface and excite the phosphor screen of the Charge-Coupled Device (CCD) camera, as shown in Figure 12b. During raster scanning, local Kikuchi patterns as shown in Figure 12a are processed by EBSD software, which identifies Kikuchi bands, based on which the grain orientation is reconstructed. EBSD mapping can be carried out alongside EDX spectroscopy, thus permitting the construction of phase maps.

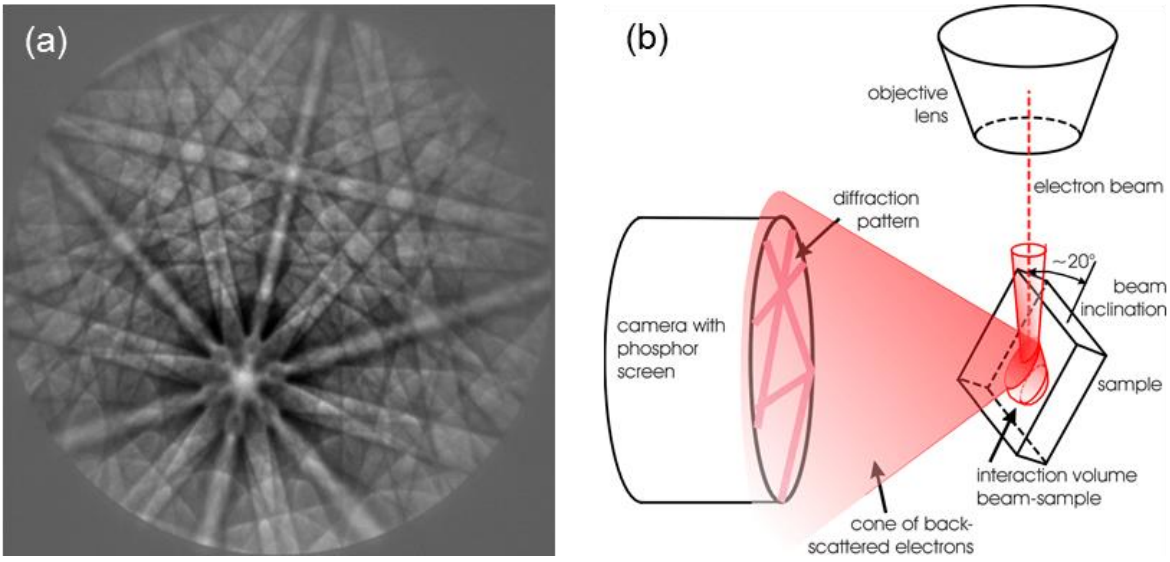


Figure 12a. Kikuchi pattern of Nb at 15 kV electron beam energy. b. EBSD setup in reflection geometry [28].

Mapping the grain orientation of nanocrystalline materials is particularly challenging, due to the large interaction volume between electron beam and sample material. As for the t-EDX,

Transmission EBSD (t-EBSD) on a tilted lamella in transmission geometry can enhance the resolution measurably. For this purpose, the lamella is tilted at angle of 45° and Kikuchi patters are collected. T-EBSD has been used at a resolution of 40 nm in §5.1, where further details regarding the setup geometry and data processing are presented.

2.3 Synchrotron X-Ray Based Techniques

Today's ability to develop highly optimised engineering materials has largely been made possible by the fundamental understanding of the structure of materials that was enabled by X-Ray characterisation in the past 100 years or so. The non-destructive interaction between X-Ray photons and matter permits the *in situ* and *operando* study of static and dynamic material properties. While early work involving X-Ray characterisation was carried out using laboratory X-Ray sources with limited photon flux, cutting edge results in today's research are often times enabled by experiments carried out at synchrotron radiation sources, which provide X-Ray beam intensities that are 6-8 orders of magnitude above laboratory source intensity and can provide photon energies of above 100 keV. In the present study, exclusively synchrotron X-Ray experiments were carried out in order to achieve high experimental resolution in both time and space. Experiments were carried out at two different synchrotrons: studies presented in §3.1, §3.2, §4.1 and §5.1 were carried out at Diamond Light Source Synchrotron (Harwell, UK), while the X-ray based techniques presented in §4.2 were obtained from experiments at the European Synchrotron Radiation Facility (ESRF, Grenoble, France).

2.3.1 X-Ray Powder Diffraction

A widely used method for the phase identification, texture analysis and strain quantification in micro- and nano-crystalline materials is synchrotron X-Ray powder diffraction, which is also referred to as Wide-Angle X-Ray Scattering (WAXS) across this thesis. For this purpose, the synchrotron beam enters the optics chamber of the beamline, where a monochromator is used to select a desired X-Ray wavelength from the incoming spectrum. The wavelength selection is highly dependent on the planned experiment, as sample thickness, beamline characteristics and involved sample materials with their respective characteristic X-Ray wavelength absorption edges need to be taken into account. The obtained monochromatic beam is then collimated by two pairs of slits to the desired size and either used to illuminate the sample in its collimated size or focused further to (sub-)micron size for local probing. X-Ray optics used for sub-micron X-Ray focusing in this thesis are Kirkpatrick-Baez (KB) mirrors, which consist of two parabolic mirrors that focus the incoming beam onto one spot as shown in Figure 13.

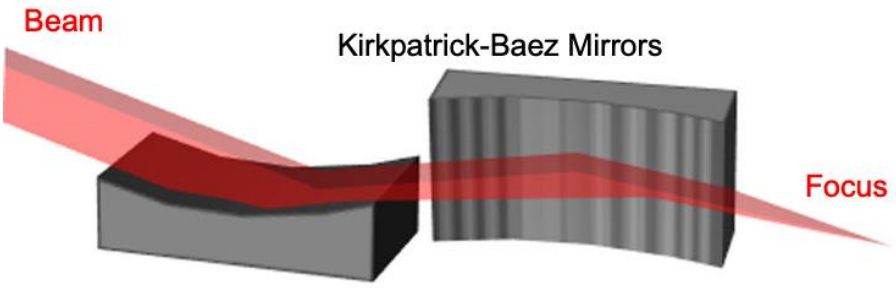


Figure 13. Kirkpatrick-Baez mirrors as X-Ray focusing optics [29].

Upon interaction with the crystalline lattice in a sample grain, the X-Ray photons gets diffracted. Under certain geometric conditions originally proposed by Sir William Bragg in 1913, X-Ray waves departing from the sample are experience constructive interference. The

geometric conditions for constructive interference underlying Bragg's law are shown in Figure 14.

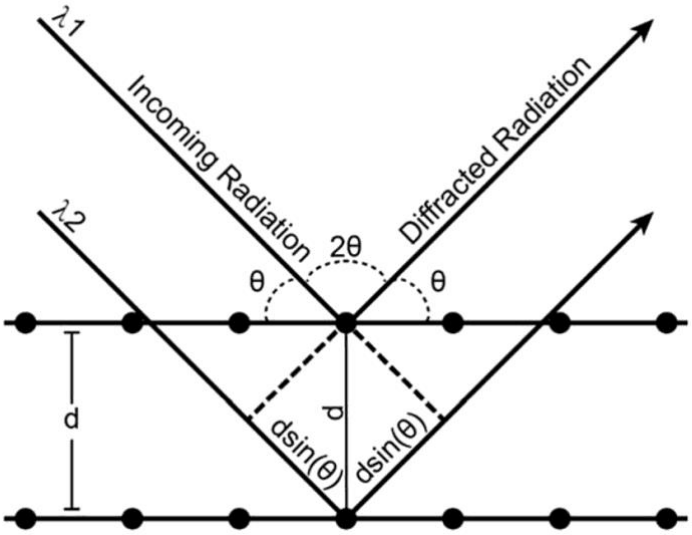


Figure 14. Geometric condition for to constructive diffraction [30]

Bragg's law can therefore be expressed as:

$$n\lambda = 2d_{hkl}\sin(\theta) \tag{1}$$

for a known X-Ray wavelength λ, the scattering angle θ and the lattice spacing d_{hkl}, where (hkl) are the Miller indices. The variable n represents the integer multiple of the wavelength that path length differences between exiting X-Rays need to equal for constructive interference. Multiple Bragg peaks in a diffraction pattern therefore represent the different lattice spacings for different Miller indices present in the crystal.

In order to extract sample data with reliable statistical relevance, a large number of grains should be illuminated with the X-Ray beam. The X-Ray beam size should therefore be chosen to be significantly larger than the expected crystallite size. When the beam interacts

with a large number of randomly oriented crystallites, a large number of them will be meeting the Bragg condition at random azimuthal angle. As a result, so called Debye-Scherrer cones are formed for different lattice spacings as shown in Figure 15, which can be collected with the help of an area detector.

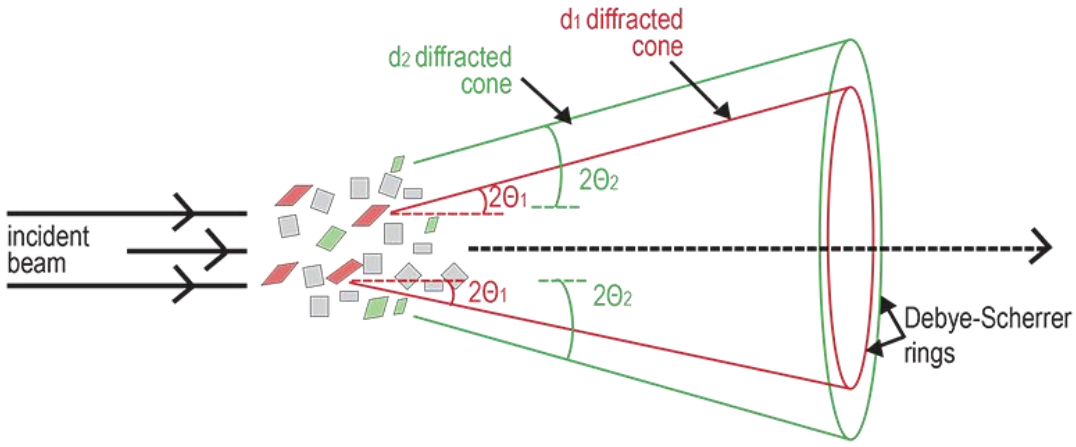


Figure 15. Illustration of Debye-Scherrer cone formation from powder diffraction [31]

Depending on the experimental details and the sample thickness, WAXS can either be collected in transmission or reflection mode. Both geometries were used in this thesis, depending on whether local probing or in-plane averaging was required for the specific experiment. The main advantage of in-plane averaging of thin film material in grazing incidence mode are the significantly enhanced sampling statistics, which provide average material properties over a large surface area. An example for this is shown in Figure 27 (§3.1). On the other hand, local elastic strains can only be probed in transmission mode, thus providing a sampling area equivalent to the beam size. In addition to the sample diffraction pattern acquisition, calibration sample diffraction patterns in transmission geometry are collected for each experiment, as these produce well known Debye-Scherrer rings which – in combination with a known beam energy- can be used to determine the exact sample-detector distance and beam centre position using 2D software fitting tools, such as DAWN [32].

Following initial calibration, measured 2D diffraction patterns are reduced to line profiles, as shown in Figure 47 and Figure 48 (§3.2). Based on a Gaussian fit of the 2θ peak position in combination with equation (1), key insights into sample properties can be obtained, which have been used across this thesis:

1. The local unit cell lattice parameters can be calculated based on the knowledge of the d-spacing, the Miller indices (hkl) and the crystallographic system. For a cubic lattice for instance, the relation between d-spacing, Miller indices and lattice parameter *a* can be expressed as

$$\frac{1}{d_{hkl}^2} = \frac{h^2 + k^2 + l^2}{a^2} \tag{2}$$

2. Local lattice strains can be calculated by comparing the measured d-spacing d_{hkl} with the unstrained d-spacing d_{hkl}^0 as follows:

$$\varepsilon_{hkl} = \frac{d_{hkl} - d_{hkl}^0}{d_{hkl}^0} \tag{3}$$

   A main challenge of this strain determination methods is the required knowledge of d_{hkl}^0. While text book values for d_{hkl}^0 can be used in theory, the difference in sample manufacturing and experimental setup make this particularly challenging. An alternative is the acquisition of diffraction patterns at a sample edge, which can be considered to be stress free. Other experimental methods have been introduced to overcome this issue, which will be presented later in this chapter. It is worth noting that strain direction is proportional to the Debye-Scherrer cone deformation direction.

It is therefore possible to separate horizontal and vertical strains by integrating only over the relevant azimuthal sections, as shown in Figure 47.

3. The grain size of nano-crystalline material can be estimated by employing the Scherrer equation, which relies on the identified Full Width at Half Maximum (FWHM) as follows:

$$\tau = \frac{K\lambda}{\beta \cos(\theta)}, \tag{4}$$

with the crystallite size τ, shape factor K, X-Ray wavelength λ, FWHM in radians β and Bragg angle θ.

2.3.2 Grazing-Incidence Small-Angle X-Ray Scattering (GISAXS)

Over the past few years, GISAXS has become an increasingly popular technique for the characterisation of thin films and coatings, as well as nano particles. This highly surface sensitive technique relies on the interaction between X-Rays and periodic sample features and has contributed significantly to the understanding of thin film formation and growth mechanisms. While normally being used in combination with SEM/TEM imaging, GISAXS offers distinct advantages over imaging techniques: no vacuum is required, large-scale averaged sample information is obtained within few seconds, thus permitting *in situ* and *operando* studies, and it is possible to determine the structure and properties of buried layers. The main drawbacks, however, are the required synchrotron setup, as well as the complex data analysis and interpretation. GISAXS is typically carried out at a beam energy between 5-20 keV, as this optimises the scattering to absorption ratio. A grazing incidence angle α_i is

chosen between 0.05° and 0.50°. The scattering geometry is shown in Figure 16. The incoming monochromatic X-Rays are scattered by the sample at an angle α_f.

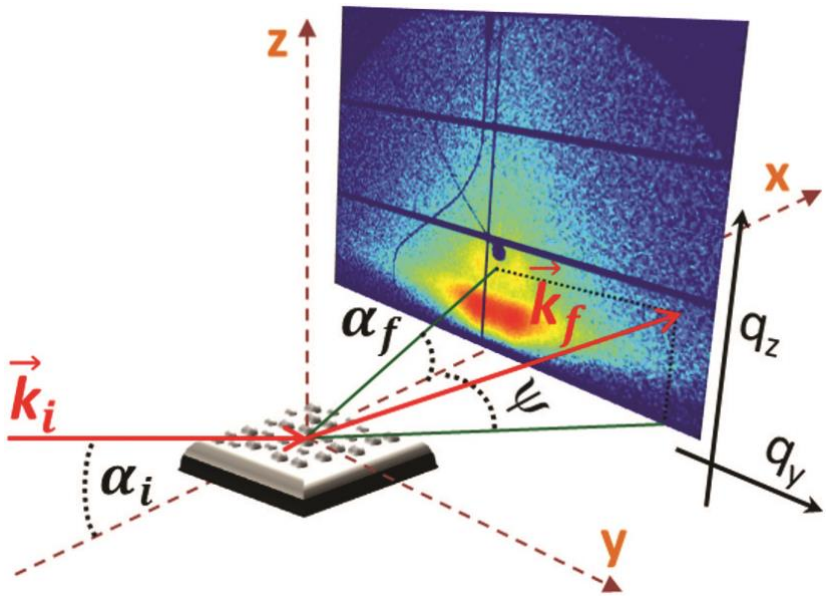


Figure 16. GISAXS Geometry and pattern [33]

The scattering vector can then be expressed as

$$q_{x,y,z} = k_f - k_i = \frac{2\pi}{\lambda}\begin{bmatrix}\cos(\alpha_f)\cos(\Psi) - \cos(\alpha_i)\\ \cos(\alpha_f)\sin(\Psi)\\ \sin(\alpha_i) + \sin(\alpha_f)\end{bmatrix}, \quad (5)$$

with the angles α_i, α_f and Ψ as shown in Figure 16. A sample-detector distance between 1 and 4 m is normally chosen for GISAXS, permitting the capture of feature sizes between few nanometres and several hundred nanometres. The high intensity of the specular beam reflection is normally blocked by a beam stop, in order to prevent detector damage, which can be seen as black circle in Figure 16. The scattering intensity depending on the lateral electron density variation can then be described as:

$$\mathrm{I}(q) = \langle|\mathrm{F}|^2\rangle \mathrm{S}(q_{\parallel}), \tag{6}$$

where the scattering Intensity I(q) can be split into a form factor F and an interference function $\mathrm{S}(q_{\parallel})$. The form factor can be expressed as Fourier transform of the scattering object shape:

$$\mathrm{F}(q) = \Delta\rho \int \mathrm{e}^{iq\cdot r}\, \mathrm{d}V \tag{7}$$

Further effects that need to be accounted for are reflection-refraction effects occurring at substrate-layer and layer-layer interfaces, which make an analytical interpretation of experimental GISAXS patterns particularly challenging. For this reason, a forward modelling approach was chosen in this thesis, which involved the simulation of sample geometry obtained by other techniques, followed by refinement in order to match observations. For the analysis of GISAXS data in §4.2 the BornAgain software package [34,35] was used, which permits the creation of repetitive surface and buried layer features on a repetitive grid. An overview over different primitive shapes available in BornAgain are shown in Figure 17a, while the resulting patterns obtained from the Born approximation are shown in Figure 17b, respectively. Different particle and layer materials are taken into account by their refractive index

$$n \equiv 1 - \delta + i\beta\,, \tag{8}$$

with real material-specific parameters δ and β. The real part of the phase velocity is related to δ, while the so-called extinction coefficient β is related to the linear absorption coefficient.

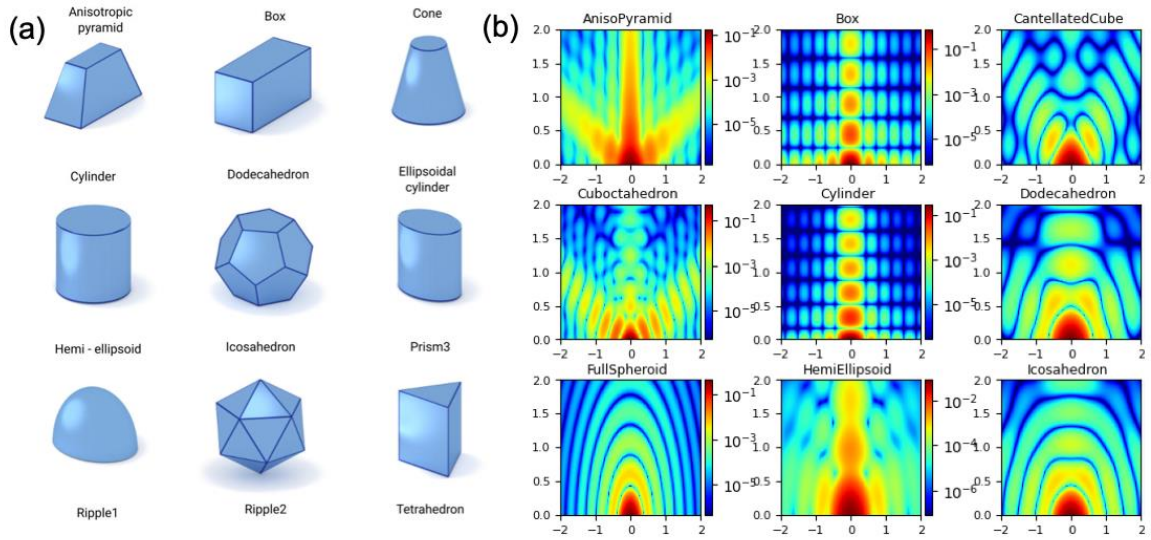


Figure 17a. Primitive shapes available in the BornAgain software package (excerpt), and b. resulting patterns from Born approximation [36].

2.3.3 Coherent Ptycho-Tomography

A recently developed and powerful computational volume imaging technique is ptycho-tomographic imaging, which relies on the acquisition of overlapping coherent diffraction patterns from a sample. This permits reconstructing the image of the sample cross-section, after which the sample is rotated by a small angle and the procedure repeated. Based on the obtained slice reconstructions, a volumetric model of the sample can be computationally reconstructed using iterative algorithms, which then permits looking at desired cross-sections in any orientation. Ptycho tomographic imaging is employed in §5.1, where further details about the reconstruction algorithm and beam conditions are provided.

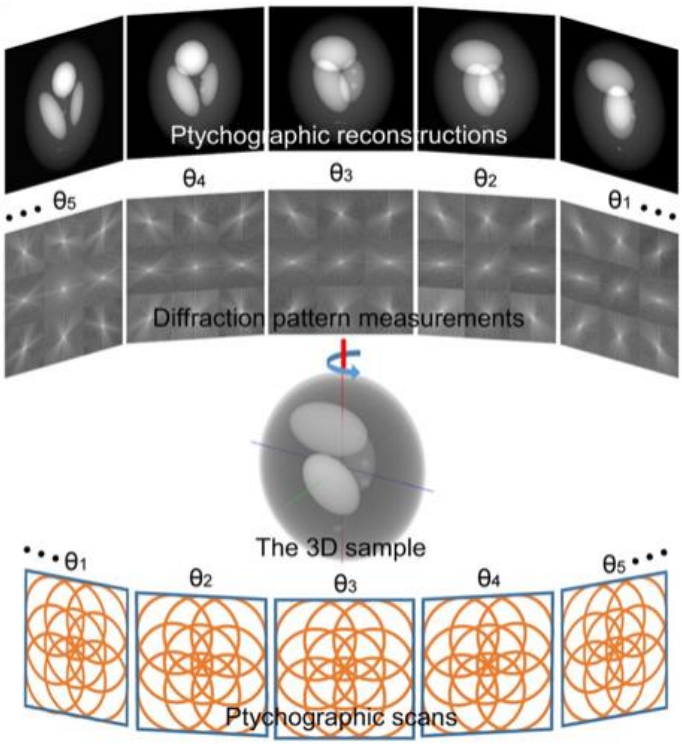


Figure 18 3D Ptycho Tomography: schematic diagram [37]

2.3.4 $\mathrm{Sin}^2(\Psi)$ technique

As mentioned in the description of X-Ray powder diffraction in §2.3.1, a stress-free reference lattice parameter d_0 is normally required for strain and stress quantification. As the determination of this parameter is usually - if at all possible - challenging, the $\sin^2(\Psi)$ technique can be employed for the determination of residual stress. The technique is particularly popular, as it can be carry out in laboratory X-Ray diffractometers at comparably low X-Ray energy. It relies on lattice parameter change measurements collected at different sample tilt positions on the same location of the sample, resulting in an angle Ψ between the sample surface normal and the scattering vector, as shown in Figure 19.

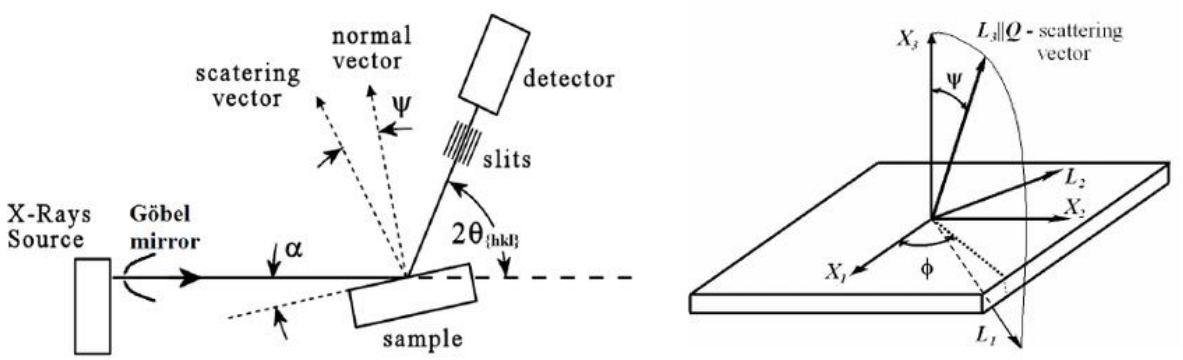


Figure 19. Geometry of the $\sin^2(\Psi)$ technique [38]

When plotting the observed strain versus $\sin^2(\Psi)$, the most general analytical formation is an ellipsoid:

$$\varepsilon_\Psi = \frac{d_\Psi - d_{\Psi=0}}{d_{\Psi=0}} = \boldsymbol{A} + \boldsymbol{B}\, sin^2\,\Psi + \boldsymbol{C}\, sin(2\Psi),$$
$$\mathbf{A} = \frac{1}{\mathrm{E}}\{\sigma_{33} - 2\nu\sigma_{11}\}, \mathbf{B} = \frac{1+\nu}{\mathrm{E}}\{\sigma_{11} - \sigma_{33}\}, \mathbf{C} = \frac{1+\nu}{E}\sigma_{13}. \quad (9)$$

An alternative to measurements involving point detector line profile acquisition and diffractometer tilt for Ψ variation is the $\sin^2(\Psi)$ analysis using high energy synchrotron radiation at grazing angle. Due to the shallow angle of the incoming X-Ray beam, Debye-Scherrer rings collected using a 2D area detector can be used for $\sin^2(\Psi)$ analysis without stage tilt, thus permitting to obtain the residual stress state in thin films with a single frame acquisition. In post-processing, the Debye-Scherrer rings are subdivided into several azimuthal bins, the angle of which can be approximated as Ψ tilt. This method has been used for the thin film residual stress determination in this thesis. It can be seen from equation (9) that the three-dimensional residual stress state can be extracted from nonlinear least square ellipse fitting, as has been carried out in §3.1. Subsequent strain and stress evolution can then

be monitored by simple WAXS, as the reference stress is known. Further details regarding data processing are provided in the chapter.

2.3.5 X-Ray Reflectivity

For the analysis of thin films and multilayer coatings, XRR is an indispensable tool. It relies on the observation of the specular peak intensity with varying incident and reflected beam angle in $\theta - 2\theta$ geometry, as shown in Figure 20. When performed at a synchrotron radiation source, the incident beam is fixed and the sample is rotated at an angle θ, with a point or 2D detector mounted onto a diffractometer arm at varying angle 2θ. When an area detector is used, the overall image intensity can be integrated and reduced to a single data point.

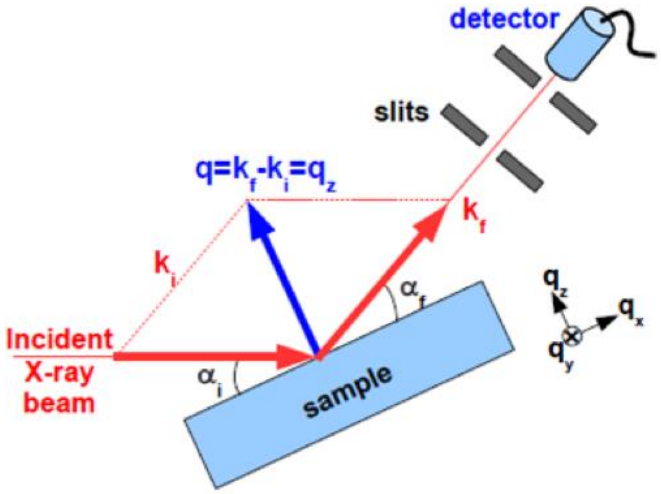


Figure 20. X-Ray Reflectivity Geometry [39]

Based on the phase velocity related material parameter δ in the refractive index (equation (8)), a proportional relation between the measured reflected intensity I and the layer thickness d can be expressed as

$$I \propto \cos\left(\frac{4\pi d}{\sqrt{\sin^2(\theta - 2\delta)}}\right). \tag{10}$$

Based on the deviation from the predicted Fresnel reflectivity intensity profile, layer roughness, thickness and density can be extracted using multi-parameter fitting software such as GENX [40]. The influence of surface roughness, layer thickness and density of a single layer on substrate is shown in Figure 21. This knowledge has been used in §4.2 of this thesis to analyse the dynamic changes within nano-multilayers at elevated temperatures.

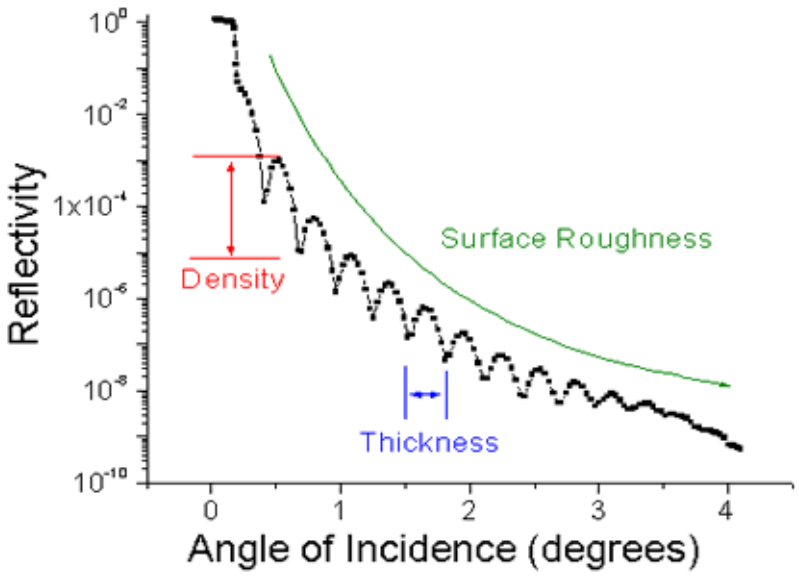


Figure 21. Influence of single layer thickness, density and surface roughness on the obtained X-Ray Reflectivity profile [41].

2.4 Microscale Mechanical Characterisation

Advanced mechanical characterisation techniques for the determination of local residual stresses, which require computational processing of FIB/SEM data are presented in this section. Residual stress is normally introduced into thin films and nano-multilayers by energetic PVD or thermal mismatch between substrate and coating – both of which result in a uniform equi-biaxial stress state across the sample a scale between 10^{-6} and 10^{-3} m. When looking at the (sub-)nanometre scale, however, the residual stress distribution shows increased variation between bulk material, grain boundaries and defects. This scale-

dependent residual stress state can be classified into Type I, II and III residual stress. While Type I represents the macroscopic residual stress, Type II refers to the grain average and Type III to stresses arising at the atomic level, which are for instance caused by defects. These residual stresses at different scales are additive and can be expressed as

$$\sigma^{RS} = \sigma^{RS,I} + \sigma^{RS,II} + \sigma^{RS,III} \tag{11}$$

A schematic representation of the multi-scale nature of residual stress in polycrystals is shown in Figure 22.

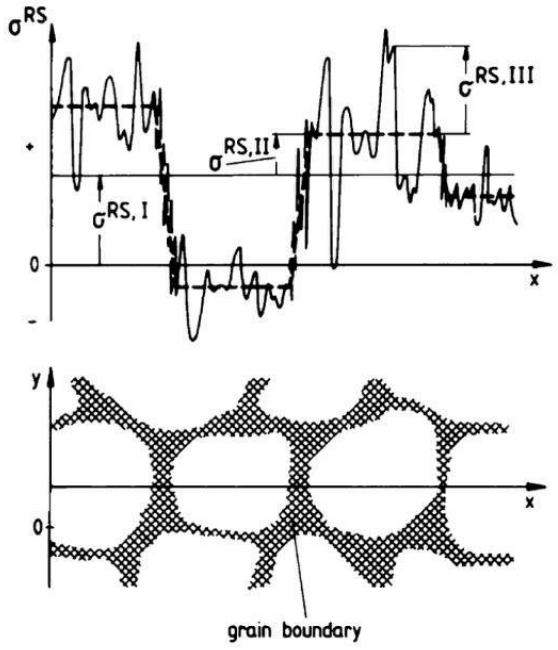


Figure 22. Variation of residual stress at different scales in polycrystalline materials [42].

Due to the nano-crystalline properties of thin films and ultra-thin films, attempts at probing the residual stress state with FIB-SEM methods can only deliver the Type I residual stress, which is averages over a large number of grains. Insights into Type II and III residual stress

can therefore only be obtained by TEM analysis. For the purpose of this thesis, two FIB-SEM techniques for the determination of Type I residual stress have been employed and will be presented in the following.

2.4.1 Focused Ion Beam – Digital Image Correlation

The combination of FIB ring-core milling with DIC provides a powerful and flexible tool for profiling and mapping absolute residual stress values at the micron scale. Several steps are required to obtain the in-plane stress values within the gauge volume defined by the central island in the ring-core geometry from the strain relief profiles. First, a ring-core with a diameter of between 2-20 μm is milled into the sample surface in a step-wise fashion by using the Focused Ion Beam. In between the milling steps, high resolution SEM images (Figure 23a) are acquired. This process is terminated at the milling depth which guarantees complete strain relief. Subsequently, a MATLAB-based Digital Image Correlation package [43] is employed to track the displacements of points at sample surface (tracking markers), as illustrated in Figure 23b. By determining the slope of the displacement versus position, the strain change (relief) can be determined for each step in comparison with the initial, residually stressed state, as shown in Figure 23c. As the FIB milling progresses towards greater depths, the relief strain saturates and reaches a constant value, as can be seen on the stress relief profiles in Figure 23d.

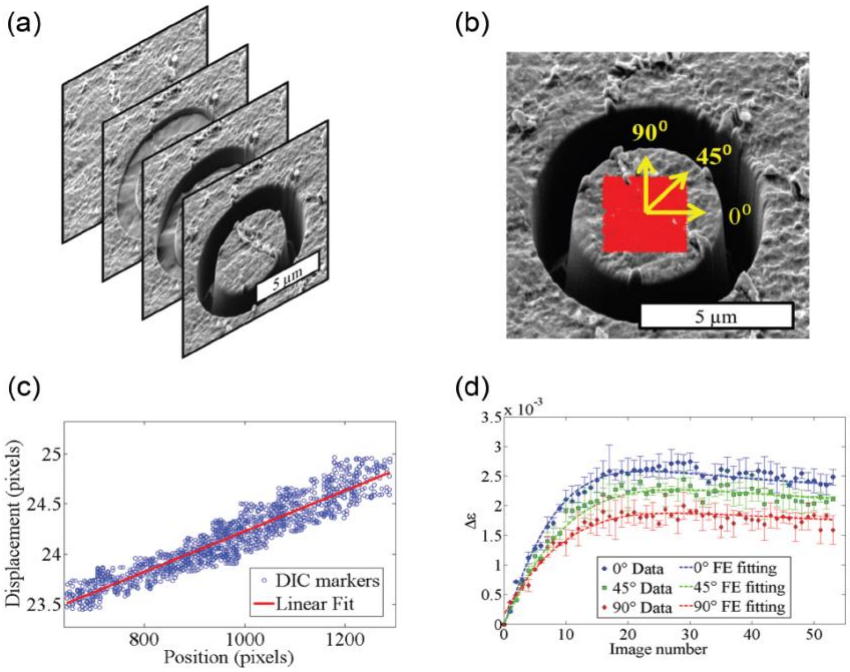


Figure 23. Steps required for a local two-dimensional stress analysis. (a) Incremental acquisition of SEM images during milling. (b) DIC marker tracking on the central core region. (c) DIC marker displacement compared to their reference position (points) and averaged displacement (red line). (d) Strain relief analysis based on the DIC marker displacement evolution.

A large amount of information can be extracted from the strain relief profiles. Firstly, the average residual stress in the central material island can be determined. From the complete elastic strain relief values $\Delta\varepsilon_{yy}^{\infty}$ for multiple directions, the residual stresses in the two principal directions, σ_{xx} and σ_{yy} can be calculated using Hooke's law and a knowledge of material elastic constants:

$$\sigma_{xx} = -\frac{E}{1-\nu^2}\left[\Delta\varepsilon_{xx}^{\infty} + \nu\Delta\varepsilon_{yy}^{\infty}\right] \tag{12}$$

$$\sigma_{yy} = -\frac{E}{1-\nu^2}\left[\Delta\varepsilon_{yy}^{\infty} + \nu\Delta\varepsilon_{xx}^{\infty}\right] \tag{13}$$

The negative sign introduced for the conversion from strain to stress in equations (12), (13) reflects the fact that the elastic strain relief of the central material island probed by DIC is directed in opposite direction to the residual stress. This means, for instance, that material under tensile residual stress will undergo contraction upon stress relief.

To obtain the complete elastic strain relief value $\Delta\varepsilon_{yy}^{\infty}$, a fitting function derived from finite element simulations of the strain relief in the central material island is employed:

$$f\left(\Delta\varepsilon_{yy}^{\infty}, z\right) = 1.12\Delta\varepsilon_{yy}^{\infty} \cdot \frac{z}{1+z}\left[1 + \frac{2}{1+z^2}\right], \tag{14}$$

where $z = (h/0.42D)$. The process for point-wise residual stress evaluation can be repeated for multiple ring-core features placed across the Region of Interest (RoI) to obtain the desired stress profile. For large grained polycrystalline materials with a grain size in the order of several microns, the variation of the ring-core diameter permits probing Type I and Type II residual stress, as shown in Figure 24. Due to the very fine grain structure of thin films, even the smallest ring-core diameter of 2 µm is significantly above the nano-scale grains, thus providing a measurement for the Type I residual stress.

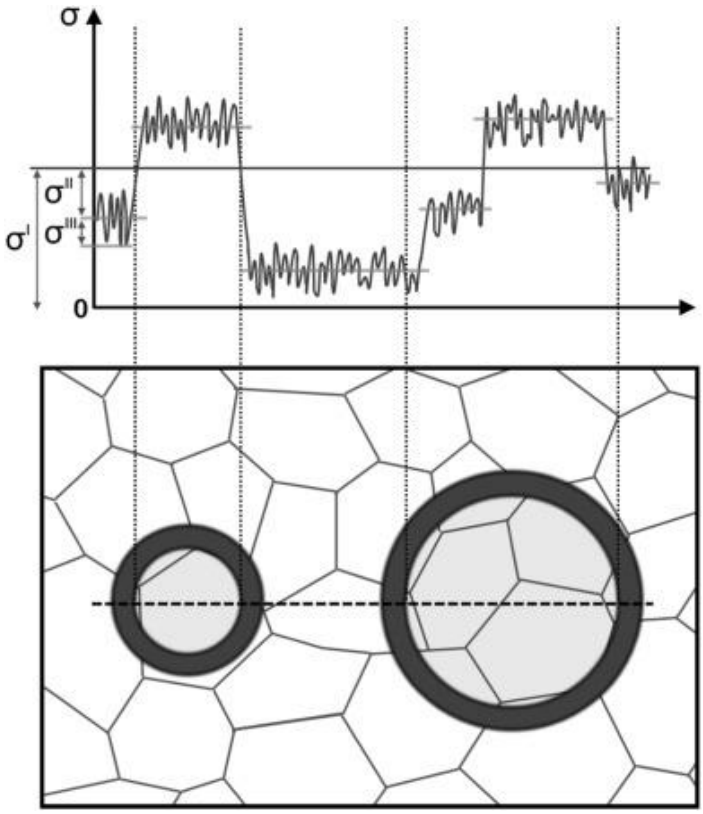


Figure 24. Illustration of Type II and III residual stress probed by FIB-DIC ring-core markers of different diameter.

Additional information can be extracted from the strain relief profiles by means of FIB-DIC depth profiling, which permits the local resolution of residual stresses versus milling depth. For this purpose, the unknown eigenstrain distribution versus depth needs to be reconstructed based on the observed surface strain relief. At the depth *h*, the strain relief *e* can be formulated as

$$e\left(\frac{h}{D}\right) = \int_0^{\frac{h}{D}} \mathrm{F}\left(\frac{z}{D}\right) \varepsilon^*(z)\, d\left(\frac{z}{D}\right), \tag{15}$$

with the normalised depth *h/D* with respect to the ring-core diameter *D* [44]. *Z* is the eigenstrain-dependent depth $\varepsilon^*(z)$, and $\mathrm{F}\left(\frac{z}{D}\right)$ is a single variable influence function describing the incremental contribution to the surface strain relief from eigenstrain. To obtain the local depth-resolved eigenstrain distribution, equation (15) can be obtained with respect to *h/D* via differentiation:

$$\varepsilon^*\left(\frac{h}{D}\right) = \frac{\frac{\mathrm{d}e(h/D)}{\mathrm{d}(h/D)}}{\mathrm{F}\left(\frac{h}{D}\right)} \tag{16}$$

The depth-resolved in-plane strain can then be calculated as

$$\varepsilon = -\varepsilon^*, \tag{17}$$

which yields the residual stress given known elastic material constants. FIB-DIC residual stress depth profiling is used in this thesis for the analysis presented in §3.1.

2.4.2 Micro-Cantilever Deflection Analysis

Finally, a method for the uniaxial stress determination in thin films is micro-cantilever deflection analysis, which is used as complementary method in §3.1 for stress value confirmation. For this method, a cantilever of several micron size is freed of surrounding material using FIB. Depending on the prevailing residual stress state, the cantilever deflects upwards for tensile residual stress or downwards for compressive residual stress, as shown in Figure 25. Based on SEM measurements of the tip deflection and known cantilever geometry, the residual stress state can be calculated. The analytic expression for the stress determination based on classic beam bending theory is provided in §3.1, where micro-cantilever deflection was employed as an independent technique for the confirmation of FIB-DIC measurements.

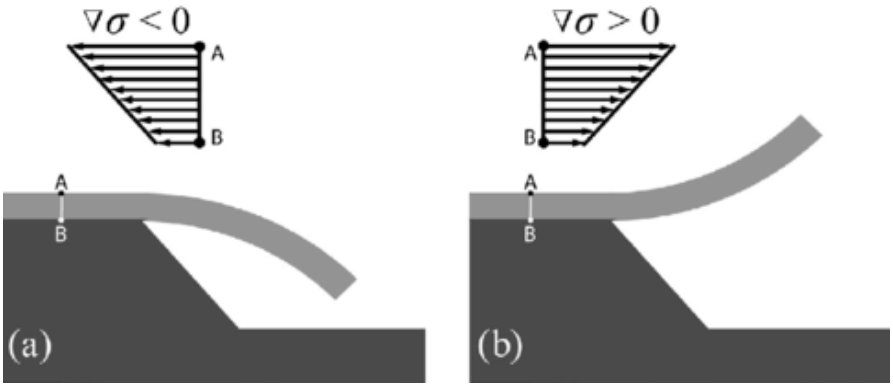


Figure 25. Residual stress dependent micro-cantilever deflection for in-plane a. compressive residual stress b. tensile residual stress [45].

3 The effect of energetic deposition conditions on the mechanical properties of thin films

3.1 Nano-scale residual stress depth profiling in Cu/W nano-multilayers as a function of magnetron sputtering pressure

3.1.1 Introduction and Literature Review

Nano-multilayers allow for the design of materials with unique mechanical, electrical, optical and functional properties by combining the advantages of different materials in a layered structure [46]. Copper and tungsten (Cu/W) multilayers are promising candidates for the thermal management at micro and nano scale, combining the excellent thermal and electrical conductivity of Cu with the low thermal expansion and high mechanical strength of tungsten [47–49].

Magnetron sputter deposition as one of the most popular PVD methods includes a wide range process parameters, such as the argon working pressure, the target power and the substrate bias and temperature. These parameters can be used to fine-tune the stresses and the microstructure at the nanoscale during deposition [50]. Influencing factors have been systemically studied for decades [51], however, thicknesses used in technology have reduced significantly since then, away from several micrometre thick coatings towards the (sub-) nanometre scale, while the demands for thermal and mechanical reliability have increased. To bridge this gap, thorough knowledge of the relationship between deposition parameters and spatially resolved thin film properties are required. In the same time, analysis methods have improved significantly, allowing deeper insights into material property distributions as ever before.

Accurate estimations of residual stress are a key factor for their reliability design of nanostructured thin films and coatings [52]. Many applications, such as microelectronics, Micro Electromechanical Systems (MEMS), and sensors rely on the structural integrity of coatings, which are often only few nanometres thick. The arising complex stress field during energetic deposition, such as magnetron sputtering, is difficult to predict accurately, due to the number of interlinked mechanisms at atomic level involved [53]. Experimental measurements are therefore of crucial importance for understanding and designing the residual stress in thin films.

Recent advances in the resolution of combined FIB-SEM devices have allowed for the development of new methods for the spatially resolved study of residual stresses at the nano scale [54]. Two main approaches have been presented recently: cantilever-based [19,55] and ring-core based [56,57]. The first type relies on deflection measurement of a coated cantilever, while removing individual material layers with the FIB and observing the change of deflection, allowing to calculate the stress state of the coating at a resolution of around 50 nm. The advantage of this method lies in the fact that no surface preparation is required, as the deflection is easily measurable. A clear disadvantage, however, is the fact that the cantilever is usually being milled on an edge of the sample, which requires sample cutting at the risk of stress field modifications. Sectioning the sample in preparation for cantilever milling thus carries the risk of disturbing the pre-existing stress field.

Ring-core based techniques rely on the creation of a stress-free material island by step-wise material removal [58]. During strain relief, frames are being acquired, which later allow for the reconstruction of the residual stress state. As this method requires a very high level of accuracy in surface point correlation via DIC, patterned surfaces need to be prepared for this method. One large advantage, however, is the possibility to probe the stress state at any location on the sample without altering the stress state. In addition, the milling times required

are significantly lower as compared to micro-cantilevers, with a duration of around 20-40 minutes per measurement point, depending on the ring-core diameter. For this analysis, the ring-core depth profiling method was employed [58], which will be further explained in the following section. To confirm the FIB-DIC results, a micro-cantilever was milled in the centre of the sample and the deflection profile was extracted.

Finally, major advances regarding the availability, brilliance and focusing capability of synchrotron light sources in the recent years have allowed to perform spatially resolved stress measurements of thin films and coatings by nano-diffraction. Albeit very complex sample preparation, this method permitted reliable insights into the residual stress state of coatings [59]. To confirm and expand the insights gained from the FIB-SEM methods, we employed classic wide-angle X-Ray diffraction for $\sin^2(\psi)$ analysis [53,60,61] to extract averaged residual stress magnitude present in the multilayer. The results presented in this section will be thoroughly discussed.

The residual stress variation during nucleation, grain boundary formation, single film growth and multi-layer deposition is complex and combines several mechanical effects. Understanding how the residual stress in nano-multi-layered systems arises during deposition at different working gas pressures therefore requires breaking the deposition process into smaller, mechanically meaningful intervals. In a first step, a single layer of tungsten is being deposited onto a Si substrate. Subsequently, the deposition is interrupted for a short period of time, after which a layer of copper is grown on the tungsten surface. This process is then being repeated for further nine bilayers of Cu/W. During these individual deposition steps, the residual stress within the coating changes significantly.

During nucleation and island growth on the substrate, the global average stresses are close to zero, due to the lack of a uniform film [53]. After the initiation of island coalescence, the residual stress becomes tensile, as the free surfaces convert into grain boundaries. During

this process, it is of energetic advantage for the islands to accommodate internal tensile strains in order to form a uniform film and share grain boundaries with neighbouring islands [62]. As soon as the film has grown to a uniform layer, the effects of energetic particle bombardment begin to dominate the stress state. The phenomenon, known as 'atomic peening', affects the residual stress state significantly [63]. Highly energetic particles impacting the surface lead to recoil implantation of coating surface atoms and integration of argon atoms into the films. More specifically, the impact of particles on the surface also incorporates defects into the structure through displacement sequences within the grains [53]. The momentum propagation during magnetron sputter deposition can lead to both the motion of atoms to energetically favourable sites, such as vacancies, but also to the creation of point defects such as interstitials. These effects add up to a highly densified layer, which is stored mechanically as compressive residual stress.

Changing the in chamber pressure modifies the stress state significantly – a phenomenon that has been well-known for many years [51]. Several phenomena contribute to this effect: firstly, the larger quantity of Ar atoms in between the sputtering target and the sample surface result in a significantly lower mean free path length for the sputtered Cu and W atoms. The atomic peening effect is therefore reduced by a significant amount, as there is a larger momentum transfer between the working gas and the sputter material, resulting in a lower impact energy at the sample surface. This also leads to a reduced level of atomic implantation in between the grain boundaries. Finally, in addition to the lack of atomic peening and grain boundary implantation, a high working pressure inside the magnetron chamber leads to the tensile stress due to the formation of an under-dense columnar growth morphology, which is typical for refractory metals such as tungsten [53].

3.1.2 Material and methods

3.1.2.1 Multilayer deposition

Five multilayer systems were deposited onto naturally oxidized monocrystalline silicon (001), which were cleaned prior to deposition by acetone and ethanol rinsing, and dried under nitrogen flow. The working pressure (P) was varied from sample to sample using the following chamber pressures: P_1 = 0.50 Pa, P_2 = 0.66 Pa, P_3 = 0.74 Pa, P_4 = 0.81 Pa and P_5 = 0.89. Before deposition, the target was clean sputtered while the substrates were protected by a shutter. Each multilayer consists of ten bilayers of Cu/W 50/50 nm thin films were deposited at room temperature (RT) by planar magnetron sputtering in DC mode using Ar as working gas in a high vacuum system (base pressure ~$1 \cdot 10^{-5}$ Pa), resulting in a total film thickness of 1 μm. The sputtering rate was calibrated using X-ray reflectometry (XRR). Each of the W and Cu targets were 7.6 cm in diameter, with a purity 4N (i.e., 99.99%). The thin films were deposited at a constant target power of 130 W, using unbalanced magnetron, on grounded rotated substrates. The target-to-substrate distance was 18 cm.

3.1.2.2 FIB-DIC ring-core depth profiling

The FIB-DIC ring-core method is a well-established and thoroughly verified method for the semi-destructive probing of residual stresses at the micron scale. It is based on the gradual removal of material in a ring-core shape (Figure 26) with the intermediate acquisition of SEM frames at each milling steps. Mechanically disconnecting the central material 'island' from the surrounding strain field leads to a full elastic strain relief. This can be observed by tracking surface points of the central island using DIC in post-processing at an accuracy of around $\varepsilon \approx 10^{-5}$, which can then be used to back-calculate the average residual stresses present in the probed volume prior to milling, if the elastic properties of the material are known. Recent

advances in this technique allow to extract the depth-dependant stress and strain profiles in milling direction, based on the FIB-DIC strain relief profiles and by employing the eigenstrain theory [9].

As the DIC requires a trackable surface pattern to correlate images from different milling steps without altering the residual stress state of the samples measurably, a 4.1 nm thin Au/Pd layer was deposited on top of the multilayers using a commercial sputter coater (SC7620, Quorum Technologies) at a sputtering rate of 0.092 $nm \cdot s^{-1}$. A fixed target-to-sample distance of 45 mm was chosen, and the process current was adjusted to 18 mA. Subsequently, the surface was exposed to the FIB at a low beam current of 0.20 nA at 30 kV, creating a nanoscale surface speckle pattern [64] without affecting the multilayer beneath. This was confirmed by cross-sectional high-resolution SEM imaging. To confirm that the Au/Pd contrast layer did not alter the residual stress state in the multilayer systems, a 30 nm thin layer of Au/Pd was deposited on a 75 μm Kapton substrate, while the curvature was recorded *in situ*. The substrate did not show any change in curvature, confirming that the residual stress within the DIC contrast layer can be neglected for further analysis.

Subsequently, ring-cores of three different diameters were milled step-wise into the sample using FIB. The diameter of the ring-core was chosen according to the desired depth-sensitivity, as the sensitivity for strain reconstruction is limited to a depth-to-diameter ratio of h/d = 0.4. In the final analysis, a maximum of h/d = 0.25 was used. As a consequence, the chosen ring-core diameters for this analysis were D_1 =10 μm, D_2 = 5 μm and D_3 = 3 μm, and for each diameter three ring-cores were produced to minimise the statistical scatter of results (Figure 26). While D_3 returned the best depth resolution for the coating, D_1 probed further into the substrate and was used to analyse the interaction between substrate and coating. D_2 as intermediate diameter improved the data statistics of both the coating and the upper part of the substrate by providing additional data points. The FIB was operated at a beam energy of

30 keV and a beam current of 0.20 nA for the D_1 and D_2 ring-cores. For the D_3 ring-cores, however, a lower beam current of 0.04 nA was chosen to minimise the ion beam damage [65–68] of the smaller central island surface area. After each milling step, five SEM images were acquired for DIC analysis to improve the tracking statistics. As each ring-core affects the residual stress field due to local strain relaxation, the correct spacing needs to be chosen in between measurement points. It was shown that a distance in between ring-cores of five times the ring-core diameter is sufficient to avoid any mechanical interaction between points [54]. Therefore, the distance in between points corresponds to 5·D of the larger ring-core, respectively (Figure 26).

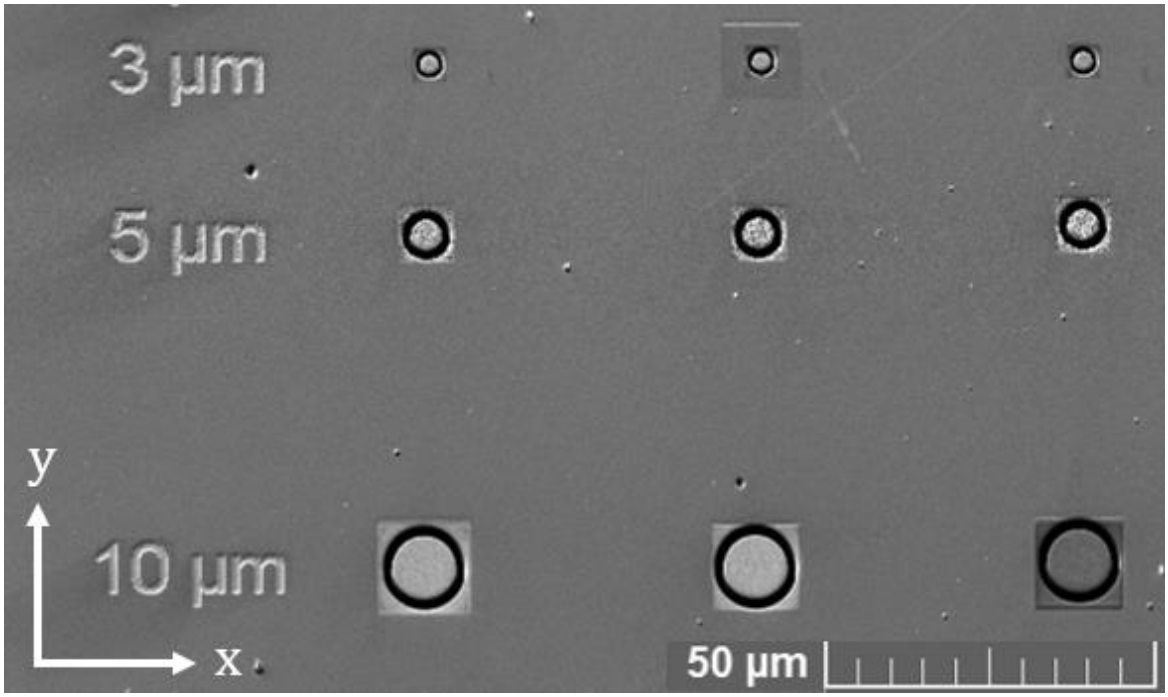


Figure 26. Arrangement of FIB markers for DIC depth-profiling analysis. Ring-core diameter indicated on the left.

3.1.2.3 Synchrotron XRD

To confirm the obtained FIB-DIC measurements, WAXS experiment was performed at the B16 beamline at Diamond Light Source (UK) in grazing angle scattering geometry. The

chosen photon energy was 18 keV with a beam size of 250·250 μm^2, collimated by crossed slits, and a grazing angle of α = 1°, resulting in a large interaction volume of the beam with the coating and therefore improved pattern statistics. The WAXS patterns were acquired for 360 s using an Image Star 9000 detector at a sample-detector distance of $66 \cdot 10^{-3}$ m, which was calibrated using a Lanthanum hexaboride (LaB_6) sample. The setup is shown in Figure 27.

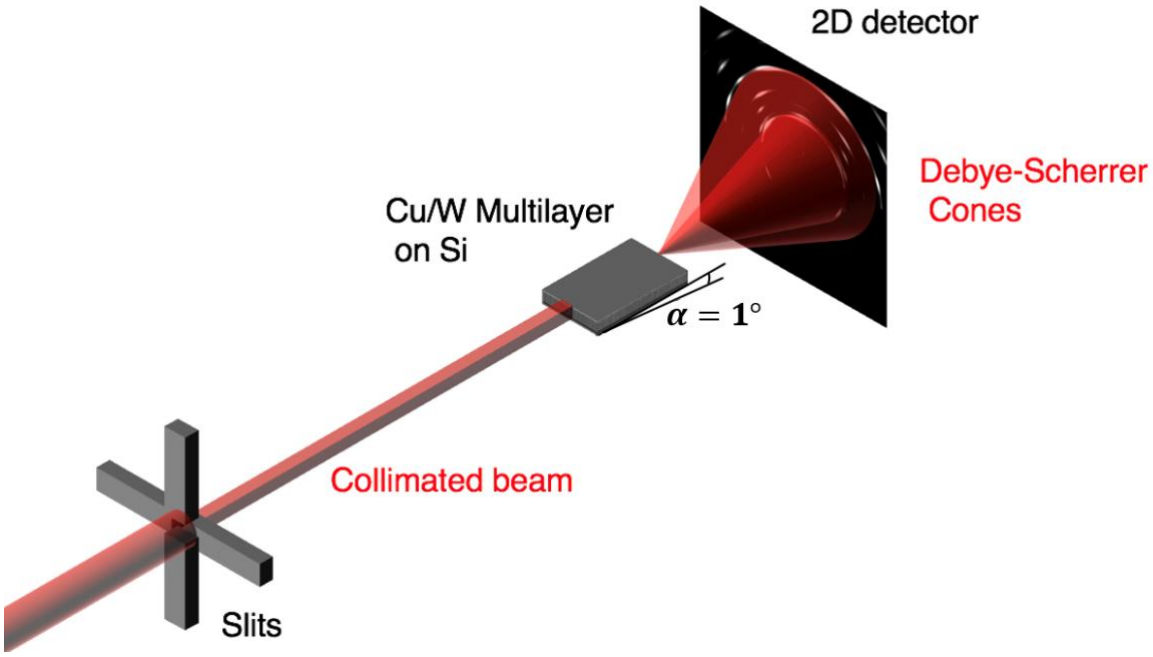


Figure 27. Synchrotron WAXS setup using collimated X-Ray beam and 2D area detector

The obtained WAXS diffraction patterns are shown in Figure 28, along with the identified phases and crystal orientations. Only the upper half of the Debye-Scherrer rings was used for further analysis, as the lower half was mostly absorbed by the substrate and did not contain any additional information for strain reconstruction due to the two-fold symmetry of powder diffraction rings.

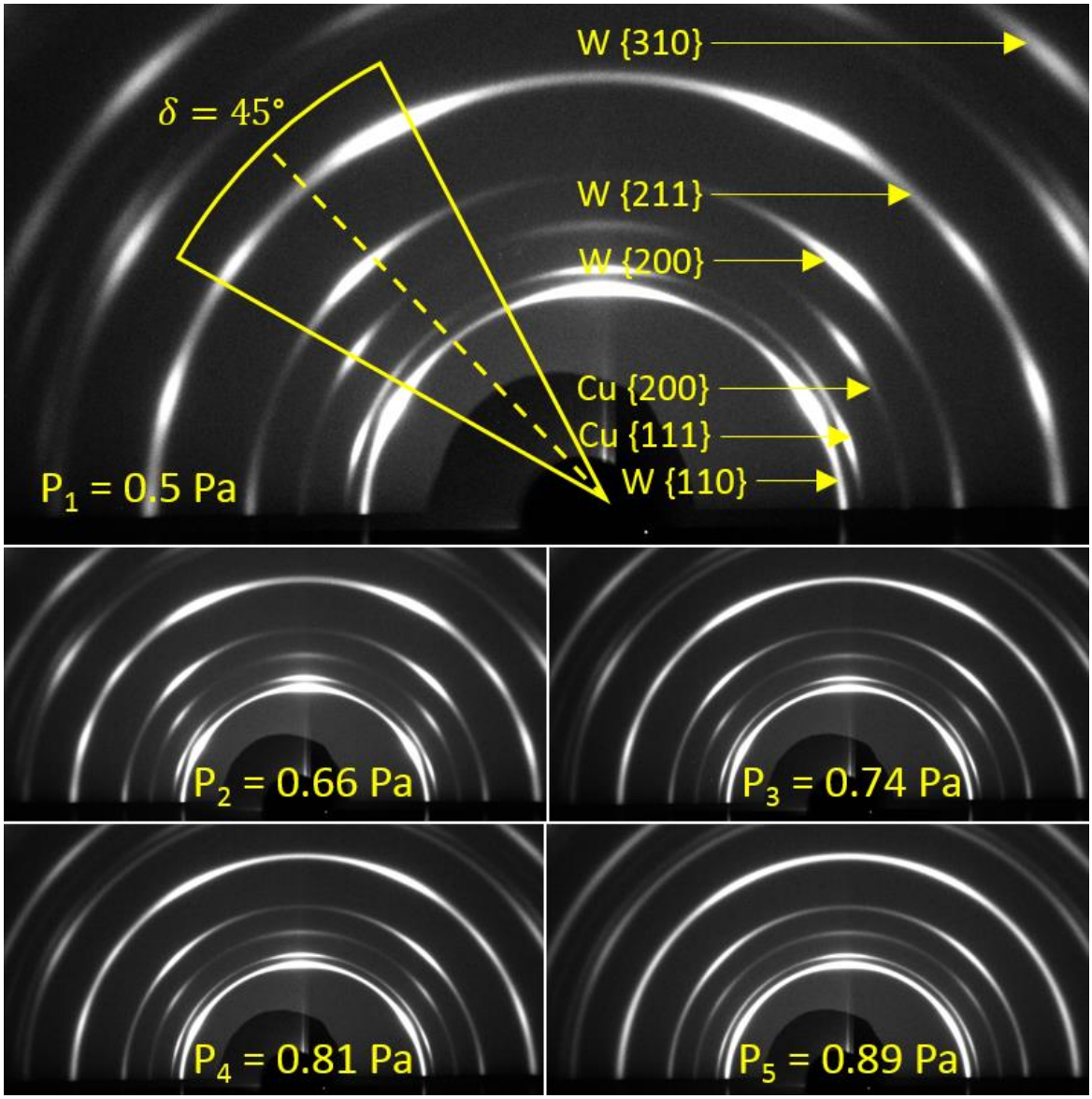


Figure 28. Synchrotron WAXS patterns of Cu/W 50/50 nano-multilayers deposited at different magnetron Ar working pressures. Crystal orientations are identified in the top figure.

3.1.3 Micro-Cantilever Deflection

To cross-check the measured residual stresses within the coating by a further independent method, a micro-cantilever was milled at the centre of the sample deposited at P_1 = 0.5 Pa, using the FIB at 30 keV energy and 0.2 nA beam current, following the early work of Steve Roberts and David Armstrong at the Engineering Department Oxford. In this way, it was

ensured that the analysed stress field was undisturbed, as opposed to machining a micro-cantilever at a cut cross-section. One arising consequence, however, is the non-square shape of the cantilever cross-section caused by the inclined angle during milling, which needs to be accounted for an accurate residual stress reconstruction. Subsequently, SEM frames were acquired at an electron beam energy of 5 keV. Shape, dimensions and deflection of the cantilever are shown in Figure 29a, alongside the measurements extracted from the SEM frames shown in Figure 4b.

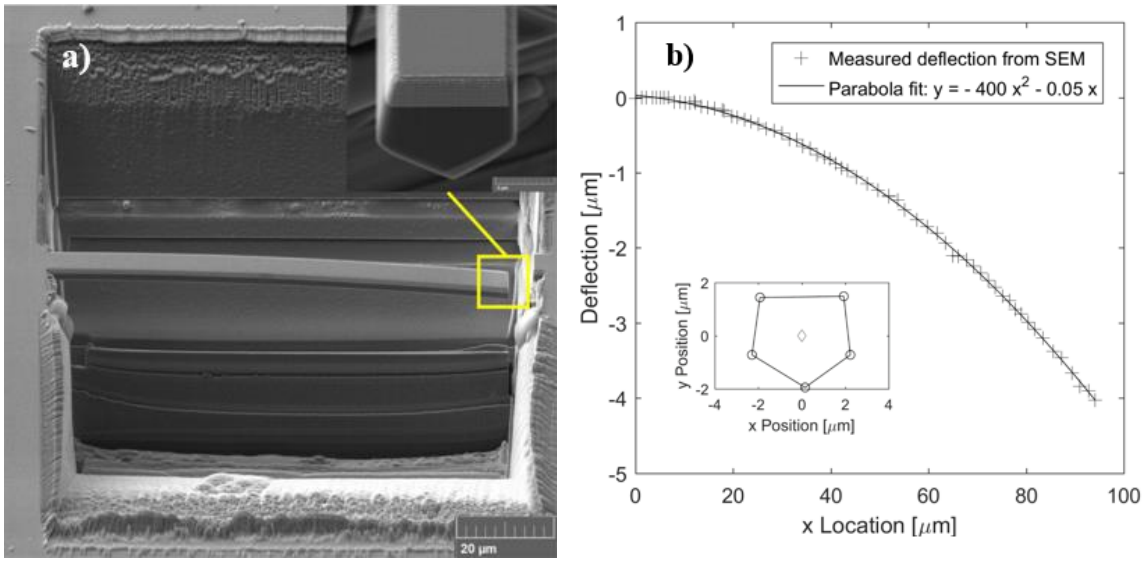


Figure 29a. Deflected micro-cantilever prepared by FIB milling. Top right corner: shape and dimensions of the cross-section, showing a clear contrast between Cu/W coating and Si substrate. b. Deflection measured from SEM data, plotted alongside parabolic fit. Box: cross-section of cantilever from SEM frame.

3.1.4 Calculation

3.1.4.1 FIB-DIC micro-ring-core milling

To obtain full-field displacement and thus strain relief profiles, a MATLAB based DIC software was used to track surface points [69]. Subsequently, the strain relief profiles for the three measurement points of each ring-core diameter were averaged to a single profile. From this averaged strain relaxation profile, the residual elastic strain depth profile was

reconstructed by following the approach described in [58]. The analysis was performed by analysing information provided by the strain relief curves lying within the normalised range $0.015<h/D<0.25$. Where h the milling depth and D is the ring-core diameter [58]. An example of strain relief profiles for the sample deposited at P_5 = 0.89 Pa is shown in Figure 30 for all three ring-core diameters against the FIB material removal depth, h. The 95% confidence interval shown as shaded area around the relaxation profile is determined by two error sources: 1) the uncertainty of the DIC process δ_{DIC}, which is determined by the tracking error of pixels which are smoothed by a Gaussian filter; 2) in order to extract the average strain relief taking place in the central ring-core island monitored by DIC, a first order polynomial is fitted to the displacement across the pillar diameter along the sought direction. The slope of this polynomial corresponds to the relaxation strain, leading to a slope fitting error δ_{fit}. These two errors are then combined by following the appropriate error summation rules.

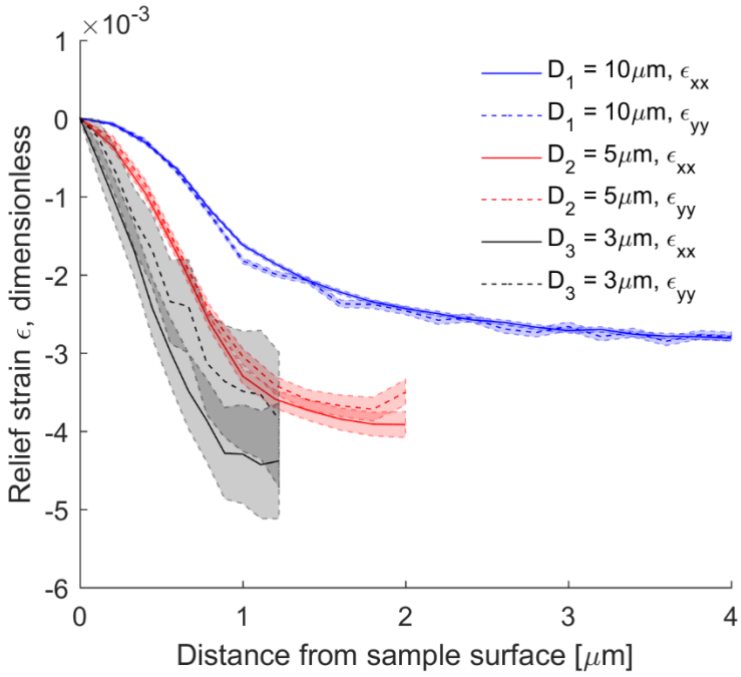


Figure 30. Relief strain for ring-cores of different diameters on the sample deposited at a magnetron working pressure of P_1 = 0.89 Pa. The shaded areas around the plot lines represent the 95% confidence interval. Probing depth and ring-core diameter were varied in order to obtain high resolution DIC data for different probing depths, resulting in high-resolution relief strain profiles ranging from the sample surface down to the substrate-coating interface.

Converting the obtained elastic strains to stresses [58] requires the Young's modulus E and Poisson's ratio ν, which were assumed to be 102 GPa and 0.34 for nano-crystalline Cu and 338 GPa and 0.36 for nano-crystalline W, respectively [46]. These properties were averaged by following the rule of mixture and considering a material ratio of Cu:W of 1:1, resulting in average elastic properties of $\bar{E}_{Cu/W}$ = 220 GPa and $\bar{\nu}_{Cu/W}$ = 0.35. To calculate the stress within the substrate, a Young's Modulus of E_{Si} = 160 GPa and a Poisson's ratio of 0.27 were used [70], which explains the discontinuity of the residual stress profiles at a depth of 1 µm, caused by a change of elastic material properties used for calculation.

The resulting stress depth profiles are shown in Figure 31, which clearly reveal a transition in residual stress profiles from compression to tension with increasing magnetron chamber pressure during thin film deposition. The depth resolution of the shown stress graphs, which is directly linked to the milling step size, corresponds to the thickness of individual layers (50 nm). The 95% confidence boundaries resulting from averaging the probed stresses for several ring-core diameters and several measurement points per diameter are shown as shaded areas around the stress profiles. The larger error close to the multilayer surface can easily be explained by looking at the strain relaxation profiles in Figure 30. Smaller ring-core diameters increase the uncertainty significantly, due to their smaller DIC tracking surface area. As the smaller ring-core diameters probe the stresses closed to the surface, the error increases in this region.

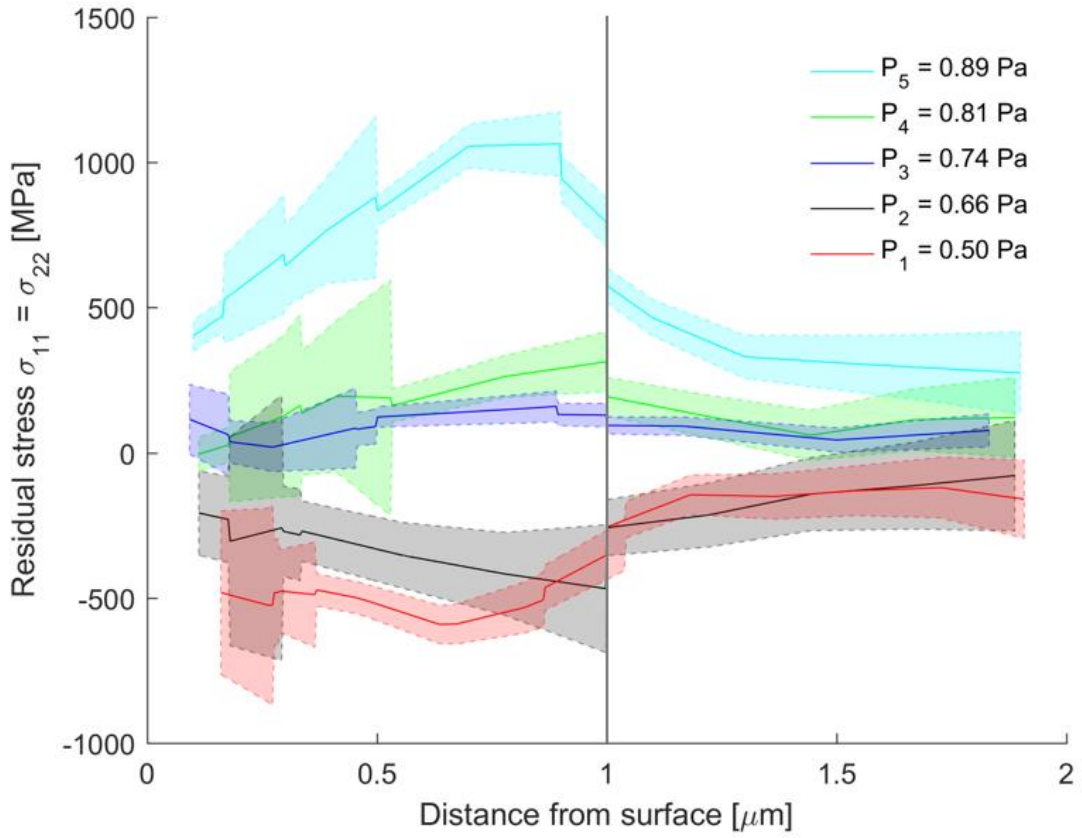


Figure 31. Residual stress depth profiles for different magnetron working pressures obtained from the FIB-DIC ring-core method. The shaded areas around the plot lines represent the 95% confidence interval.

3.1.4.2 $Sin^2(\Psi)$ analysis of XRD data

In order to extract the residual stress from the obtained WAXS patterns, the $sin^2(\psi)$ technique was used. Having been developed in the early stages of experimental residual stress analysis, the $sin^2(\Psi)$ technique is often being referred to as a method of reference to determine residual stresses [17]. As an experimentally easy and non-destructive near-surface technique, it is mainly used to obtain averaged residual stress values, due to the comparably large beam size of laboratory X-Ray sources.

In contrast to the synchrotron XRD pattern acquisition chosen for this work, the traditional laboratory setup relies on a sample being illuminated with photons at an energy of around 8 keV. The obtained Bragg peaks are then collected by a point detector, resulting in a

one-dimensional 2θ vs. intensity line profile. This traditional laboratory setup therefore requires tilting the sample around a line parallel to its surface (Ψ angle), to capture the stress induced lattice distortions can be observed by a shift in the measured 2θ peak position. The resulting $\sin^2(\psi)$ vs. lattice parameter profiles can then be used to extract the average residual stress within the beam interaction volume.

A much faster way of capturing the $\sin^2(\Psi)$ behaviour involves the use of high energy WAXS with high photon flux, as presented in section 3.1.2.3. The use of area detectors with small pixel size and at short sample-detector distance allows to collect the full diffraction ring, as the 2θ range is narrowed down by the high photon energy. As the Debye-Scherrer cone angle approaches 90°, the scattering vector $\boldsymbol{k}_{\psi}$ is moving on a plane perpendicular to the laboratory coordinate system, which is approximately perpendicular to the sample surface at sufficiently small angle of incidence α. This scattering geometry results in a residual stress probing direction normal to the sample surface (Figure 32).

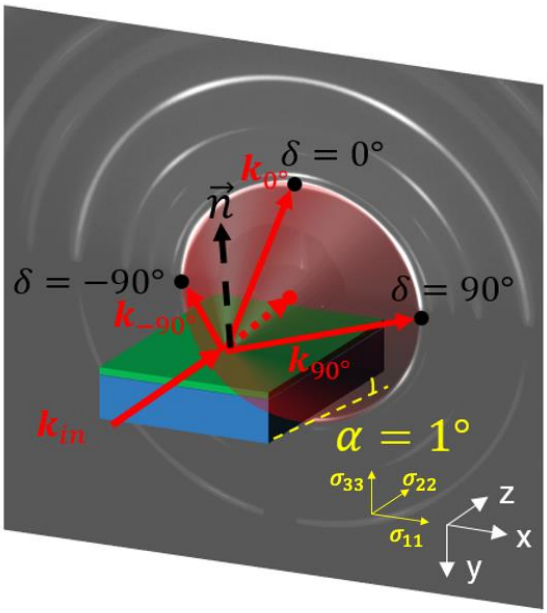


Figure 32. Diffraction geometry during synchrotron WAXS acquisition. Red: incoming and diffracted wave vectors $\mathbf{k}_{in}$ and $\mathbf{k}_{\delta}$. Beamline coordinate system in white. Coordinates are shown in Synchrotron convention, with z pointing in the direction of the beam.

To extract the $\sin^2(\Psi)$ behaviour of the coating, the obtained patterns were integrated by azimuthal binning in 22.5° steps, starting from the central δ = 0° position up to $\delta \lesssim \pm 90°$, resulting in a total number of nine measurement points. The comparably large step size for integration was chosen due non-uniform patterns caused by texture. Fit2D was used for integration, after an initial calibration using the acquired LaB6 diffraction pattern. High accuracy distortion correction was performed based on the calibration pattern prior to the experimental data analysis, ensuring the exclusion of spurious results. Four fully available Debye-Scherrer rings (Figure 28) were selected for azimuthal integration: W{110}, Cu{111}, Cu{200} and W{200}, of which all showed a linear $\varepsilon_{\Psi\phi}^{hkl}(\sin^2(\Psi))$ profile.

To calculate the angle Ψ based on the azimuthal angle δ, the following relationship was employed [60]:

$$cos(\psi) = sin(\alpha)\, sin(\theta) + cos(\alpha)\, cos(\theta)\, cos(\delta) \tag{18}$$

Depending on the residual stress state within the diffracting material volume, the $\varepsilon_{\Psi\phi}^{hkl}(\sin^2(\Psi))$ behaviour can adopt different shapes [71]. To determine the residual stress state with the highest accuracy, the following relation based on an elliptical stress-strain relationship were adopted [72]:

$$\varepsilon_{\phi\Psi} = \frac{d_{\phi\Psi} - d_0}{d_0}$$

$$= \frac{1+\nu}{E}\{\sigma_{11}\cos^2\phi + \sigma_{12}\sin(2\phi) + \sigma_{22}\sin^2\phi$$

$$- \sigma_{33}\}\sin^2\Psi + \frac{1}{E}\{\sigma_{33} - \nu\sigma_{11} - \nu\sigma_{22}\} + \frac{1+\nu}{E}\{\sigma_{13}\cos(\phi)$$

$$+ \sigma_{23}\sin(\phi)\}\sin(2\Psi) \qquad (19)$$

The angle ϕ refers to the rotation of the sample around the global y-axis (Figure 32). The same elastic properties E and ν were used as shown above for the FIB-DIC depth profiling analysis. Further justification for this assumption despite stronger texture at lower deposition pressure will be provided later, based on the ratio of $\sigma_{Cu}$to σ_W. The reference lattice parameter d_0 was set to be the d-spacing at δ = 0, which will be justified at a later point.

Based on the origin of residual stresses within nanometric multilayers through island growth and grain boundary atom implantation, we can assume an equi-biaxial residual stress field in the surface plane direction of the sample. This simplifies the problem by assuming that $\phi = 0, \sigma_{11} = \sigma_{22}$, which yields

$$\varepsilon_\Psi = \frac{d_\Psi - d_{\Psi=0}}{d_{\Psi=0}}$$

$$= \frac{1+\nu}{E}\{\sigma_{11} - \sigma_{33}\}\sin^2\Psi + \frac{1}{E}\{\sigma_{33} - 2\nu\sigma_{11}\} \qquad (20)$$

$$+ \frac{1+\nu}{E}\sigma_{13}\sin(2\Psi).$$

This can be rewritten as:

$$\varepsilon_{\Psi} = \frac{d_{\Psi} - d_{\Psi=0}}{d_{\Psi=0}} = \boldsymbol{A} + \boldsymbol{B}\, sin^2\Psi + \boldsymbol{C}\, sin(2\Psi),$$
$$\boldsymbol{A} = \frac{1}{E}\{\sigma_{33} - 2\nu\sigma_{11}\}, \boldsymbol{B} = \frac{1+\nu}{E}\{\sigma_{11} - \sigma_{33}\}, \boldsymbol{C} = \frac{1+\nu}{E}\sigma_{13}. \quad (21)$$

It can easily be seen that the only component showing a measurable sensitivity towards a change in $d_{\Psi=0}$ is the ellipse intercept with the y-axis **A**. For the further analysis, only the parameters **B** and **C** will be used, as they show no significant sensitivity towards a change in d_0. It is therefore possible to determine the composite residual stress $\{\sigma_{11} - \sigma_{33}\}$ and the shear stress σ_{13} without accurate estimation of d_0.

The out-of plane stress (σ_{33}) and shear stress (σ_{13}) components were found to be negligible compared to the in-plane component. The calculated linear fits representing $\varepsilon_{\Psi} = \boldsymbol{B}\sin^2\Psi$ are thus shown in Figure 33 alongside the experimental data. The presented data shows the evolution of the $\sin^2(\psi)$ behaviour depending on different magnetron chamber deposition pressures. The data error bars indicate the 95% confidence intervals for the Gaussian fitting of the diffraction peaks, based on the following error calculation for strain:

$$\delta_{\varepsilon\Psi} = \varepsilon_{\Psi} \cdot \sqrt{\left(\frac{\sqrt{\left(\delta_{d\Psi}\right)^2 + \left(\delta_{d\Psi=0}\right)^2}}{d_{\Psi} - d_{\Psi=0}}\right)^2 + \left(\frac{\delta_{d\Psi=0}}{d_{\Psi=0}}\right)^2} \quad (22)$$

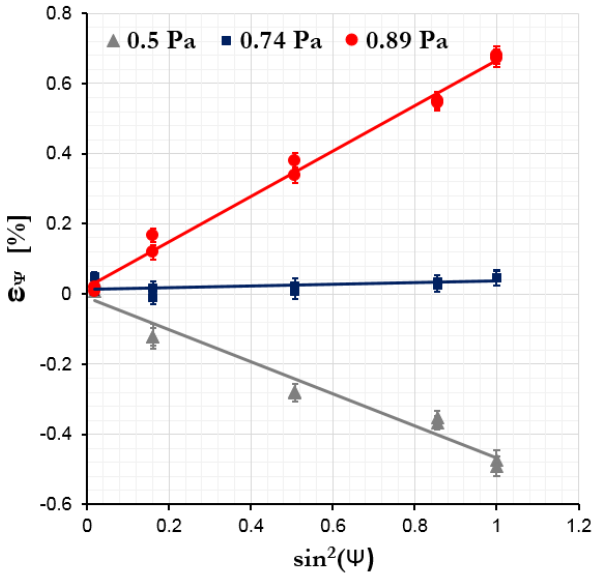


Figure 33. $Sin^2(\psi)$ profiles of the W{110} reflection after deposition at three different magnetron chamber pressures. Points: experimental WAXS data. Dashed line: fitted line profiles.

The so obtained in-plane stress value $(\sigma_{11} - \sigma_{33})$ are shown in Figure 34 and Figure 35, respectively. The data clearly indicates significantly higher magnitudes of residual stresses within W as compared to Cu. As this behaviour is clearly indicating a strong dominance of isotropic W on the averaged residual stress, considerations regarding the orientation-dependence of the elastic properties of Cu would not affect the final average measurably. Further confirmation for this simplification can be drawn from the excellent agreement of experimental data between FIB-DIC and XRD analyses, as shown on Figure 35. Figure 34 shows a residual stress variation in W from $\sigma_{11} - \sigma_{33} = -1 \pm 0.46$ GPa at 0.5 Pa deposition chamber pressure to 1.49 ± 0.38 GPa at 0.89 Pa chamber pressure.

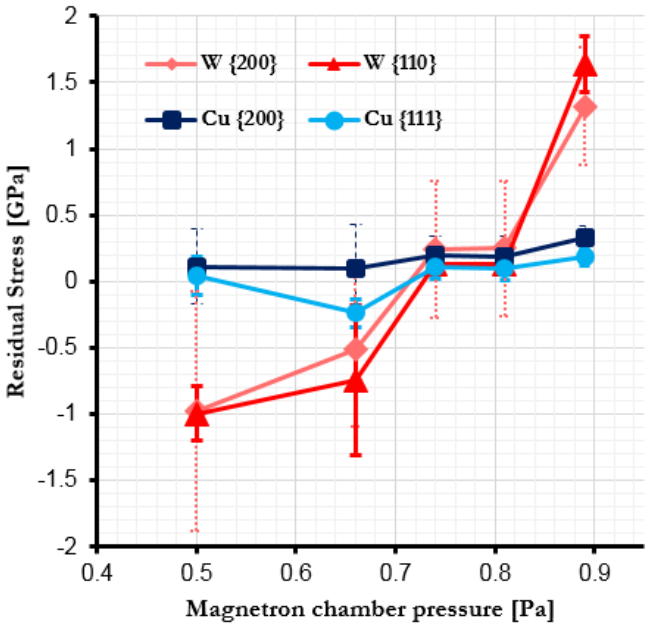


Figure 34. Residual stresses σ_{11}, based on ellipse fitting parameter B for individual W and Cu grain orientations.

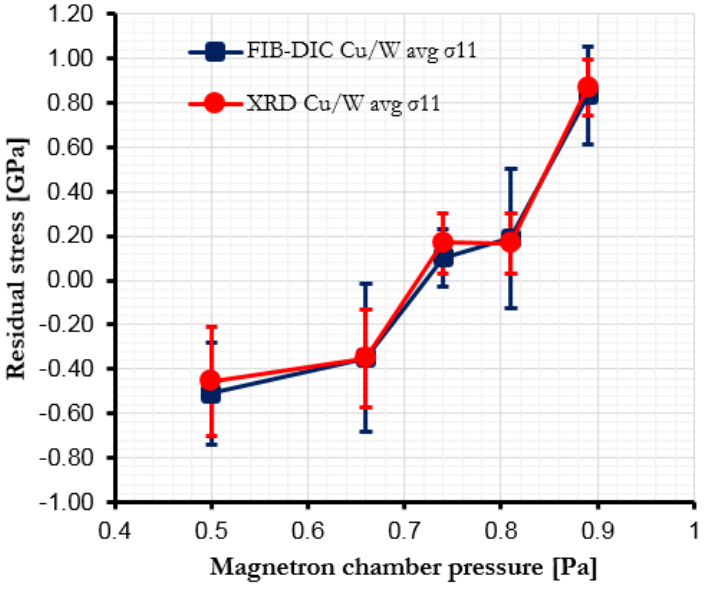


Figure 35. Comparison of residual stresses obtained from FIB-DIC and XRD measurements.

3.1.4.3 Micro-cantilever deflection

In order to compare the measured FIB-DIC with the deflection of a micro-cantilever, a forward calculation approach was chosen, following the eigenstrain deflection model of Korsunsky et al. [73]. A micro-cantilever was modelled to contain the residual stress profile obtained from FIB-DIC analysis, while assuming a linear variation of residual stress within the substrate down to a depth of 3.38 μm, corresponding to the total thickness of the micro-cantilever. Based on this residual stress profile and the cross-sectional geometry obtained from the real micro-cantilever, a curvature was predicted. To describe the residual stress within the cantilever, the following formulation was chosen:

$$\sigma(y) = E^*(y) \cdot (a + b \cdot y) - E^*(y) \cdot \varepsilon^*(y), \tag{23}$$

in which y is the coordinate pointing from the coating surface downwards, $E^*(y)$ is Young's modulus depending on y, b is the curvature of the cantilever deflection, $\varepsilon^*(y)$ is the eigenstrain profile as a function of depth and a refers to the component of strain that is uniform across the section and corresponds to the compressive deformation of the cantilever [73]. Equilibrium conditions lead to the following relationships for resultant force and moment, using a beam width function w(y):

$$F = \int \sigma(y) \cdot w(y)\, dy = 0 \tag{24}$$

$$M = \int \sigma(y) \cdot w(y) \cdot y\, dy = 0 \tag{25}$$

In the final step, the predicted curvature was compared to the one measured from the real micro-cantilever. Using the eigenstrain profile $\varepsilon^*(y)$ obtained from FIB-DIC returned a predicted curvature of -754±56 m^{-1}. This result is in excellent agreement with the

experimental data presented in 3.1.3, which shows a curvature of -800±18 m^{-1}, resulting in a relative difference of only ~6%. To calculate the cantilever curvature based on the eigenstrain profile provided by FIB-DIC analysis, the following Young's modulus profile was used, based on the material properties introduced in 3.1.4.1. The profile is shown in Figure 36.

$$E^*(y) = \begin{cases} 220\ GPa, y \leq 1\mu m \\ 160\ GPa, y > 1\mu m \end{cases} \quad (26)$$

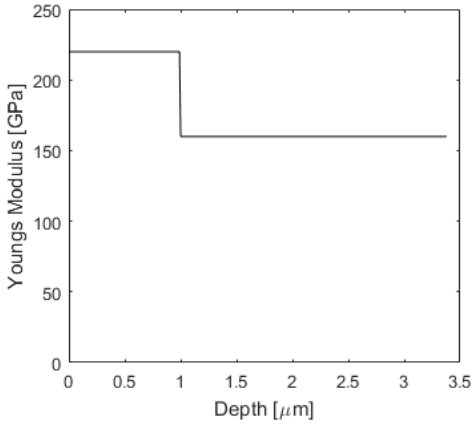


Figure 36. Distribution of the Young's modulus vs. depth used for predicting the cantilever deflection.

The eigenstrain profile $\varepsilon^*(y)$ obtained from DIC analysis was approximated using a fourth order polynomial and by assuming a drop in eigenstrain to zero at a depth of 3.38 μm, which corresponds to the total thickness of the micro-cantilever. The resulting eigenstrain function is given by

$$\varepsilon^*(y) = p_1 \cdot x^4 + p_2 \cdot x^3 + p_3 \cdot x^2 + p_4 \cdot x + p_5, \quad (27)$$

$$p_1 = -2.77 \cdot 10^{20}, p_2 = 1.92 \cdot 10^{15}, p_3 = -4.21 \cdot 10^{9}, p_4 = 2348,$$

$$p_5 = 0.001731,$$

and shown in Figure 37.

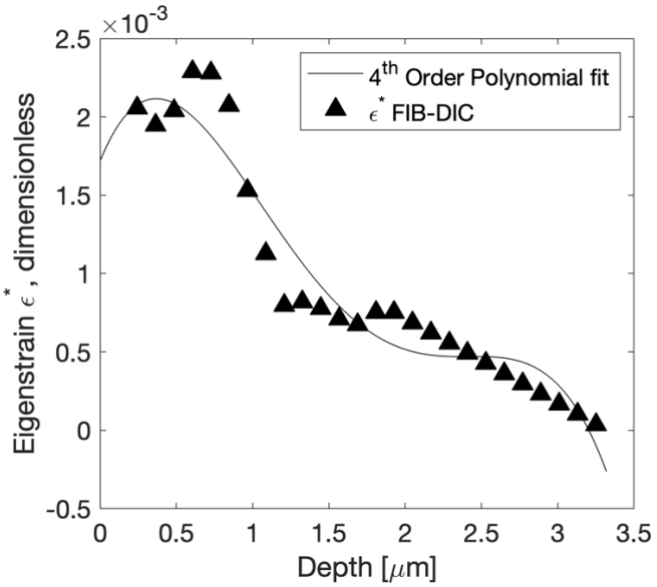


Figure 37. Eigenstrain profile obtained from FIB-DIC, extrapolated to a depth of 3.38 μm for predicting the cantilever curvature and presented alongside the 4th order polynomial fit, selected for optimised R-square (R-square = 0.93).

To represent the geometry of the cantilever cross-section, the following dependence of width vs. depth was determined, which is shown in Figure 38:

$$w(y) = \begin{cases} 3.852 \cdot 10^{-6} + 0.3122 \cdot y, y \leq 2.162\ \mu m \\ 12.5626 \cdot 10^{-6} - 3.7162 \cdot y, y > 2.162\ \mu m \end{cases} \quad (28)$$

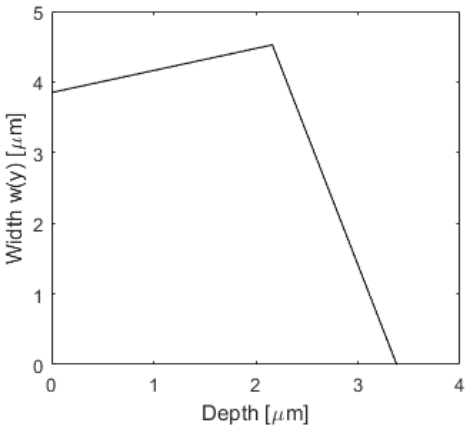


Figure 38. Width of the cantilever vs. depth as extracted from SEM frames for predicting the cantilever curvature.

These formulae were inserted into the following relations based on (24) and (25), taking into account the change of geometry and material properties with depth y:

$$F = \int_{y=0}^{1\cdot10^{-6}} \sigma(y') \cdot w(y')\, dy' + \int_{y=1\cdot10^{-6}}^{2.162\cdot10^{-6}} \sigma(y') \cdot w(y')\, dy' + \int_{y=2.162\cdot10^{-6}}^{3.38\cdot10^{-6}} \sigma(y') \cdot w(y')\, dy' = 0 \tag{29}$$

$$M = \int_{y=0}^{1\cdot10^{-6}} \sigma(y') \cdot w(y') \cdot y'\, dy' + \int_{y=1\cdot10^{-6}}^{2.162\cdot10^{-6}} \sigma(y') \cdot w(y') \cdot y'\, dy' + \int_{y=2.162\cdot10^{-6}}^{3.38\cdot10^{-6}} \sigma(y') \cdot w(y') \cdot y' dy' = 0 \tag{30}$$

This returns the linear system of equations

$$A = \begin{bmatrix} 2.13 & 2.86\cdot10^{-6} \\ 2.86\cdot10^{-6} & 5.38\cdot10^{-12} \end{bmatrix} \begin{bmatrix} a \\ b \end{bmatrix} = \begin{bmatrix} -0.00255 \\ -2.25\cdot10^{-9} \end{bmatrix},$$

The solution gives a = 0.0022 and b = -753.67±56m^{-1}.

3.1.5 Results

The high spatial resolution of the FIB-DIC and eigenstrain nanoscale depth profiling method allowed to reveal the details of the stress variation within Cu/W nano-multilayers, as well as the stress-affected zone within the substrate.

The residual stress profiles clearly indicate the location of the stress peak at around $0.75 \cdot t_c$ distance from the sample surface, with t_c being the thickness of the multilayer coating. While approaching zero stress towards the sample surface, the stress peak magnitude can lie significantly above the average stress measured by XRD, as shown by graph P_1 in Figure 31 - an information which is particularly useful for the mechanical design of coatings. A clear correlation between the argon working pressure and the multilayer stress was made, showing a transition from compressive residual stresses at low working pressures to tensile residual stresses at higher pressures. It should be noted that not only the average stress value magnitude increases for low/ high working pressures, but also the difference between the peak stress and the average stress, making it highly important to consider the detailed stress profiles for reliability design under these deposition conditions.

Further insights include the stress transfer from coating to substrate. Starting from the substrate-coating interface, the residual stress asymptotically approaches the stress-free state at a depth of around 3 μm, which can be determined from extrapolation. Even though the performed XRD analysis can only provide averaged stress levels, it adds a significant amount of insights to this analysis, as the residual stress obtained by XRD and $\sin^2(\psi)$ can be calculated for Cu and W separately.

Micro-cantilever deflection measurements confirmed the residual stress level determined by FIB-DIC analysis and hence supported the calculations based on a combination of FIB-DIC and XRD analysis. The agreement between FIB-DIC and micro-cantilever measurements was excellent, with a difference of around 6%.

3.1.6 Discussion

The residual stress state of thin films changes continuously during the magnetron sputter deposition: from tensile residual stresses during island coalescence to compressive residual stresses at low working pressures due to intergranular atomic implantation and atomic peening effects. As reflected in the residual stress profiles presented in Figure 31, it is easily possible to modify the residual stress state by changing the working Ar pressure inside the magnetron chamber. The presented data supports previous models [51,53], which suggest that a reduction in mean free path length of sputtering atoms reduces the atomic peening effect and may lead to the formation of columnar growth morphology with reduced density.

A hierarchical analysis of stresses has been proposed using three different independent and complementary techniques: firstly, XRD allowed assessing both Cu and W average through-thickness residual stress magnitudes. By using exclusively $\sin^2(\psi)$ ellipse fitting parameters which were independent of the stress-free lattice parameter d_0, a robust analysis method was developed and employed. Consequently, detailed insights into the strain accommodation mechanisms within different materials and grain orientations were obtained (Figure 34).

Further to the above, the use of FIB-DIC ring-core milling permitted to study the stress accommodation within the coating multilayer-substrate systems spatially resolved at a high resolution of around 50 nm. Significant stress peaks became apparent, especially for the samples deposited at P = 0.89 Pa (Figure 31), suggesting that under-dense columnar growth in combination with a reduction of atomic peening significantly increases the difference between average and peak stress within the coating. In addition, the residual stress profiles showed that peak stresses occur in proximity to the substrate-coating interface, which facilitates mechanical failures at the substrate-coating interface. A discontinuity in the mechanical properties across this interface might promote mechanical failure further.

Finally, the deflection of a micro-cantilever was predicted, based on the residual strain relief profiles obtained from FIB-DIC, which matched the experimentally determined cantilever curvature with high accuracy. The proposed way of calculation takes into account the fact that the actual cantilever cross-section was not rectangular in the centre of the sample due to geometric constrains during ion beam milling. This technique turned out to be an ideal tool for the confirmation of experimental results obtained by novel experimental techniques.

If chosen carefully, residual stress becomes an additional degree of freedom available during engineering design process, not only by changing structural integrity properties but also functional ones. For instance, compressive residual stress in coatings can improve the tensile properties due to a pre-straining of the material. Not only the sign and magnitude of residual stress is important, but also gradients of residual stress can play an important role in modifying the final product's properties. For example, a uniform stress distribution is usually preferred, in order to avoid stress localisations within the coating, which may result in failure below the expected level of loading. In this respect, using the lowest possible working argon pressure to create compressive residual stress would not be the best solution from the structural point of view, as a compressive peak is deposited in near-substrate region which might give rise to failure. Instead, choosing a slightly higher pressure might help the reliability of the coating by creating a uniform residual stress distribution. If used in thermal applications, however, tensile residual stresses can be of advantage, as they may avoid buckling upon thermal expansion, if the coating has a higher thermal expansion coefficient than the substrate. Again, choosing the highest average residual stress could be detrimental, considering the tensile peak in the near substrate region. These examples show clearly the importance of the knowledge of stress profiles at high resolution as compared to average stress values which can easily be extracted from X-Ray diffraction patterns.

3.1.7 Conclusions

High resolution depth profiles, as provided by the FIB-DIC analysis, revealed for the first time, how deposition conditions influence the stress distribution within nano-structured Cu/W coatings. While previous studies were only able to observe average stresses, it has become clear that these averages can significantly underestimate the confined peak stresses. Therefore, relying on averaged data from XRD for stress design and reliability considerations might lead to unexpected failure at locations of peak stress through mechanisms such as interfacial slip, void formation and crack propagation. The data obtained from the FIB-DIC depth profiling technique was cross-correlated with traditional synchrotron XRD methods and showed a high level of agreement.

3.2 Probing the deformation and fracture properties of Cu/W nano-multilayers by *in situ* SEM and synchrotron XRD strain microscopy

3.2.1 Introduction and Literature Review

Thin coatings and multilayers with individual film thickness down to a few nanometres enable the design of materials with novel and carefully tailored thermal, mechanical, and functional properties. These properties arise as a consequence of the confinement of inhomogeneous mechanical, chemical and electromagnetic fields within nano-scale strata and nano-grains of material. External thermal and mechanical loading can cause structural damage and significantly decrease or undermine the performance of coating systems. In order to improve the reliability of coating systems by design, a profound understanding must be sought of the deformation and failure mechanisms in these systems. In particular, when thin nano-multilayer coatings on highly deformable polymer substrates are subjected to stretching, coatings display a fracture pattern that consists of apparently randomly spaced parallel cracks running normally to the principal

stretching direction. With increasing substrate stretch further cracks appear in between previous fractures, leading to an increase in the crack density, and a reduction in the mean inter-crack spacing. With further loading the coating develops additional transverse fracture pattern consisting of cracks that run parallel to the stretch direction.

The statistical properties of the parallel cracking patterns in thin brittle coatings on ductile polymer substrates have been fairly extensively explored previously. Several approaches to the simulation of the stress and strain distributions have been proposed [74–76], most of them based on the so-called shear lag model [77]. In [74], Lunt et *al*. proposed a simple shear lag model that leads to a linear ("tent function") stress-strain distribution within uncracked segments. The basic assumption of the model was the presence of a constant limit to the shear stress mediating the load transfer from the substrate to the coating (Figure 39a). The model gives rise to the "linear tent" strain profile illustrated in Figure 39b. Apart from the evident simplicity and ease of application, another important aspect of the Lunt et *al*. model is the assumption of stochastic variation of the coating limit strain, indicated by the upper curve in Figure 39b. The assumption is made that fracture occurs when local strain value reaches the critical limit strain. In combination with the stochastic nature of the limit strain this means that there exists an upper bound on the strain profile.

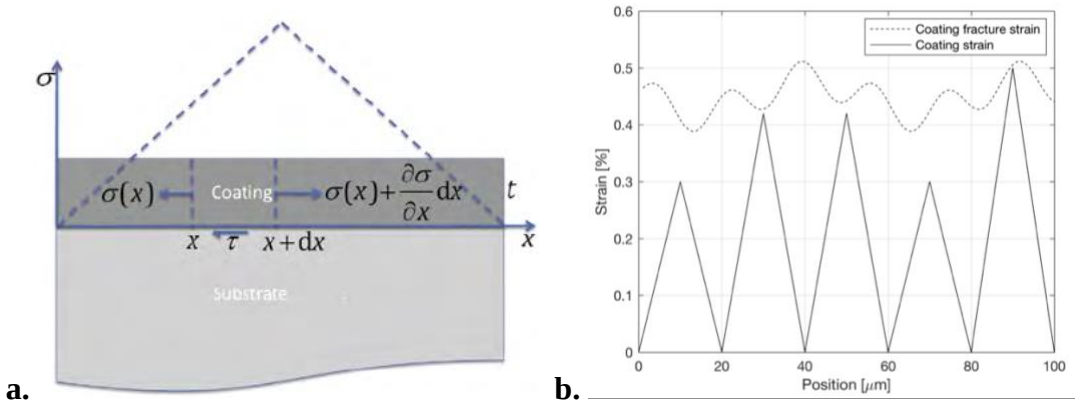


Figure 39. a. Linear shear lag model based on constant shear stress τ, and b. strain distribution in a cracked coating according to the Lunt et al. model [74].

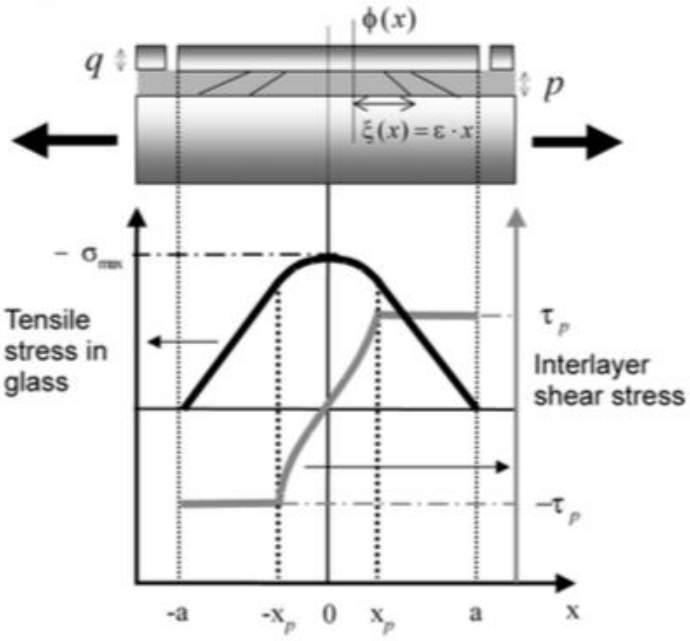


Figure 40. The variation of stress within the coating according to model incorporating an elastic-ideally plastic interface layer [75].

A more complex model of coating deformation and fracture was reported in [75]. This approach uses the concept of an interface layer between the substrate and the coating that transfers the load by shear. It is worth noting that the introduction of an interlayer with distinct elastic-ideally plastic properties is required for the derivation of the predicted stress distribution within the coating. When the interlayer is fully yielded, a linear variation of the coating strain with position arises. On the other hand, whilst the interlayer is still in the elastic regime, the strain variation within the coating follows the solution in the form of hyperbolic cosine (Figure 40**)**.

Whilst these models offer a means of rationalising the observed cracking behaviour and some of the statistics derived therefrom, e.g. such as the evolution of mean crack spacing with the underlying strain, nevertheless, direct experimental measurements of two-dimensional strain distributions that arise in these systems under stretching using a combination of independent analysis techniques remains lacking till now, even though other previous models supported by smaller-scale measurements using synchrotron radiation and Raman spectroscopy have been

presented before [78,79]. The present study focuses on *in situ* strain microscopy of a Cu/ W nano-multilayer on a Kapton substrate under uniaxial tensile loading using scanning synchrotron XRD microscopy and SEM. The results of the two methods are cross-validated and compared with the prediction of two existing deformation models, and an improved model is proposed that combines the attractive features of both approaches. The insights obtained in this way are discussed in the context of the determination of coating fracture properties.

3.2.2 Materials and methods

Cu/W nano-multilayer with the layer thickness of 18/6 nm, respectively, were deposited onto a 125 μm Kapton® substrate by ion beam deposition, starting with a Cu layer and ending with a W layer (Figure 41). The multilayer consists of ten periods of the copper/tungsten bilayer combination, with the total film thickness of around 240 nm. The Cu/W thin films were deposited at room temperature by ion beam sputtering with a focused Ar+ ion gun at 1.2 keV multicusp radio-frequency source in a NORDIKO-3000 system. During film growth, the ion-gun was supplied with a constant incident radio-frequency power of 165 W and constant Ar flux of 10 standard cubic centimetre per minute. The 150 mm diameter targets were sputtered during 10 min allowing both ion-gun stabilization and target pollution cleaning caused by vacuum break. The ion-gun axis was inclined at 45° to the normal of the surface target while the sample surface was parallel to the target plane. The sputtering chamber was pumped down to a base pressure of $2 \cdot 10^{-6}$ Pa while the working pressure during film growth was ~10^{-2} Pa. Substrates were preliminary cleaned with acetone and ethanol and finally dried with an argon gas jet prior to their introduction in the deposition chamber. Tungsten and copper growing rates were previously calibrated by XRR and were found to be 0.05 nm s^{-1} and 0.16 nm s^{-1}, respectively. XRR was performed in order to evaluate sample stratification using the Bragg law at a grazing incidence angle. Energy-dispersive X-ray spectroscopy was used in a scanning electron microscope to

determine the atomic concentrations of Cu and W in the films and to estimate the effective W and Cu sublayer thicknesses per period employing the period obtained by XRR.

For uniaxial tension experiments, coated sheet were cut into dogbone-shaped specimens, as illustrated in Figure 41. The low layer thickness and the immiscibility of Cu and W in each other mean that the two materials exist as distinct phases within the coating, and are extremely fine-grained [80]. The mechanical response of the nano-multilayer to stretching is determined by the physical mechanisms by which deformation is accommodated within the structure. Of particular interest is the degree of ductility vs brittleness shown by these systems that is likely to be governed to a large extent by the obstacles to dislocation glide offered by interphase and grain boundaries, leading to significant deviation from bulk behaviour of either constituent material.

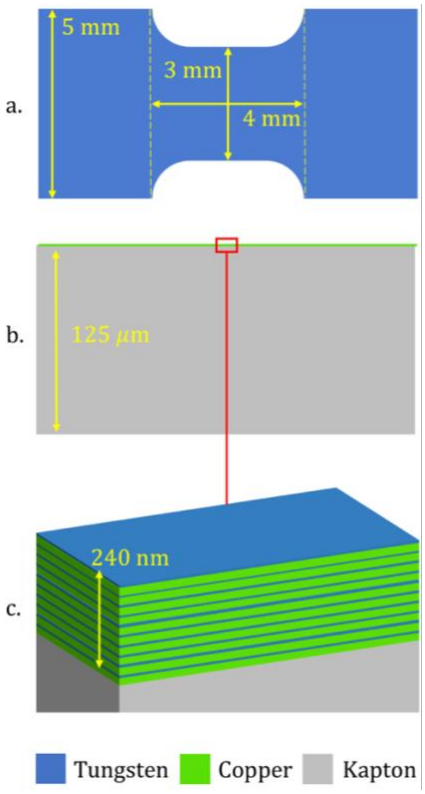


Figure 41. Illustration of the dogbone Cu/W 18/6 sample geometry used in the in situ uniaxial tensile stretching experiments: **a.** Top view **b.** Side view **c.** Nano-multilayer detailed view.

3.2.3 Results

A MicroTest uniaxial tension/compression stage (Deben, UK) was used for the purpose of *in situ* mechanical testing experiments on the Cu/W 18/6 multilayer dogbone samples, as detailed below.

3.2.3.1 Fast frame rate *in situ* SEM observation of cracking pattern evolution

3.2.3.1.1 Fast frame rate experiment

In order to obtain initial characterisation of the overall cracking behaviour of the coating, the tensile stage was placed inside the vacuum chamber of a Tescan LYRA3 XM FIB-SEM instrument (MBLEM, Multi-Beam Laboratory for Engineering Microscopy, Department of Engineering Science, University of Oxford, UK). The sample was subjected to stretching at the constant strain rate of $\dot{\varepsilon} = 4\times10^{-4}$ s^{-1} until the substrate failed in tension. In the course of continuous sample extension, SEM images of a RoI at the sample surface were acquired repeatedly. Due to the fast crack formation, image acquisition at a high frame rate was required. However, the implication was that in this fast frame acquisition mode the image resolution was limited, and therefore insufficient for detailed digital image correlation analysis of the results to extract strain profiles.

3.2.3.1.2 Fast frame rate experiment interpretation

The SEM image sequence obtained using fast frame rate acquisition conditions reveals the appearance of new cracks that leads to the increase in crack density and reduction of the mean distance between cracks. In order to quantify this observation, the following procedure was adopted: from the recorded sequence of frames of the kind shown in Figure 42a, inverted grey value line profiles were obtained, as shown Figure 42b. The spacing between adjacent cracks

was determined to good precision by fitting Gaussian peaks to determine the centre position, and computing the distance between their neighbouring cracks. Following this procedure, the mean crack spacing was calculated from the ensemble of inter-crack distances for a given applied strain value. Figure 43 illustrates the dependence of the mean inter-crack spacing on the applied strain (markers), which is shown together with the power law fit given by $f(x) = 13.05 + 24.87 \cdot (x - 2.23)^{-2.15}$. It is apparent from considering the plot that the average inter-crack spacing converges towards a constant value of around 17µm at a substrate strain of ~4%, beyond which only minor changes in crack spacing can be detected. This is likely to be associated with the gradual change in the shear transfer mechanism: while perfectly elastic transfer is dominating at low substrate strains, perfectly plastic behaviour of the shear interface causes the mean crack width to saturate at larger strains beyond 4%. These preliminary results provide important insights into such key system parameters as the critical strain values for the onset and saturation of cracking, etc.

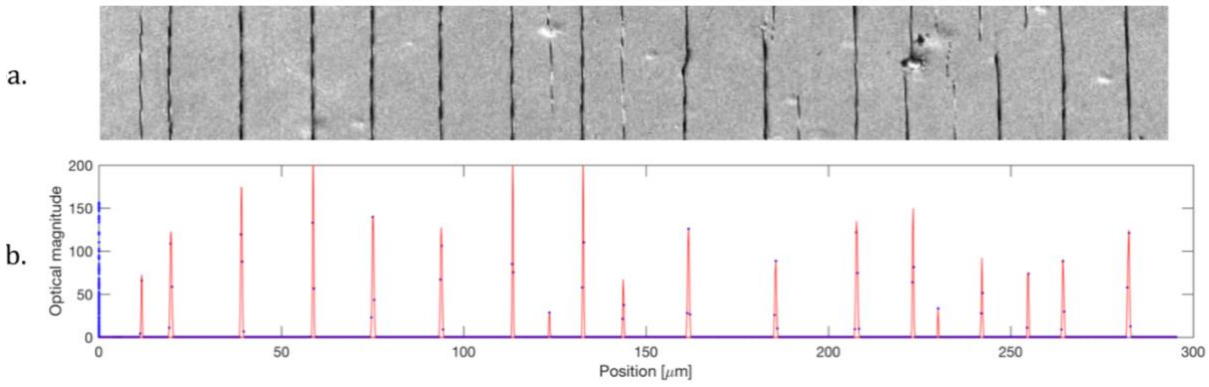


Figure 42. Interpretation of the fast frame rate SEM image sequence: **a.** Detail of the SEM frame recorded at $\varepsilon = 5.5\%$. **b.** The inverted grey value profile plot (markers) and the curve consisting of fitted Gaussian peaks (continuous line). The apparent brittle fracture at the surface might be driven by W fracture behaviour at the multilayer surface.

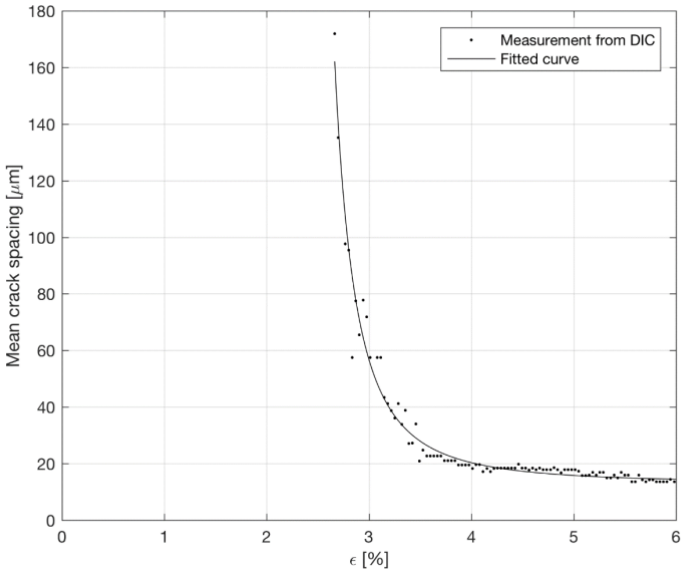


Figure 43. The spacing between neighbouring cracks vs. substrate strain (markers), shown together with the power law fit to the data (continuous curve).

3.2.3.2 DIC strain mapping using high resolution *in situ* SEM tensile experiment

3.2.3.2.1 High resolution *in situ* tensile experiment

To enable the subsequent use of digital image correlation for strain microscopy interpretation, high image quality and contrast are needed. Contrast was achieved by depositing platinum dots on the sample surface using gas injection system. A non-repetitive pattern [81] was chosen to avoid aliasing that is known to be caused by pattern regularity (Figure 44).

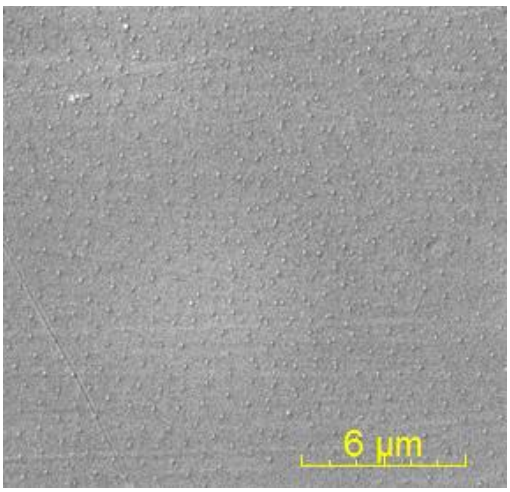


Figure 44. Non-repetitive platinum dot pattern on the coating surface for optimised DIC tracking.

The sample was stretched in a stepwise fashion, with the strain step of $\Delta\varepsilon = 2.5\times10^{-3}$, up to the total strain of $\varepsilon = 0.1475$. A high resolution image was acquired at each value of stretch applied to the sample.

3.2.3.2.2 DIC analysis of high resolution *in situ* tensile experimental data

DIC is a technique that allows the evaluation of displacement fields at the resolution sufficient for obtaining maps of total strain both in the elastic and plastic deformation regimes. The displacements of the tracking markers at sample surface are determined at sub-pixel resolution throughout the course of deformation. The displacement field is averaged along vertical lines (perpendicular to the force), and then interpolated using a smoothing spline before differentiation to obtain the strain variation in the longitudinal direction (x). The strain distribution obtained using this approach for the total strain $\varepsilon = 7.4\%$ is shown in Figure 45. The strain profile shows a strain concentration in the centre of the coating platelet with a maximum of about 2.7% that is reached at the position ~12 μm.

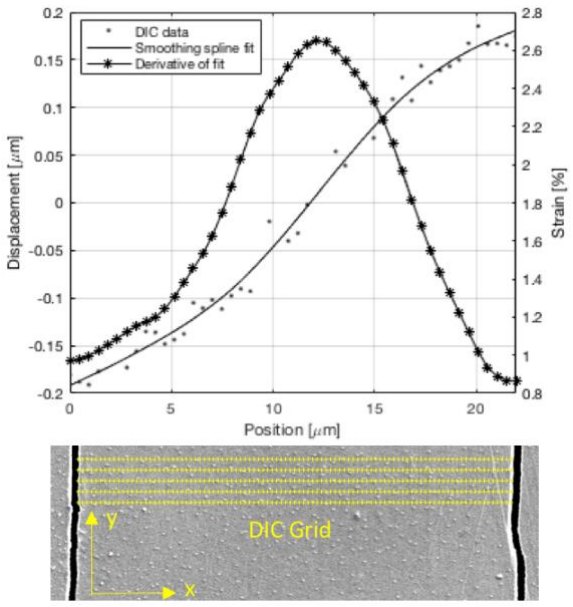


Figure 45. Displacement profile for the overall applied strain $\varepsilon = 7.4\%$ obtained from DIC analysis (left vertical scale) and the strain profile obtained by differentiation (right vertical scale).

Although DIC analysis reveals the nature of strain variation between fracture, it returns the values of *total strain* in the coating that is given by the sum of elastic and plastic strain components. Direct conversion from strain to stress is impossible on the basis of this data. In order to determine the variation of the elastic strain component within the coating we performed synchrotron XRD in situ stretching experiments that are reported below. Since the DIC analysis provides both the elastic and plastic strain component, the obtained strain of around 2.7% is significantly higher than the maximum elastic strain component of 0.65% determined by XRD, which will be presented and discussed in the following section.

3.2.3.3 Synchrotron X-ray diffraction *in situ* tension

3.2.3.3.1 Synchrotron X-ray diffraction *in situ* tensile experiment

The experiment was performed on B16 Test Beamline (Diamond Light Source, Oxford, UK) using X-Rays with the energy of 12.4 keV obtained using a multi-layer monochromator (MLM) with a beam spot size of around 2×2 μm that was created using a compound refractive lens (CRL). The sample was mounted in the loading device in the vertical plane (designated *x*-*y* in the laboratory coordinate system), with the incident beam travelling along the *z*-axis perpendicular to the sample surface. The setup used for this procedure is illustrated in Figure 46. For each map, multiple Debye-Scherrer rings were acquired from each beam position on the specimen by translating the sample stage across a rectangular grid (Figure 46b) with a step size of 2 μm in the horizontal loading direction (*x*) and steps of 5 μm in the vertical transverse direction (*y*). Each position in the map thus collected corresponds to a frame containing a 2D Debye-Scherrer diffraction pattern. Once the map data was acquired at a given overall strain applied to the sample, a further extension was applied until the next strain value was reached,

and the data collection was repeated. A total of six maps were acquired for the overall strain values of $\varepsilon = 0.3\%$, 3.5%, 5.2%, 8.5%, 13.9% and 18.2%.

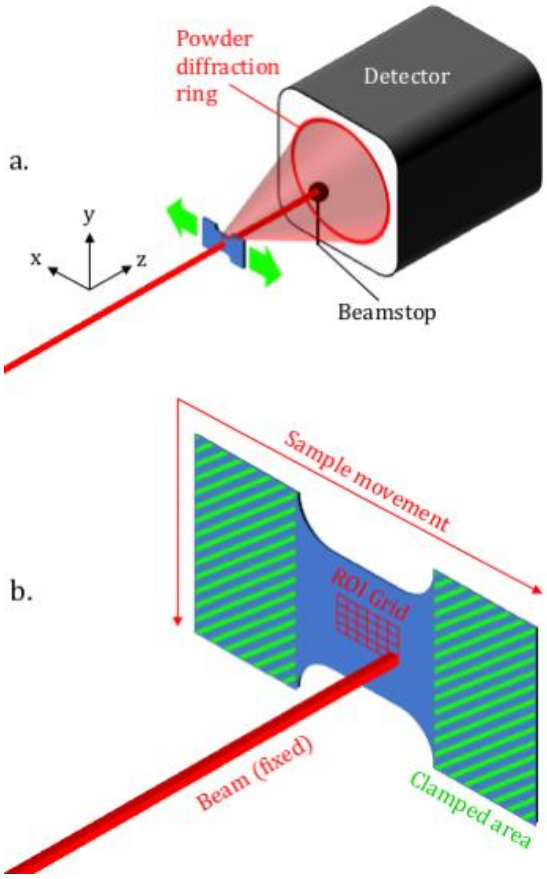


Figure 46. Synchrotron XRD scanning microscopy setup for two dimensional strain mapping: **a.** Debye-Scherrer ring and detector position with laboratory coordinate system, **b.** Illustration of the location and arrangement of the XRD data collection grid for ROI mapping.

3.2.3.3.2 Strain and stress maps from XRD data

The precision, efficiency and speed of strain analysis by synchrotron XRD opens up the possibility of performing strain microscopy in fine-grained samples that exhibit sufficiently strong scattering. The nano-crystalline nature of the object of the present study ensures that spatially resolved in plane strain mapping can be carried out on a sample subjected to *in situ* stretching. 2D diffraction patterns collected at each point in the raster scan were analysed by radial-azimuthal binning ("caking") [82]. Given the normal beam incidence at sample surface

and small coating thickness that is much lower than the X-ray attenuation length at the relevant energy, the entire coating thickness is illuminated and contributes to the formation of the Debye-Scherrer ring pattern. The strongest reflection in the pattern corresponds to the {111} family of planes in the Cu layers. Due to the multilayer morphology of the coating subjected to in-plane stretching, the strain values derived from the analysis of Cu diffraction data are taken as representative of the deformation in the W interlayers. No interfacial sliding or interlayer debonding occurs during the extension, as is evident from previously published TEM studies of sample cross-section that shows no evidence of damage as these interfaces [80]. Provided the interfaces between Cu and W remain intact, the strain within the individual layers must be the same in accordance with the Voigt assumption, as this is a consequence of pure kinematics of deformation.

The usual calibration procedures for the detector to sample distance were applied [82]. For each raster position of beam spot on the sample, equivalent 1D profiles were obtained in terms of intensity as a function of the scattering angle from pattern segments spanning a chosen azimuthal direction.

The algorithm for the strain evaluation consists of the following steps [82]:

(i) Find the pattern centre with the help of the calibration sample frame

(ii) Transform the experiment polar plots into Cartesian reference by polar *re-binning* of the frame pixels into circular arc bins (Figure 47a, b)

(iii) Choose an angle range, over which the intensity profile is summed radially

(iv) Fit a Gaussian peak to the data for each of the two main directions ϕ_{xx} and ϕ_{yy} (Figure 48)

(v) Obtain the strain by using the reference 2θ-peak position $2\theta_0$ and the strained peak position 2θ, respectively:

$$\varepsilon = \frac{\theta_0 - \theta}{tan(\theta_0)}. \tag{31}$$

For this strain evaluation an averaging range of $\Delta\phi_x = \Delta\phi_y = 10°$ around the main directions ϕ_{xx} and ϕ_{yy} was chosen to reduce the noise.

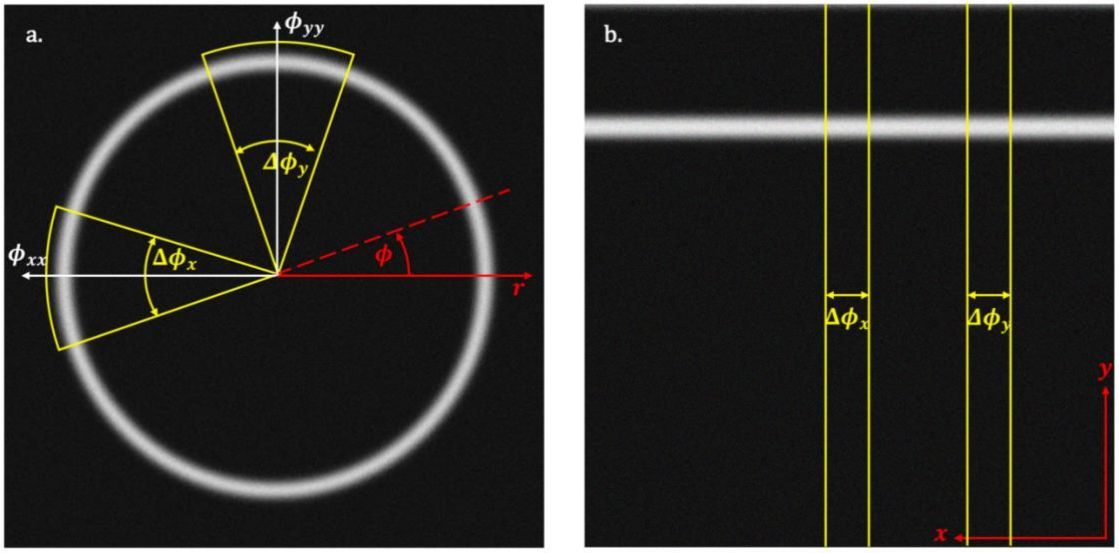


Figure 47. Debye-Scherrer ring in polar coordinates with the two main directions $\phi_{yy} = \frac{\pi}{2}$ and $\phi_{xx} = \pi$ for ε_{yy} and ε_{xx}. **b.** Cartesian transformation of **a.** in laboratory coordinates

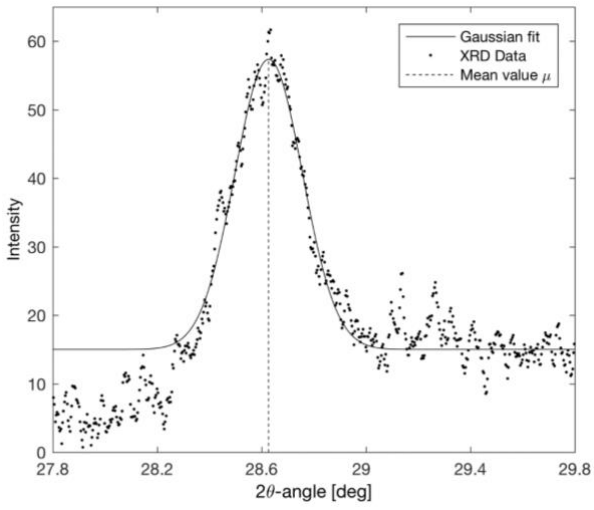


Figure 48. Illustration of the fitted Gaussian intensity profile from experimental XRD data

The maps of strain component ε_{xx} in the direction of applied loading are shown in Figure 49. The error of the strain calculation due to peak fitting was quantified and found to be $\pm 0.08\%$ with a confidence of 95%. The case studied here demonstrates one of the crucial advantages of strain microscopy: despite the probe size of ~2μm being too large to resolve individual crack opening, the strain reduction caused by the occurrence of fracture that extends to larger distances is readily detectable. On the strain maps shown in Figure 49 cracks appear as "valleys" of low strain (blue colour), whereas in the uncracked segments the strain values increase towards a peak. The sequence of maps shows that a distribution of low strain values in the sample subjected to small stretch (0.3%, Figure 49a) becomes inhomogeneous after the application of 3.5% and 5.2% stretch (Figure 49b, c). Subsequent stretching causes apparent fragmentation of the multilayer coating accompanied by the reduction of the mean strain.

The strain values appearing in the XRD maps lie in the range 0-0.6%. It is clear that an upper strain limit persists even when the underlying stretch values exceed 18.2%. This suggests that the extension capability of the multilayer is strain-limited. The determination of the limiting strain is the purpose of the analysis that follows below.

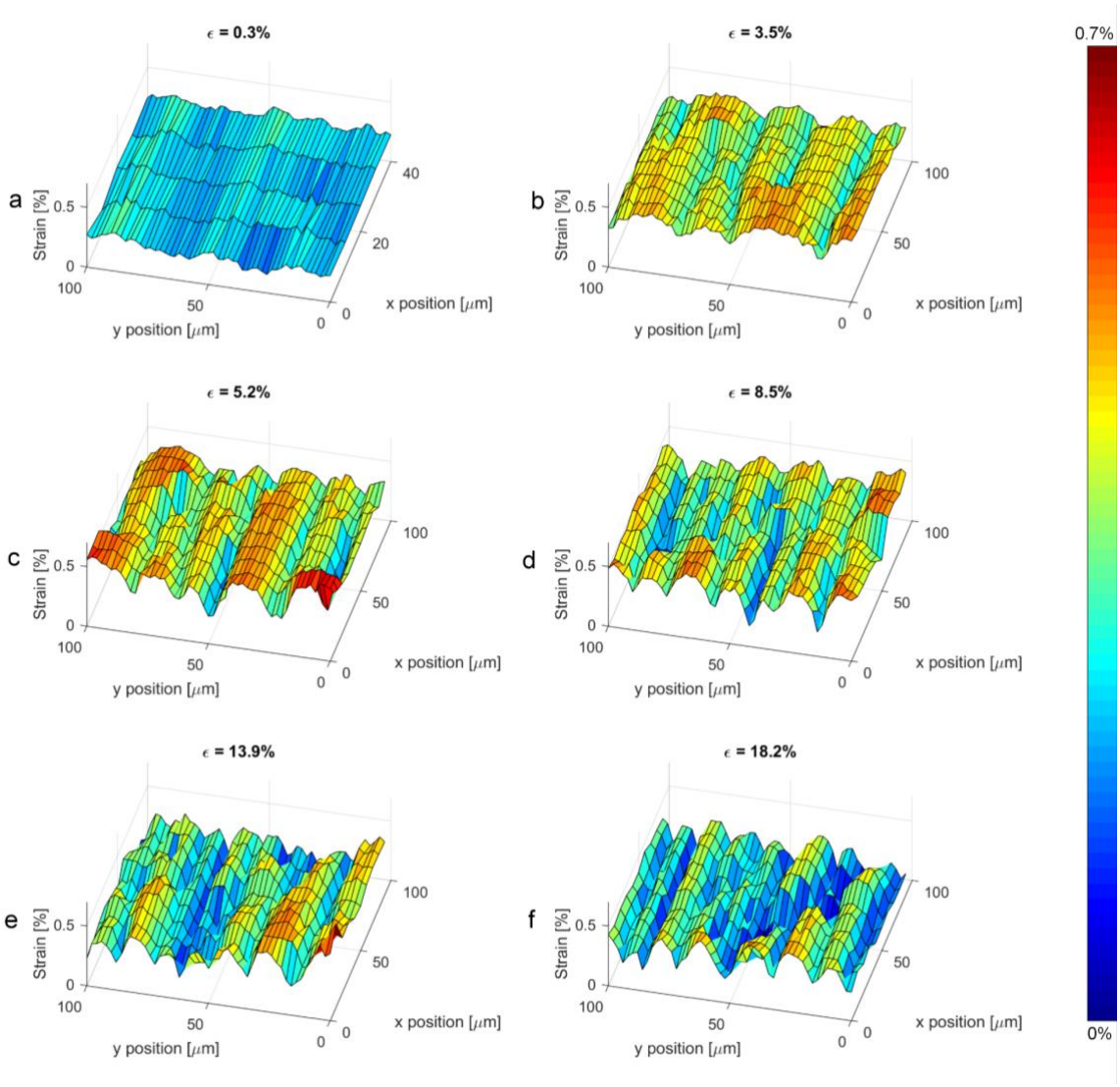


Figure 49. Synchrotron XRD strain maps for different substrate stretch values.

Closer examination of the strain distributions at different substrate stretch values is carried out with the help of line profiles shown in Figure 50. The most remarkable aspect of these plots consists of the fact that the strain values within the multilayer coating appear to be bounded from above. This upper bound strain value decreases with the increasing substrate stretch, from ~0.6% at the stretch of 5.2% to ~0.5% at the stretch of 18.2%. In other words, the elastic strain within the multilayer coating measured by diffraction represents only a small fraction of the substrate stretch. This indicates that the strain is also accommodated in the coating by the increasing opening of the cracks between coating blocks, and by plastic

deformation of the multilayers. Nevertheless, it is worth noting that the elastic strain in the coating measured by diffraction represents the correct basis for stress calculation in the coating.

Another important observation concerns the strain profile between cracks: at the lower stretch of 3.5% it appears to be approximately parabolic, whilst at the higher stretch of 18.2% the profile appears to become sharper, closer to a triangular "saw-tooth" profile.

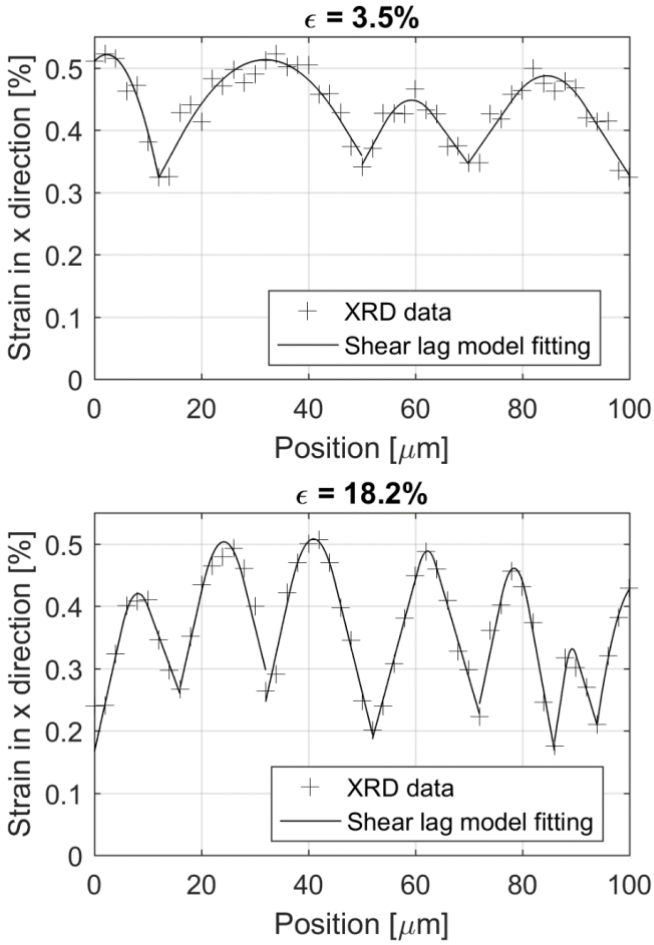


Figure 50. Strain distributions for substrate stretch values of $\varepsilon = 3.5\%$ and 18.2%.

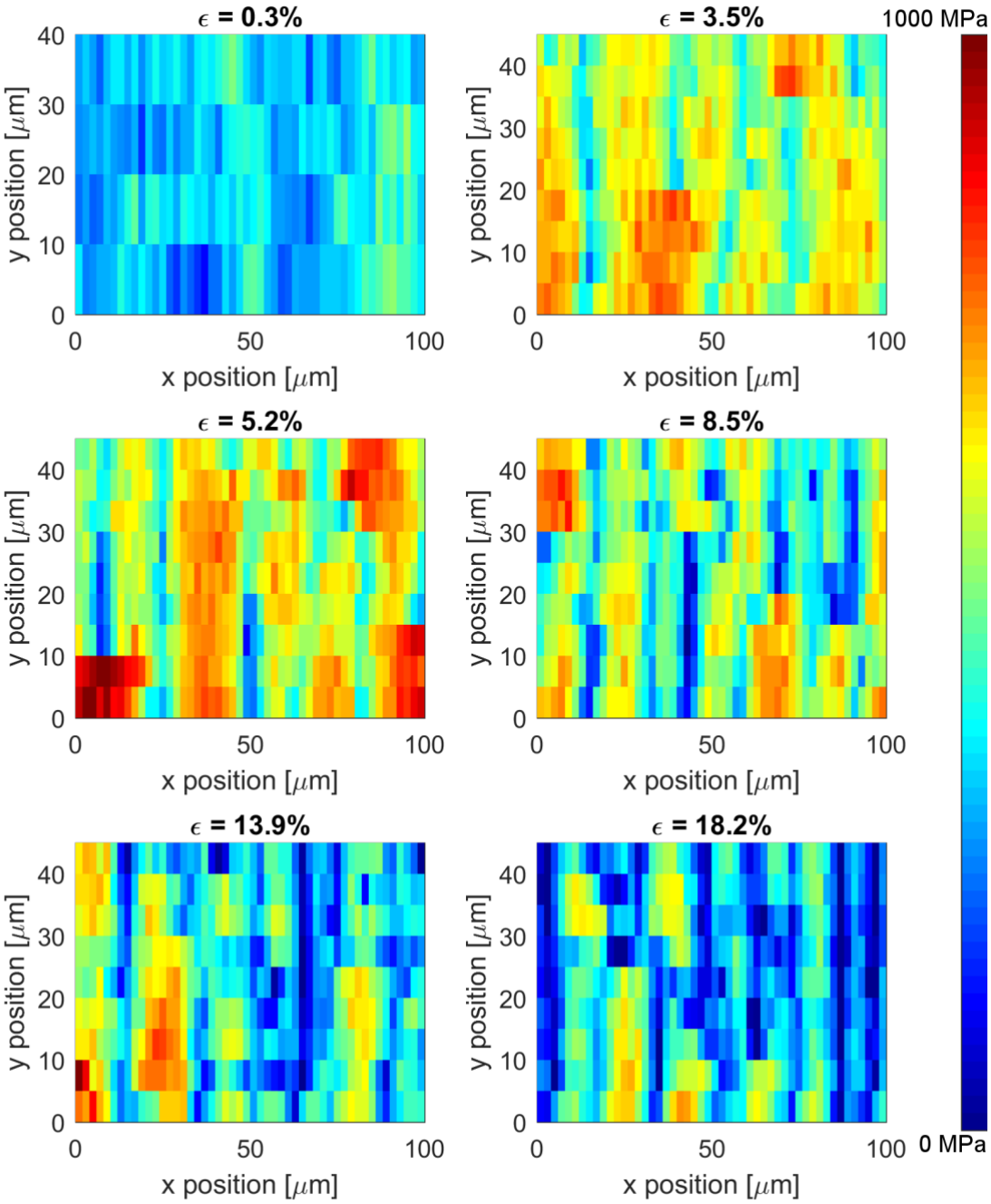


Figure 51. Stress maps for σ_{xx} calculated from the experimental strain data.

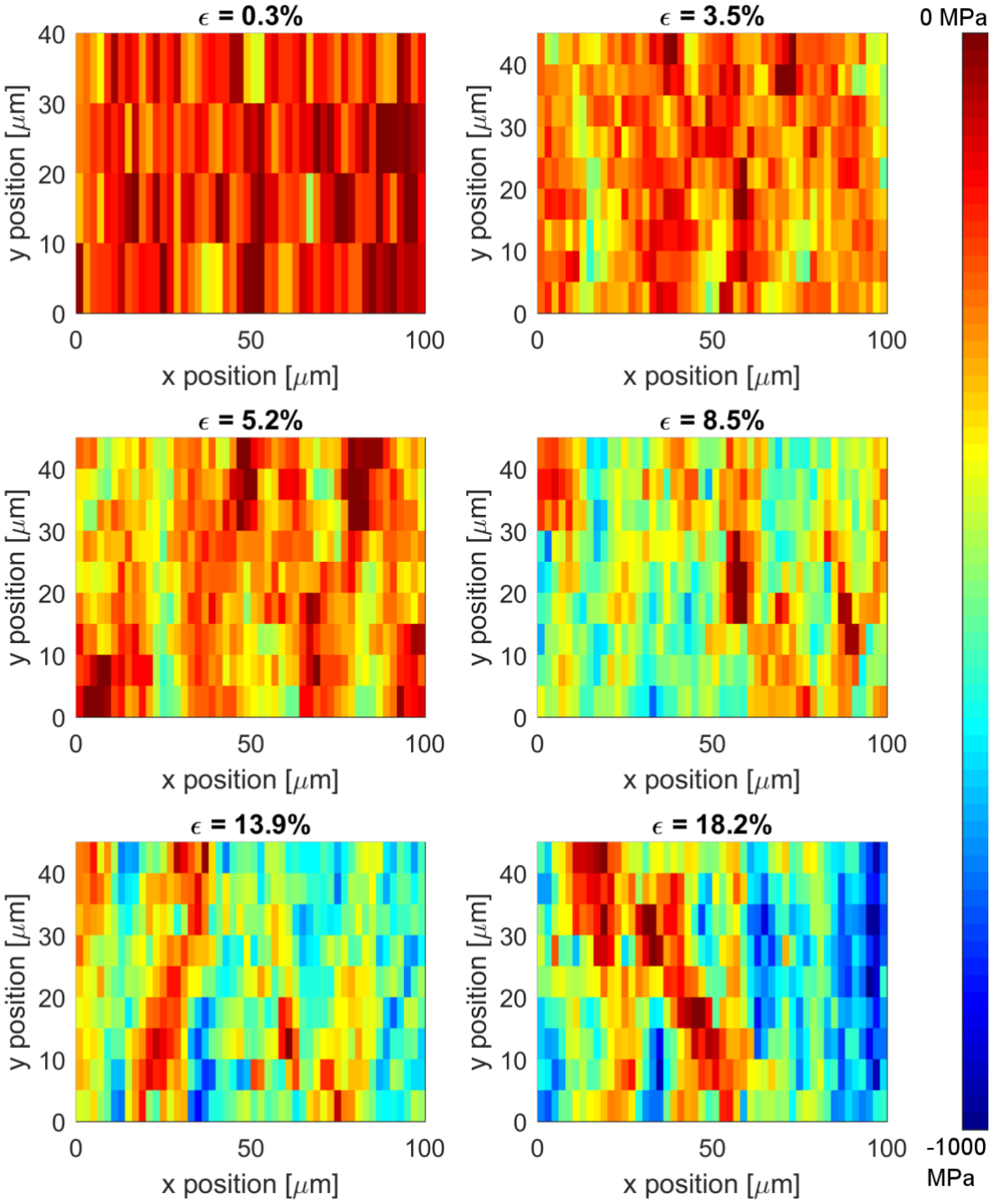


Figure 52. Stress maps for σ_{yy} calculated from the experimental strain data.

In the analysis that follows we assume that the Voigt uniform strain assumption persists throughout the coating's thickness, for the reasons discussed in 3.3.2. Adopting plane stress approximation for the stress-strain relationship, we write Hooke's law in the form:

$$\begin{bmatrix}\sigma_{xx}\\ \sigma_{yy}\end{bmatrix} = \frac{E}{1-\nu^2}\begin{bmatrix}1 & -\nu\\ -\nu & 1\end{bmatrix}\begin{bmatrix}\varepsilon_{xx}\\ \varepsilon_{yy}\end{bmatrix}. \quad (32)$$

Young's Modulus E and Poisson's Ratio ν for the multilayer are obtained by volume-weighted averaging of the individual components' properties, according to Table 1.

Material	Young's Modulus E [GPa]	Poisson's Ratio ν
Kapton®	2.5 [83]	0.34 [83]
Cu	102 [84]	0.34 [85]
W	338 [86,87]	0.36 [87]
Cu/W 18/6	161	0.35

Table 1. Volume averaged material properties for the nano-multilayer on substrate.

The maps of stress component σ_{xx} and σ_{yy} calculated using the above assumptions are shown in Figure 51 and Figure 52**.** Figure 52 clearly shows the increase of compressive stress in the transverse *y* direction with increasing substrate stretch ε. An explanation for this is presented by Frank, Handge et al. [78]. Their proposed model explains the compressive stress with a decrease of the overall stress and strain in tensile direction caused by coating fragmentation which, as a consequence, leads to a mismatch between the elastic deformation between coating and substrate.

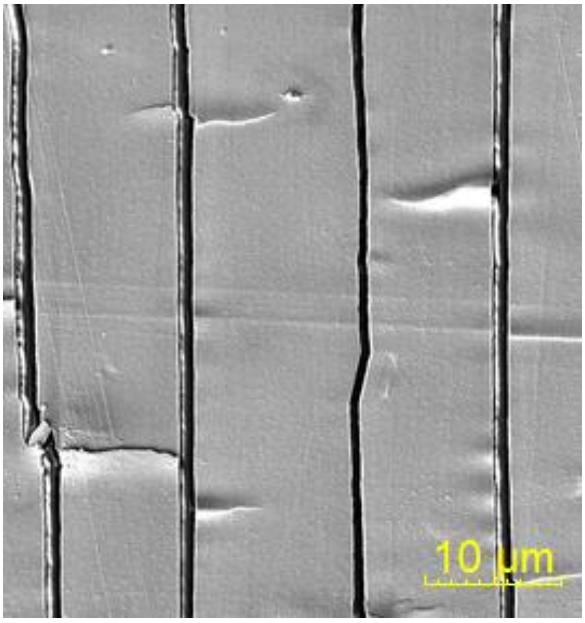


Figure 53. Compressive buckling and cracking at a substrate strain of $\varepsilon \cong 18\%$

3.2.4 Discussion of existing models

In this section the experimental results reported above are compared with the existing theoretical models of coating fracture on a ductile substrate subject to tensile stretching presented in the introduction.

The model presented by Lunt et al. presents the concept of a local limit strain $\bar{\varepsilon}(x, y)$ which is itself distributed within a range defined by the values $\check{\varepsilon}$ and $\hat{\varepsilon}$:

$$\check{\varepsilon} = \min_{x,y}\left(\bar{\varepsilon}(x,y)\right), \qquad \hat{\varepsilon} = \max_{x,y}\left(\bar{\varepsilon}(x,y)\right). \tag{33}$$

In this context the *in situ* stretching experiments reported in the present study can be viewed as a procedure that probes the stochastic distribution of the limiting strain values $\bar{\varepsilon}(x, y)$ within the coating. Indeed, upon the application of an increase in the underlying substrate

stretch, the entire "saw tooth" profile grows until a strain maximum reaches the local limiting strain value [74]. Coating fracture takes place at this point, upon which the maximum strain value is reduced, and the process continues until a critical condition is reached at another location. The local strain maxima observed in the profiles of Figure 48 therefore provide a point probe of the limit strain value landscape. Further stretching affects the distribution of limiting strain within the coating, by causing cracking at the locations of high strength, where strain continues to grow until the limit is reached, and low strength, where the local limiting strain is reached quickly. Thereby the width of the limit strain distribution, $\hat{\varepsilon} - \check{\varepsilon}$, becomes narrower. This interpretation is consistent with the observations reported in Figure 50, and also opens up interesting connections with the so-called "fibre bundle" model of material failure [88].

The second model previously presented by McGuigan et *al.* [75] introduces the concept of a shear interlayer as a strain mediator between substrate and coating. Although in the system studied presently such interlayer cannot be readily identified structurally, it may arise as a deformation-induced boundary layer at the interface between the soft polymer substrate and hard coating. It is interesting to note that the predictions of model [75] illustrated in Figure 40 show a qualitative agreement with the profiles reported in Figure 50.

3.2.5 An improved model

In this section we propose an improved approach to the description of stress within the coating that aims to combine the simplicity of model [74] and the accuracy of model [75]. The advantage of this approach is that it gives rise to an accurate stress profile prediction (as evidenced by the comparison with experiment below), but obviates the necessity of introducing an additional interlayer material between the substrate and coating.

Based on the equilibrium conditions for the coating, the interfacial shear and the internal coating stress are related as (Figure 54):

$$\frac{\partial\sigma(x)}{\partial x} = \frac{\tau(x)}{t}. \tag{34}$$

Here *t* denotes the coating thickness. Integration leads to:

$$\sigma(x) = \frac{1}{t} \cdot \int \tau(x)\ dx \tag{35}$$

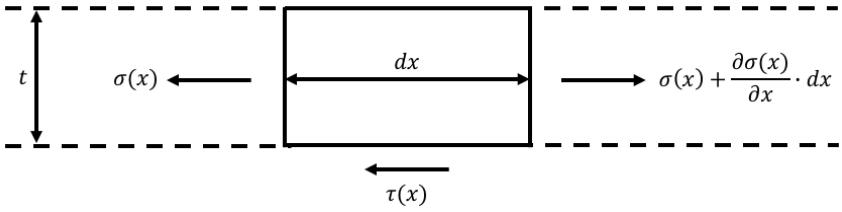


Figure 54. Equilibrium within an infinitesimal element of the coating on substrate.

The substrate is assumed to follow an elastic-ideally plastic material behaviour in shear. The applied substrate stretch is constrained by the hard coating, resulting in a shear stress distribution $\boldsymbol{\tau(x)}$ at the substrate-coating interface. From the central point in the unbroken coating fragment, where shear strain between substrate and coating is equal to zero due to symmetry, interfacial shear strain increases with distance, until the yield shear stress $\boldsymbol{\tau_y}$ of the substrate material is reached at point $\boldsymbol{a}$ (Figure 55). Due to the integral relation above, the resulting stress distribution follows a parabola within this elastic region. Between $\boldsymbol{a}$ and the corner of the coating element $\boldsymbol{d}$, shear stress remains constant at the value of $\boldsymbol{\tau_y}$, giving rise to a linear stress distribution. In summary, the shear stress distribution can be written as

$$\boldsymbol{\tau(x)} = \begin{cases} \boldsymbol{\tau_y} & , \quad \boldsymbol{x < -a} \\ \boldsymbol{-\tau_y \cdot \frac{x}{a}} & , \quad \boldsymbol{-a \le x \le a} \\ \boldsymbol{-\tau_y} & , \quad \boldsymbol{x > a} \end{cases} \tag{36}$$

The location of $\boldsymbol{a}$ is determined by the combination of the yield strain and the stretch of the substrate.

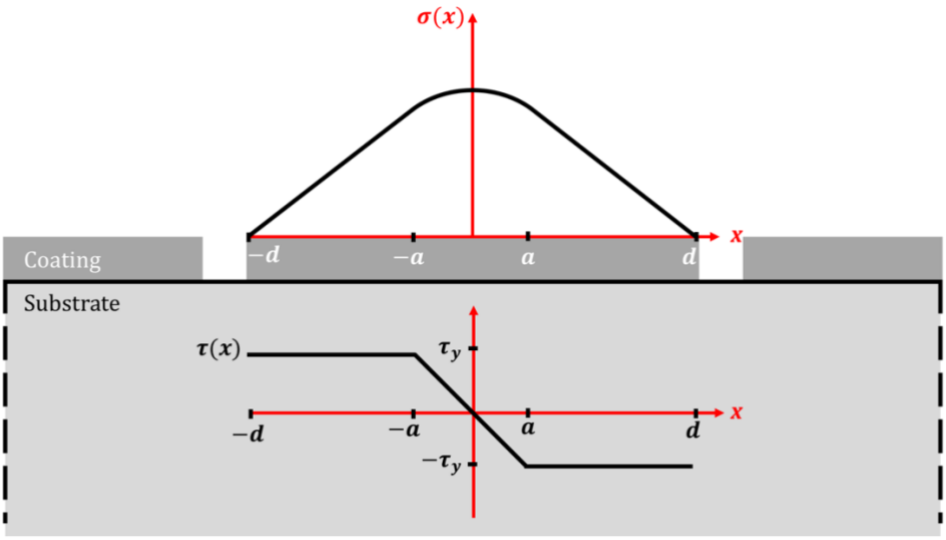


Figure 55. Shear lag model for the elastic-ideally plastic substrate behaviour.

The details of the shear transmission across the substrate-coating interface are of particular interest here. Most of the substrate thickness experiences the strain equal to the applied stretch, yet at the interface the substrate material is constrained to have the same strain as the coating. This means that there must exist a narrow layer of material that accommodates a transition between high strain in the bulk of the substrate, and low strain at the interface. This accommodation requires large shear strain that gives rise to the shear stress that can be approximately described by the equations given in (36).

3.2.6 Model discussion and experimental validation

The directly observable implication of the above model is the fact that the half-width of the elastic region $\boldsymbol{a}$ must become smaller at higher substrate stretch values. Therefore, the parabolic part of the stress function narrows down and the linear part between $\boldsymbol{a}$ and $\boldsymbol{d}$ becomes more prominent within the stress curve. This behaviour can be confirmed by the strain plots shown

in Figure 56. While in Figure 56a the entire elastic strain distribution (directly related to the coating stress) for the total substrate strain of 3.5% can be approximated equally well by a parabola, in Figure 56b the linear part of the variation is clearly apparent for the total substrate strain of 18.2%, in the *x*-position range between 7 and 10 μm. This is also supported by comparing the accuracy of a parabolic and a model fitting for Fig. 18b. While the R-squared value of a parabola reaches a value of 0.94, the model fitting approximated the data with a R-squared value of 0.99.

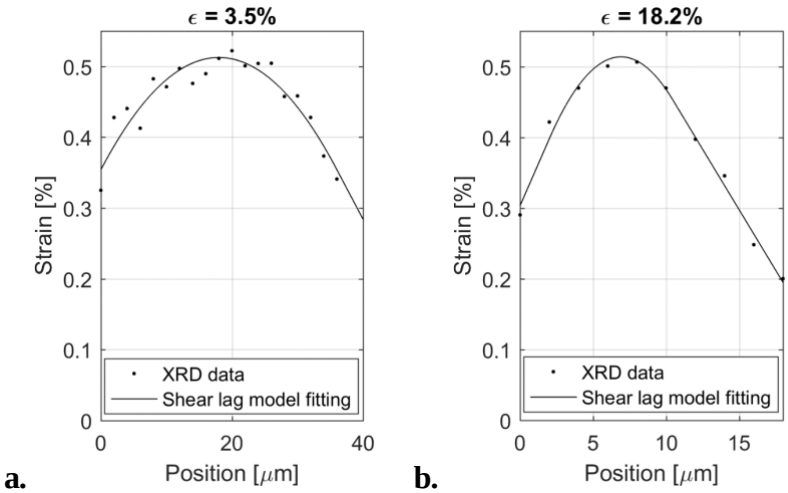


Figure 56. Coating elastic strain distribution from XRD data and model fitting. **a.** Substrate stretch = 3.5% **b.** Substrate stretch = 18.2%.

The evaluation of the slope of the multilayer coating strain profile as a function of position and its substitution in equation (34) leads to the estimate of the shear flow stress of the substrate lying around 100 MPa.

3.2.7 Conclusions

In this section, a combination of *in situ* scanning electron and X-ray diffraction microscopy was used to investigate the mechanics of stretching of thin metallic nano-multilayer coating on

a compliant polymer substrate. It was shown that *in situ* microscopy is a powerful tool for the evaluation of sample deformation behaviour at micrometre resolution. Deep insights were obtained into the mechanical response of the Cu/W 18/6nm multilayer coating. In particular it was possible to establish that the tensile limit strain for coating fracture is stochastically distributed within the range $0.5\% < \bar{\varepsilon} < 0.65\%$.

The experimental results were analysed in the context of theoretical models of the load and deformation transfer between substrate and coating. It was found that the Lunt et *al*. model [74] has the advantages of simplicity and explicit accounting for the statistics of coating strain limit. However, the strain profile predicted by this model provides only a partial match to the observations at higher substrate stretch values. On the other hand, the McGuigan et *al*. model [75] offers a better prediction of the strain distribution. The necessity of introducing an elastic-ideally plastic shear interlayer to effect the solution presents is limitation that was overcome by the newly introduced shear lag model, which was validated by comparison with XRD strain profiles.

The findings of this study demonstrate that the combination of electron and X-ray scanning microscopies can provide improved insight into the micro-mechanics of complex nano-structured systems, ultimately helping the improvement of performance and reliability of thin film systems by design.

3.3 Determining the Mode I fracture toughness of Cu/W nano-multilayers on compliant substrate using Digital Image Correlation

3.3.1 Introduction and Literature Review

Crack nucleation and propagation in thin films and coatings may cause premature failure under external load. A multitude of interdependent factors influence the fracture resistance in such materials, such as the intrinsic microstructural properties, the balance between ductile and brittle responses, and the residual stress state resulting from the manufacturing history [53], as well as the type and direction of applied loading. A theory frequently employed in engineering design for brittle and semi-brittle materials is Linear Elastic Fracture Mechanics (LEFM). This popular failure criterion relies on the determination of the Stress Intensity Factor (SIF) that describes the elastic deformation fields in an annular region surrounding the crack tip, also known as K-field. Failure is expected to occur once the critical value of the SIF is reached, for instance, K_{IC} for pure mode I loading. K_{IC} can be readily determined for bulk materials using standardised mechanical testing procedures. When evaluating the fracture properties of thin and ultra-thin materials, however, standard test procedures cannot be applied. A multitude of adapted approaches [89] have therefore been developed and presented in the past: bending [90,91], buckling [92,93], scratching [94,95], micro-cantilever indentation [96,97], bulge testing [98], as well as nano-indentation [99,100] tests have proven successful at determining the critical parameters for failure criteria. Unfortunately, extensive sample preparation [90,98] is often times required, which involves the risk of modifying the coating structure and its response to loading. FIB preparation of nano-scale cantilevers, for instance, can significantly modify the mechanical properties within surface layers affected by ion implantation [65,101]. Furthermore, these test methods are often limited to film

thicknesses of several microns, which makes testing of sub-micron to sub-nanometre thin films hardly feasible.

Nowadays, cutting-edge developments in electronics and surface modification rely on ultra-thin films and coatings that exhibit carefully designed material properties at the (sub-) nanometre scale. Nanostructured metallic multilayers enable precise tailoring of novel mechanical and functional coating properties by combining the desired characteristics of different individual materials. The resulting multilayers possess enhanced properties compared to the individual component materials. Crack growth, for instance, can be hindered by crack deflection along multilayer interfaces [102], resulting in increased fracture toughness. Further advantageous mechanical properties can be related to the confinement of nanograins in nano-scale strata, which hinder dislocation motion. Combining copper and tungsten in a nano-multilayer at a bilayer thickness ratio of 18:6 nm results in a coating material with high hardness, low thermal expansion coefficient and excellent thermal transport properties, which is of particular interest for thermal management applications at the micron scale. The immiscibility of Cu and W ensures clear phase separation along sharp interfaces. Further applications have been identified in the neutron radiation industry, where Cu/W multilayers could serve as shielding material [103]. For these applications, the mechanical integrity of the coating material is of utmost importance, as exposed substrate area might not provide sufficient shielding.

In this section, we present a novel approach for the determination of K_{IC} in Cu/W nano-multilayers with a total thickness of 240 nm on Kapton substrate, which relies on surface displacement analysis obtained from DIC analysis of SEM micrographs. We then confirm the validity of our approach with FEM modelling and benchmark the obtained K_{IC} against the existing literature data.

3.3.2 Materials and Methods

3.3.2.1 Materials

Ten bilayers of Cu/W 18/6 nm were deposited onto 125 µm thick pre-cut Polyimide (Kapton) substrate in dog-bone shape (Figure 57b) for mechanical testing, resulting in a coating thickness of 240 nm. The deposition was carried out at room temperature by ion beam sputtering with a focused Ar + ion gun at 1.2 keV multicusp radio-frequency source in a NORDIKO-3000 system [46]. During film growth, the ion gun was supplied with constant radio-frequency power of 165 W and constant Ar flux of 10 standard cubic centimetre per minute (sccm). The 150 mm diameter targets were sputtered during 10 min allowing both ion-gun stabilization and target pollution cleaning caused by vacuum break. The ion gun axis was inclined at 45° to the normal of the surface target whilst the sample surface was parallel to the target plane. The sputtering chamber was pumped down to a base pressure of $2 \cdot 10^{-6}$ Pa whilst the working pressure during film growth was ~ 10^{-2} Pa. Substrates were preliminarily cleaned with acetone and ethanol and finally dried with an argon gas jet prior to their introduction in the deposition chamber. Tungsten and copper growth rates were previously calibrated by XRR and were found to be $0.05\ \mathrm{nm\ s^{-1}}$ and $0.16\ \mathrm{nm\ s^{-1}}$, respectively. XRR was performed in order to evaluate sample stratification using the Bragg law at a grazing incidence angle. Energy-dispersive X-ray spectroscopy was used in a SEM to determine the atomic concentrations of Cu and W in the films and to estimate the effective tungsten and copper sublayer thicknesses per period employing the period obtained by XRR. The multilayer cross-section of a thin, electron-transparent lamella imaged using STEM at 20 keV beam energy shown in Figure 57a clearly reveals the multilayer structure with sharp Cu/W interfaces.

3.3.2.2 *In situ* uniaxial tensile experiment

The tensile specimen with dimensions shown in Figure 57b was clamped inside a uniaxial DEBEN *in situ* micro-tensile stage at a gauge length of 4 mm and mounted inside the chamber of a Tescan LYRA 3XM FIB-SEM instrument. To reduce aliasing and improve the DIC tracking, a grid of non-repetitive 'sunflower' pattern of dots shown in Figure 57c with a size of 11x11 μm^2 was deposited onto the surface of the sample using an in-chamber platinum deposition system [104]. As the pattern was formed of unconnected nano droplets, the fracture properties of the sample were not altered. To ensure crack growth across the patterned RoI, an adjacent surface notch with the length of approximately 49 µm and width of approximately 0.3 µm was introduced using FIB at a beam current of 0.04 nA and at the accelerating voltage of 30 keV. The resulting surface preparation is shown in Figure 57d. A small pre-existing flaw in form of a small crack in the ROI was identified and is marked with a yellow arrow.

Subsequently, the sample was elongated by approximately 240 µm in 24 steps of 10 µm. Before the experiment and in between extension steps, high-resolution SEM images were acquired at the beam energy of 5 keV. Negligible sample relaxation in between loading steps was observed, as shown in the force versus displacement plot in Figure 58. The RoI with dimensions of 6x6 μm^2 on which the DIC markers were tracked is shown for four selected extension values corresponding to the labels in the left plot in Figure 58.

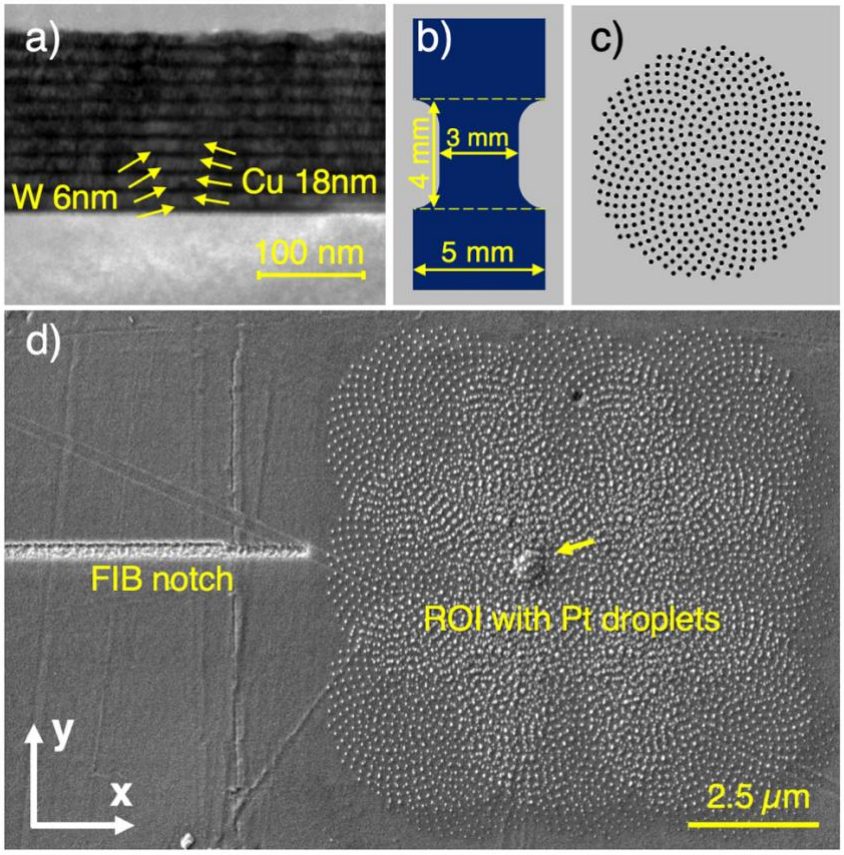


Figure 57 a. STEM Image of Cu/W multilayer cross-section showing clear layer separation between Cu (light) and W (dark). b. Dog bone specimen shape and dimensions. c. Non-repetitive sunflower pattern used to prevent DIC aliasing. d. Sample surface preparation for controlled crack growth and improved DIC tracking, including FIB notch (left) and Pt droplet pattern for improved DIC tracking (right). A small pre-existing crack in the coating is indicated with an arrow.

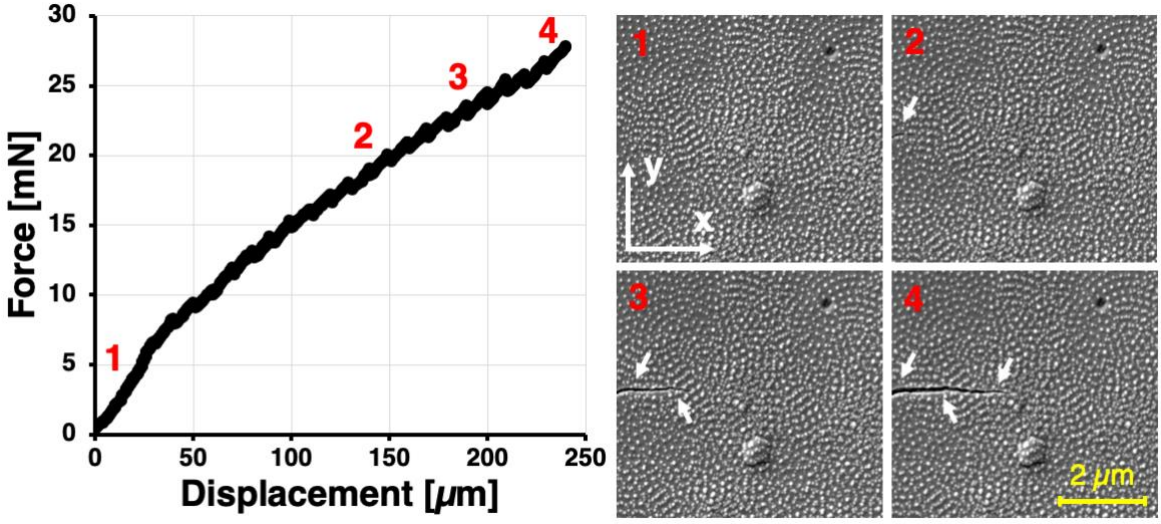


Figure 58. Left: Micro-tensile stage data showing elongation versus force during in situ tensile experiment. Right: DIC ROI at different elongations indicated in the force-displacement graph.

3.3.2.3 DIC analysis and fitting

To evaluate the displacement of surface markers with respect to the strain-free reference state, post-experimental DIC was carried out using a MATLAB-based software package [43]. The displacement field in x- and y-direction, u_x and u_y, around the crack tip under plane stress assumption and Mode I loading can be expressed as [105]:

$$\mathrm{u_x} = \frac{K_I}{2\mu}\sqrt{\frac{r}{2\pi}}\cos\left(\frac{\theta}{2}\right)\left[\frac{3-\nu}{1+\nu} - 1 + 2\sin^2\left(\frac{\theta}{2}\right)\right] \tag{37}$$

$$u_y = \frac{K_I}{2\mu}\sqrt{\frac{r}{2\pi}}\sin\left(\frac{\theta}{2}\right)\left[\frac{3-\nu}{1+\nu} + 1 - 2\cos^2\left(\frac{\theta}{2}\right)\right], \tag{38}$$

with the notations are μ for the shear modulus, and ν for Poisson's ratio.

The properties of Cu and W component materials are shown in Table 1, alongside the Cu/W mechanical properties obtained by the rule of mixture (Voigt model). The shear modulus of the Cu/W 18/6 nm multilayer was calculated as $\mu_{Cu/W} = \frac{E_{Cu/W}}{2(1+\nu_{Cu/W})}$ according to the material constants provided in Table 2 [106], resulting in a value of $\mu_{Cu/W} = 59.6\ GPa$.

	Young's Modulus E [GPa]	Poisson's Ratio ν
Cu (nano-crystalline)	102	0.34
W (nano-crystalline)	338	0.36
Cu/W 18/6	161	0.35

Table 2. Material properties used for K_{IC} fitting

3.3.2.4 Numerical Simulation

A fundamental hypothesis made in the experimental determination of the critical stress intensity factor via DIC was that K' evaluated from the surface displacement of the coating around the crack tip during propagation is representative of K'' in the coating in the absence of the substrate, i.e. $K' = K''$. This hypothesis was thoroughly tested and validated in the present study through modelling and comparison with literature data, so that the validity of the obtained K_{IC} from DIC for the isolated coating was verified. Two independent FEM simulations under plane stress assumption were created using COMSOL Multiphysics package. In order to evaluate whether full-field fitting of the coating displacement and stress fields ahead of the crack tip lead to identical results independent of the substrate, Model 1 was simulated as a thin film on compliant substrate, while Model 2 was simulated as free-standing coating, as shown in Figure 59. In a first step, a fixed displacement was applied to Model 1, resulting in a stress intensity K_I at the crack tip. Subsequently, a fixed displacement for Model 2 was found iteratively, resulting in a matching K_I value. Finally, the two displacement fields were compared in order to verify whether these also deliver the identical K_I based on LEFM fitting.

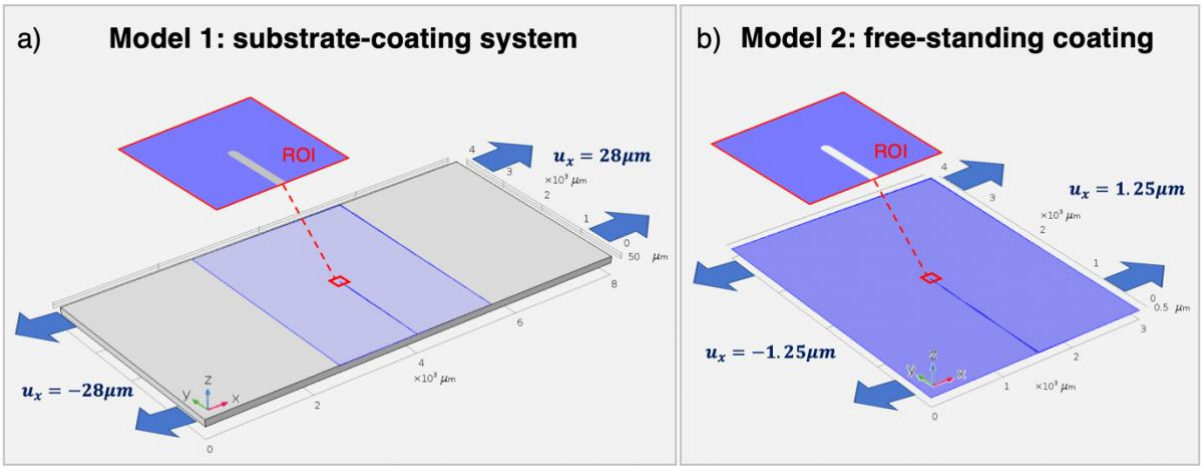


Figure 59a. COMSOL Model 1 geometry overview showing Kapton substrate (grey) with Cu/W coating (blue). Blue arrows indicate prescribed uniaxial displacement. ROI highlighted in red. b. COMSOL Model 2 geometry overview showing free standing Cu/W coating (blue).

For Model 1, a Kapton substrate with dimensions of 8000x4000x125 µm^3 was generated and coated with a thin film of dimensions 3000x4000x1 µm^3. Perfect adhesion at the substrate-coating interface was assumed, since no coating debonding was observed during the *in situ* experiment. An elongated notch was introduced into the coating with a crack tip radius of 1 µm and a length of 2000 µm, as shown in Figure 59a. A prescribed symmetric total displacement of 56 µm in x-direction at the substrate ends was applied, resulting in an overall substrate strain of around 0.7%. In addition, rigid motion suppression for the entire model was applied in order to prevent translational and rotational motions. While the material parameters shown in Table 1 were used for the coating, a strain-dependent Young's modulus was implemented to model a realistic elasto-plastic behaviour of the Kapton substrate. Based on the force-strain data shown in Figure 58 and a known sample cross-sectional area of 3000x125 µm^2, the Young's modulus in the linear-elastic region up to $\varepsilon = 0.9\%$ was determined as E_1 = 2 GPa, while it was found to be E_2 = 0.94 GPa in the region beyond $\varepsilon = 0.9\%$. A Poisson's ratio of $\nu = 0.35$ was used based on Kapton manufacturer data [83]. Identical coating material parameters were used for Model 2, which simulated a piece of free stranding coating of the same dimensions as described in Model 1 as is shown in Figure 59b. The ROI around the crack tip is highlighted in red. A prescribed symmetric total displacement of 2.5 µm in x-direction was applied at the sample ends in order to match the stress intensity at the crack tip obtained from Model 1.

3.3.3 Results and Discussion

3.3.3.1 DIC fitting

The displacement fields u_x and u_y obtained from DIC analysis of experimental data at loading step 4 in Figure 58 are shown in Figure 60a and Figure 60c. Nonlinear least square fitting was used to determine the critical stress intensity factor describing the displacement field around the Mode I crack opening according to equations (37) and (38), which returned a value of $K_{IC} = 4.8 \pm 0.05\ \mathrm{MPa}\sqrt{\mathrm{m}}$ for u_x and $K_{IC} = 4.8 \pm 0.02\ \mathrm{MPa}\sqrt{\mathrm{m}}$ for u_y in a 95% confidence interval. The resulting displacement field fits based on linear-elastic fracture mechanics for u_x and u_y are shown in Figure 60b, d.

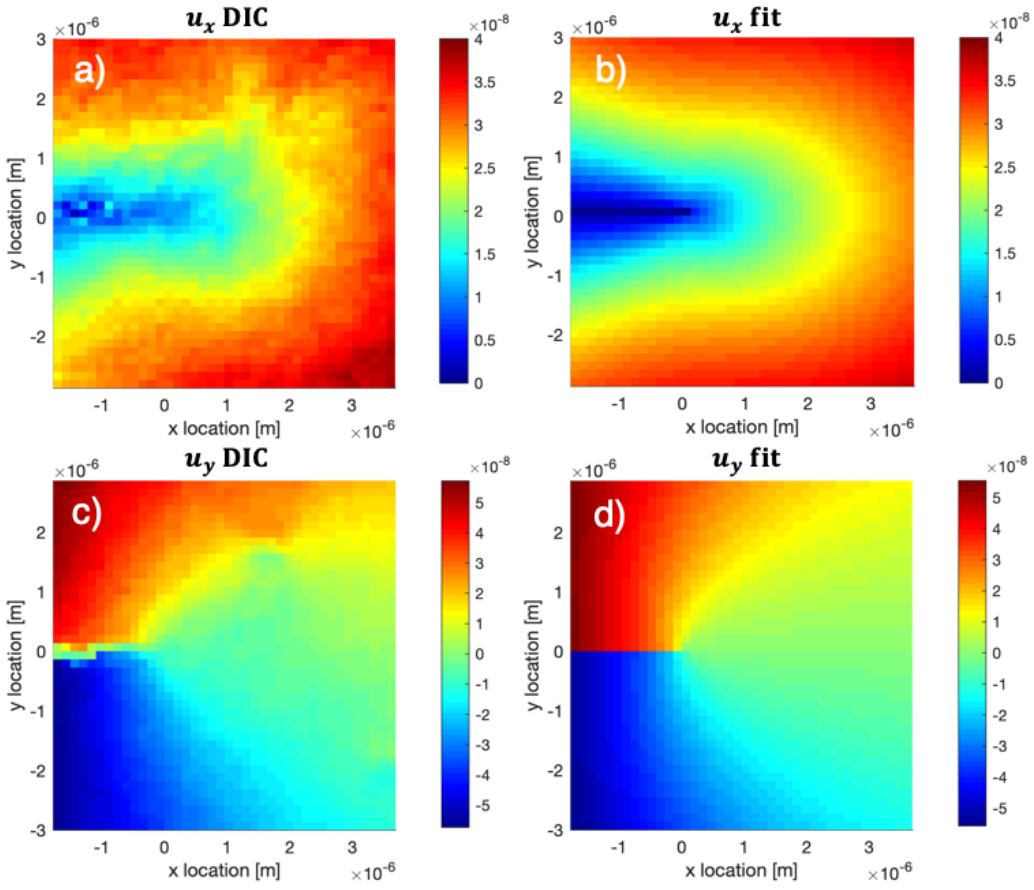


Figure 60. Results of DIC analysis alongside fitted results predicted by LEFM. a) DIC results of displacement in x direction b) Fit of x-displacement field based on linear elastic fracture mechanics for $K_{IC} = 4.8 \pm 0.05\ \mathrm{MPa}\sqrt{\mathrm{m}}$. c) DIC results of displacement in y direction. d) Fit of y-displacement field based on linear elastic fracture mechanics for $K_{IC} = 4.8 \pm 0.02\ \mathrm{MPa}\sqrt{\mathrm{m}}$.

To verify the obtained K_{IC} value, the result was compared to literature data obtained using different testing methods on similar systems. While no values for the fracture toughness of Cu/W nano-multilayers could be found in the literature, extensive data for pure Cu thin films of different thicknesses was published by Hirakata et al. [107] and Keller et al. [108]. The result comparison shown in Figure 61 confirms a fracture toughness property of Cu/W nano-multilayers very close to the expected K_{IC} for a pure Cu film of identical thickness. As the Cu/W 18/6nm nano-multilayer consists of 75% Cu by thickness, a material behaviour close to Cu appears reasonable. A square root dependence between film thickness t and the critical stress intensity was found, which can be described as [98]

$$K_{I,C} = \sqrt{0.5 E k_{sl} t}, \tag{39}$$

with k_{sl} as single fit parameter representing the effective stress resistance to shear lip formation. The corresponding fit shown as dotted line in Figure 61 returned a value of $k_{sl} = 1.19 \pm 0.03 \frac{GJ}{m^3}$ for Cu/W 18/6, which can also be thought of shear fracture stress of 1.19 ± 0.03 GPa. Furthermore, the size-dependent fracture properties of pure W micro-cantilevers studied by Ast et al. [109] indicate a similar fracture toughness range between 3 MPa$\sqrt{\text{m}}$ for single crystalline W up to around 6 MPa$\sqrt{\text{m}}$ for nanogranular W with a grain size of around 790 nm. Finally, further studies on the fracture toughness of Cu/Cr nano-multilayers with different bilayer periods [110] showed a very close critical stress intensity factor of around 5 MPa$\sqrt{\text{m}}$ for a Cu/Cr nano-multilayer with an individual layer thickness of 12.5 nm. It can be estimated that for the Cu/Cr nano-multilayer and the Cu/W nano-multilayer the grain size within individual layers was equivalent to the layer thickness (12.5 nm and 18 nm, respectively), as described in [110] for Cu/Cr and as estimated from the TEM data shown in Figure *69* for Cu.

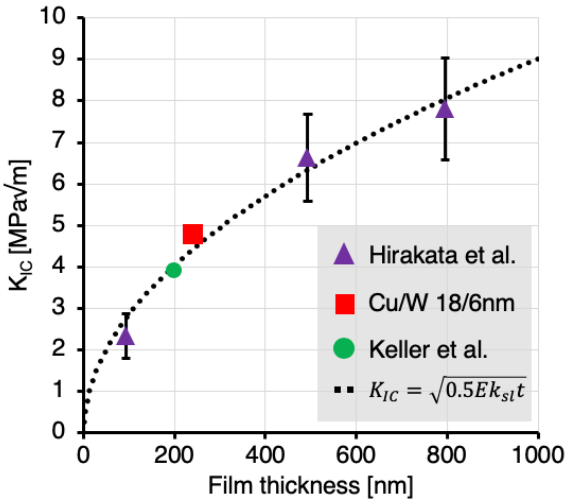


Figure 61. Comparison of the obtained K_{IC} for Cu/W with literature data on free-standing Cu thin films vs. film thickness. Dotted line: square root fit of the literature data according to equation (39).

3.3.3.2 Simulation results

The resulting horizontal stress component distributions σ_{xx} for both Model 1 and Model 2 are shown in Figure 62. While a stress concentration at the notch tip can be observed in both models, the horizontal stress σ_{xx} in Model 2 is overall significantly lower as compared to Model 1. The driving force underlying the elevated overall stress level in Model 1 is the adhesion between substrate and coating, which leads to stress transfer across the interface through shear deformation of the substrate. A detailed description of this mechanism based on the shear lag theory can be found in [46,111]. The following analysis will be focused on the question whether the stress and displacement fields in the ROI labelled '2' in Figure 62 are comparable for both Model 1 and Model 2.

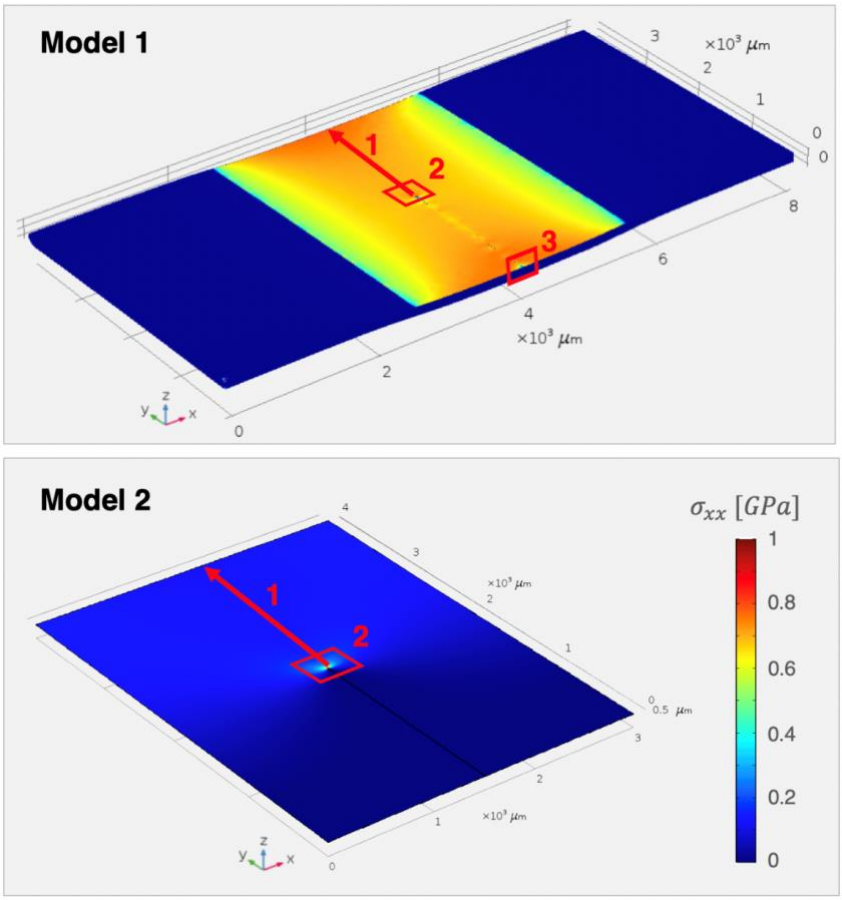


Figure 62. Resulting horizontal stress σ_{xx} from prescribed displacement at the sample end for Model 1 (substrate-coating system) and model 2 (free-standing coating). 1: location and direction of σ_{xx} line plot. 2: Region of interest for full field fitting. 3: Region of interest for the analysis of substrate stress.

In a first step, the singularity dominated region or K-field was identified, in order to fit the stress intensity factor K_I. For this purpose, the line profiles of the horizontal stress distribution σ_{xx} ahead of the notch tip were compared for both Model 1 and Model 2 along the direction labelled '1' in Figure 62. The result shown as double-logarithmic plot in Figure 63 shows identical stress behaviours for both models in the region ranging from the notch tip up to a distance of around 5.5 µm. Both curves can be subdivided into three distinct regions [112]: the plastic zone in close proximity of the notch tip labelled 'A', the linear region representing the K-field labelled 'B', and the far field dominated by the sample constraints labelled 'C' for the substrate-coating system. It is clearly visible that the linear region suitable for the

determination of the stress intensity factor is significantly larger in Model 2, while the stress distribution in Model 1 beyond 5.5 µm from the notch tip is dominated by the stress transferred from the substrate to the coating. Based on this information, a region of interest ranging from 0.25 µm to 5.5 µm ahead of the crack tip was selected for further analysis and full-field fitting of the displacement and stress fields.

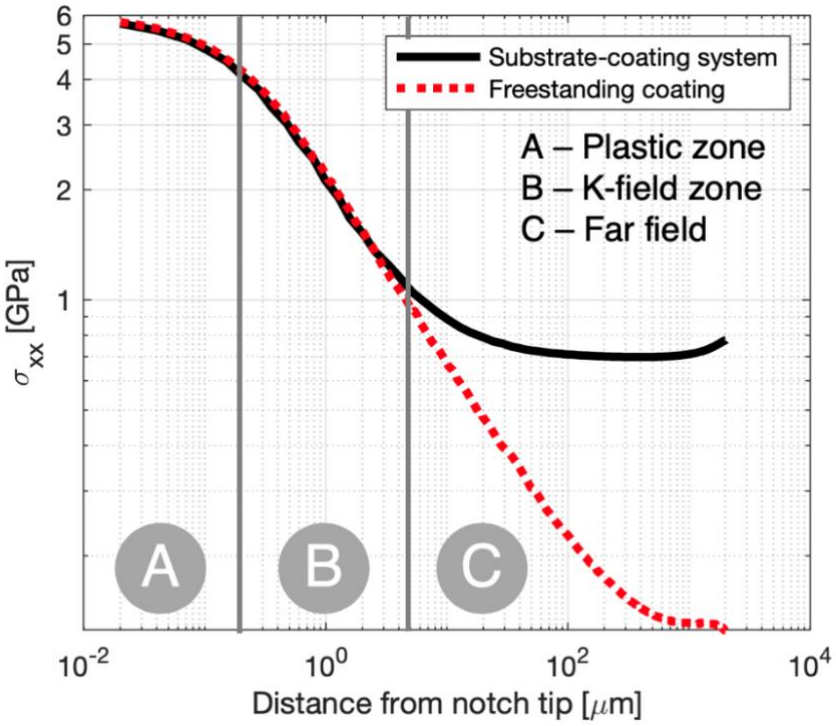


Figure 63. Double-logarithmic line profile of the horizontal stress component σ_{xx} in y-direction ahead of the notch tip. Stress values for the substrate-coating system (Model 1) are displayed as solid black line, stress values for the free-standing coating (Model 2) are displayed as dotted red line. A subdivision of different zones for the substrate-coating system (Model 1) are labelled as A, B and C, representing the plastic zone, K-field and far field.

Subsequently, the stress field σ_{xx} in the region labelled 'B' in Figure 63 was fitted for both models using the following relation based on linear-elastic fracture mechanics [105]:

$$\sigma_{xx} = \frac{K_I}{\sqrt{2\pi r}} \cos\left(\frac{\theta}{2}\right)\left[1 + \sin\left(\frac{\theta}{2}\right)\sin\left(\frac{3\theta}{2}\right)\right] \tag{40}$$

The fits shown as surface plot in Figure 64 reveal identical stress and displacement behaviours for both Model 1 and Model 2 in the singularity dominated zone. Non-linear least square fitting of the simulation results revealed the stress intensity values based on the stress field $\sigma_{xx}(x, y)$ and the displacement field $u_x(x, y)$. Identical stress intensity values of $K_I = 5.027 \pm 0.063\ MPa\sqrt{m}$ were obtained for all four sets of simulation data.

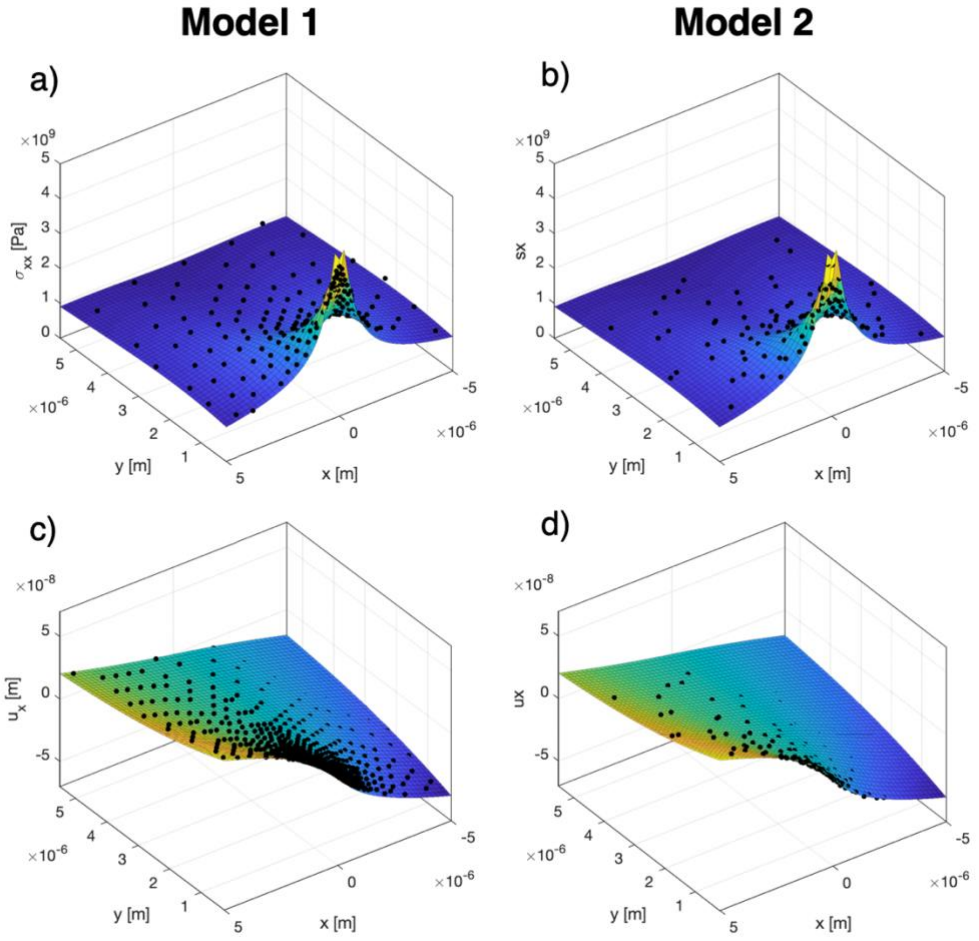


Figure 64. Simulation results (black markers) and fits (surface plots) of stress and displacement fields in the singularity dominated zone for Model 1 and Model 2. a) Stress field ahead of the crack tip for Model 1. b) Stress field ahead of the crack tip for Model 2. c) Displacement field ahead of the crack tip for Model 1. d) Displacement field ahead of the crack tip for Model 2.

The above-presented results clearly indicate that estimating the stress intensity factor of coating material is possible based on the surface displacement field of a coating-substrate system in which only the substrate experiences external loading. However, this approach is only valid in the K-field dominated zone ahead of the crack tip, which can be identified as a linear region in a double-logarithmic plot of the stress field ahead of the crack tip, as shown in Figure 63. The large difference in stress in the far field region ('C' in Figure 63) clearly shows the limits of this technique, as only a small region close to the notch tip can be used for the analysis carried out above. High-resolution microscopic imaging techniques as used in this study are therefore required to capture the displacement at the scale of the K-field size. This made SEM/DIC analysis particularly suitable for this study, as the identified K-field dominated zone had a radius of around 5 µm.

Finally, the behaviour of the coating-substrate interface (region '3' in Figure 62) was studied based on simulation results. A high concentration of stress σ_{xx} in horizontal direction around the notch opening was found, as shown in Figure 65. The coating gap was found to act as 'crack tip' reaching vertically into the substrate. The stress levels found in the substrate near the crack opening exceed the linear elastic regime of the substrate by far and lead to local plastic deformation. As the substrate becomes significantly more compliant when stretched beyond its yield point, the stress concentration along the substrate-coating interface permits further crack opening resulting in a higher stress concentration at the notch tip, despite the strong substrate-coating bond. The displacement field near the crack tip and crack opening is therefore mainly representative of the coating material, as the plastically deformed substrate does not restrain the coating in this zone. At further distance from the crack, the substrate-coating bond is intact and continues to drive the crack growth and opening. It is thus possible to use the near-crack region for K_{IC} determination of the coating material.

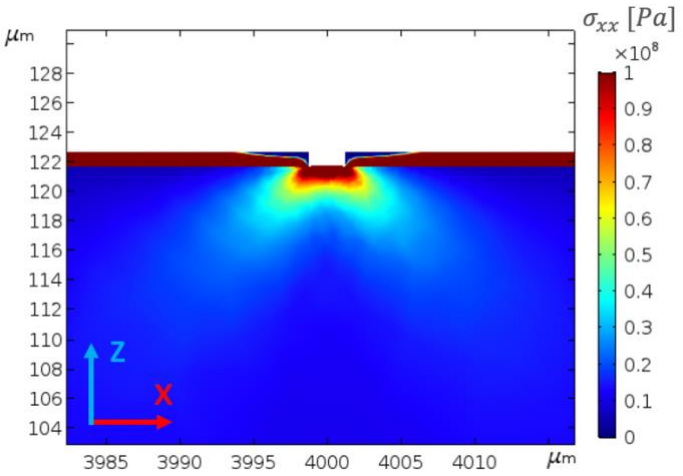


Figure 65. Horizontal stress distribution at the substrate coating interface around the notch opening revealing high level of stress concentration in the substrate.

3.3.4 Conclusion

A multi-step approach for the determination of the Mode I critical stress intensity factor K_{IC} in Cu/W nano-multilayers on compliant Kapton substrate based on DIC analysis of controlled uniaxial crack growth was presented in this work. 2D displacement field fitting in close proximity of the crack tip based on linear elastic fracture mechanics was used to obtain the critical stress intensity factor of $K_{IC} = 4.8 \pm 0.05\ \mathrm{MPa}\sqrt{\mathrm{m}}$. Excellent agreement with literature values for pure Cu thin films of similar thickness as well as Cu/Cr nano-multilayers of similar bilayer period was found.

To confirm the validity of the chosen approach, two independent FEM simulations were developed and compared. The first model simulated a thin film on compliant substrate. The second model simulated a free standing thin film of the same dimensions. By applying a prescribed displacement at both ends of the first model, thus imitating the experimental setup with a micro-tensile stage, a stress intensity at the crack tip was created. A matching stress intensity was then iteratively found for model 2 by applying a fixed displacement. In order to identify whether the displacement field ahead of the crack tip in the substrate-coating model is representative of the mechanical properties of the coating material, both the displacement

and stress field were compared across both simulations. Identical stress intensity factors were found across both simulations for a limited region dominated by the K-field. The experimental determination via DIC was therefore confirmed as appropriate. Finally, the mechanisms permitting crack opening despite a strong substrate-coating bond were revealed based on the simulation of the substrate-coating system, according to which local plastic deformation of the substrate is permitting the crack to open and grow.

4 The effect of energetic deposition conditions on the thermal and diffusion properties of nanostructured coatings

4.1 Controlling Thermal Diffusivity, Residual Stress and Texture in W/Cu Nano-Multilayers by Magnetron Chamber Pressure Variation

4.1.1 Introduction and Literature Review

Understanding and controlling the thermal and mechanical properties in thin films and coatings during deposition is of utmost importance for their reliable use in challenging environments. Depending on the intended field of application, thermal diffusivity, residual stress and grain texture need to be carefully chosen and controlled during manufacturing and processing. A common way of manufacturing nano-layered coatings is Argon-assisted MSD. The effect of the magnetron chamber pressure on the residual stress state [51,113,114], stress distribution [106] and microstructure [115–117] has been analysed and discussed in the past. Further literature work includes the analysis of the effect of magnetron pressure variation on the electrical and thermal properties of Cu-Ta films [118], as well as the study of the structural and thermal property changes in GaN film deposited at varying magnetron working gas pressures [119]. In-depth insight into the link between the working gas pressure, thermal diffusivity and residual stress, however, remains lacking in the literature.

W/Cu nano-multilayers (NMLs) as target materials for plasma-facing components in fusion reactors [120] and as protective coatings in nuclear fission reactors [103] have shown promising thermal, mechanical, microstructural and functional properties, that are closely related to the means of manufacturing and processing. Combining the high thermal

conductivity of copper with the low thermal expansion coefficient of tungsten makes W/Cu NMLs a material of choice for thermal management applications, while maintaining high mechanical coating strength [121]. The interfacial structure of nano-granular W can additionally serve as a sink for radiation-induced defects [103]. To ensure structural integrity in these challenging and safety critical environments, a fundamental understanding of the consequences of deposition conditions on the material properties is urgently needed. Here, we present experimental evidence showing a clear link between magnetron chamber pressure, thermal diffusivity, residual stress and laminate microstructure.

4.1.2 Materials and Methods

Three different W/Cu nano-multilayers were deposited at room temperature onto a single crystal [001] oriented Si substrate using planar DC magnetron sputtering at different Ar flow rates and at constant target power of 130 W for tungsten and 54W for copper, resulting in a magnetron chamber pressure of P_1 = 0.50 Pa, P_2 = 0.74 Pa and P_3 = 0.89 Pa during deposition, respectively. The substrate bias was 0V for all samples. Cu and W target purity was 4 N (99.99%) with a diameter of 7.5 cm, respectively, while the target-to-substrate distance of the unbalanced magnetron was constant at 18 cm. The angle between substrate normal and Cu and W targets was 25°, respectively. Each multilayer consisted of 10 bilayers of W/Cu 50/50 nm), resulting in a total coating thickness of 1 µm. The growth rates for both Cu and W were previously calibrated for two different chamber pressures P_1 = 0.50 Pa and P_2 = 0.74 Pa by XRR and were measured to be 1.1 Å s^{-1} for Cu and 1.1Å s^{-1} for W, independent of the chamber pressure variation. The interruption in between deposition of successive layers was 5s.

High resolution cross-sectional SEM imaging using a BSE detector was combined with EDX analysis of all three samples at an electron energy of 10 keV, after FIB milling of trenches using a beam current of 0.2 nA and an accelerating voltage of 30 keV. The SEM images

shown in Figure 66a-c indicate a decrease in interface sharpness and increase in layer waviness with increasing deposition pressure. This was further confirmed by EDX line profiles, that show a uniform intensity versus depth for the sample deposited at P = 0.5 Pa (Figure 66a), while a decreasing intensity amplitude towards the substrate-coating interface is observed at higher deposition pressures (Figure 66 b,c). The copper distribution in the near-interface layers of the sample deposited at P = 0.89 Pa is nearly uniform, indicating a poor interface quality, which can be linked to an increased roughness between immiscible Cu and W layers.

WAXS patterns in reflection geometry at an incidence angle of 1° with respect to the sample surface were acquired at Diamond Light Source Synchrotron Beamline B16 (Didcot, UK) at a beam energy of 18 keV and a beam size of 250x250 μm^2 for 360s using an Image Star 9000 detector at a sample-detector distance of 66 mm. The obtained Debye-Scherrer rings [106] for samples deposited at different deposition pressures are shown in Figure 66d-f, alongside diffraction peak identification.

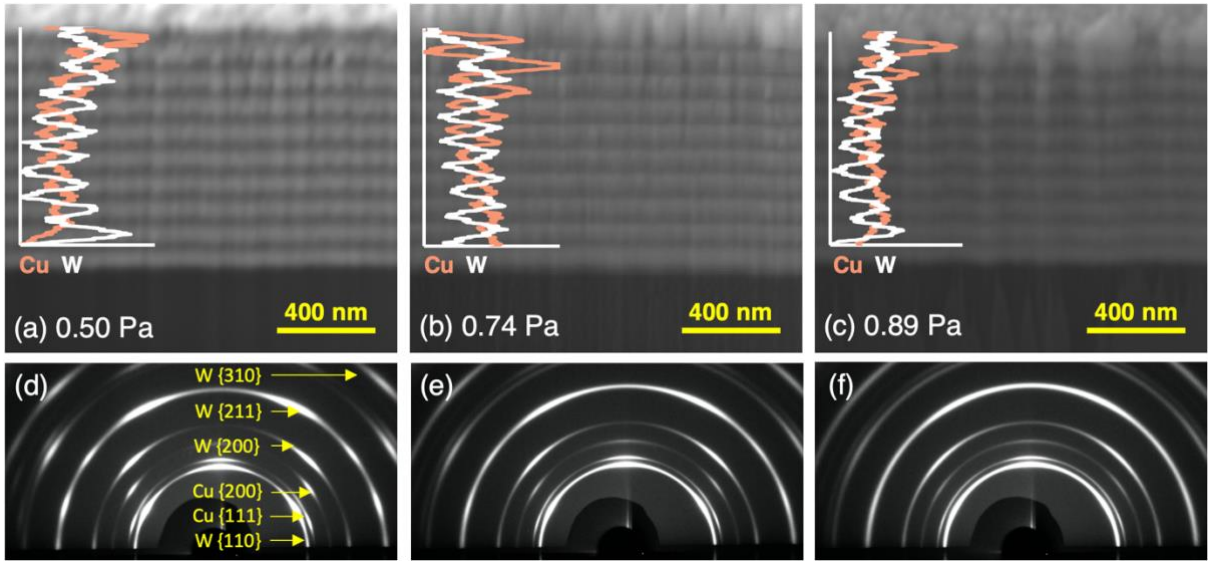


Figure 66. (a)-(c). High resolution cross-sectional SEM frames of W/Cu NML deposited at different magnetron chamber pressures, alongside nominal EDX signals for Cu and W distribution along the coating depth. (d)-(f) Debye-Scherrer rings obtained for the samples shown above using 18 keV synchrotron radiation [106], revealing a transition from highly textured coating material to reduced texture.

Non-destructive mapping of the thermal diffusivity was carried out using laser-induced transient grating spectroscopy (TGS) [122–126] by members of the Felix Hofmann Group, Department of Engineering Science, University of Oxford. For this purpose, two laser pulses are crossed at a fixed angle at the sample surface creating a spatially periodic interference pattern with a wavelength of 2.758 ± 0.002 µm. This results in a spatially periodic heating of the sample, as shown in Figure 68a. Thermal expansion subsequently leads to sample surface displacement, thus creating a transient displacement grating. A third continuous probe beam, diffracted by this transient temperature and displacement grating, is used to determine the decay period of the temperature and displacement grating, from which the thermal diffusivity can be deduced. For the selected TGS wavelength, the thermal diffusivity signal is dominated by material up to a depth of ~0.9 µm, thus ensuring averaging coating measurements without a significant contribution of the Si substrate.

4.1.3 Results and Discussion

While strong intensity variations along the azimuthal direction are visible for all Cu and W reflections in Figure 66a, this effect decreases - particularly for the W{211} reflection - in the samples deposited at 0.74 Pa and 0.89 Pa (Figure 66e,f). This trend is observable at reduced level for the Cu {111} and Cu {200} reflections, indicating the existence of mildly textured copper and randomly oriented tungsten at higher deposition pressures. These observations indicate a change in crystal growth dynamics during MSD depending on the mean free path length of the incoming Cu and W atoms, which affects their kinetic energy. Based on the findings presented in [127], the mean free path length of Cu and W atoms during sputtering at 0.5 Pa and 0.89 Pa magnetron chamber pressure can be estimated as 1.5 cm and 0.7 cm, respectively. As a consequence, the average number of interactions between sputtered metal and atmospheric Ar atoms doubles at 0.89 Pa magnetron chamber pressure as compared to

0.50 Pa. Previous Monte Carlo simulations of the sputter deposition of Si and Mo at a target-substrate distance of 18 mm and Ar pressure of 0.44 Pa revealed a particle energy at the substrate of 14.4 eV and 7.7 eV for Mo and Si, respectively. Furthermore, the variation of the sputtered atom energy with increasing target-substrate distance and working gas pressure was analysed in [128], indicating an exponential decay in particle energy with an increase in pressure or distance. Other studies have previously reported noticeable changes in texture for magnetron bias voltage variations [18], which again modify the kinetic energy of sputtered atoms. The additional kinetic energy of incoming particles at lower Ar pressure therefore leads to an increase in adatom surface mobility, ultimately resulting in the formation and growth of highly textured grains and sharper interfaces.

To combine the analysis of the relationship between deposition conditions and the residual stress distribution within the coating with thermal properties, FIB-DIC depth profiling results presented in §3.1 were used. Ring-core sizes of 3 µm, 5 µm and 10 µm (Figure 67c) were chosen to achieve the desired surface sensitivity, which was highest for the smallest ring core diameter, while the largest ring core was used to determine stresses at the substrate-coating interface. The setup geometry inside the FIB-SEM is shown in Figure 67b. Software tracking of surface features (Figure 67d) during post experiment DIC analysis reveals the relief strain versus milling depth, which enables reconstructing of the prevailing in-plane residual stress distribution within the coating. A detailed description of the method can be found in §3.1. The result of this analysis shown in Figure 67a re-iterates the clear correlation between the magnetron chamber pressure during deposition and the resulting residual stress state, ranging from -500 MPa compression at 0.5 Pa Ar pressure to 1000 MPa tension at 0.89 Pa. Furthermore, pronounced stress peaks near the substrate-coating interface can be observed,

that lie significantly above the average coating stress that would be determined using classical techniques such as $\sin^2(\Psi)$ X-ray analysis.

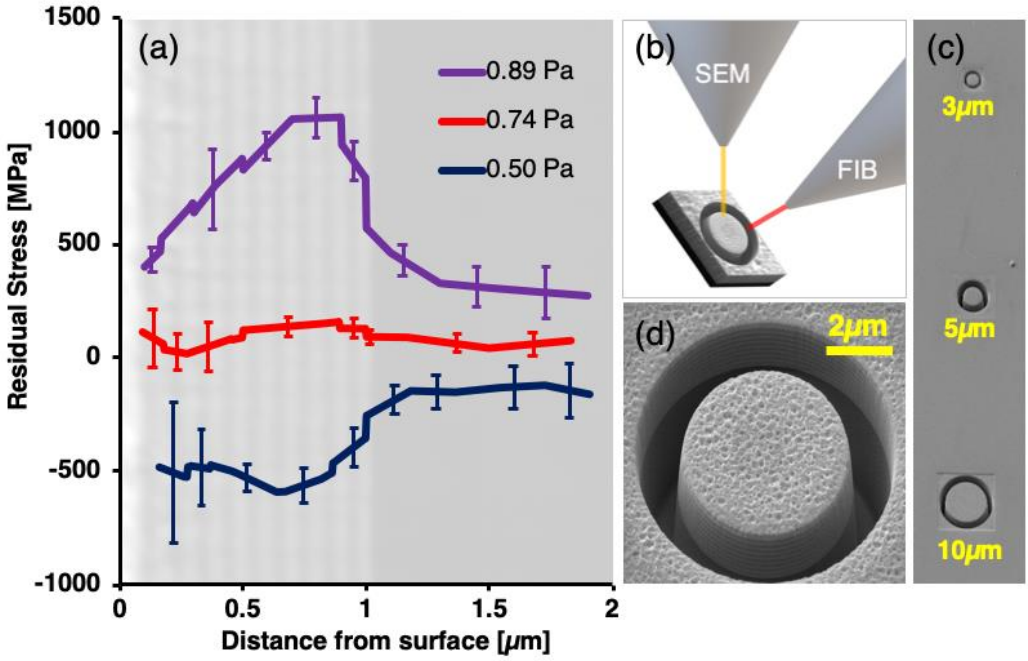


Figure 67 (a) Residual Stress versus depth for samples deposited at different magnetron chamber pressures, revealing a clear transition from compressive to tensile stress with increasing pressure. Stress maxima/ minima can be seen near the substrate/ coating interface. (b) Schematic of the FIB-DIC milling/ acquisition geometry and process. (c) SEM frame showing the different ring-core radii used for depth resolved in-plane residual stress reconstruction. (d) 5µm ring-core imaged after full strain relief

The observed stress transitions from tensile to compressive can be explained by considering the interaction between sputtered metal atoms and working gas [53]: a low Ar atmosphere pressure results in a high kinetic energy of sputtering atoms when reaching the sample surface. The kinetic energy of Cu at a pressure of 0.5 Pa, for instance, can be estimated to be within a range of $\overline{\varepsilon_{Cu}}(eV) \approx [7.7; 14.4]$, with higher energies expected for W atoms, due to its higher atomic mass. Based on the data provided in [128], it can be estimated that increasing the working pressure by a factor of 1.8 results in a decrease in particle energy by a factor of around 10. In an attempt to compare these values with literature data stating an energy range

for self-interstitial formation in Cu between 2.5 eV and 5.7 eV [129] and 8.9-9.6 eV in W [130], it becomes apparent that large scale kinetic energy driven interstitial formation is possible at 0.50 Pa, but not at 0.89 Pa. In addition, collision cascades caused by a low proportion of highly energetic particles with kinetic energies several times higher than the mean value can result in vacancy elimination and layer densification [131]. While the formation of interstitials in a lattice with low vacancy density causes intragranular compressive residual stress at lattice scale [53], further insertion of highly energetic particles into the grain boundaries adds additional in-plane compressive residual stress. As a consequence of this 'atomic peening' process, pronounced compressive residual stress across the multilayer system can be observed at low deposition pressures. With increasing chamber pressure the kinetic energy of the sputtered atoms drops significantly, resulting in reduced adatom mobility, higher vacancy density, and the formation of a reduced density columnar morphology [132,133]. The attracting forces between column boundaries without the 'atomic peening'-induced compressive residual stress results in a build-up of tensile residual stress [134] comparable to the effect observed during island coalescence in the early stages of thin film formation [135], also known as 'island zipping'.

Based on the obtained TGS data, the thermal diffusivity was averaged over a grid of 6 by 6 points with a spatial resolution of 100 µm for each sample, the results of which are shown alongside their 95% confidence interval in Figure 68b. Averaged coating stresses obtained from FIB-DIC depth profiling were added to the graph for comparison. A linear magnetron chamber pressure dependence can be observed for both the thermal diffusivity and average residual stress. While the residual stress transitions from compressive to tensile, the thermal diffusivity decreases from $3.3 \cdot 10^{-5}\ \mathrm{m}^2/\mathrm{s}$ at 0.50 Pa to $2.6 \cdot 10^{-5}\ \mathrm{m}^2/\mathrm{s}$ at 0.89 Pa.

The significant reduction in thermal diffusivity of over 20% can be explained by microstructural changes induced by the deposition conditions. Lattice point defects incorporated during MSD at higher Ar pressure through Ar atom entrapment and the mechanisms mentioned in the previous section result in increased electron scattering rates [136,137]. Increased roughness of Cu/W interfaces at higher magnetron pressures as observed from cross-sectional SEM imaging in Figure *66* might further decrease the thermal diffusivity as compared to the sharper interfaces obtained at lower deposition pressures.

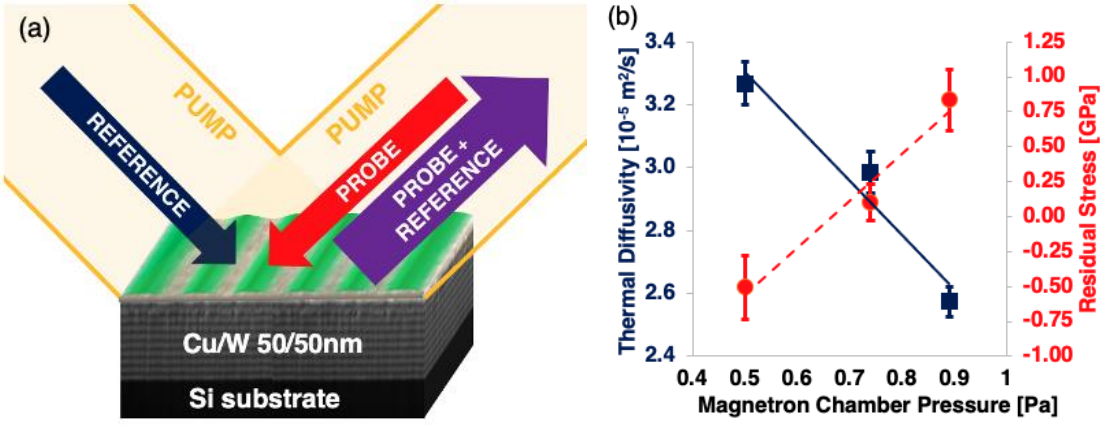


Figure 68(a) Schematic of the transient grating spectroscopy setup used to determine the thermal diffusivity within the multilayer coating. (b) Thermal diffusivity and averaged in-plane residual stress measurements versus magnetron chamber pressure during deposition.

4.1.4 Conclusion

A clear correlation between magnetron chamber pressure and the texture, residual stress and thermal diffusivity of W/Cu nano-laminates was established. The interaction between the working gas and sputtered atoms was identified as key driver underlying the observed property changes: lower kinetic energy of particles reaching the substrate surface leads to the formation of low density columnar growth in the nanoscale strata, resulting in defect accumulation. At lower pressures the ‘atomic peening’ effect enables the formation of highly densified and textured material by interstitial formation and vacancy filling through collision

cascades during deposition. In addition, increased interface roughness between Cu and W layers might contribute to a reduction in thermal diffusivity. This knowledge is particularly useful for the design of coatings that are intended to be used in both thermally and mechanically challenging environments. Low magnetron pressure should hence be employed for applications that require compressive residual stress and high thermal conductivity within the coating.

4.2 Stress-Assisted Thermal Diffusion Barrier Breakdown in Ion Beam Deposited Cu/W Nano-Multilayers on Si Substrate Observed by *in situ* GISAXS and Transmission EDX

4.2.1 Introduction and Literature Review

Thermal diffusion in nano-structured metallic multilayers is governed by a multitude of interlinked material properties that arise as a consequence of deposition technique and parameters [53]. Amongst these properties are preferred crystal orientation (texture), grain size and shape, residual stress, density, defect structure, but also the individual layer thickness determining the volume fraction of the material at or near interfaces. In this context Cu/W NMLs on Si substrate are of particular interest due to their mutual immiscibility and resulting clear phase separation. In micro- and nano-technology applications, tungsten is employed as diffusion barrier between Si and Cu [138]. Cu/W multilayer coatings are further investigated as radiation-tolerant coatings and heat sinks in plasma-facing components [103], due to the large number grain boundaries and layer interfaces, which serve as point defect sink [139]. For this safety-critical field of application a detailed understanding of the thermal diffusion and degradation mechanisms at elevated temperatures is of utmost importance.

The combination of Cu and W, however, is prone to degradation caused by environmental influences, such as elevated temperatures, oxygen and electromagnetic radiation. While other material combinations such as complex iron oxides exhibit a higher thermal stability [140,141], Cu/W multilayer systems exhibit an abrupt structural breakdown at elevated temperatures, which results in the degradation of the layered structure.

Various aspects of this breakdown have been discussed in the literature, while the key elements of understanding the dynamics of inter- and intralayer nano scale diffusion remain fragmented or lacking. A particularly detailed study of nano-structural transformations within Cu/W NML systems at elevated temperatures was presented by Cancellieri et al. [142–145], according to which degradation can be subdivided into the following key stages: after the stress-driven formation of Cu nano-crystals at the sample surface at $T > 400°C$ and a shape change of these particles at $T > 600°C$, Cu is re-inserted to the multilayer structure at $T > 700°C$, resulting in a Cu/W nano-composite structure. The driving force underlying the NML transformation was identified with the reduction of Gibbs free energy by the minimisation of internal interfaces. A model for determining the grain boundary diffusion coefficient for Cu along W grains depending on the residual stress state in W layers presented in [145] showed that compressive residual stress increases the barrier to diffusion. Further to the above described findings involving mostly vertical grain boundary diffusion, *in situ* micropillar compression of Cu/TiN multilayers at ambient and elevated temperatures reported in [146] revealed in-plane Cu transport, before coalescence into micro-crystals at micropillar sides. The size of these crystals was reported to be independent of the layer thickness. The observed stress-assisted diffusional flow was explained using a Coble creep model, which links the material strain rate with stress and temperature [147].

This previous work, however, was mostly limited to sample surface observations during heating, while diffusion phenomena within the sample preceding degradation could

not be observed in this way. To overcome this issue, we present an extensive multi-technique analysis of the diffusion and degradation in IBD Cu/W NMLs on Si substrate, combining large scale averaging techniques such as synchrotron *in situ* XRR, *in situ* GISAXS and WAXS with locally probing techniques such as TEM imaging, EDX analysis and Atomic Force Microscopy (AFM). This combination of methods permits the observation of diffusion mechanisms within and between buried layers of nanostructured coatings before any changes become apparent at the sample surface.

In the present section, we use the obtained experimental insights into the as-deposited and temperature-dependent properties of the sample to reveal how the high kinetic energy of sputtered particles during ion beam deposition results in a complex in-plane residual stress state, pronounced defect structure and columnar grain morphology. At moderately elevated temperature, the combination of highly compressive residual stress and low thermal activation energy for defect diffusion result in density decrease. Low-temperature Coble creep and diffusional Cu transport are described well by the analytical expressions that capture the dependence on Cu and W stresses. It was found that the stress-assisted Cu diffusion along W grain boundaries towards the Si substrate results in the formation of copper silicate accompanied by rapid volumetric expansion, ultimately resulting in the observed large-scale morphological multilayer transformation.

4.2.2 Materials and Methods

4.2.2.1 Ion beam deposition

The microstructure of thin films and coatings is determined by the chosen deposition technique and the associated deposition parameters [148–150], as well as post-deposition

thermal annealing [151]. While a wide range of deposition techniques are available, IBD was used in this study for the manufacture of multilayer coatings with precise layer thickness control. Ten bilayers of Cu/W were deposited onto 600 µm single crystalline Si wafers obtained from an industrial source with [001] orientation, starting with W. The deposition was carried out at room temperature by ion beam sputtering with a focused Ar + ion gun at 1.2 keV multicusp radio-frequency source in a NORDIKO-3000 system [46]. During film growth the ion gun was supplied with constant radio-frequency power of 165 W and constant Ar flux of 10 sccm. The 150 mm diameter targets were sputtered during 10 min allowing both ion-gun stabilization and target pollution cleaning caused by vacuum break. The ion gun axis was inclined at 45° to the normal of the surface target whilst the sample surface was parallel to the target plane. The sputtering chamber was pumped down to a base pressure of $2 \cdot 10^{-6}$ Pa whilst the working pressure during film growth was ~ 10^{-2} Pa. Substrates were preliminarily cleaned with acetone and ethanol and finally dried with an argon gas jet prior to their introduction in the deposition chamber.

4.2.2.2 *In situ* X-Ray Reflectivity Measurements

To quantify the thickness, roughness and density evolution of the Cu/W NML at different temperatures, XRR measurements were carried out at the BM28 (XMaS) beamline at the European Synchrotron Radiation Facility (ESRF, Grenoble, France). A photon energy of 12.4 keV and beam size of 0.5x0.2 mm^2 were chosen. The sample was attached to an 8 mm diameter heater with PEEK lid using ceramic adhesive, which was then mounted onto a diffractometer. The heater remained under high vacuum throughout the experiment to avoid sample oxidation. Data collection in a 2θ-range between 0° and 6° was carried out at room temperature using an Avalanche PhotoDiode (APD) mounted onto a KF16 flange, followed

by one scan at 250 °C. GenX software [40] was used to fit a sample model matching the experimental XRR data and extract the sample parameters at both temperatures.

4.2.2.3 Wide angle X-ray Scattering

WAXS patterns in reflection geometry at an incidence angle of 1° with respect to the sample surface were acquired at Diamond Light Source synchrotron Beamline B16 (Didcot, UK) at a beam energy of 18 keV and a beam size of 250x250 μm^2 using an Image Star 9000 detector. A sample-detector distance of 66 mm was determined from LaB_6 standard calibration using DAWN software package [32].

4.2.2.4 *In situ* Grazing-Incidence Small-Angle X-Ray Scattering Measurements

GISAXS is a surface and interface scattering technique that is ideally suited to detect nano scale periodic features buried within or present on the surface of samples [152]. Due to the very shallow angle of incidence between beam and sample surface this technique provides large scale averaged geometric distribution statistics. Temperature-dependent GISAXS patterns during a single heat ramp from 30 °C to 400 °C were acquired in steps of 10 °C at the BM28 beamline at ESRF. An incidence angle slightly above the conventional GISAXS range (0.05° and 0.5°) of 0.66° was chosen, as it revealed additional lateral and vertical roughness correlation information compared to shallower angles at which the GISAXS pattern was averaged to one large feature without distinct layer separation . The sample environment was identical to the one used for the XRR analysis. An X-ray photon energy of 8 keV with a beam size of 100x80 μm^2 was chosen to achieve the best possible resolution of the GISAXS patterns on the detector. A PILATUS3 300K area detector with a pixel size of 172x172 μm^2 and a resolution of 487x619 pixels split into three detector modules was used.

A sample-detector distance of 1.56 m was determined using a AgBh standard calibration sample, followed by analysis in the DAWN software package [32], which was used to simulate and match the experimentally obtained GISAXS patterns [34,35].

4.2.2.5 Transmission Electron Microscopy

TEM lamellas of a pristine sample and the sample used for the *in situ* GISAXS experiment were extracted and thinned using a Tescan Lyra3 FIB-SEM. The lamellas were sectioned using Ga FIB at a voltage of 30 kV and beam current of 11 nA, followed by fine polishing and thinning at 0.2 nA beam current. TEM images were acquired at an electron beam energy of 200 keV using a JEOL JEM-2100 TEM at the Research Complex at Harwell (RCaH, Harwell, UK). In addition, STEM on the sample obtained from the GISAXS experiment was combined with t-EDX inside the Tescan Lyra3 FIB-SEM at an electron beam energy of 20 keV and a working distance of 5 mm, which enabled the local identification of materials based on their characteristic X-ray emission energy at a resolution of 40x40 nm^2.

4.2.2.6 Atomic Force Microscopy

AFM measurements of the Cu/W NML surface in as-deposited state and after *in situ* GISAXS heating were acquired at the Laboratory for In Situ Microscopy (LIMA, Department of Engineering Science, University of Oxford) using a Veeco Dimension 3100 in tapping mode. A surface area of 0.6x0.6 μm^2 was scanned for the sample in reference state, while a map of the surface area of 5x5 μm^2 was acquired for the heated sample, in order to capture the newly formed large surface features. ProfilmOnline [153] was used for AFM data processing and rendering.

4.2.2.7 *In situ* SEM heating

Finally, to enable sample surface observations during heating, *in situ* SEM analysis of a Cu/W NML was carried out using a Zeiss Evo LS15 SEM in combination with the heating module of a 5kN tensile stage (Kammrath & Weiss, Germany). The multilayer sample was placed on the surface of the heating module, which was then heated in a stepwise fashion from RT up to 400°C, while SEM frames were acquired. The working distance and beam energy were 20 mm and 10 keV, respectively.

4.2.3 Results and Discussion

4.2.3.1 Reference state characterisation

Prior to studying the thermal stability of the Cu/W NMLs, TEM and XRD based characterisation of as-deposited samples was performed to determine the layer thickness, density and texture. The TEM image in Figure 69a shows 10 bilayers of Cu and W on Si substrate with increasing layer waviness towards the sample surface. This phenomenon has been observed and described in the past and can largely be attributed to columnar growth during energetic film deposition. A formula for calculating the wavelength of the oscillation $D = 3H+7$ nm presented in [154] based on the thickness of the thicker layer H and returned an estimated wavelength of 46 nm for H_{Cu} = 13 nm, as estimated from TEM images. This estimate showed excellent agreement with TEM observations and indicates the presence of cylindrical columnar morphology with a diameter of around 46 nm.

Further to the direct cross-sectional TEM observations, WAXS data shown in Figure 69b was used for phase identification and texture analysis. Face-centred-cubic (FCC) Cu with {111} and {200} crystallographic orientations was confirmed from Debye-Scherrer rings, while the body-centred-cubic (BCC) $\alpha-$W phase with {110} and {200} crystallographic

orientations was present. Pronounced fibre texture was present in all phases, as can be seen from the strong azimuthal intensity variations of the Debye-Scherrer rings shown in Figure 69b. It was previously shown that the presence of strong texture in magnetron sputtered Cu/W NMLs at low Ar pressure co-exists with in-plane compressive residual stresses and increased thermal diffusivity [155]. Since the Ar pressure during IBD was around one order of magnitude below the magnetron sputtering chamber pressure, a reduced level of interaction between highly energetic sputtered metal atoms and Ar atoms inside the deposition chamber can be assumed. A previous comparative study confirmed this assumption [21], by showing that while magnetron sputter deposition emits particles in an energy range between 1-100 eV when reaching the sample surface, ion beam deposited particles can reach up to 1000 eV, thus enabling the implantation of self-interstitials in Cu [156] when considering the kinetic particle energy of around 20 eV [157] required for their formation. As a result, self-interstitial formation and 'atomic peening' [158], as well as atom insertion into grain boundaries [159] result in highly densified Cu and W layers under compressive residual stress. Indeed, the residual stress state of identical Cu/W NML systems deposited using the identical deposition system was evaluated in the past [160] and found to be -6.6 GPa for W and -0.4 GPa for Cu, as determined by $\sin^2(\Psi)$ analysis. The average film stress was determined by substrate curvature analysis and was found to be -1.0 GPa [160]. While a W stress of -6.6 GPa seems high at first, a recent study has shown that nanocrystalline tungsten with a crystal size of 10 nm is able to sustain considerably larger compressive stresses [161]. The depth-profile of the in-plane stress distribution within the Cu/W NML on Si substrate can be assumed to be near 0 GPa at the sample surface, while a pronounced stress peak near the NML-substrate interface is present [106].

The X-ray reflectometry profile of the Cu/W NML in reference state at room temperature is shown in Figure 69c alongside the fitted profile using GenX software. The

obtained average layer parameters listed in Table 3 show the thickness and roughness of Cu and W layers. Furthermore, a high relative layer density found in both nanocrystalline Cu and W reached 94% of their bulk material density [162], which further provides supporting experimental evidence for the presence of self-interstitials arising from the above described layer densification mechanisms, as well as vacancy defects, which lower the overall density below single crystal level.

Sample temperature	30 °C	250°C
W thickness [nm]	5.86 ± 0.01	5.25 ± 0.07
W roughness [nm]	1.07 ± 0.001	1.65 ± 0.01
Cu thickness [nm]	12.97 ± 0.02	13.59 ± 0.04
Cu roughness [nm]	1.35 ± 0.002	3.44 ± 0.04
W density [g/cm^3]	18.13 ± 0.01 (94% bulk)	16.94 ± 0.14 (88% bulk)
Cu density [g/cm^3]	8.43 ± 0.04 (94% bulk)	7.92 ± 0.06 (88% bulk)
Si roughness [nm]	0.28 ± 0.02	1.27 ± 0.21

Table 3. Cu/W NML average layer thickness, roughness and density at 30°C versus 250°C as obtained from XRR profile fitting.

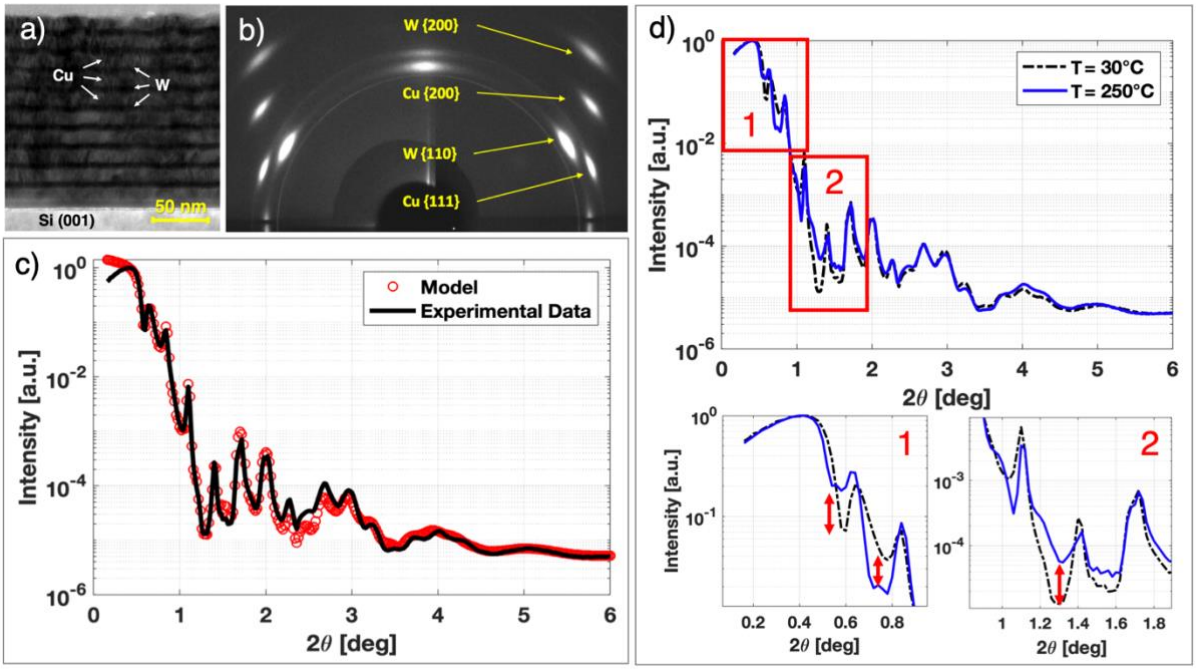


Figure 69. (a) Cross-sectional TEM image of the Cu/W nano-multilayer showing the Si substrate and individual Cu (bright) and W (dark) layers. (b) Debye-Scherrer rings of NML with identified reflections indicating highly textured material. (c) Experimental XRR profile (black line) and simulated model (red circles). (d) XRR profile before (black dashed line) and after heating (blue continuous line).

4.2.3.2 Structural evolution upon thermal treatment

XRR intensity profiles were further acquired at 250 °C, as shown in comparison with the reference scans in Figure 69d. While the overall intensity versus 2θ distribution is similar to the reference state, distinct differences are identifiable in the regions labelled '1' and '2'. Amplitude changes revealing differences in layer density and layer roughness [163] are highlighted by red arrows in the magnified regions shown underneath the graph. The layer thickness, density and roughness at 250 °C for both Cu and W are compared with the reference state in Table 3. A significant decrease in layer density by 6% upon heating was observed for both materials, while an increase in layer roughness by a factor of 1.5 and 2.5 was observed for W and Cu, respectively. The layer thickness data in Table 3 reveals that the overall thickness of Cu and W bi-layer remained constant at 18.8 nm between XRR scans. At

the same time, the Cu layer thickness increased by 0.6 nm, while the W layer thickness decreased by the same amount. This clearly points at the consequence of interface diffusion activity between Cu and W layers. Within the two-component GENX model, the newly formed boundary layer was assigned to the Cu layer, indicating that the boundary layer density was closer to that of Cu than that of W, corresponding to the diffusion of W atoms into the Cu layer. This process proceeds alongside the observed reduction in W layer density shown in Table 3. Furthermore, whilst the overall stack thickness was preserved, superficial Cu 'islands' appeared as a consequence of Cu atomic transport towards the multilayer surface between 230 °C and 250 °C as shown in Figure 71. Considering the increase in the Cu layer thickness this necessarily leads to the reduction of Cu layer density. This is discussed in further detail in the following section.

One possible driver underlying the diffusion of Cu towards the sample surface which further results in a density decrease is the thermal activation of Cu self-interstitial motion, which was shown to require less thermal energy as compared to vacancy motion [156,164]. Vacancy-interstitial annihilation can further contribute to the volumetric expansion and decrease in density [165]. These mechanisms, however, can only be speculated on and require further high resolution TEM analysis. Thermal expansion of the layers, however, was found to have a minimal contribution to the observed changes in layer thickness, with a Cu expansion of 0.39 % for a temperature increase of 230 °C, assuming a thermal expansion coefficient of $\alpha_{Cu} = 17.7 \cdot 10^{-6}$ 1/K [166]. Considering the lower thermal expansion coefficient of nanocrystalline W with $\alpha_W = 4.5 \cdot 10^{-6}$ 1/K [167], the in-plane thermal expansion of Cu is hindered by the W layers, resulting in an increase in in-plane compressive residual stress within Cu layers by around 300 MPa and a decrease in W in-plane residual stress. While the initial grain size of nano-crystalline Cu and W deposited by IBD was found to correspond to the individual layer thickness in previous studies [160], grain coarsening in nano-multilayers

at elevated temperature was identified and described in the literature for comparable systems [168], thus suggesting that significant grain growth occurred during the thermal annealing of the Cu/W system in this study.

In summary, thermal activation of diffusion processes at 250 °C resulting in measurable microstructural changes in both Cu and W were confirmed experimentally – an activation temperature significantly below other values reported in the literature based on surface observations during heating. Highly compressive in-plane residual stresses and a complex defect structure, both of which were introduced by ion beam deposition, are suggested as underlying reasons alongside thermal diffusion at the layer boundaries.

To gain further insights into the temperature-dependent evolution of the microstructure at higher temperatures, GISAXS patterns were collected between 30 °C and 400 °C. In its as-deposited state the NML exhibits a periodic vertical GISAXS pattern with a period corresponding to the Cu/W bilayer thickness (Figure 70a). Additional intensity contributions related to reflection and refraction phenomena at interfaces within the multilayer, however, make a detailed analysis of individual peaks challenging. The intensity loss of pattern features along the Q_Z direction is representative of the interface roughness [169], with a steeper decay towards higher Q_Z representing a higher degree of interface roughness. The specular peak is shown as red dot in the centre of the frame at $Q_Y = 0$ nm^{-1} and $Q_Z = 0.825$ nm^{-1}. Distinct lateral peaks are visible at $Q_Y = \pm 0.13$ nm^{-1}, corresponding to a lateral in-plane geometric ordering of 48 nm. This is in strong agreement with the estimated columnar grain diameter of 46 nm based on TEM images. Further in-plane ordering at low Q_Y between ± 0.0265 nm^{-1} is visible in the pattern centre, indicating ordering at larger length scales of $\geq$237 nm. Based on this information and combined with the data obtained from XRR fitting, a hierarchical microstructural multilayer model was implemented in the BornAgain software package, as illustrated in Figure 70c showing the experiment geometry

and Figure 70d showing the model side view. For this purpose, columnar multilayer morphology was simulated by means of cylindrical layered mesocrystals consisting of alternating 40 nm diameter Cu and W particles with heights of 12.5 nm and 5.9 nm, respectively, as shown in Figure 70d. The Cu/W particles with an intercolumnar spacing of 48 nm (characteristic length 'a' in Figure 70c) were embedded in a Cu/W multilayer structure which is indicated by the transparent layers in Figure 70d. To account for the lateral ordering at low Q_Y, the mesocrystals were arranged within the model in a hexagonal grid with a spacing of 237 nm (length 'b' in Figure 70c). While further model accuracy could be achieved by adding additional mesocrystal clusters with a variation of spacings instead of embedding a single cluster in continuous Cu and W layers, the present simulation delivered excellent agreement with the experimentally obtained GISAXS pattern, as shown in Figure 70b. A smooth and uniform sample surface in the sample reference state was confirmed by *in situ* imaging of the sample surface during heating, as shown in Figure 71f. It was therefore experimentally confirmed that ion beam deposition of Cu/W NMLs results in the formation of Columnar grain structures during deposition.

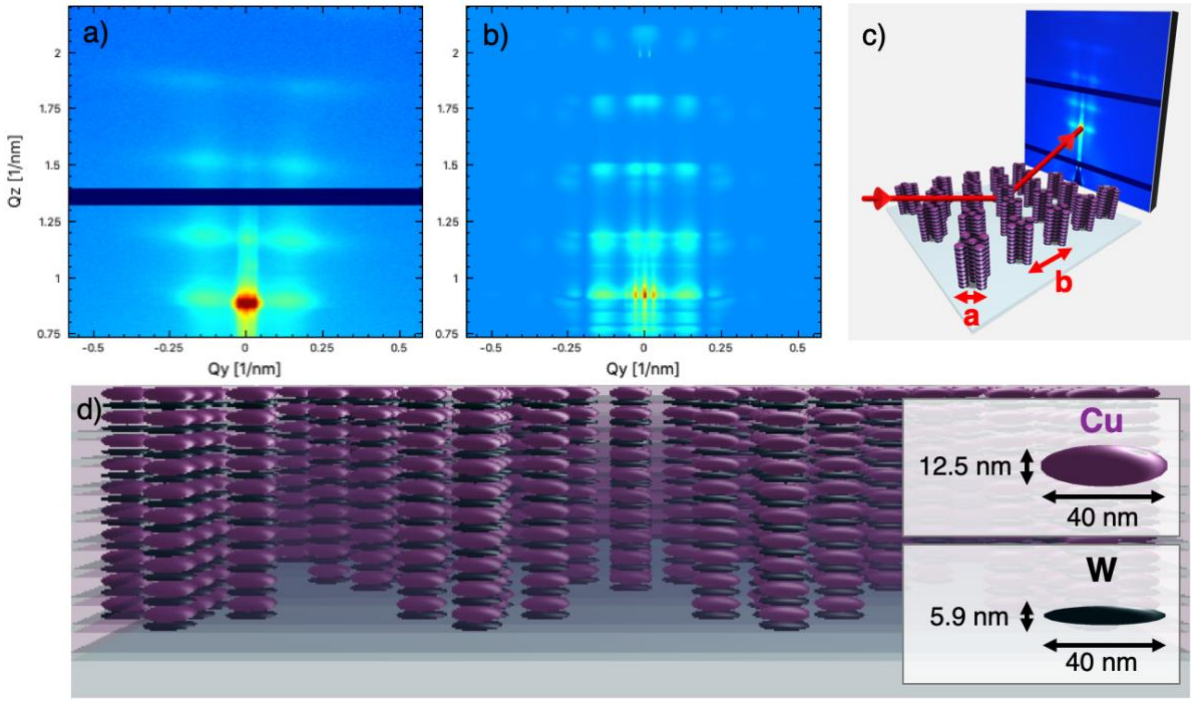


Figure 70. (a) GISAXS pattern of Cu/W NML at 30°C. (b) Simulated Cu/W GISAXS pattern based on BornAgain material model. (c) Overview of BornAgain model and scattering geometry. Cu/W columnar grains are shown on Si substrate, alongside incoming and reflected beam. While the Cu and W particles are embedded in Cu and W layers in the simulation, they have been removed from the illustration for the purpose of visibility. (d) Sideview of rendering showing the simulated multilayer microstructure with columnar Cu/W growth. Dimensions are indicated on the right.

Upon heating, first changes in the scattering intensity distribution were observed at a temperature of 230 °C, as shown in Figure 71b. Peak blurring along the Q_Z direction was observed, resulting in a decreased vertical spacing between individual peaks thus indicating an increase in Cu layer thickness and decrease in density, as previously confirmed by XRR at 250 °C. While these changes were observed within buried layers and interfaces, no changes on the sample surface were identified from *in situ*, in-SEM sample heating at the same temperature (Figure 71f-j). In contrast, the formation of randomly spaced surface crystals was observed at T = 280 °C, as shown in Figure 71h. The crystal composition was confirmed as pure Cu from EDX spectroscopy. At the same temperature, the GISAXS pattern showed an increase in intensity at higher order Q_Z peaks indicating an increase in vertical layer correlation, which may be related to changes in layer roughness. Particularly the third order peak at Q_Z = 1.35 nm^{-1} notably increased in intensity in addition to feature sharpening. Combined with the observed Cu surface crystal formation, it can be assumed that the Cu atoms released from highly densified nanocrystals during heating that led to a layer thickness increase at 230 °C started migrating in vertical direction towards the sample surface at 280 °C. While the origin of the surface crystal Cu couldn't be attributed to specific layers, nanoscale transport mechanisms described in the literature indicate that they are to a large extent composed of material from buried Cu layers due to the prevailing residual stress state in the sample. Furthermore, a shift of intensity from the lower lateral peaks towards lower Q_Y at the pattern centre can be observed, which can be interpreted as a large-scale transformation

from a regularly spaced columnar structure towards larger and more randomly spaced and sized objects, for instance by columnar grain coalescence.

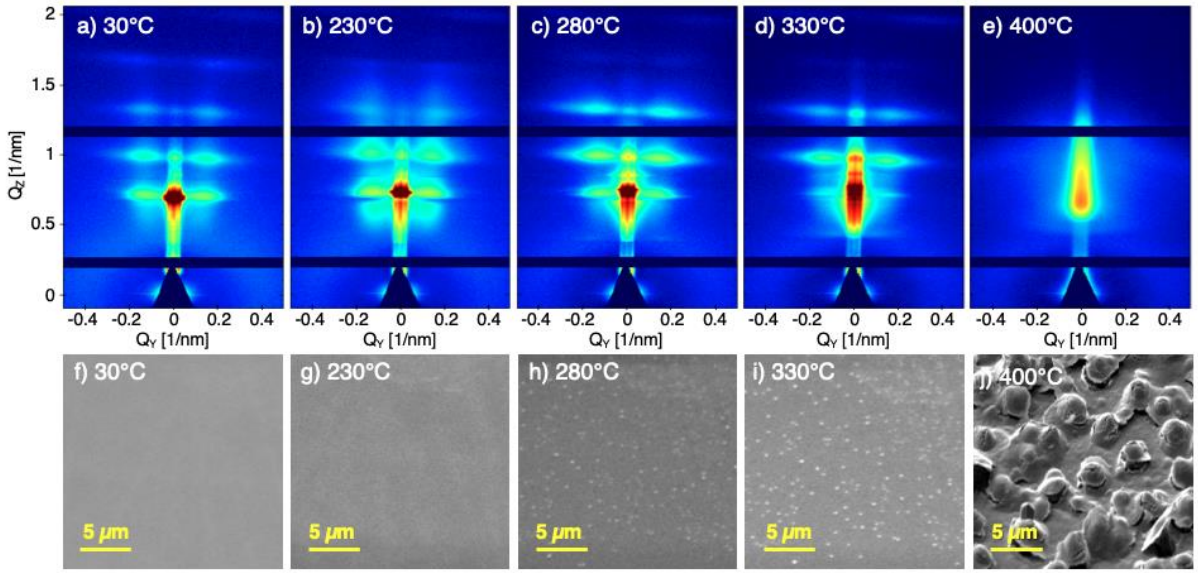


Figure 71. a-e: temperature-dependent GISAXS patterns. f-j: in situ in-SEM surface observations during temperature increase.

4.2.3.3 Diffusion modelling

A feasible diffusion mechanism of Cu along W grain boundaries towards the free sample surface has been described recently [145], however, the observed onset temperature of 280 °C for surface crystal formation in this study lies significantly below the 400 °C reported. While the materials and layer thicknesses involved are identical to the literature data, differences in residual stress state and defect structure are the possible drivers underlying the lower thermal stability. While the samples presented in [144,145] were deposited using magnetron sputter deposition with a resulting residual stress state of -3 GPa and -0.5 GPa compressive residual stress for W and Cu, respectively, IBD employed for the samples presented in this section induces a more pronounced defect structure during deposition, as well as a higher level of compressive residual stress. Based on previous study it is known that

the in-plane stress gradient along the vertical direction ranges from a stress-free surface layer to a compressive stress peak near the NML-substrate interface [106]. As a consequence, diffusional transport from highly compressive buried Cu layers towards the stress-free surface appears to be the underlying transport mechanism. The diffusion coefficient of Cu atoms along W grain boundaries with account taken of the residual stress in the W layers is expressed in [145] as follows:

$$D_b(\sigma) = D_0 \cdot e^{\frac{\sigma_{ii,W}\Omega}{3RT} - \frac{E_A^*}{kT}} \tag{41}$$

with a pre-exponential factor of the self-diffusivity of nanocrystalline Cu D_0, an in-plane tungsten interlayer first stress invariant of $\sigma_{ii,W} = \sigma_{11,W} + \sigma_{22,W}$ $(\sigma_{33} = 0)$, a diffusion activation volume Ω, the Avogadro gas constant R, temperature T, a diffusion activation energy E_A^*, and the Boltzmann constant k.

Furthermore, micropillar compression of Cu/TiN NMLs at elevated temperatures [146] revealed anomalous plastic flow of Cu alongside a significant reduction in Cu 0.5% yield stress at a temperature of 200 °C to around 0.81 GPa. This value lies close to the above estimated Cu residual stress at 250°C, indicating that the Cu layer has been compressed beyond yield stress at this point. The observed outflow of Cu from the micropillar boundary was explained using a Coble creep model depending on the stress state in Cu layers:

$$\frac{d\varepsilon}{dt} = \dot{\varepsilon} = A_c \frac{\delta'}{d^3} \frac{\sigma_{Cu} V_{Cu}}{kT} D_{GB} \tag{42}$$

with the strain rate $\dot{\varepsilon}$, a geometric pre-factor A_c, the grain boundary width δ', the layer thickness d, the Cu atomic volume V_{Cu}, the residual stress in Cu layers $\sigma_{Cu} = \sigma_{11} = \sigma_{22}$, and the diffusion coefficient in the grain boundary D_{GB}.

The stress-driven Cu diffusion observed in the present study appears to be similar to the micropillar compression induced plastic flow [146], however, with in-plane compression generated by a combination of residual stress and thermal expansion coefficient mismatch, resulting in vertical diffusion as opposed to vertical nano-indenter driven compression resulting in in-plane plastic flow. Equations (41) and (42) can therefore be combined to obtain a model for the stress-assisted migration of Cu towards the sample surface. While the model in [145] focuses on the effect of residual stress in the W interlayer on the diffusion of Cu across this interlayer, the model presented in [146] only considers the role of the applied stress on the Cu layer for diffusion analysis. Combining these two models therefore yields a model accounting for the implications of residual stresses in both Cu and W layers and the effect on the material transport towards the sample surface. As a result, an expression describing the residual stress-driven diffusion of in-plane compressed copper in vertical direction across W barrier layers was obtained:

$$\frac{d\varepsilon}{dt} = \dot{\varepsilon} = A_c \frac{\delta'}{d^3} \frac{\sigma_{Cu} V_{Cu}}{kT} D_0 \cdot \mathrm{e}^{\frac{\sigma_{ii,W}\Omega}{3RT} - \frac{E_A^*}{kT}} \tag{43}$$

For further calculation, the parameters shown in Table 4 were employed.

Parameter	Value
D_0 [170]	$3 \cdot 10^{-9}$ m²/s
$\sigma_{11,W} = \sigma_{22,W}$	$-6.6 \cdot 10^{9}$ Pa
Ω [145]	$7.69 \cdot 10^{-6}$ m³/mol

E_A^* [170]	$1.025 \cdot 10^{-19}$ J
A_C [146]	148
δ' [146]	$0.5 \cdot 10^{-10}$ m
d	$13 \cdot 10^{-9}$ m
σ_{Cu}	$-0.4 \cdot 10^{9}$ Pa
V_{Cu} [146]	$8.78 \cdot 10^{-30}$ m^3

Table 4. Parameters used to calculate temperature-dependent Coble-creep strain rate.

The resulting temperature dependent Coble creep strain rate within a Cu layer was calculated and is shown in Figure 72. It becomes apparent that the residual stress state in the Cu layer has a strong effect on the strain rate and thus the nanoscale transport. For a residual stress of -0.4 GPa in the Cu layer and -6.6 GPa in the W layer, the Coble creep strain rate at 280 °C was calculated as $-4.35 \cdot 10^{-3}$ 1/s, which provides a convincing explanation for the observed surface crystal formation temperature.

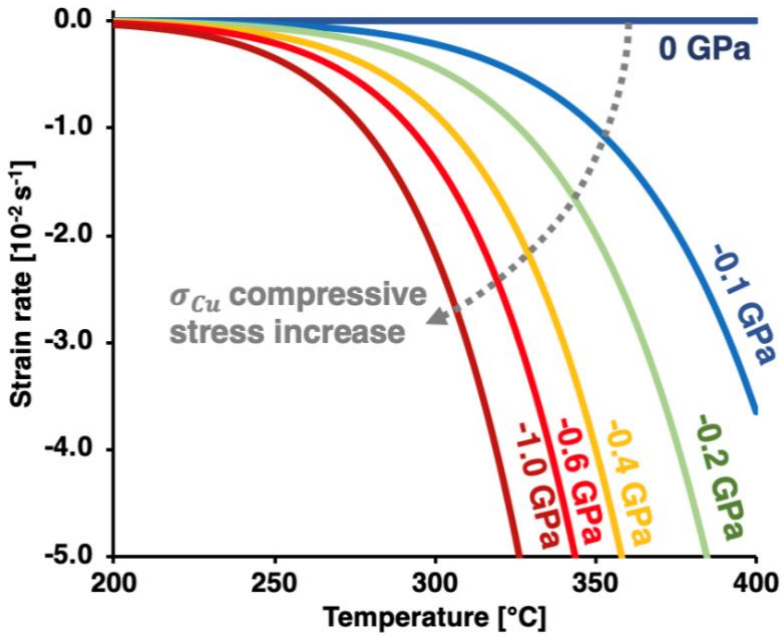


Figure 72. Evolution of Cu layer strain rate vs. temperature and layer stress.

Subsequently raising the sample temperature to 330 °C resulted in a further significant intensity shift from $Q_Y = \pm 0.13$ nm^{-1} towards the pattern centre, indicating the gradual disappearance of lateral ordering and formation of random large-scale structures buried within the multilayer structure, while surface crystals grow further, as shown in Figure 71d,i. The further reduction in lateral peak intensity at $Q_Z = 0.68$ nm^{-1} may partly be caused by the obstruction of the exiting X-ray photons by the surface Cu crystals. A significant increase in low-Q_Y intensity (red peak) further confirms the transformation from evenly spaced columnar grains towards large-scale and more random ordering. Finally, increasing the temperature beyond 330 °C resulted in a gradual collapse of the sample nanostructure both in lateral and vertical direction, as shown in the final GISAXS pattern in Figure 71e that shows single specular peak in the pattern centre at 400 °C. Looking at the SEM frame in Figure 71j acquired after heating the sample to 400 °C clearly shows the significant microstructural transformation that has occurred during heating, with spheroidal features being buried underneath a thin surface layer.

To further investigate the composition of these micro-particles and understand the mechanisms leading to their formation, cross-sectional TEM and t-EDX analysis of the sample heated during the GISAXS experiment was carried out. For this purpose, a thin, electron transparent TEM lamella was created using Ga+ FIB, as described in the materials and methods section above. T-EDX on TEM lamellae was used to limit the interaction volume between sample and electron beam, resulting in a significantly improved local resolution. The lamella cross-section of the sample after heating is shown in Figure 73. The material map in Figure 73a clearly shows the significant diffusion driven transformation. The nanostructured Cu layers have coalesced into flat spheroidal microparticles buried underneath a thick tungsten layer. The identified surface Pt layer was deposited prior to lamella cutting for surface protection. The material distribution within the Cu micro-particles was identified

based on quantitative stoichiometric analysis, as shown in the graph underneath the material map. The particle was composed of 75 atomic % Cu and 25 atomic % Si, indicated the presence of the orthorhombic or tetragonal [171] η''- Cu_3Si phase, while the presence of the η and η' phases are unlikely due to the higher formation temperature required [172]. TEM images shown in Figure 73b-d show the different stages of Cu_3Si microparticle formation: Cu penetration across the W diffusion barrier into the Si substrate results in the precipitation of Cu_3Si, leading to a significant volumetric expansion [173] as can be seen in Figure 73b. A reason for the delayed diffusion of Cu into Si as compared to previously described diffusion towards the free sample surface can be found by looking at the thermal expansion coefficient mismatch between W and Si. Since the W diffusion barrier layer showed excellent adhesion with the Si substrate, W expansion was hindered by interfacial adhesion. While near-surface W layers experienced a decrease in residual stress caused by Cu expansion, the first W layer on Si experienced an increase in compressive residual stress. According to equation (1) this reduces the thermal diffusion significantly, resulting in a delayed nanoscale mass transport at higher temperature range, once the Cu compressive residual stress reaches the threshold value required for diffusion along the highly compressive W grain boundaries. Once Cu diffuses into the substrate, the expanding Cu-Si alloy breaks across the multilayer structure, permitting the absorption of further interlayer Cu, while additional Si from the substrate contributes to particle growth by sustaining the formation of Cu_3Si (Figure 73c). In the final stage, the multilayer structure has been entirely deprived of Cu, leaving a layered pure W structure on top of the Cu_3Si particles (Figure 73d). A possibility of increasing the thermal stability of diffusion barriers was identified in recent studies [174,175] by adding a second phase and thus improving the electronic properties of the resulting composite material, which may be used to improve the stability of the W diffusion barrier between Cu and Si. Further to the above-described mechanism of copper-silicate formation, the presence and role of oxygen in

the multilayer system was analysed, as the presence of oxygen anions can lead to a significant change in electronic parameters [176,177]. A substrate surface oxide layer with a SiO_2 thickness of around 0.5 nm originating from room temperature surface oxidation before multilayer deposition was identified based on the TEM image in Figure 69a. While t-EDX confirmed that no oxygen was present in the Cu_3Si alloy, the formation of SiO_2 areas underneath the copper-silicate protrusions was observed, as can be seen in Figure 73a.

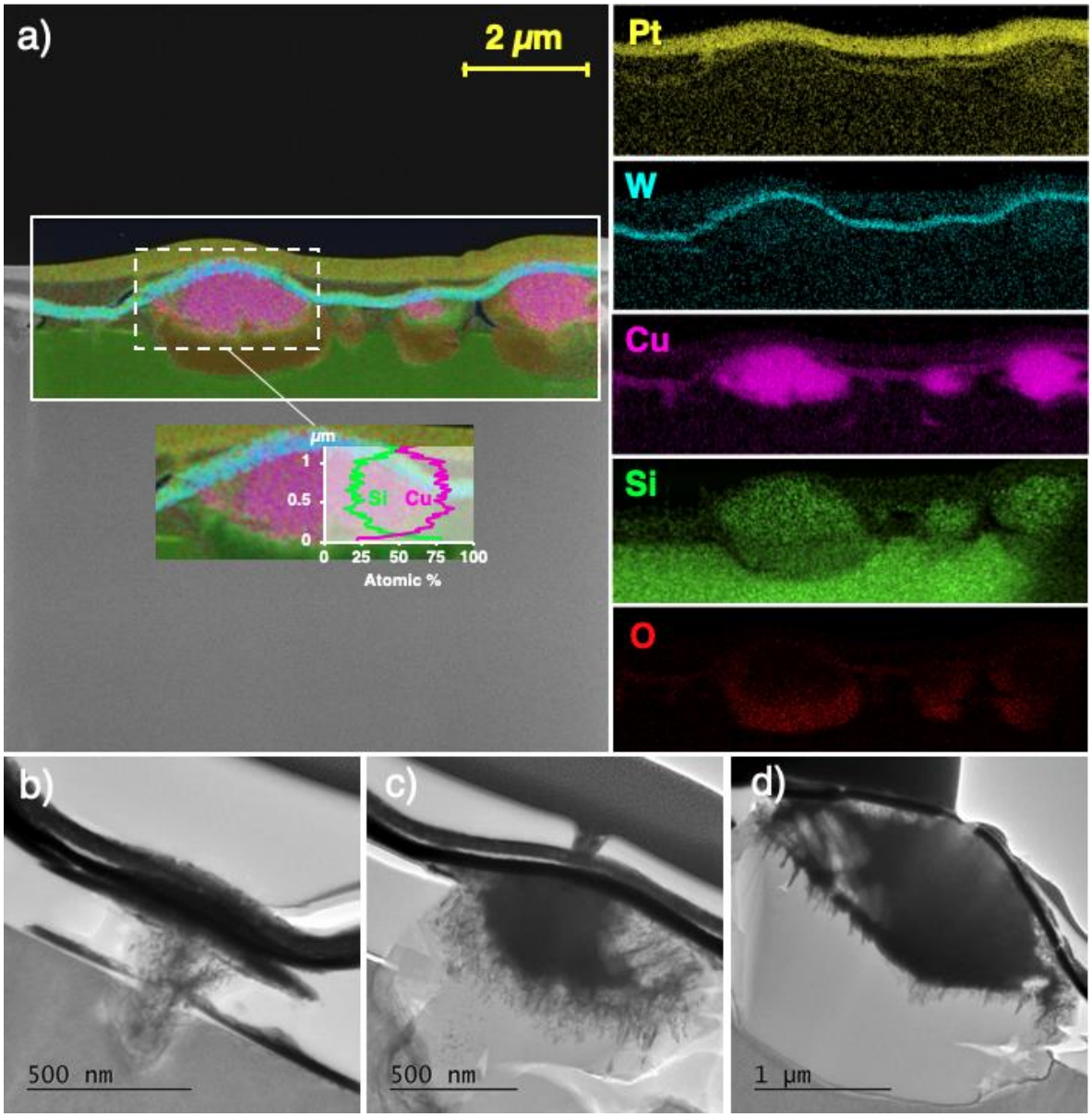


Figure 73. Cross-sectional TEM Lamella of Cu/W nano-multilayer on Si substrate after heating to 400 °C, showing a full degradation of the layered structure. (a) Left: Transmission EDX map showing the material distribution after heating. Local atomic percentage is shown

in the detail frame underneath. Right: Detailed maps for each element showing the exact local material distribution. (b-d) TEM images of spheroidal particles in different stages of growth from early stage (b) to final particle (d).

Finally, the described large-scale transformation was confirmed by comparative AFM surface scans carried out before and after heating. The scan in reference state shown in Figure 74a shows regular surface peaks with an average spacing of around 50 nm, thus corresponding to the previously determined columnar grain spacing. A large contrast in both shape and size of the objects can be seen in the post heating scan shown in Figure 74b, which confirms the presence of microparticles with a height of around 1 µm and a diameter of around 3 µm.

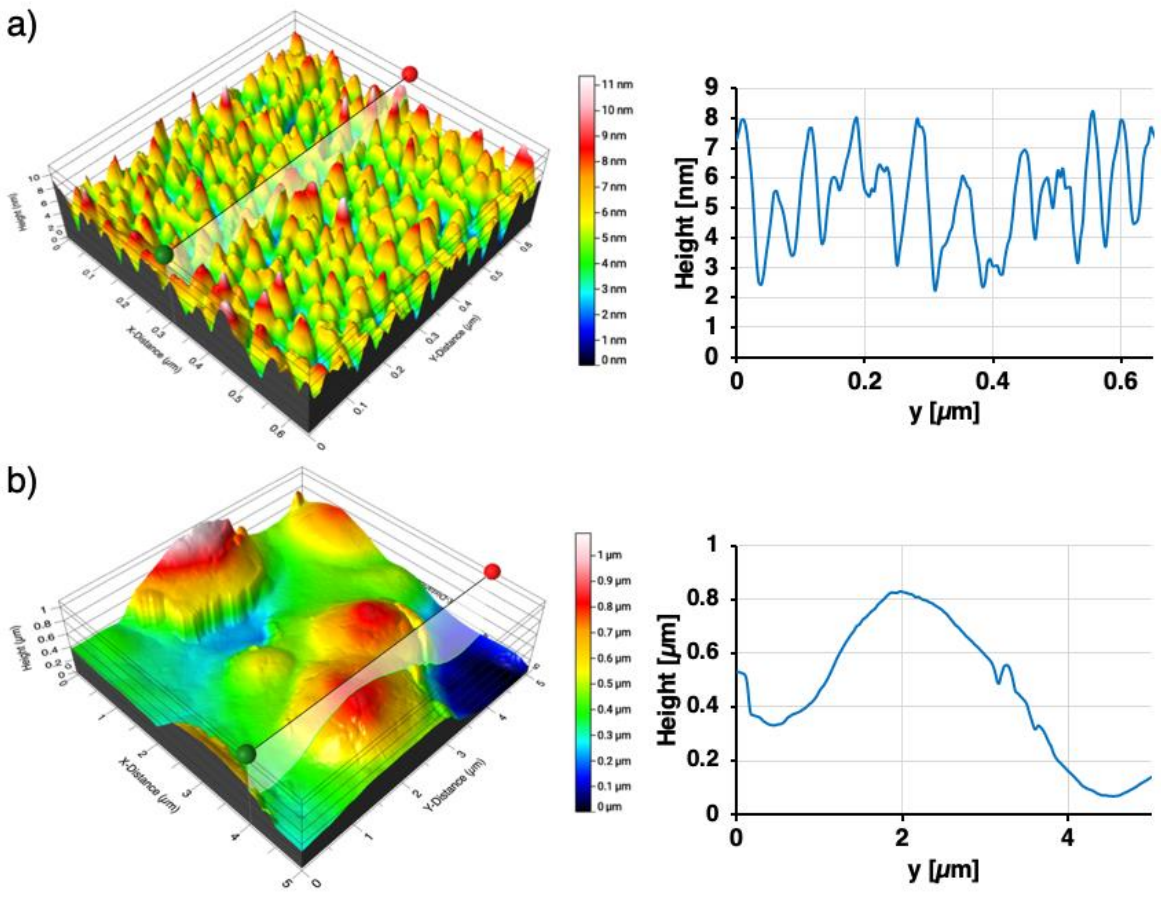


Figure 74. AFM scans of the sample surface (a) in reference state and (b) after heating. Line profiles shown on the right are indicated by the black line on the left.

In summary, based on the experimental insights described above, the following degradation mechanism of Cu/W NMLs on Si substrate was identified:

1) Ion beam deposition induced vacancy diffusion is activated at T > 230 °C, resulting in interface diffusion in between Cu and W layers, Cu layer thickness increase, W layer decrease, as well as roughness increase and density decrease (Figure 75b).
2) Additional compressive stress in Cu layers at 280 °C exceeds the nanocrystalline yield stress. As a consequence, stress-induced Coble creep results in nano-scale Cu diffusion along W grain boundaries towards the sample surface. The formation of Cu nano crystals can be observed on the sample surface (Figure 75c).
3) Beyond 330 °C a large-scale microstructural transformation can be observed: thermally induced stress in the lower Cu layers exceeds the diffusion threshold in the W diffusion barrier. As a consequence, Cu diffuses into Si substrate, resulting in η''-Cu_3Si formation associated with rapid volumetric expansion, thus breaking down the layered structure, resulting in Cu absorption and complete transformation into η''-Cu_3Si (Figure 75d,e).

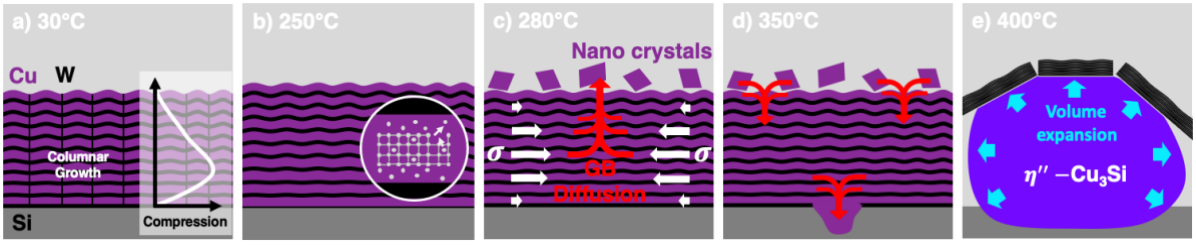


Figure 75. Illustration showing the mechanism leading to large-scale microstructural breakdown in Cu/W nano-multilayers on Si substrate.

4.2.4 Conclusion

Three key results were presented in this study: firstly, a novel and powerful combination of advanced experimental methods was employed to obtain temperature-dependent insights into stress and diffusion mechanisms within buried layers of nanostructured materials. Secondly, the effect of highly energetic particle deposition methods on the thermal stability and residual stress state was discussed before the background of defect formation and diffusion. A clear link between deposition conditions, nano-scale defect structure and thermal instability was established. Finally, this new understanding was used to develop a detailed description and model of the Coble creep induced strain within Cu layers, resulting in vertical diffusion of Cu across W layers into the Si substrate. It was found that the pronounced compressive residual stresses and defects arising from ion beam deposition contribute to large extent to the degradation of the nanostructured coating through a mechanism of Cu diffusion into the Si substrate, ultimately resulting in a transformation of nanostructured Cu layers into η''- Cu_3Si protrusions. Considering the low onset temperature and complex diffusion mechanism underlying structural degradation, the use of pure Cu/W nano-multilayers as radiation-tolerant coating and heat sink in plasma-facing components does not seem suitable, as temperatures are likely to exceed the identified critical diffusion onset temperature of 250 °C. Further investigations into possible stability enhancements of Cu/W nano-multilayers - for instance by introducing stabilising impurity phases - need to be pursued in future work to unlock enhanced temperature stability, while benefiting of the multilayer capability as point defect sink for radiation damage.

5 Advanced energy materials in technological applications: interaction of diffusion, stress and degradation in cathode particles and multilayer thin film batteries

5.1 Synchrotron X-ray quantitative evaluation of transient deformation and damage phenomena in a single Nickel-rich cathode particle

5.1.1 Introduction and Literature Review

Li-ion batteries are seen as the technology of choice for many energy storage applications, including electronics, grid storage, electric vehicles (EV). As the need for higher energy density batteries continues, research is focused on the development of cathode materials with higher useable capacities. The so called NMC compositions ($LiNi_xMn_yCo_zO_2$, where $x+y+z = 1$) have proven successful in this endeavour. These materials have been synthesised in a variety of compositions (NMC111, NMC622, NMC811), with higher nickel contents providing higher energy densities, despite reducing electrochemical and mechanical cathode stability, leading to loss of capacity retention over cell life [178,179]. The present study focuses $LiNi_{0.8}Mn_{0.1}Co_{0.1}O_2$ (NMC811), which is widely regarded as the state of the art cathode material. Capacity loss in NMC811 is evident from the first charge, with losses of up to 10% as a consequence of the first 'formation' cycle [180–182]. Over extended cycling complex chemomechanical interactions linking lithium diffusion, anisotropic lattice strain, surface oxygen depletion and cathode particle degradation have been identified as other reasons for performance fading over cycling [183–186]. At the crystal lattice scale, the cycling-induced mechanical degradation is caused by the anisotropic lattice expansion during lithium (de-)intercalation. Depending on the crystal lattice orientation within primary

crystallites [187], large stresses exceeding the material cohesive strength can arise at grain boundaries, resulting in crack nucleation and propagation [184,188,189]. An example for fracture and void formation is shown in appendix A.1. At particle level, cracking exposes more surface area to the electrolyte, causing further degradation of the active cathode material through multiple mechanisms: phase transformation [190], cathode-electrolyte parasitic reactions [191–195], and transition metal dissolution [196,197]. Cracking and debonding of primary particles further contribute to the capacity fade phenomenon by interrupting electron conduction from detached fragments to the cathode conductive matrix [186,198], thus preventing further contribution to charging and discharging [196]. Recent efforts aimed at optimising the charging behaviour of NMC811 include the use of coatings [199], the design of core-shell particles with a Ni-rich core [200], and secondary particles with optimised lithium diffusion pathways between particle boundary and core [201,202].

The key aspect of diffusion and degradation processes is their transient nature at particle scale. Pristine spheroidal NMC particles rely on intra- and intergranular Li+ and electron conduction from the particle-electrolyte interface into the particle core. Interrupting electrochemical processes for diffraction measurements initiates charge re-balancing, thus masking lithiation and lattice parameter anisotropy along the radial particle direction. To understand underlying breakdown mechanisms, experimental techniques must be able to probe undisturbed charging/ discharging processes at high resolution in both time and space. Characterising the electromechanical behaviour of NMC particles *operando* at the micron-scale poses a significant experimental challenge. As a result, direct experimental *operando* evidence for the evolution of both stress state and structural integrity in single secondary Li-ion cathode particles has remained lacking. Previously published *operando* experiments on single particles were limited to qualitative, averaged analysis of the degradation phenomena

[203,204] and electrochemical processes [180,205–210]. Detailed *post mortem* characterisation of microstructural changes within secondary NMC particles or full cathodes provided insights into the consequences of degradation [185,211–213]. However, the dynamic phenomena driving degradation cannot be captured using this approach. In this section, direct evidence is reported, which was obtained using synchrotron science techniques for *operando* sub-micron X-ray diffraction and *in situ* lensless coherent ptycho-tomography. Combined with FEM modelling and additional ex-situ material characterisation, a deep model-based understanding of the mechanisms that underlie particle degradation is developed, which can ultimately improve the design and fabrication of Ni-rich cathode materials.

5.1.2 Materials and Methods

5.1.2.1 T-EBSD Analysis

T-EBSD analysis was carried out on a thin, electron transparent lamella extracted from a cracked particle charged to 100% State-of-Charge (SoC) at a rate of C/3, following one formation cycle at a rate of C/10. Kikuchi patterns were collected in transmission geometry at an angle of 45 degrees and their grain orientation indexed using NMC811 unit cell information implemented for this purpose based on literature data [214], as shown in Figure 76. A Tescan LYRA3 instrument was used for the t-EBSD acquisition at a beam energy of 20 keV and a pixel size of 40x40 nm^2. The obtained Euler angles in the sample x-y geometry were converted to *c*-axis vectors, based on which the angle α between the radial particle direction from the particle centre to the t-EBSD measurement location and the local *c*-axis

was determined, as illustrated in Figure 76. Higher statistical occurrences of angles around 90 degrees were accounted for by normalising the angle distribution curve by $1/(0.5\sin(\alpha))$.

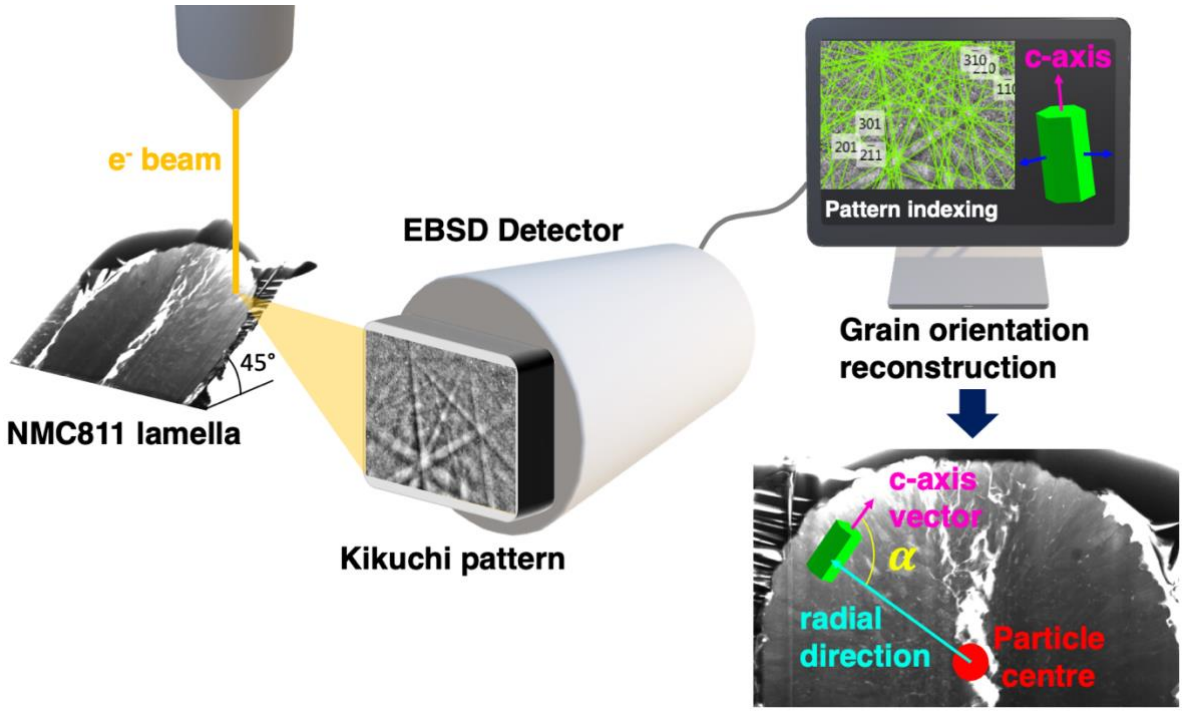


Figure 76. Illustration of the t-EBSD acquisition process (left) with subsequent pattern indexing and grain orientation reconstruction (right). Bottom right: illustration of the angle α between radial direction and *c*-axis vector used for determining the lithium diffusion direction

5.1.2.2 Operando Single Particle Diffraction

A custom synchrotron beamline setup, as illustrated in Figure 77, was built for the B16 beamline at Diamond Light Source, permitting a single NMC811 particle to be charged in Argon atmosphere, while acquiring diffraction patterns. Samples were prepared by sputter-coating industrial standard nano-manipulator needles with Aluminium, in order to prevent any tungsten oxidation during particle charge. One single particle per needle was attached inside the vacuum chamber of a Tescan LYRA3 XM FIB-SEM instrument using a platinum gas injection system. The samples were stored in a mobile vacuum container with desiccant pad at low vacuum. To mount the sample, it was removed from the container and held

underneath a constant stream of argon, before being lowered into the Kapton container filled with Argon. The same procedure was followed for lithium disc, which were individually stored in a sealed vacuum containers until the experiment. A LiTFSI:PYR13 ionic liquid droplet was deposited onto the Li disc in Argon environment through a syringe, avoiding exposure to air. The particle was charged using a BioLogic SP-300 potentiostat in 30 pA constant-current mode, starting from a voltage of 3.0V at a C-rate of 0.025 for a total duration of 15500s. An upper voltage limit of 4.5V was set as termination condition, however, due to increased internal resistance and resulting overpotential caused by the use of low vapour pressure ionic liquid, charging stopped prematurely at a SoC of 10.3%.

The SoC was determined post-experimentally by estimating the volume of the particle based on SEM images, yielding a particle volume of $2.13 \cdot 10^{-15}$ m^3. Assuming a density of $\rho_{NMC811} = 2200\ \mathrm{kg/m^3}$ [181], the total particle mass was estimated to be $4.69 \cdot 10^{-12}$ kg. Assuming a specific capacity of 275.5 mAh/g provided by the powder supplier, combined with the transferred capacity at the end of charge of 28.3 mAh/g, this results in a final SoC of 10.3%.

KB mirrors were used to focus the 19 keV beam to a vertical and horizontal full width at half maximum of 380 nm and 800 nm, respectively. The vertical scanning path ranged from the lower end of the Al-coated tungsten needle to the lower free edge of the attached particle. Diffraction patterns for (003) and (104) reflections were acquired for 20s using a Photonic Science Image Star 9000 detector with a resolution of 3056x3056 pixels and individual pixel size of 31x31 μm^2. A sample-detector distance of 131.67 mm was determined using LaB_6 powder diffraction calibration. Image files were calibrated, integrated and reduced using the DAWN Science software package [32] and finally converted to d-spacing using MATLAB.

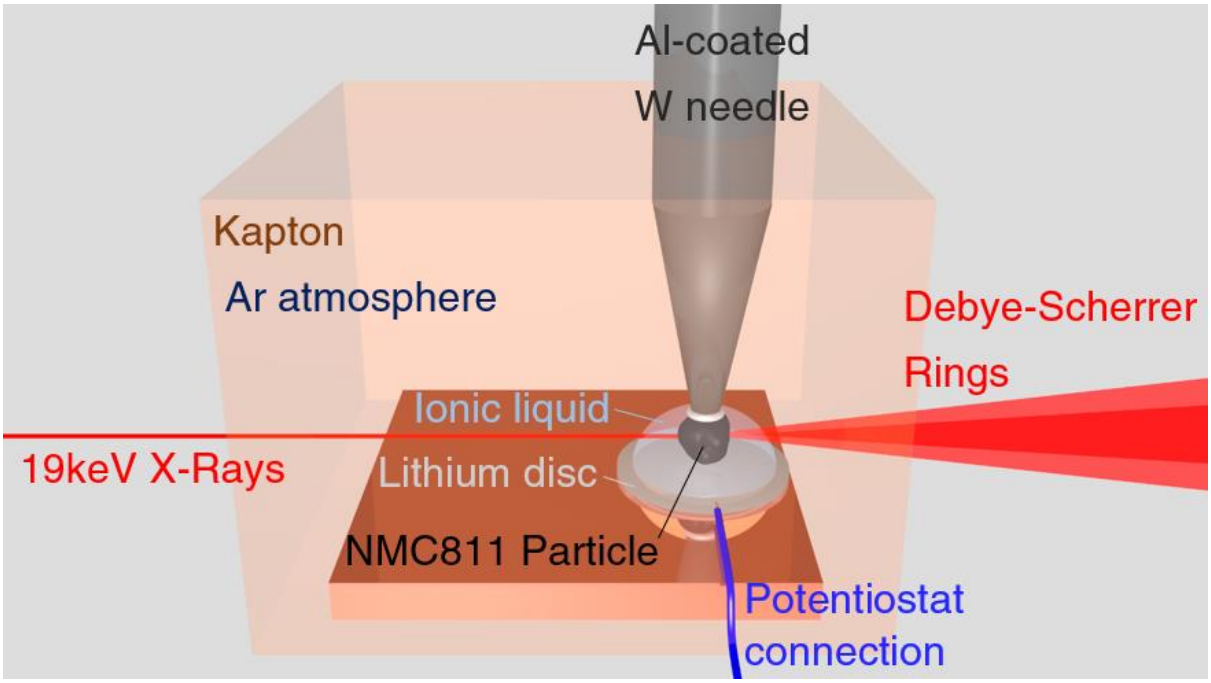


Figure 77. Custom-built *operando* NMC 811 sample environment for synchrotron beamline, permitting (i) charge of a single cathode particle, (ii) acquisition of diffraction patterns and (iii) operation in inert gas atmosphere.

5.1.2.3 Full cell *operando* diffraction

In a second experiment at Diamond Lightsource Beamline B16, a custom cell design was used for *operando* XRD measurements at an X-Ray energy of 19 keV and a beam size of 10.1x2 mm^2. Carbon windows on either side of the cell allowed X-rays to pass through with little attenuation, while also doubling as current collectors. Measurements were carried out in transmission mode. The cell was made into a half cell configuration with NMC 811 being measured vs a Li metal anode. 1M LiPF6 in EC:DMC (50:50) was used as the electrolyte system. The cell was charged from 3.4 to 4.4V at a rate of 0.5C. Following the identical calibration and integration procedure as described for the single particle measurements, the c-axis and a-axis lattice parameter evolution were reconstructed using MATLAB. The results of the average cathode lattice parameter evolution versus SoC are shown in Figure 78.

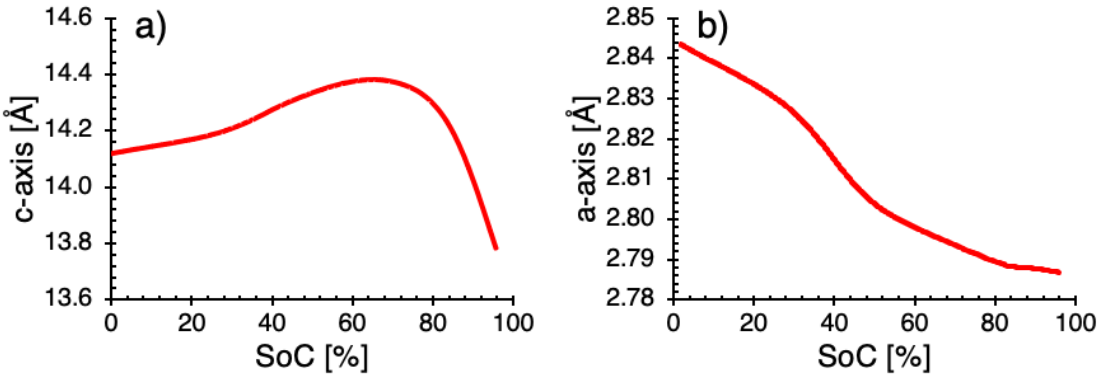


Figure 78. Lattice parameter evolution during full cell charge of NMC811 at a rate of 0.5C. (a) C-axis lattice parameter. (b) A-axis lattice parameter.

5.1.2.4 In situ Ptychography and Reconstruction

Ptychographic imaging was carried out on the I13-1 beamline (coherence branch) at Diamond Light Source, U.K. A similar sample setup as for the *operando* particle diffraction was built for the experiment. The particle was charged at a C-rate of 0.205 up to an SoC of 17.8% for a total duration of 3100s. As for the diffraction experiment, the voltage reading was not reliable due to overpotential induced by the use of ionic liquid. A particle mass of $5.23 \cdot 10^{-9}$ g was determined by multiplying the reconstructed tomography volume with a density of $\rho_{NMC811} = 2200\ kg/m^3$. Assuming a specific capacity of 275.5 mAh/g provided by the powder supplier, combined with the transferred capacity at the end of charge of 49.0 mAh/g, this results in a final SoC of 17.8%.

A Fresnel zone plate with beam stop and order sorting aperture were used to focus coherent X-rays at an energy of 9.7 keV onto the sample which was place slightly downstream of the focus. Diffraction patterns were collected in the far-field 9.47m from the sample using an Excalibur detector, which features an array of Medipix3 chips and has a 55µm x 55µm pixel

size. For each angular projection 256 diffraction patterns were generated by raster scanning with an aperiodic 1μm step over an area of 16 x 16 μm^2. Ptychography scans were repeated for 600 evenly spaced angular positions of the sample rotated though 180°.

The diffraction data was cropped to 512 x 512 pixels around the optical axis in order to include only statistically significant counts. Ptychographic reconstructions were performed using 500 iterations of the ePIE algorithm [215] which resulted in a sample pixel size of around 43nm x 43nm. Prior to tomographic reconstruction the sample phase was unwrapped and had a phase ramp subtracted. Alignment of the projection stack was based on the sequential re-projection algorithm with the tomography reconstructions carried out using the standard filtered back-projection algorithm.

5.1.3 Results and Discussion

5.1.3.1 Void Formation Upon First Charge

$LiNi_{0.8}Mn_{0.1}Co_{0.1}O_2$ cathodes were obtained from an industrial supplier, charged to 4.2V and discharged to 3.0V from pristine state at a rate of C/10. Subsequently, they were charged to levels of 50% and 100% SoC at a rate of C/3, respectively. Initial *post mortem* characterisation of the void evolution versus SoC was performed by creating FIB cross-sections through the bulk cathodes, revealing microstructural details in the centre of the spherical NMC811 particles. Sectioning of the cathode was carried out using Ga FIB at a voltage of 30kV and a beam current of 11nA, followed by fine polishing at 0.2nA. The observed fragmentation is shown in Figure 79, with voids highlighted in orange. The electron-conductive PVDF matrix can be seen in between particles. Combining the formation cycle with one single charge was thus sufficient to drive strong fragmentation and void formation, causing significant and irreversible loss in maximum capacity of around 10% after first

charge. Intergranular voids result in reduced internal Li and electron conductivity, a significantly increased charge-transfer kinetic resistance and therefore lower attainable charging rates. In addition, fragmentation of secondary particles leads to de-bonding and electrical isolation of primary particles, which stop contributing to electrochemical processes due to a lack of electron conductivity through the enclosing electrolyte [196].

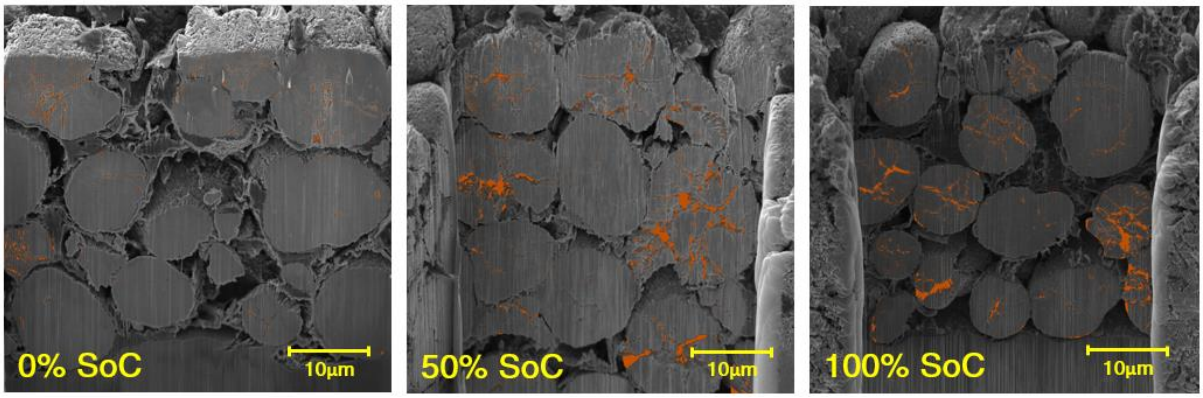


Figure 79. Intergranular void evolution vs. SOC in NMC811 material observed by FIB-SEM cross-sectional imaging. Cracks and voids highlighted in orange.

5.1.3.2 Diffusion Pathways in Core-Shell Particles

$LiNi_{0.8}Mn_{0.1}Co_{0.1}O_2$ cathodes were charged to 4.2V and discharged to 3.0V from pristine state at a rate of C/10. Subsequently, they were charged to 100% State of Charge (SoC) at a rate of C/3. Stoichiometric ratios were obtained from t-EDX performed on a thin, electron-transparent lamella containing half of a fractured particle at the electron energy of 20 keV, thus reducing the sample-beam interaction volume and increasing the resolution as compared to bulk sample measurements. The lamella was produced and fine-polished using FIB milling and revealed the grain orientation of primary particles in the shell. The data in Figure 80a show the progressive concentration gradients for Ni, Mn and Co along the radial particle direction. A Mn-rich surface with composition of $LiNi_{0.5}Mn_{0.3}Co_{0.2}O_2$ (NMC532) was found, while a bulk material composition of NMC811 was confirmed. To determine the crystal

orientation of primary particles and the orientation of the local *c*-axis, t-EBSD mapping was performed alongside the t-EDX analysis at the electron energy of 20 keV. For this purpose, back-scattered electron diffraction patterns showing Kikuchi bands [216] were acquired in transmission mode and indexed, revealing local phase and grain orientation information. The obtained t-EBSD map with colour-coded Euler angles is shown in Figure 80b, alongside a STEM micrograph of the lamella and an illustration of primary particles in the core and shell. Elongated, radially oriented particles are visible in the particle shell, while smaller, randomly shaped particles were found in the particle core.

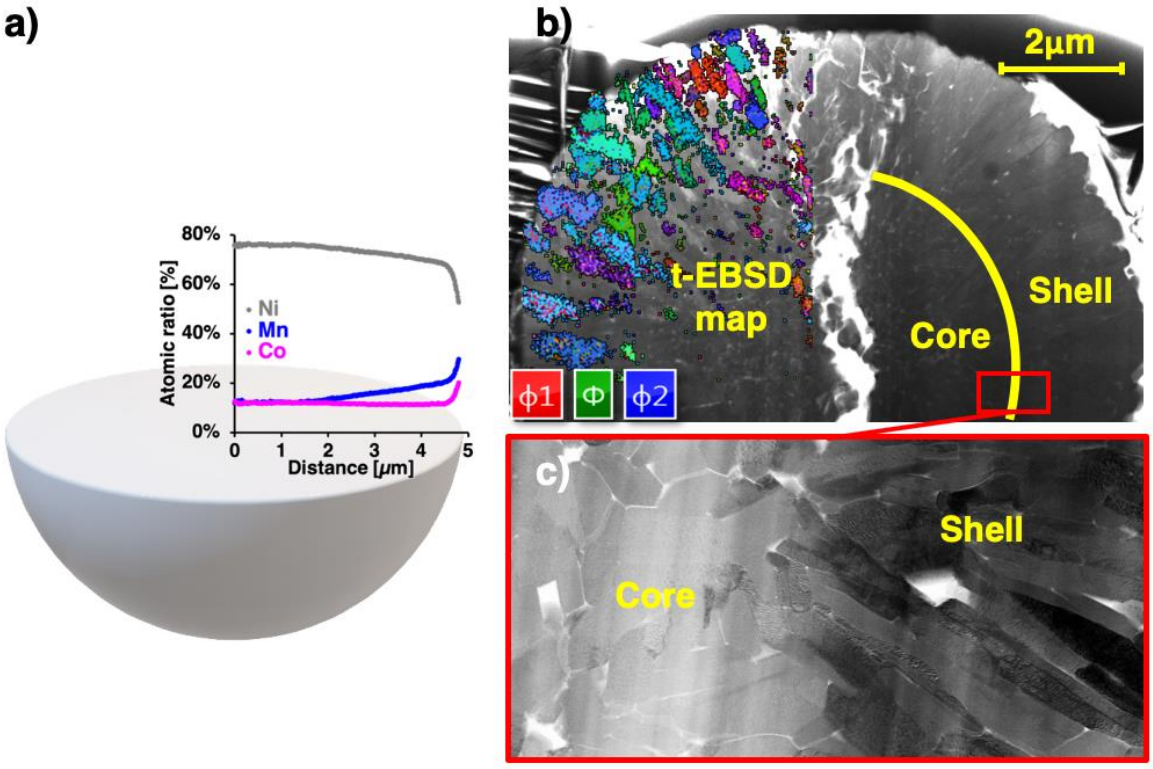


Figure 80. (a) Radial atomic ratio of Ni, Mn and Co as determined by EDX spectroscopy. (b) Lamella containing fractured half-particle after charge to 100% SoC. Left half: t-EBSD map of local unit cell Euler angles with respect to the Cartesian scanning coordinate system. Right half: indication of core-shell interface (c) detailed STEM image of core-shell interface with elongated, radially aligned particle in the shell and smaller, randomly oriented particle in the core.

Subsequently, the obtained Euler angles were converted from Cartesian coordinate base to the angles between the radial direction (from particle centre to t-EBSD measurement point) and the *c*-axis of the hexagonal particle lattice. The findings were normalised with respect to the statistical frequency of angle occurrence within a sphere. The angle distribution shown in Figure 81a confirmed a carefully designed grain orientation distribution within the secondary particle shell, resulting in radially aligned Li diffusion layers with respect to the particle centre, as illustrated in Figure 81b.

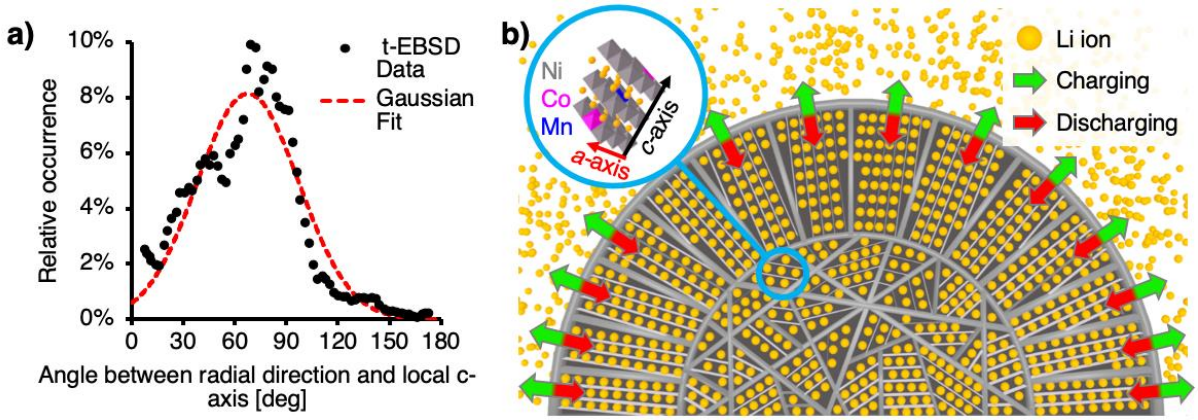


Figure 81. (a) Distribution of angles between *c*-axis of hexagonal primary particle lattice in the particle shell and particle radial direction. Red: Gaussian fit. (b) Rendered image of a core-shell particle based on t-EBSD data. Radial alignment of primary particle Li layers allows faster diffusion from the electrolyte towards the randomly oriented core during discharge (red arrows pointing into particle), and in the inverse direction during charge (green arrows pointing out of particle). Top left: hexagonal unit cell of NMC811.

The experimentally confirmed diffusion pathway optimisation by design enables higher Li diffusion rates, however, it may also have a detrimental impact on the mechanical stability of spherical secondary particles. Preferential expansion and contraction directions of the hexagonal NMC811 lattice perpendicular to the lithium diffusion direction can cause large stresses between grains and within the microsphere overall, and lead to Mode I (opening), II (in-plane shear) and III (out-of-plane shear) fracture [105], as depicted in Figure 82. A close relationship between microstructure and cracking mode can be seen in Figure 82c: while

radial Mode I cracks travel along the elongated grains in the shell, crack deflection resulting in Mode II cracking along the core-shell interface is visible. This ultimately leads to electrical isolation of active material.

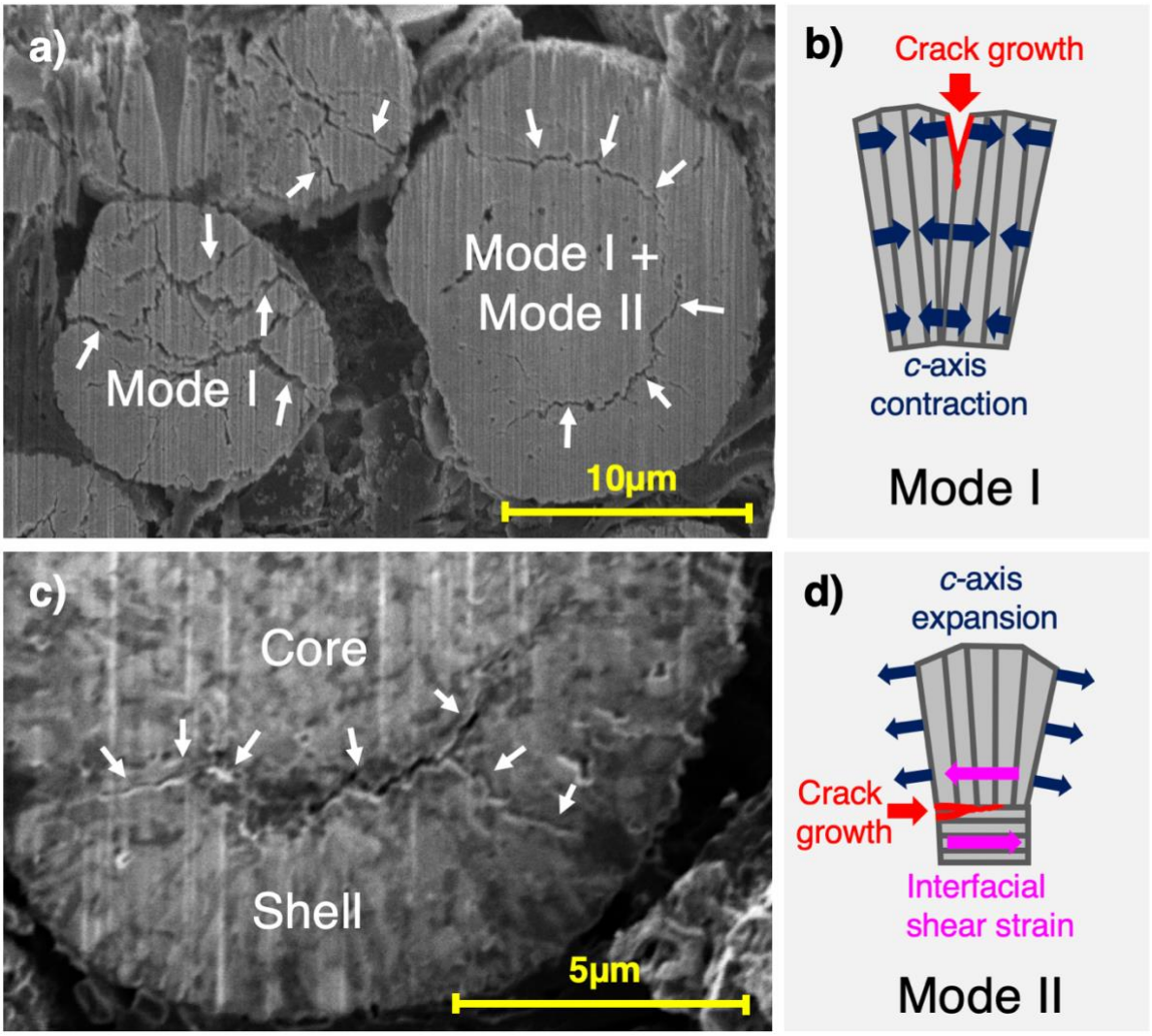


Figure 82. (a) SEM image of NMC811 cathode cross-section after a single charge to 100% SoC at C/3. Arrows indicate locations of fracture. (b) Illustration of Mode I (opening) fracture between two primary NMC particles. (c) High resolution FIB image of lower half of larger particle shown in (a). Crack deflection from radial to azimuthal direction is clearly visible. (d) Illustration of Mode II (in-plane shear) fracture between two primary NMC particles.

5.1.3.3 High local deformation upon first charge onset

To measure the lattice parameter distortion within a single core-shell particle during *operando* charging, a sub-micron focus wide-angle X-ray scattering (WAXS) experiment was performed at the B16 Test beamline at Diamond Light Source, to collect local probes of the lattice parameter variations within a single particle. A pristine single NMC811 particle with the mass of $4.69 \cdot 10^{-9}$ g was attached to an Al-coated nano-manipulator tungsten needle using an in-SEM Pt gas injection system. The particle was immersed in a LiTFSI:PYR13 ionic liquid droplet to substitute the more volatile and air-sensitive electrolyte [217]. A lithium disc served as anode and a Kapton container, as well as a Faraday cage with X-ray inlet and outlet windows, were built around the setup. The volume was continuously flushed with Argon, ensuring an inert gas sheath atmosphere and minimal electromagnetic disturbances. A photon energy of 19keV was selected using a multilayer monochromator and focused onto the particle using KB mirrors, resulting in a beam size of around 380 nm on the sample. A low current potentiostat was connected to the tungsten needle with attached particle (cathode) and the Li disc (anode). The particle was charged up to a SoC of 10.3%, while a line scan across the particle was repeatedly acquired. The implications of the large overpotential introduced by the use of ionic liquid with high internal resistance meant that the experimental data were limited to the SoC range of 0% to 10.3%, as determined by current readings and the specific capacity of NMC811.

Debye-Scherrer diffraction rings of the 003 and 104 reflections representing the *c*- and *a*-axis, were collected using an Image Star 9000 detector (Photonic Science Ltd, UK) and integrated azimuthally. The results presented in Figure 83, showing the local c- and a-lattice parameter evolution during charge from 0% to 10.3% SoC along the particle radius, reveal the rise of significant local strain gradients during the early stages of the formation cycle, which would have been masked by averaging techniques. The free secondary particle surface

closest to the lithium anode (location 4, Figure 83) experiences an expansion of the hoop-oriented *c*-axis from 14.20Å at 0% SoC to 14.30Å at 10.3% SoC, as well as a contraction of the radially oriented *a*-axis from 2.850Å at 0% SoC to 2.835Å at 10.3% SoC. *C*-axis expansion in hoop direction leads to the formation of compressive residual hoop stress in the particle shell, while contraction of the *a*-axis lattice parameter in radial direction leads to tensile residual stress in radial direction. As the illuminated material volume in locations 2 and 3 increasingly contains contributions from inactive primary particles under tension in the core, the resulting lattice parameter distributions represent a superposition of increasing and decreasing lattice parameters, which ultimately cancel each other out along the beam path through the particle centre in location 1.

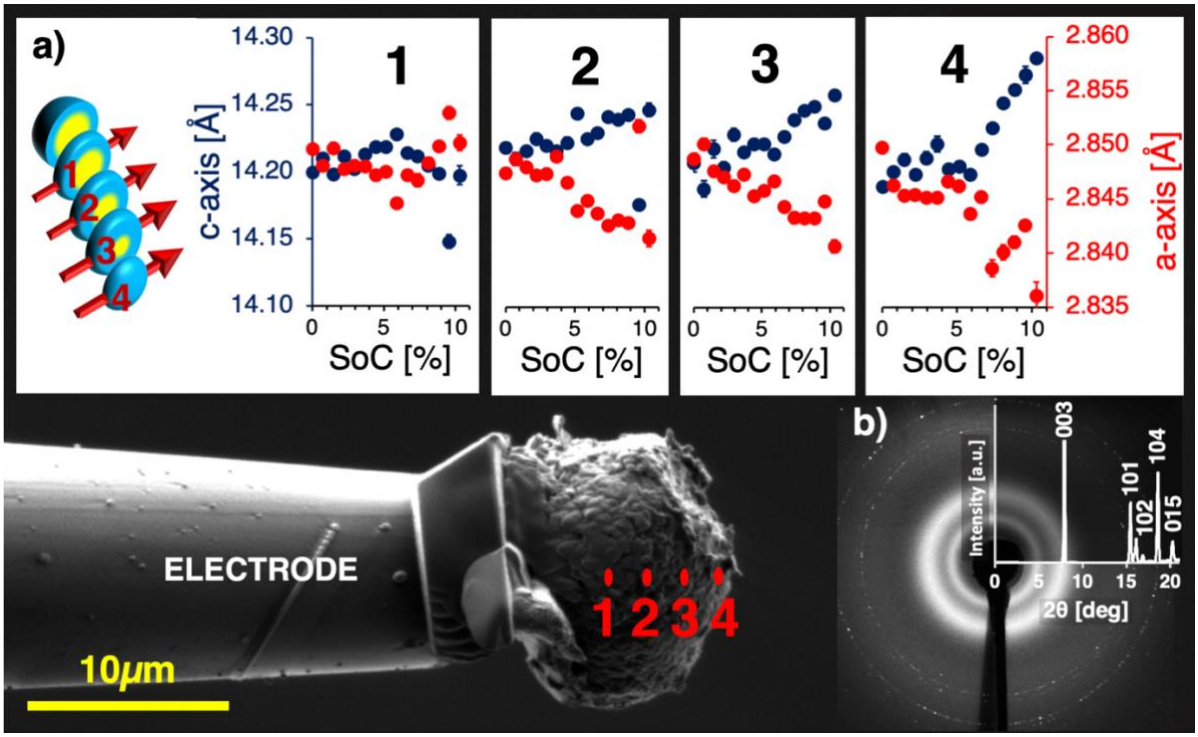


Figure 83. (a) Left: illustration of X-Ray beam path across particle with lattice parameter gradient ranging from de-lithiated (blue) to lithiated (yellow) state. Right: local *c*-axis and *a*-axis lattice parameter variation within single NMC811 particle during charge from 0% to 10.3% SoC. Points at particle surface exposed to the electrolyte (blue on left hand side cartoon) experience increasing *c*-axis expansion and *a*-axis contraction, whilst the converse occurs at particle core (yellow on left hand side cartoon). (b) Left: single X-Ray detector frame showing Debye-Scherrer rings alongside integrated intensity and identified peaks. The two broad rings in the centre originate from ionic liquid. Right: SEM micrograph of single NMC811 particle attached to Al-coated W needle using Pt deposition.

Averaging *operando* strain measurements of a full NMC811 cathode were carried out for lattice strain comparison under identical beam conditions, but without the use of focusing KB mirrors to ensure sufficient averaging for reliable probing statistics. The cathode was charged from 3.4 to 4.4V at a C-rate of 0.5. Average lattice strains at 10.3% SoC were found to be 0.18% for the c-axis and -0.19% for the a-axis, as compared the observed inter-particle strain at single particle level of 0.71% at 10.3% SoC for the *c*-axis and -0.53% for the *a*-axis. Due to the anisotropic lithium intercalation and de-intercalation and resulting uneven lattice parameter distribution within a single particle, averaging measurements mask local peak strains during charge and discharge. The above-presented comparison of single particle results with averaging measurements reflect the unique insights gained by local probing by *operando* diffraction.

Stress analysis of the particle deformation obtained from *operando* XRD revealed the stress distribution in hoop and radial direction along the particle radius, as shown in Figure 84. Assuming a stress free reference state before charging, pronounced compressive stresses of up to -1 GPa were found in the particle shell at a SoC of 10.3%, while tension of around 0.4 GPa was present in radial direction. As the lattice parameters in locations 1 and 2 were probed and averaged along the diameter of the particle, local stresses were masked by averaging and thus resulted in near zero stress values.

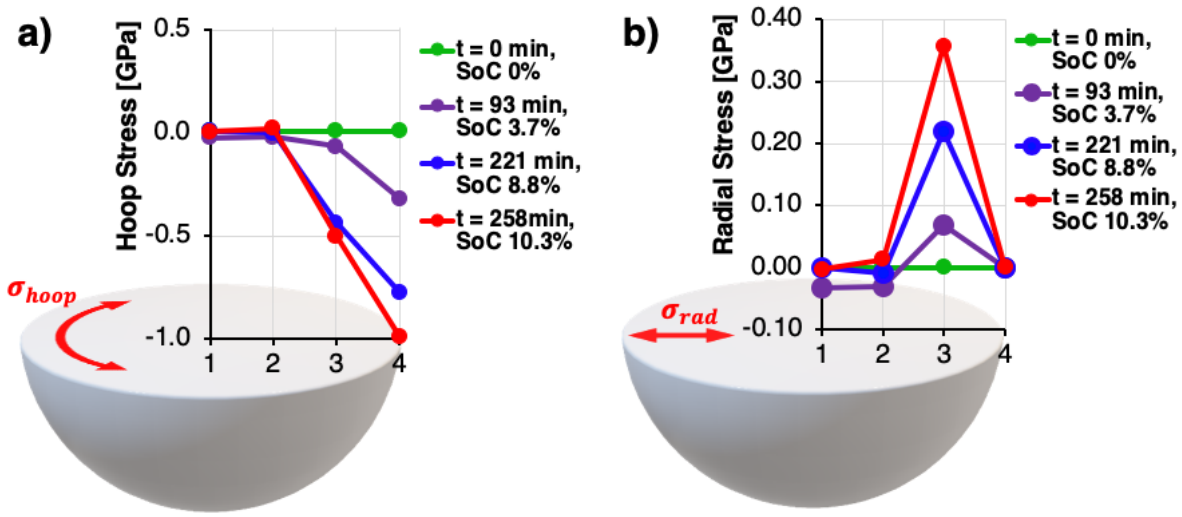


Figure 84. Reconstructed stress state along the particle radius vs. time and SoC, based on the lattice parameter data shown in Figure 83. Assumption: stress-free pristine particle. (a) Hoop stress. (b) Radial Stress. The stresses were calculated based on Hooke's law.

Considering the designed radial grain orientation of the shell particles, the observed high stresses at low SoC appear to provide a reasonable explanation for the high incidence of void formation and intergranular fracture observed using FIB-SEM cross-sectional imaging shown in Figure 82 and appendix A.1 (Figure 79). A significantly reduced deterioration rate of maximum capacity observed across literature in subsequent cycles can be explained by the significant amount of distributed micro-cracking and pseudo-plastic deformation during the first charging cycle, during which cracks and voids are formed initially.

5.1.3.4 First charge degradation observed by nano-resolution Ptycho-Tomography

Ptychographic imaging was performed at the I13-1 beamline at Diamond Light source and combined with *in situ* particle charging, permitting the comparison of 3D tomographic data of *one and the same* single particle before and after charge with a voxel size of 43x43x43 nm^3. This approach overcomes the well-known challenge of comparing different particles in *ex situ* and *post mortem* experiments, in which the prior damage state of different particles

being compared cannot be known. The present *operando* approach ensures that the observed particle degradation can be compared to the pristine state of the same particle, and can be unequivocally ascribed to charging-related damage, as opposed to pre-existing particle damage inherited from particle manufacturing. A similar setup described above for the single particle diffraction experiment was employed, allowing to charge a single pristine NMC811 particle of mass $5.23 \cdot 10^{-9}$ g to a SoC of 17.8%, thus demonstrating the effect of high-rate charging on the structural integrity of NMC811. A higher SoC was reached than in the previous experiment to ensure the capture of mechanical fracture within the particle. The reconstructed particle Ptycho-Tomography slices in Figure 85 show significant microstructural degradation after one single charge to 17.8% SoC. Two types of cracks can be identified and show agreement with those observed in Figure 82, namely, radial cracks reaching from the particle centre to the particle boundary (represented by blue arrows), and cracks in hoop direction along the core-shell interface (red arrows) – both of which limit lithium diffusion significantly.

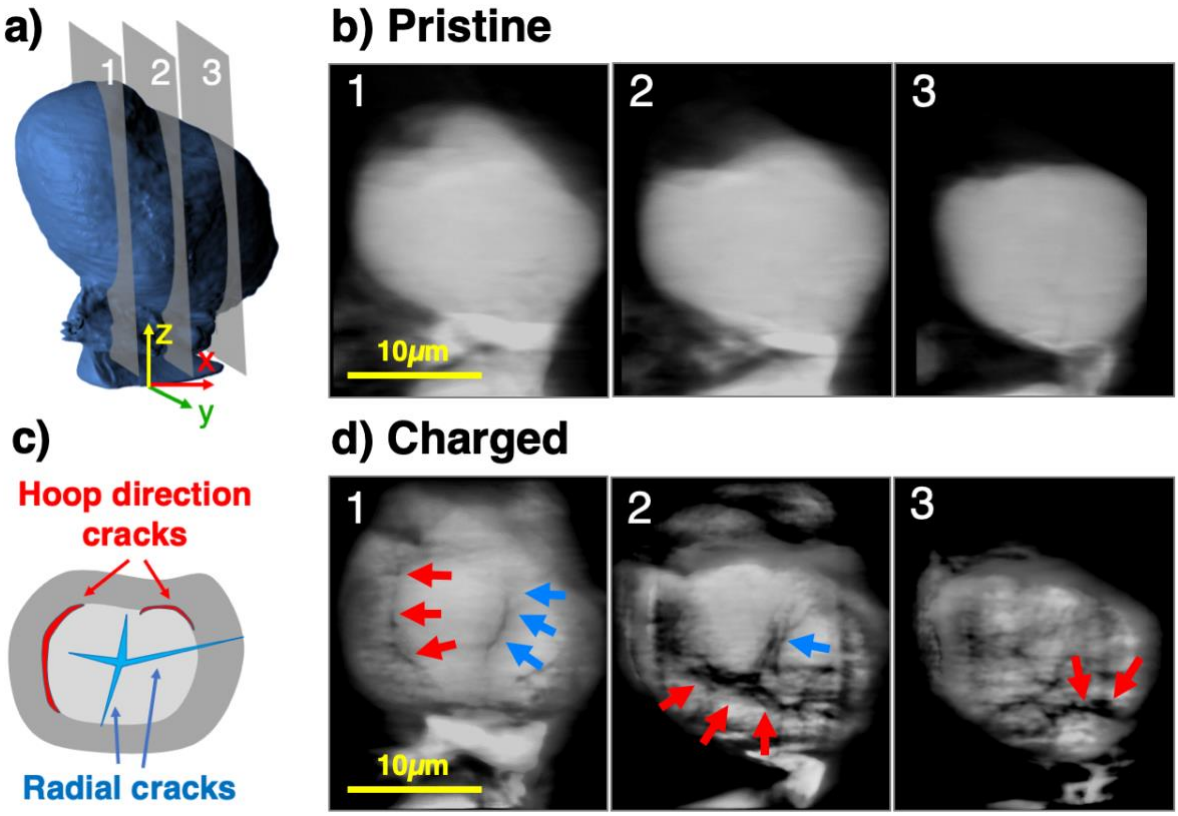


Figure 85. (a) 3D Ptycho-Tomography reconstruction of a single particle in pristine state with indication of cross-sectional planes 1-3 shown on the right. (b) Reconstructed ptychography slices of pristine single particle. (c) Crack types observed after single charge: cracks in radial direction initiated in the core (blue) and cracks in hoop direction along core-shell interface (red). (d) Reconstructed ptychography slices after a single charge up to 17.8% SoC, revealing significant microstructural degradation in radial direction (blue arrows) and along the core-shell interface (red).

5.1.3.5 Modelling and Simulation

A coupled diffusion-strain simulation was implemented in COMSOL Multiphysics®, which combined the solution of a generalised diffusion equation with sequentially coupled strain and stress analysis. More precisely, the model consisted of solving the diffusion equation for a Li-concentration gradient within the particle using a prescribed boundary concentration. In a second step, the calculated concentration was related to strain in prescribed expansion directions based on the t-EBSD results presented above and finally converted into stress. A lithium concentration of 20% was assumed for a fully charged particle, while a lithium

saturation of 100% was assumed for the fully discharged state. A simplified model of a secondary particle was realised by creating a 90° circle sector and applying appropriate symmetry conditions, resulting in a 2D particle slice under plane strain approximation. The particle radius R was chosen to be 10µm, while the values for density ($\rho_{NMC811} = 2200\,\mathrm{kgm^{-3}}$ [181]), Young's modulus ($E = 170\,\mathrm{GPa}$ [218]) and Poisson ratio ($\nu = 0.25$ [219]) were obtained from literature. The diffusion coefficient of Li in NMC 811 was adopted from literature ($D_{Li} = 10^{-10}\,\mathrm{cm^2 s^{-1}}$ [207,220]) and assumed constant. Subsequently, diffusion and expansion dicrections were prescribed. The core-shell type particles were modelled by prescribing homogenous diffusion (blue area in Figure 87a) and expansion (blue area in Figure 87b) properties in the core of the particle, thus approximating a secondary particle core composed of small primary particles with random crystal orientations. The nanorod shell was modelled to permit diffusion exclusively in radial direction (red area in Figure 87a) and expansion only in hoop direction (red area in Figure 87b). This radial diffusion behaviour was mathematically expressed by the diffusion coefficient of a core-shell particle c_{CS}:

$$c_{CS} = \begin{pmatrix} Dx & 0 \\ 0 & Dy \end{pmatrix} = D_{Li}\begin{pmatrix} \mathrm{H}' + \cos(\arctan2(y,x)) \cdot \mathrm{H} & 0 \\ 0 & \mathrm{H}' + \sin(\arctan2(y,x)) \cdot \mathrm{H} \end{pmatrix}. \quad (44)$$

$\mathrm{H}' = f(x, y, w, R_T, R)$ and $\mathrm{H} = f(x, y, w, R_T, R)$ are two smooth Heaviside functions, which describe the transition from homogenous to radial diffusion properties and are depending on the location *x*, *y*, as well as the transition radius R_T and the transition width *w*. H' dominates the diffusion behaviour up to R_T for the particle core, after which the diffusion for the shell is described by H. Figure 86 shows an example of the horizontal diffusion coefficient component

Dx, along with all parameters used to define the Heaviside function. The transition width *w* was chosen to be 0.1µm, as the core-shell particles usually exhibit a rather abrupt change in morphology between core and shell.

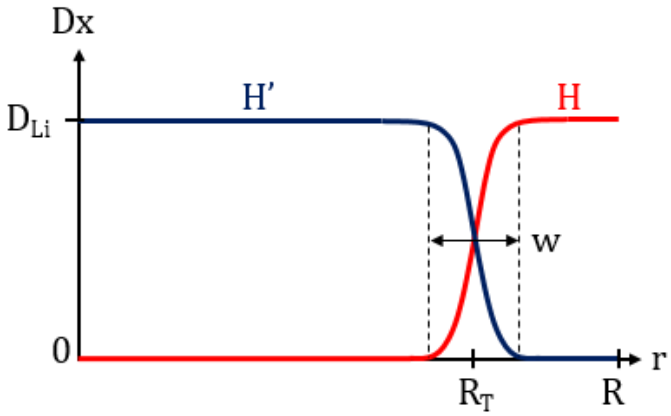


Figure 86. Example of the diffusion coefficient definition for the horizontal diffusion coefficient component Dx in horizontal direction for a core-shell particle.

The general time-dependent diffusion equation for a concentration *u* solved in this model is given by:

$$\frac{\partial u}{\partial t} + \nabla \cdot (-c\nabla u) = 0 \qquad (45)$$

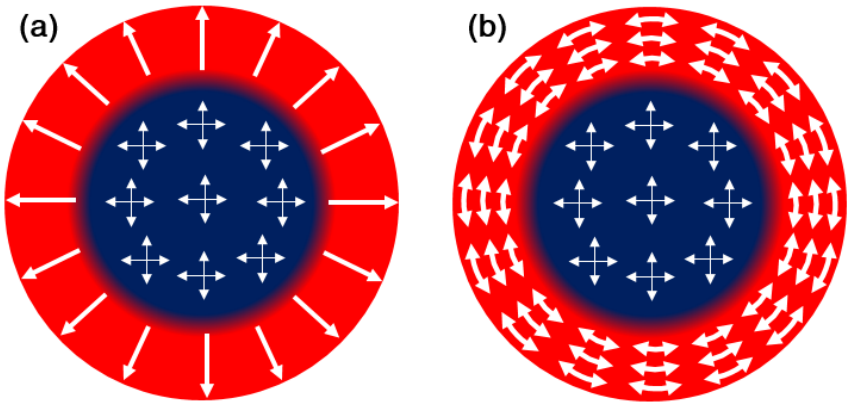


Figure 87. Diffusion and expansion directions for core-shell and homogenous, randomly oriented particle. (a) Diffusion coefficient of a secondary core-shell particle transitioning from homogenous properties (blue) to radial diffusion properties (red). (b) Expansion directions of a core-shell secondary particle transitioning from isotropic expansion (blue) to hoop expansion (red) perpendicular to the diffusion direction.

To simulate a full charge followed by discharge, boundary conditions were selected according to experimental charging and discharging profiles found in the literature [221], which indicate that reversible linear charging behaviour is possible in a lithiation state ranging from around 20% to slightly below 100%. For a full charge of the NMC811 particle the initial lithiation state within the particle was set to 100%. A Dirichlet boundary condition prescribing a Li saturation of 20% outside the particle was applied at the particle boundary. The diffusion problem was then solved. In a second step, the diffusion state was linked to a volumetric expansion of the linear-elastic material by prescribing eigenstrain [9,222], assuming a volumetric unit cell contraction of $\Delta V \approx 4\%$ upon full charge [196]. A radial diffusion direction in the shell of core-shell particles was assumed for enhanced lithium diffusion towards the particle centre. The expansion/ contraction direction of the unit cells was therefore prescribed in hoop direction, perpendicular to the diffusion direction (Figure 87b). The core of the core-shell particle was modelled isotropic, resulting in euqi-biaxial expansion without shear strain. The expansion coefficient for a core-shell particle e_{CS} was defined as (46):

$$e_{CS} = \begin{pmatrix} e_x & e_{xy} \\ e_{yx} & e_y \end{pmatrix}$$

$$= \Delta V \begin{pmatrix} \mathrm{H}' + \sin\left(\mathrm{atan2}(y,x)\right)^2 \cdot \mathrm{H} & -\cos\left(\mathrm{atan2}(y,x)\right)\sin\left(\mathrm{atan2}(y,x)\right) \cdot \mathrm{H} \\ -\cos\left(\mathrm{atan2}(y,x)\right)\sin\left(\mathrm{atan2}(y,x)\right) \cdot \mathrm{H} & \mathrm{H}' + \cos\left(\mathrm{atan2}(y,x)\right)^2 \cdot \mathrm{H} \end{pmatrix}$$

With the same H and H' as employed for the diffusion problem. Similarly, the expansion coefficient for a randomly oriented particle e_R was defined as

$$e_R = \begin{pmatrix} e_x & e_{xy} \\ e_{yx} & e_y \end{pmatrix} = \Delta V \begin{pmatrix} 1 & 0 \\ 0 & 1 \end{pmatrix}. \quad (47)$$

Finally, based on the lithiation state *u*, the strain tensor ε was defined as

$$\varepsilon = \begin{pmatrix} \varepsilon_{11} & \varepsilon_{12} \\ \varepsilon_{21} & \varepsilon_{22} \end{pmatrix} = u \begin{pmatrix} e_x & e_{xy} \\ e_{yx} & e_y \end{pmatrix}, \quad (48)$$

based on which the stress distribution within the particle was caclulated.

The same procedure was followed to determine the strains, stresses and lithium concentration distribution upon discharge, for which the boundary conditions were modified. The lithium saturation within the particle was set to 20%, while the Dirichlet boundary condition was set 100%, simulating lithium diffusion into the particle upon discharge. All simulation results are presented in the following section.

Figure 88 shows the distribution of concentration, radial stress and hoop stress along the particle radius as a function of time during charge and discharge. Figure 88a, b represent the full de-lithiation evolution from 100% to 20% and vice versa within 10800s or 3 hours. The prescribed diffusion coefficient D_{Li} obtained from literature [207,220] thus results in an

effective charge rate of C/3, showing good agreement with real-world Li-NMC battery testing and applications.

The time-dependent hoop stresses at the particle core and shell during charge and discharge, which are shown in Figure 89, reveal peak stresses at time t = 1080s. Stresses ranging from -4 GPa compression at the particle boundary to 1.5 GPa tension at the particle core can be expected to exceed the cohesive strength between particles by far, resulting in void formation, crack nucleation and growth. Lithium deintercalation from the particle boundary leads to an abrupt increase in *c*-axis lattice parameter, resulting in compressive boundary hoop stresses, which are balanced by tensile hoop stresses in the particle core. This simulated behaviour showed good agreement with *operando* diffraction data shown in Figure 83, as well as the radial cracking pattern observed by Ptycho-Tomography shown in Figure 85. Radial stresses remained tensile across the particle during charge, thus providing a good explanation for the observed cracks in hoop orientation at the core-shell interface in Figure 85. This also agrees with the reduction in *a*-axis lattice parameter in radial direction observed by XRD in Figure 83. After time t = 1080s the stresses reduce without returning to a stress-free state. Upon discharge, the sense of stresses within the particle is invert between compressive and tensile, and *vice versa*, before returning to zero stress. All calculated stresses were obtained based on the assumption of a residual stress-free sample before the initial charge. As this assumption is difficult to verify experimentally, real stresses might be shifted by the amount of prevailing residual stress before first charge. Furthermore, inelastic processes that modify the material properties and response and lead to strain accumulation have also been ignored in this simulation.

The graphs in Figure 88 and Figure 89 clearly show why averaging experimental techniques fail to determine the real stress state within NMC cathodes during charge, as the integral of hoop stresses along the radius lie significantly below the locally observed stresses.

Clearly, the realistic mechanisms that underlie Li intercalation and de-intercalation are significantly more intricate. However, the overall mechanical implications and some quantitative insights obtained by the combination of experimental and modelling studies presented here are representative and in good agreement with previous studies [189]. The simulation described here provides reliable insights into the mechanical processes underlying fracture, although attendant chemical processes such as the formation of additional solid-electrolyte interfaces or oxygen depletion of surface layers are ignored. Excellent agreement between the simulated and observed radial and hoop stress profiles shown in Figure 84 was confirmed. Given the high magnitudes and gradients of stresses within the particles during the initial charge, the greatest proportion of plastic deformation and primary particle de-bonding (micro-cracking) are likely to occur immediately during the first charge and discharge ('formation') cycle, with tensile stresses during discharge being the main driver for particle-level damage. During subsequent cycles, the accommodation of unit cell volume changes of up to 4% does not require similar magnitudes of additional plastic deformation and micro-fracture. The degradation therefore proceeds at a significantly reduced rate, with cyclic fatigue being the main mechanical driver, alongside electrochemical degradation processes. Optimising diffusion pathways in the core-shell secondary particles by orienting the lithium conduction pathways in the radial direction permits a faster transport of lithium ions from the electrolyte towards the centre of the particle, and results in higher achievable charge rates. In terms of the mechanical consequences for the durability of the cathode material, however, these appear to be somewhat detrimental to the long term performance.

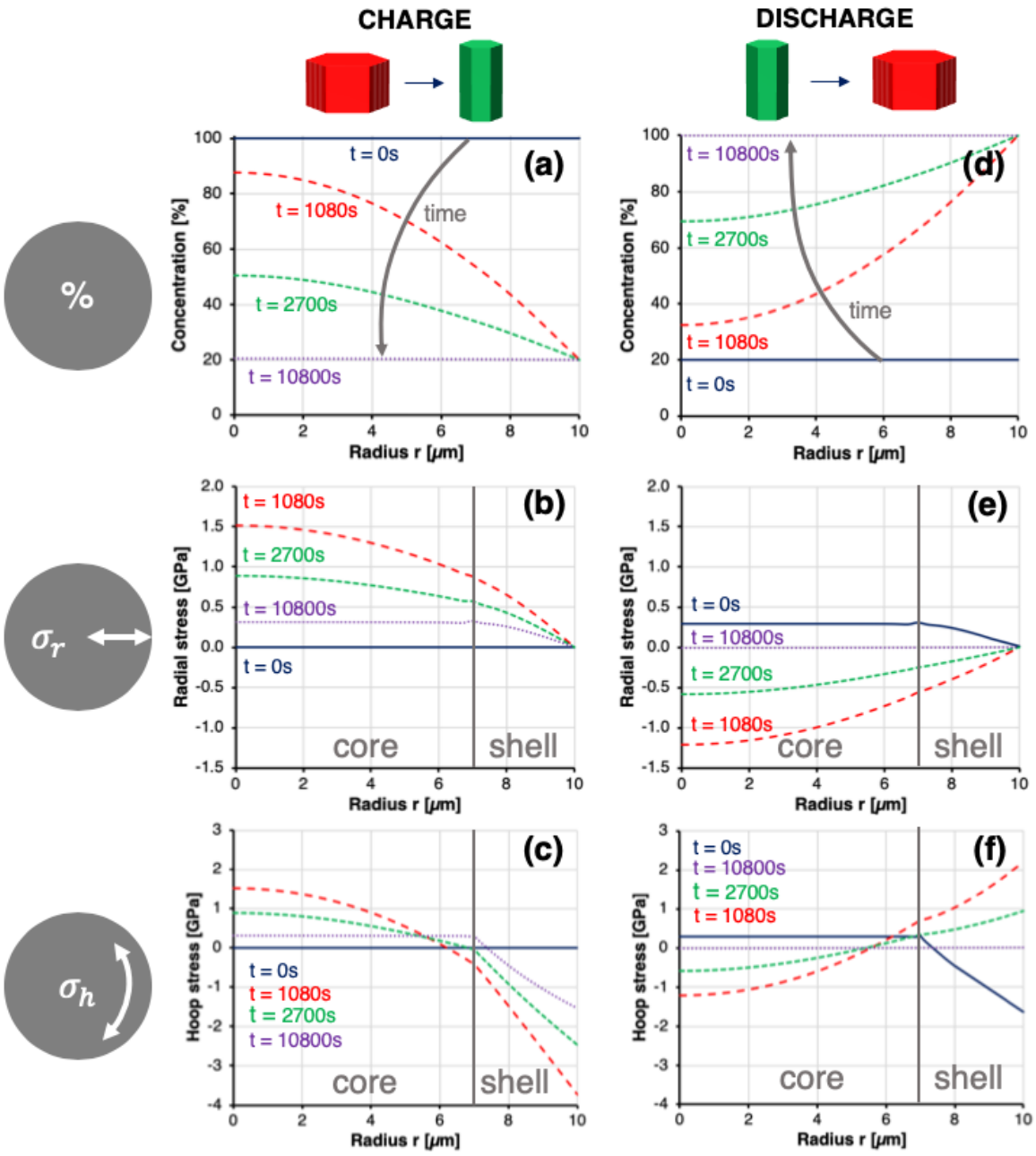


Figure 88. Solution of the coupled diffusion-strain model including concentration, radial stress and hoop stress distribution within a secondary NMC particle cycling. (a) Concentration (b) radial stress distribution and (c) hoop stress distribution during charge. (d) Concentration (e) radial stress distribution and (f) hoop stress distribution during discharge.

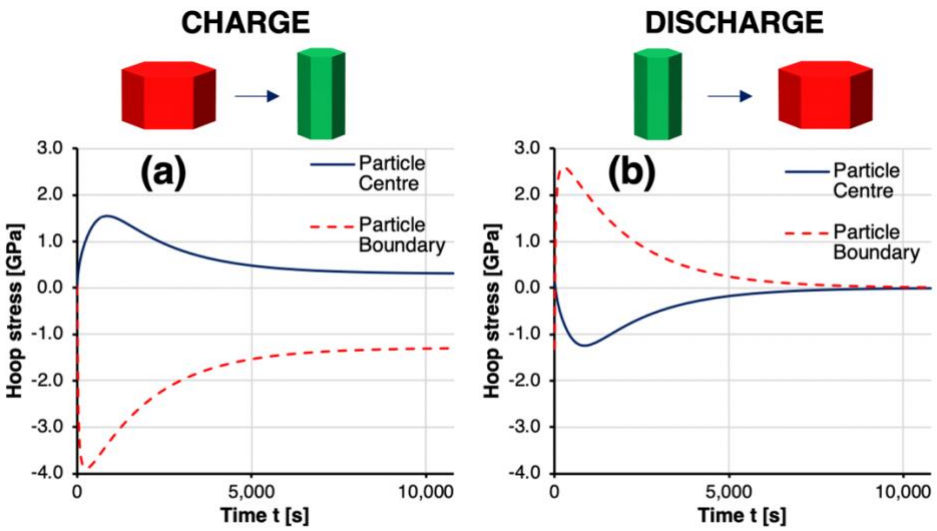


Figure 89. Simulated hoop stress evolution versus time during (a) charge and (b) discharge in the core and shell of a secondary particle.

5.1.3.6 Discussion

Combining the results of *operando* X-ray diffraction with *in situ* tomographic imaging demonstrates that a large proportion of the damage observed during the first charge stems from the electrochemical and mechanical phenomena triggered by lithium de-intercalation, especially at high charging rates. Tensile stress in the particle core balancing the compressive hoop stress caused by an expansion of the *c*-axis in the shell leads to void formation in the core, followed by radial crack growth towards the particle shell, as summarised in Figure 90. Red arrows in Figure 90d highlight that crack growth is impeded when reaching the particle shell, which further supports a change in stress along the radial direction from tensile to compressive. In addition, a decrease in the radially oriented *a*-axis lattice parameter leads to tensile residual stress in radial direction, resulting in hoop-oriented cracks between shell core and shell, which are shown in Figure 90d and indicate a reduced core-shell interfacial strength. This permits further crack propagation along the core-shell interface and partial electrochemical isolation of the Ni-rich NMC811 particle core. FEM simulation results showing the simultaneous formation of peak tensile stresses in the particle core and peak

compressive hoop stresses in the particle shell (Figure 89a) shortly after the onset of charging confirm the described mechanisms underlying the experimental observations. Tensile radial stresses along the radial direction were also confirmed by FEM simulations (Figure 88b) and support the assumptions made regarding the formation of core-shell interface cracks. Finally, the FEM results predict inverted stress values during particle discharge, which gives rise to further fracturing upon first discharge. We note that stresses in subsequent cycles are unlikely to reach identical peak stresses due to the "particle training" associated with distributed micro-cracking and pseudo-plastic deformation, which enable the particle to accommodate stresses with a smaller amount of further fragmentation.

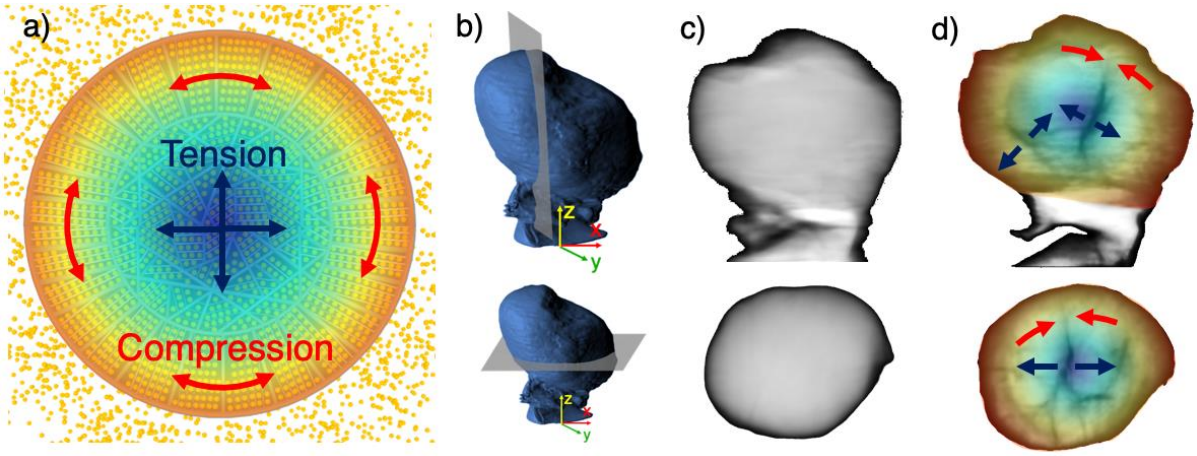


Figure 90. (a) Illustration of lattice parameter change determined by *operando* synchrotron XRD, with compressive stress in the hoop direction of the shell (red) and tensile stresses in radial direction (blue). (b) 3D tomographic reconstruction of NMC811 particle indicating cutting planes. (c) Pristine NMC811 particle cross-section. Upper picture: vertical cross-section, lower picture: horizontal cross-section. (d) NMC811 particle after single charge to 17.8% SoC. Upper picture: vertical cross-section, lower picture: horizontal cross-section. Blue arrows indicate crack growth driven by tension, red arrows indicate crack arrest by compressive hoop stress in the particle shell.

The experimental evidence presented in this work additionally points at a diffusion limit induced phase separation during the intercalation wave, resulting in a 'shrinking core' scenario, as first described by Fraggedakis et al. [223]: while XRD tomography and SEM

imaging techniques revealed crack growth along the core-shell interface, diffraction data confirmed the presence of high tensile stresses in radial direction. This mechanism can contribute to increased internal resistance in two different ways, depending on whether or not electrolyte is present in the newly formed void: 1) lacking the conducting properties of electrolyte, Li-ions can no longer be transported across the fractured part of the core-shell interface, resulting in a reduced Li-ion diffusion rate from boundary to core. 2) Crack channels connecting the void with the particle boundary are present and enable the transport of electrolyte into the newly formed void. This promotes chemical side reactions due to the exposed additional surface area, such as the formation of a Solid-Electrolyte Interface (SEI) and surface oxygen depletion, which are likely contributors to further degradation.

5.1.4 Conclusion

A novel experimental multi-technique approach for the quantitative evaluation of NMC811 particle degradation upon first charge was presented in this work. The combination of nanoscale synchrotron X-ray analysis with locally resolved structural insights obtained from t-EBSD mapping revealed the presence of a complex stress state upon de-lithiation during charge, which was shown to be strongly correlated with the designed microstructure of core-shell type particles. The locally measured strains, particularly in the particle shell, exceeded the averaged data obtained from conventional full cathode diffraction by far and highlight the drawbacks that diffusion rate optimisation of Ni-rich particles can have on their structural integrity. Based on the observed degradation mechanisms, two main fracture modes were found to underlie primary particle decohesion. To expand on the insights gained from the experimental data, a multiphysics model of the interlinked Li diffusion and strain state within a single particle was created. Excellent agreement between the experimental XRD data obtained during the onset of single particle charge as well as the structural degradation

observed by in situ ptycho-tomographic imaging and the simulation data was found. The presence of peak strains in radial and hoop direction during the early stages of charge was confirmed experimentally, while an inversion of stresses predicted by FEM suggests further significant particle degradation during the first discharge.

5.2 Improving Ultra-Fast Charging Performance and Durability of All Solid State Thin Film Li-NMC Battery-On-Chip Systems by in situ TEM Lamella Analysis

5.2.1 Introduction and Literature Review

Driven by the exponential growth of the internet of things (IoT) in the past decade [224], a significant increase in demand for communicating devices without hardwire for either power or communications has emerged. To meet this demand, specialised micro-scale, fast charging, and high-energy Li-ion batteries with carefully designed cathode and electrolyte materials are required, in addition to a highly scalable manufacturing process. In this context, thin film, solid state $LiNi_{1/3}Co_{1/3}Mn_{1/3}O_2$ (Li-NMC) batteries with Li_3PO_4 electrolyte produced by physical vapour deposition (PVD) can be employed in a wide range of emerging cutting-edge technological applications. These include, amongst others, flexible electronics and wearable medical devices [2,225,226], as well as autonomous microelectro-mechanical systems (A-MEMS), which find increasing use across biology, medicine, agriculture and environmental monitoring [227]. The key advantage of employing PVD for thin film battery manufacture include the ability to deposit all battery components directly onto a chip, thus enabling precise tailoring of the battery properties and dimensions to match application requirements.

Solid state thin film batteries overcome structural integrity challenges described in §5.1 thanks to a high level of material design control during manufacturing. This way, they enable extraordinarily high charge rates of more than 14 mA cm^{-2} (3600C) [234] thanks to two effects: firstly, the large surface-to-volume ratio present in the multilayer system results in short Lithium diffusion pathways from anode to cathode, making these systems ideal candidates for the use of solid electrolyte due to the limited effects of increased resistance as compared to liquid electrolyte. Secondly, precisely controlled PVD parameters in vacuum permit the creation of a cathode-electrolyte interface with extremely low resistance [234], thus allowing an interface with defined atomic structures. This impurity-free and atomically controlled interface lead to a full charge and discharge cycle at high current density. At the same time, the use of solid state electrolyte increases operational safety by preventing the risk of a thermal runaway [235]. Long-term cycling stability was further confirmed for the thin film batteries used in the present study, with very limited capacity loss observed over 100 cycles following an initial significant capacity drop of around 28% after the first cycle [236]. Addressing the cause of this initial capacity drop is fundamental for the further optimisation of thin film battery performance and reliability. A key aspect of microstructural control during cathode deposition is the grain orientation, which crucially impacts the Li^+ ion diffusion direction, strain accommodation, and determines the mechanisms of degradation [232]. Preferential expansion and contraction directions of the hexagonal unit cell during first charge and discharge can result in a significant stress build-up that ultimately leads to battery degradation. In this study, we correlate the cathode microstructural orientation and stress state with strain and fracture observation obtained from *in situ* lamella charging experiments. Supported by finite element simulations, our experimental results give rise to the use of grain orientation selection as a means of strain accommodation and charging performance design.

5.2.2 Materials and Methods

Due to the employed Li thin film as anode top layer, the samples were highly air and moisture sensitive. To prevent performance degradation, the thin film batteries were stored exclusively in Ar atmosphere after deposition. For the transfer between glove box and FIB-SEM instrument, a pressure-sensitive self-sealing transfer module, as shown in Figure 91 was employed [237]. Based on the motion of a piston with changing pressure differential, the transfer module automatically opens under high vacuum and closes as soon as the pressure in the chamber increases. The SEM chamber was further vented exclusively with Argon to ensure an air and moisture free environment and sample re-usability.

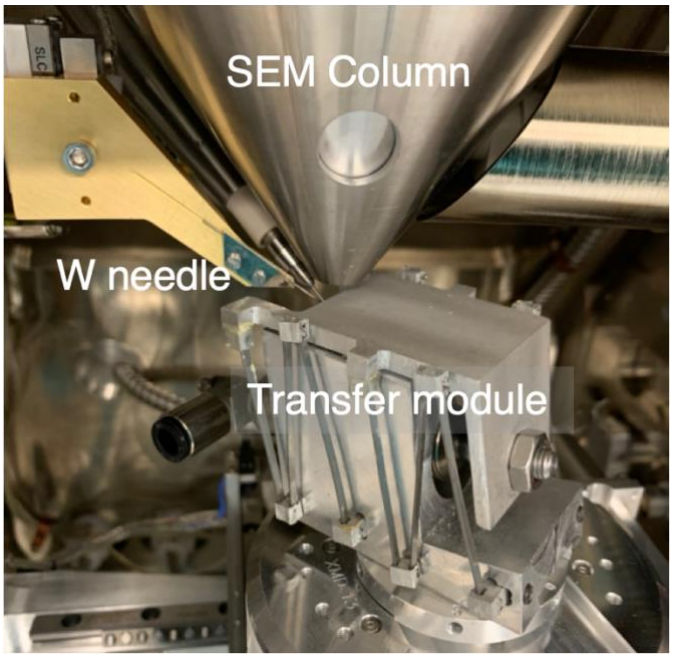


Figure 91. Self-sealing transfer module for sample transfer between glove box and FIB-SEM instrument inside the vacuum chamber. The shown geometry is used for the lamella lift-out.

5.2.2.1 All-in-vacuum deposition

Using the pulsed laser deposition (PLD) technique, $LiNi_{1/3}Mn_{1/3}Co_{1/3}O_2$ (NMC) thin films were grown on $LaNiO_3$(001) thin films on $SrTiO_3$(001) substrates. First, the substrate (5 × 5

cm^2 with a thickness of 0.5 mm) was annealed at 1100 °C for 5 min at an oxygen pressure (P_{O2}) of 1×10^{-5} Torr to prepare a step-terrace surface. Then, a $LaNiO_3$ (001) thin film, which was used as a current collector for the thin-film lithium batteries, was grown on the substrate by performing the PLD using a KrF excimer laser (wavelength of 248 nm, pulse duration of approximately 20 ns, laser fluence of 1.60 J cm^{-2}, and repetition rate of 2 Hz). A $LaNiO_3$ polycrystalline target (Toshima Manufacturing Co., Ltd.) was used for the target ablation. The substrate temperature (T_S) and P_{O2} were set as 650 °C and 2×10^{-1} Torr during the growth. An NMC thin film was deposited on the $LaNiO_3$ thin film by performing PLD by using the KrF excimer laser (laser fluence of 0.7 J cm^{-2} and repetition rate of 5 Hz). A polycrystalline target of $Li_{1.2}Ni_{1/3}Mn_{1/3}Co_{1/3}O_2$ (TOSHIMA manufacturing Co., Ltd.) was used for the target ablation. The laser intensity at a target was monitored before the growth. The target–substrate distance was approximately 47 mm. For the NMC thin-film growth, T_S and P_{O2} were set as 600 °C and 100 mTorr, respectively. Extensive X-Ray diffraction sample characterisation confirming the substrate-cathode orientation relation was carried out post deposition, as described in [236].

5.2.2.2 FIB-SEM Lamella Sectioning and *in situ* Charging

For the creation of a functioning multilayer lamella micro-battery, transmission electron microscopy (TEM) lamellae were sectioned from the multilayer battery sample using the Focused Ion Beam (FIB) of a Tescan Lyra 3XM instrument at the Multi-Beam Laboratory for Engineering Microscopy (University of Oxford, UK). After depositing a 1 µm thin protective Pt layer on the target area, a low FIB beam current of 11 nA at 30 kV accelerating voltage was chosen to avoid short circuit currents induced by the ion beam. The final dimensions of the obtained lamellae after low current ion beam surface polishing were 10x7x1 μm^2. *In situ* charging was carried out inside the FIB-SEM instrument. For this

purpose, the three top layers consisting of anode, solid electrolyte and NMC layer were partially removed to avoid short circuiting during lamella attachment. Subsequently, the substrate and current collector layers were connected to a TEM copper grid using Pt deposition. Finally, the nano-manipulator needle was attached to the protective surface Pt layer in order to establish an electric connection, as shown in Figure 96. Due to the beam sensitivity of the samples, imaging was kept to a minimum. A built-in pico-amp potentiostat normally employed for the characterisation of semiconductor materials was connected to both ends of the lamella battery and operated in potentiostatic mode. A voltage ramp from 2.5 V to 4.5 V was run for a duration of 120 s. One SEM frame before and after the charge was acquired in order to keep beam-induced damage to a minimum. A MATLAB-based Digital Image Correlation (DIC) software package [43] was used to track surface features on the NMC layer, thus permitting the calculation of x- and y- displacements, based on which horizontal and vertical strains were calculated.

5.2.2.3 Transmission EDX

Energy-dispersive X-Ray spectroscopy in transmission mode (t-EDX) is a highly effective tool for the elemental sample characterisation at high resolution, as the sample-beam interaction is limited to the lamella thickness. To enable nano-resolution analysis, thin, electron-transparent lamellae were sectioned as described in the previous section, but followed by thinning to a final thickness of around 100 nm using low current FIB polishing. T-EDX analysis was carried out at the E01 beamline at Diamond Light Source (Harwell, UK) using a JEOL ARM200CF high resolution scanning transmission electron microscope (STEM) equipped with a JEOL Centurio dual EDX detector at beam energy of 30 keV. Material maps of the region of interest (ROI) were thus acquired by counting the emitted X-Ray photons with material-characteristic wavelength.

5.2.2.4 Electron nano-diffraction

To map the lattice parameter distribution within the NMC layer in its uncharged reference state, electron nano-diffraction was carried out using the JEOL ARM200CF high resolution STEM at a beam energy of 200 keV in nanobeam electron diffraction mode. Diffraction patterns were acquired using a high speed Gatan OneView Camera. Lattice rotation mapping and lattice strain calculations were carried out using the Gatan GMS3 software package [238].

Nano-diffraction peak identification was realised using a forward simulation approach: by simulating the diffraction pattern of an $R\bar{3}m$ $LiNi_{1/3}Co_{1/3}Mn_{1/3}O_2$ unit cell using the CrystalMaker software suite [239], an exact match with the experimental pattern was achieved, thus providing full peak identification and a-axis lattice parameter information.

5.2.2.5 FIB-DIC residual stress depth profiling

The FIB-DIC ring-core method is a well-established and thoroughly verified method for the semi-destructive probing of residual stresses at the micron scale [106]. It is based on the gradual removal of material in a ring-core shape with the intermediate acquisition of SEM frames at each milling steps. Mechanically disconnecting the central material 'island' from the surrounding strain field leads to a full elastic strain relief. This can be observed by tracking surface points of the central island using DIC in post-processing at an accuracy of around $\varepsilon \approx 10^{-5}$, which can then be used to back-calculate the average residual stresses present in the probed volume prior to milling, if the elastic properties of the material are known. Recent advances in this technique allow to extract the depth-dependant stress and strain profiles in milling direction, based on the FIB-DIC strain relief profiles and by employing the eigenstrain theory [9]. Material elastic constants used for the conversion of strain into stress are presented in Table 5.

Layer	Young's Modulus E [GPa]	Poisson's Ratio
Li [240]	4.9	0.37
Li_3PO_4 [241–245]	105.9	0.25
$LiNi_{1/3}Co_{1/3}Mn_{1/3}O_2$ [219]	199.0	0.25
$LaNiO_3$ [246]	299.2	0.27
Nb:$SrTiO_3$ [247]	272.0	0.24

Table 5. Material properties used for the calculation of the residual stress depth profile based on eigenstrain analysis.

5.2.3 Results and Discussion

5.2.3.1 Compressive residual stress in the as-deposited state

Compositional characterisation of the epitaxially grown nano-multilayer battery was carried out using transmission Energy-Dispersive X-Ray Spectroscopy (t-EDX) on a thin, electron transparent lamella sectioned and polished using Focused Ion Beam (FIB). With the exception of Li that cannot be detected due to the very low characteristic X-Ray energy, the predominantly uniform distribution of other constituent elements was confirmed within the 50 nm thin $LiNi_{1/3}Co_{1/3}Mn_{1/3}O_2$ (NMC111) cathode layer lying underneath the 500 nm thick Li_3PO_4 solid electrolyte layer. The surface layer was a 1 µm thick metallic Li anode film, as revealed by Scanning Transmission Electron Microscopy (STEM) imaging. A schematic overview of the sample is shown in Figure 92a, alongside selected cross-sectional t-EDX material maps of the lamella indicated in Figure 92b.

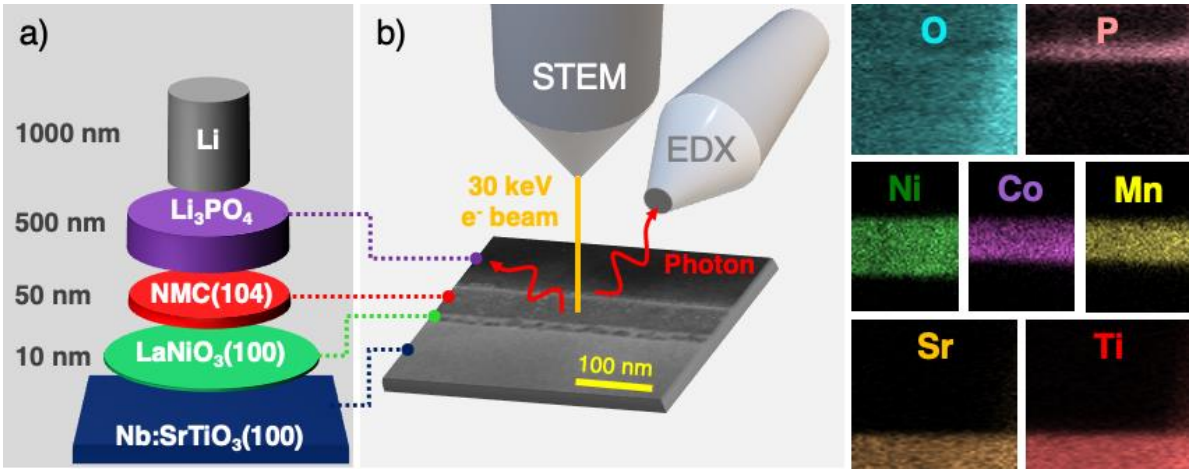


Figure 92. t-EDX layer characterisation for layer identification. a. Illustration of the individual layers composing the thin film battery. b. Selected overview of specific elemental t-EDX intensity maps colour-coded by material, showing clear layer separation.

Leveraging the nano-resolution capabilities of the FIB-DIC ring-core method, residual stress depth profiles of the multilayer battery in the as-deposited state were obtained. For this purpose, four micro ring-cores with diameters of 10 µm and 5 µm were milled into the multilayer in a step-wise manner, as shown in the micrograph in Figure 93. Before milling and in between milling steps, SEM frames were acquired which were subsequently employed for strain reconstruction using Digital Image Correlation (DIC). This well-established stress determination technique has been described in the past [44,106] and was found to provide a depth resolution of around 50 nm. The obtained x- and y-stress components are shown in Figure 93. While the out-of-plane stress component σ_{zz} can be assumed to be zero in all layers due to the proximity to a free surface, pronounced compressive residuals stresses of up to 1 GPa were found in most of the individual layers, with peak compressive stress found in the NMC111 cathode and the $LaNiO_3$ electrode. Higher compression was observed across the y-component as compared to the x-component, which is likely related to growth mechanisms of the (104) oriented NMC layer. It should be noted that the extremely low mechanical stiffness of the Li surface layer is reflected in the near zero stress value. Further to the above, it can be seen that the boundary layer within the substrate mediating between highly

compressive NMC layer and the stress-free far-field within the substrate is roughly equal in thickness to the total multilayer thickness.

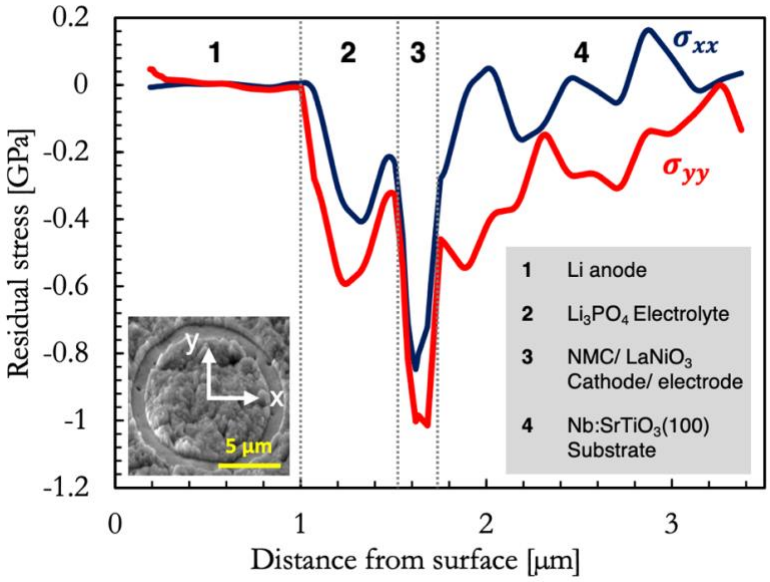


Figure 93. Residual stress depth profile obtained from depth-resolved FIB-DIC analysis with individual layer identification. Bottom left: 10 µm diameter FIB-DIC ring-core in the early stages of milling.

While the respective crystallographic layer orientation was confirmed by XRD analysis in a previous study [236], further insights into the local microstructural properties within the (104) oriented NMC111 cathode were obtained from cross-sectional electron nano-diffraction mapping of the STEM lamella at beam energy of 200 keV within the Region of Interest (ROI) highlighted in Figure 92b. A selected indexed electron nano-diffraction pattern is shown in Figure 94a. For the peak identification and related lattice parameter determination, a forward simulation approach was chosen by simulating the $R\bar{3}m$ $LiNi_{1/3}Co_{1/3}Mn_{1/3}O_2$ unit cell and finding the orientation that matched the observed diffraction pattern. Diffraction simulation along the [001] zone axis resulted in a diffraction pattern matching the Figure 94a, thus providing peak identification for all diffraction peaks. An illustration of the NMC111 unit cell is shown in Figure 94b.

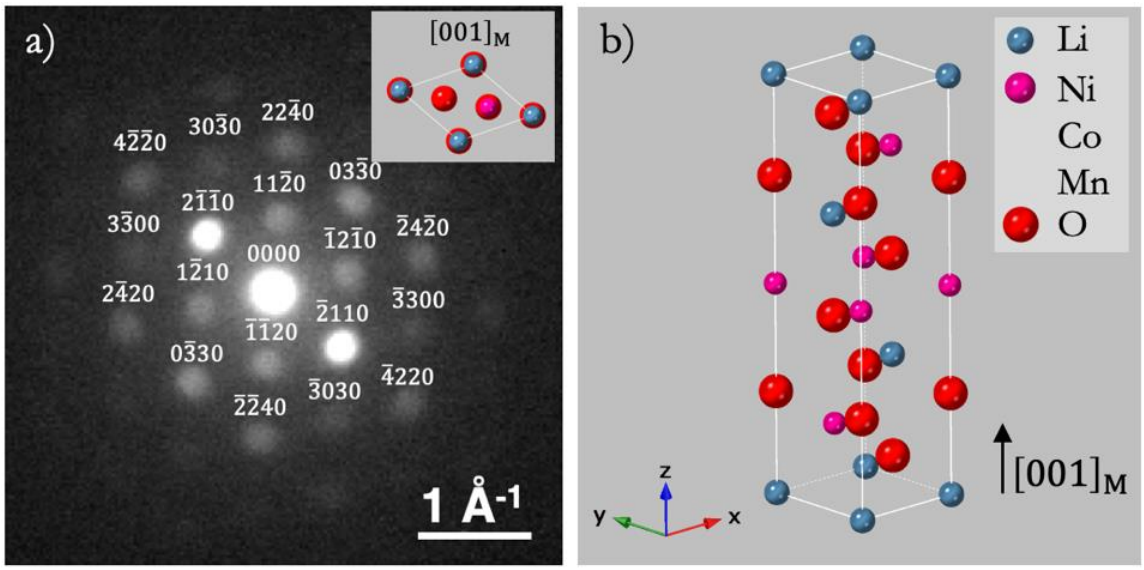


Figure 94. Electron nano-diffraction for grain orientation analysis. a. Nano-diffraction pattern obtained from TEM with identified peaks based on R$\bar{3}$m unit cell along the [001] zone axis, as indicated in the top right corner. b. Illustration of NMC R$\bar{3}$m unit cell.

Based on the cross-sectional cathode nano-diffraction maps, the local unit cell rotation around the [001] direction was determined with regard to the layer average pattern. While the STEM overview frame in Figure 92 shows a uniform cathode layer microstructure without distinct features, the misorientation map in Figure 95a reveals the presence of grains of a width comparable to the layer thickness. Low angle grain boundaries with lattice rotations of around ±5° can be clearly identified and are highlighted in red. This finding has interesting implications for the lithiation and de-lithiation behaviour during charge and discharge of the battery. Based on the assumption of uniform lithium migration across the entire cathode-electrolyte interface, a significant reduction in the interface resistance between (001) and (104)-oriented NMC111 film orientation was confirmed in a previous study [236]. In fact, small differences in grain orientation at grain boundaries (GB) may distort significantly the local lithium exchange dynamics and result in a slight reduction in the attainable charge rate in comparison to a highly ordered single crystalline layer.

In a further investigation, the nominal a-axis strain distribution at the grain level based on the layer average a-axis lattice parameter of 2.9Å was calculated for a line profile crossing two grains, as shown in Figure 95b. Clear differences between the lattice parameter values within the grain and at the boundary are visible that may be associated with intragranular variation in lithiation state of the pristine battery. As Li^+ intercalation in NMC111 materials is associated with c-axis contraction and inelastic a-axis expansion [248], the grain material can be assumed to be fully lithiated, as opposed to the grain boundary, which appears to be partly de-lithiated. Strain differences of up to 1.5% between grain and GB were found. Based on previously obtained *operando* lattice parameter data for NMC cathode material [232], it can be estimated that the a-axis lattice expansion of 1% is caused by a 1.6% c-axis contraction.

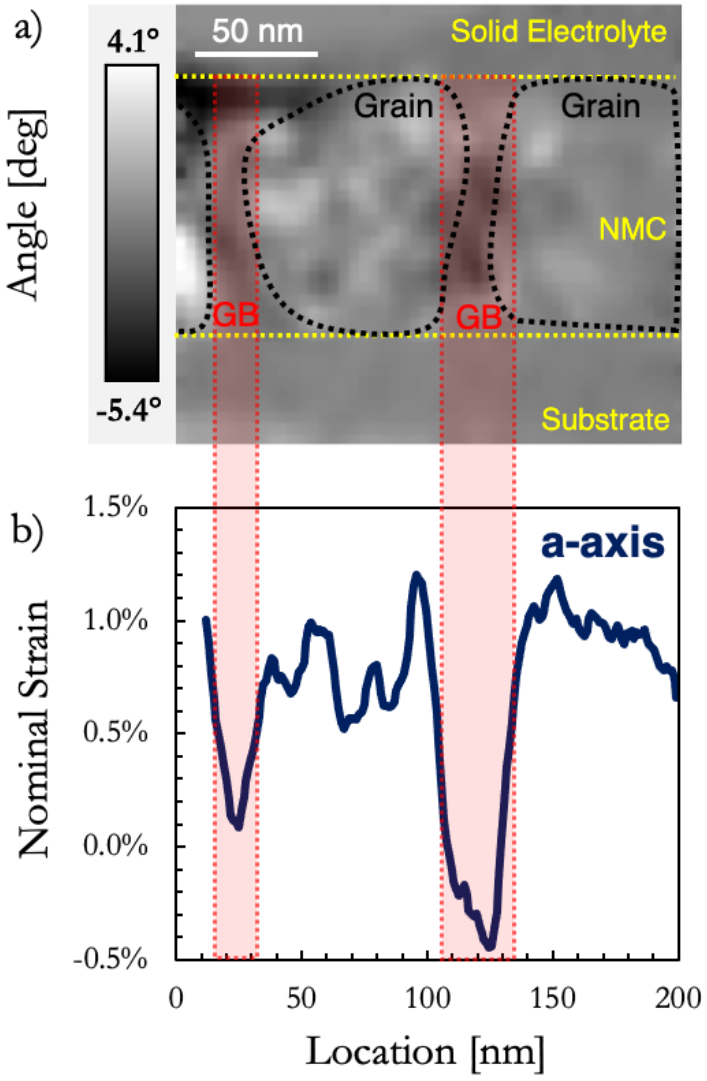


Figure 95a. Misorientation angle within NMC layer with respect to layer average clearly revealing low angle grain boundaries highlighted in red. Individual NMC grains are highlighted by black dashed line. b. Line average of nominal a-axis strain across two grains shown in a) with respect to layer average value highlighting strain gradients between grains and grain boundaries in the as-deposited state.

5.2.3.2 Strain evolution during *in situ* lamella charging

To obtain experimental insights into the de-lithiation induced cathode deformation, a 10x7x1 μm^3 lamella sample was extracted from the multilayer battery by FIB milling and polishing. A slot was created using FIB to prevent short circuit currents between anode and cathode as shown by the red arrow in Figure 96a. The cathode current collector layer was attached to a

TEM copper grid using the Pt deposition system, which was connected to the electrode of a pico-amp potentiostat. Subsequently, the W nano-manipulator needle was connected as counter electrode to the Pt surface layer deposited on top of the Li anode, as shown in Figure 96a. As a result, a fully functioning micro-battery was electrically connected to a pico-ampere potentiostat that was integrated into the FIB-SEM instrument. As the sample was particularly beam sensitive, only very few images were acquired during sample preparation and mounting at low resolution, while only one high resolution SEM image was acquired before and after charging, respectively. While this procedure prevented the time-resolved *operando* analysis of strains, it enabled a comparison of the horizontal and vertical cathode strain before and after de-lithiation. The built-in potentiostat could only be operated in potentiostatic mode by prescribing a voltage ramp. A voltage ramp from 2 V to 4.5 V was programmed for a duration of 120 s, during which the current was recorded as shown in the graph in Figure 96a and after which the voltage was held at 5V.

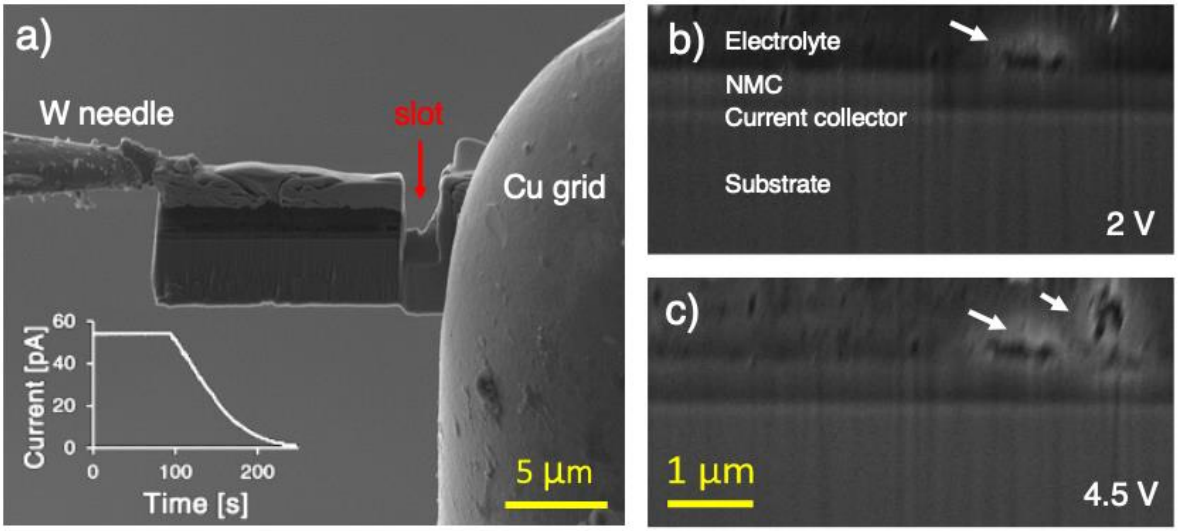


Figure 96. In situ lamella charging. a. SEM micrograph of the lamella battery with electric connection acquired after the charging experiment due to sample beam sensitivity. Bottom left: charging current versus time following voltage ramp. b. SEM micrograph of the lamella battery before and c. after charge.

DIC software [43] was subsequently employed to track surface contrast features arising from FIB polishing, also known as 'FIB curtaining', which can be seen as vertical lines in the micrographs shown in Figure 96b, c. The horizontal and vertical strain components obtained from DIC analysis were $\varepsilon_{xx} = 0.22 \pm 0.03\%$ and $\varepsilon_{zz} = 2.35 \pm 0.18\%$, respectively, while the shear strain component was determined from DIC as $\varepsilon_{xz} = -2.69 \pm 0.21\%$. Based on this data, principal strains were determined as $\varepsilon_1 = 4.18\%$ and $\varepsilon_2 = -1.61\%$, with a principal angle $\theta_P = 55.8°$. These results not only match the expected Li^+ diffusion direction of the (104) oriented cathode grains, but also indicate a significant c-axis expansion perpendicular to and a-axis contraction in the direction of the Li^+ diffusion upon de-lithiation. These results are summarised in Figure 97.

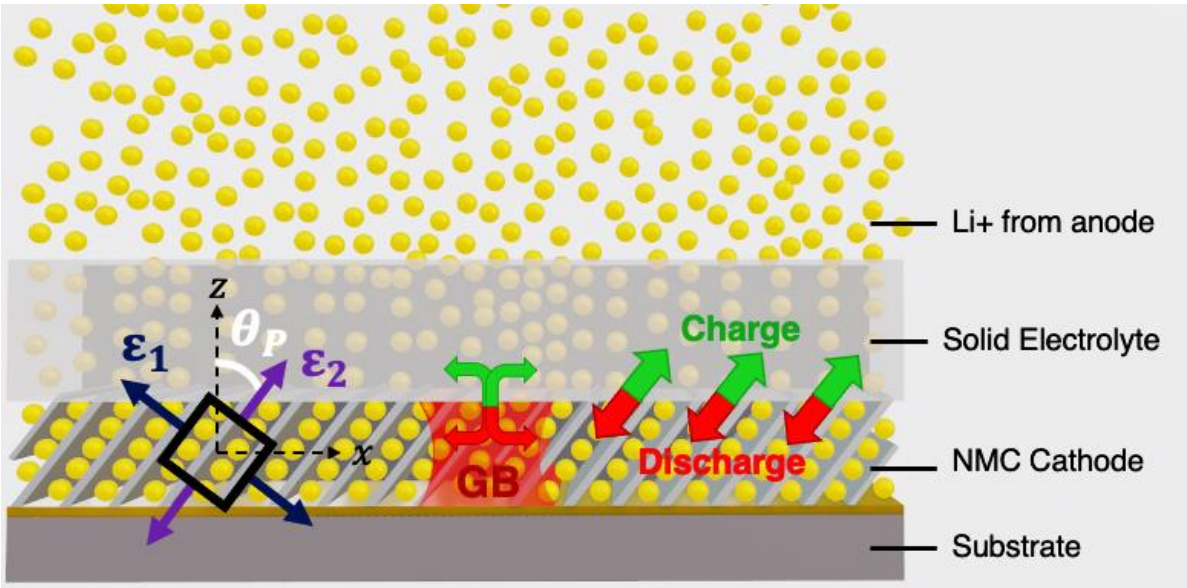


Figure 97. Illustration of the interaction between lithium migration, strain and microstructure. Principal strains and principal angle are illustrated on the left.

While the multilayer expansion is not constrained in the vertical direction, horizontal displacement and thus strain is hindered by the interlayer adhesion between solid electrolyte, cathode, and current collector. A free-standing, unconstrained NMC111 (104) layer would expand nearly equibiaxially in x- and y- direction. The presence of constraint resulted in the

expansion in horizontal direction being hindered, giving rise to stress. Based on this assumption and using typical stiffness values for the material, the de-lithiation induced stress can be quantified at a level of around -4 GPa compression. As a result, stress interaction between the compressed NMC111 layer and the surrounding layers leads to tensile residual stress being introduced in the neighbouring layers and particularly in the vicinity of layer interfaces. Stresses of this magnitude are detrimental for a nano-multilayer system composed of brittle oxides and result in failure. Indicators confirming this assumption were observed in form of newly formed voids at the NMC111-solid electrolyte interface, as can be seen by comparing Figure 96b and c, which show the micro-battery before and after charge, respectively. While a minor void identified before the first charge might have been caused by a sudden change in voltage due to the connection of the electrodes to the potentiostat, a clear increase in pre-existing void size should be noted, along with a newly formed crack. The location and shape of the newly formed crack support the hypothesis of strain-induced damage caused by cathode expansion during lithium de-intercalation upon charge. The large expansion in the vertical direction further aligns with literature data on the c-axis lattice parameter strain during charge [248]. It can be hypothesised that the observed void formation results in an increase in the interfacial resistance, which is consistent with the response observed during previous experiments [236]. The largest drop in charging current was observed between the first and second charge cycle, which aligns well with the observed mechanical degradation: after the initial crack and void formation, expansion and contraction of the cathode layer in subsequent cycles does not induce further microstructural damage of comparable magnitude, sine the material has been permanently modified by plastic deformation and voiding, leading to improved accommodation and a reduction in stiffness.

5.2.4 Modelling and Simulation

To enable a time resolved understanding of the strain and stress build-up in thin film batteries during de-lithiation upon charge, a coupled diffusion-strain simulation was implemented in COMSOL Multiphysics®, which combined the solution of a generalised diffusion equation with sequentially coupled strain and stress analysis. More precisely, the model consisted of solving the diffusion equation for a Li-concentration gradient within the NMC111 layer using a prescribed boundary concentration. In a second step, the calculated concentration was related to strain in prescribed expansion directions based on the known crystallographic (104) and (001) orientation, and finally converted into stress. A lithium concentration of 20% was assumed for the fully charged cathode, while a lithium saturation of 100% was assumed for the fully discharged state. The material parameters used are listed in Table 5.

Figure 98 shows the Li distribution within the cathode, as well as the horizontal stress and vertical strain for both (104) and (001) oriented cathode material. It can be seen that for a single charge simulated at a charge rate 3600C, cathode de-lithiation duration of 0.5 s was obtained. Experiments at of 14 $mAcm^{-2}$ (3600C) have been conducted on the present samples in previous studies [234] and are of particular interest for the study of microstructural strain and degradation, due to the resulting high stress and strain gradients, which have been quantified in this simulation. As the lithium diffusion mechanism through direct intercalation in (104) oriented cathode material versus GB dominated horizontal diffusion in (001) oriented NMC111 was not accounted for in the present model, identical de-lithiation curves can be seen in Figure 98a, b. When looking at the resulting horizontal stress, however, large differences in stress accommodation can be observed between the two analysed microstructures. (104) oriented material expands in c-axis direction during charge, resulting in equal horizontal and vertical expansion. Due to the multilayer constraint, free expansion is only possible in the vertical direction, resulting in a strain of around 1.5%, as shown in Figure

98f. The location of the cathode is shaded red. The horizontal strain component, however, is hindered by interface cohesion and results in an in-plane horizontal compressive stress of around -3 GPa, as can be seen in Figure 98d. Balancing tensile residual stresses in the adjacent layers reach values of up to around 0.4 GPa, which can be detrimental for the structural integrity of nanostructured coatings.

Significantly different results were obtained for (100) oriented material, as the de-lithiation resulted in vertical expansion of the c-axis and horizontal contraction of the a-axis. Simulated horizontal stresses were therefore tensile, reaching values of up to 0.8 GPa as shown in Figure 98c. The unconstrained vertical strain reached around 2.2% as can be seen in Figure 98e. Overall, the simulation results indicated large in-plane tensile stresses for (001) oriented NMC111 cathodes, while highly compressive stresses were identified in (104) oriented cathodes.

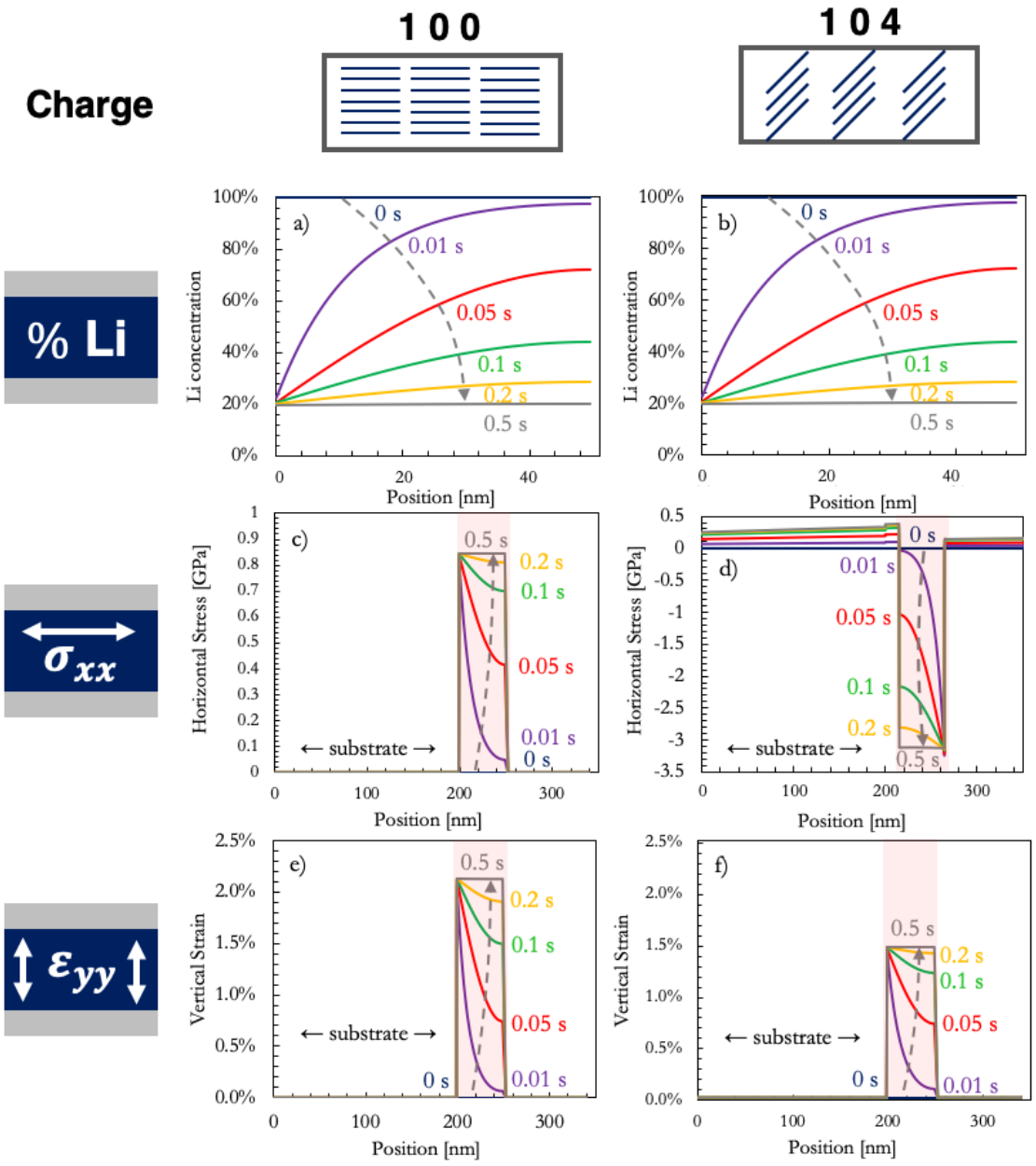


Figure 98. a,b. COMSOL simulation results showing the lithiation state versus time within the NMC layer for the (100) and (104) oriented cathode. c,d. Horizontal stress within the NMC layer for (100) and (104) oriented cathode. e,f. Vertical strain within the NMC layer for (100) and (104) oriented cathode.

5.2.5 Discussion

Combining electron nano-diffraction, FIB-DIC depth profiling and *in situ* lamella charging with DIC and multiphysics modelling clearly demonstrated that the choice of grain orientation in thin film cathodes has fundamental implications for the strain fields and degradation that unfurl in the entire solid state battery upon charging. Electron nano-diffraction revealed the strain accommodation mechanisms in the as-deposited samples with large strain variations between grains and grain boundaries, in which the grain boundaries act as strain buffers accommodating the lithium-induced a-axis lattice expansion. FIB-DIC depth profiling further showed that the as-deposited samples are under large compressive stresses, thus confirming the local nano-diffraction observations. *In situ* lamella charging in combination with DIC helped quantifying the horizontal and vertical strain within the NMC111 layer, which showed a significant expansion in the vertical direction and stress build-up in the horizontal direction.

The observed interface crack and void growth further supported the described mechanism as a significant driver underlying the increase of the cathode-electrolyte interfacial resistance between the first and second charge cycle. The formation mechanism of these defects was identified as stress accommodation by the solid electrolyte, resulting in horizontal tensile strain build-up counteracting the deposition-induced compressive residual stress and resulting in micro-scale fracture. Multiphysics simulation of the de-lithiation process further confirmed the experimental observation and showed close agreement with the experimental observations. Based on the findings described in the present work, a (104) NMC111 grain orientation appears more favourable both for moderating the interfacial resistance and due to the lack of tensile stress which was found to arise in (001)-oriented cathode material.

To prevent crack growth at the cathode-electrolyte interface, the compressive residual stress within the solid electrolyte layer could be increased, therefore ensuring mechanical expansion and contraction within the elastic regime of the solid electrolyte.

5.2.6 Conclusion

A novel experimental combination of *in situ* solid state battery lamella charging combined with Digital Image Correlation and electron nano-diffraction was used for the quantitative evaluation of strains arising within thin film batteries during charge and discharge. The obtained data was correlated with the as-deposited battery state and crystallographic orientation of the cathode, to develop in-depth understanding of the mechanisms leading to interface degradation and loss of capacity. By means of finite element simulation it was demonstrated that the horizontally constrained expansion of the (100) oriented cathode layer results in the formation of tensile stress within the cathode layer, giving rise to increased crack and void formation in the solid electrolyte layer, while the (104) oriented cathode was shown to have superior charging rates and mechanical stability. This investigation demonstrates that the modification and control of the residual stress in the cathode layer can be used to mitigate the degradation upon first charge, thus preventing significant loss of capacity that may reach up to 28%.

6 Conclusions

In this chapter, I draw conclusions from the developments and results in this thesis regarding the three major areas of study reported:

1) Evaluation and origin of mechanical properties of Cu/W nano-multilayers
2) Origins of thermal and diffusion properties in Cu/W nano-multilayers
3) Diffusion and transport properties in a single NMC811 cathode particle and thin film solid state batteries

Here I pay particular attention to the difficulties encountered in the course of research, the limitations that arose as a consequence, and offer my thoughts about the likely future developments to improve the insights that could be derived from the methodology presented.

6.1 Evaluation and origin of mechanical properties of Cu/W nano-multilayers

The results reported in this thesis concern two main aspects involving the mechanical properties of thin films and multilayers: the microstructural-mechanical property interrelationships, and the substrate-coating mechanical interaction properties. Starting with the microstructural-mechanical properties, it was identified that the effect of energetic particle bombardment during magnetron and ion beam deposition on the microstructure can be largely controlled by working gas pressure variation. Depending on this microstructural effect, different defect populations and crystallographic orientations arise that in turn control the residual stress within individual layers. The high resolution of residual stress depth profiling reported here enabled the identification of local peak stresses, which are of significant importance for enhanced reliability in thin films and multilayers. A limitation of the performed analyses was the “meso-scale” resolution of experimental techniques, i.e. the

determination of residual stresses at the depth resolution of around 50 nm, along with the averaged information about texture and grain size. However, the attempted analysis at the atomic lattice resolution using HR-TEM was not available to confirm the presence of all identified defect populations.

For the analysis of strain transfer mechanisms between compliant polymer substrates and coatings, a new model of shear-lag type was proposed for the estimation of coating strains as a function of substrate stretch. Based on the presented findings, an explanation for the observed complex fracture pattern under uniaxial load was developed. The capacity of the compliant substrate to undergo large deformation was further leveraged to develop a new method for the determination of the Mode I critical stress intensity factor in thin films and nano-multilayers – a parameter of high relevance for advanced engineering applications. To the best of the author's knowledge, the method presented here is the first published account of this approach that enables simple determination of K_{IC} on compliant substrates without significant sample preparation. Key limitations for the presented shear-lag model is the the uniaxial loading assumption that may be seen as a significant simplification of the more realistic equi-biaxial loading as a representation of substrate thermal expansion effect, or the assumption of arbitrary in-plane loading to cover all possible cases. An important requirement for accurate measurement using the newly developed method for K_{IC} determination is the presence of a highly compliant polymer substrate, as local substrate deformation is required to allow unhindered crack opening.

6.2 Origins of thermal and diffusion properties in Cu/W nano-multilayers

With the help of Transient Grating Spectroscopy, clear evidence was obtained for the ability to control thermal diffusivity in nano-multilayer coatings through process conditions. Combined with thorough microstructural analysis, insights into the origins of thermal

properties were presented and the latter were linked with the mechanical properties analysed in the previous chapter. Complex defect populations arising from deposition parameter variation were identified as drivers for both residual stress and thermal diffusivity. This important result enables the use of thermal and mechanical properties in thin films and multilayer coatings as material design objectives to allow careful material tailoring to specific applications depending on mechanical and thermal stability requirements. The observed inverse relationship between thermal diffusivity and residual stress highlighted that process control could allow obtaining either high thermal diffusivity or strong compressive residual stress in coatings, but not likely both.

In addition to the thermal diffusivity property analysis, a theoretical and experimental understanding of the thermo-mechanical stability and degradation mechanisms in Cu/W nano-multilayer coatings on Si substrate was developed. It was identified that the complex defect structure arising from Ion Beam Deposition along with the highly compressive residual stresses lead to the large-scale transport of Cu ions towards the substrate and ultimately results in complete structural breakdown. Using a novel combination of advanced synchrotron techniques, nano-scale diffusion processes and structural evolution were revealed. The study was complemented by a proposed theoretical model that was validated by the experimental observations. A limitation of this study were associated with fixed conditions of Ion Beam Deposition which did not permit chamber pressure variation. It was therefore not possible to compare the onset and structural breakdown temperatures of different samples deposited under varying conditions.

6.3 Diffusion and transport properties in a single NMC811 cathode particle and thin film solid state batteries

To apply the findings and the methodological approaches developed in the previous sections to a novel, high potential and cutting-edge application, thin film, solid state batteries were selected for *in situ* characterisation. To build up fundamental understanding of the drivers of Li-ion cathode material degradation during charge and discharge, conventional cathode secondary micro-particles were charged in a newly designed *operando* synchrotron setup. Combined with microstructural insights, it was possible to identify clearly how local grain orientation, transient Li-ion diffusion and mechanical degradation are linked. Based on this knowledge, novel all solid-state thin film batteries were analysed in a first of its kind study using Digital Image Correlation for the charge-induced strain quantification. Li-ion batteries with carefully optimised cathode-solid electrolyte interfaces and epitaxially grown cathode grains of controlled orientation were found to develop cracking at the electrolyte interface as a consequence of Lithium de-intercalation. This key result provided important insights for the future optimisation of these systems. A key limitation was the fact that this study was restricted to the development of fundamental approaches and feasibility demonstration for better understanding of the main mechanisms. However, iterative refinement of thin film cathode deposition conditions to optimise the mechanical properties was not possible.

6.4 Future Work

This thesis was deliberately and purposely focused on applicable strategies, methods and models for the control of microstructure, residual stress and thermal diffusivity in nano-multilayer coatings. In addition, one advanced technological application of nano-multilayers was chosen for demonstration, so as to showcase the importance of in-depth understanding of the relation between process control, microstructural evolution, diffusion properties and mechanical degradation. Based on these three key topics, I would like to highlight the

following opportunities for further research that are in my opinion are most promising for high-impact work:

1) Microstructural-Mechanical Properties: significant impact is expected for further lattice-resolution analysis of defect structures in thin films and nano-multilayer coatings deposited at varying magnetron chamber pressures. It would be particularly interesting to identify the presence of self-interstitials and vacancies in order to confirm the presence of defects predicted theoretically. Further use of STEM-enabled electron nano-diffraction depth profiling along a nano-multilayer cross-section would reveal local lattice strains and grain orientations and deliver further insights into the link between deposition conditions and residual stress state.
2) Thermal Properties: this study has purposely selected immiscible nano-multilayer Cu/W structures as model systems and due to the relevance of these material systems for numerous applications e.g. in micro-electronics. Quantifying the influence of residual stress on the thermal degradation onset temperature would be particularly interesting in order to confirm the thermo-mechanical diffusion model presented in chapter 4.2 of this thesis. Beyond immiscible materials, significant insights into nano-metallurgical processes are expected to be possible by depositing and heating nano-multilayers with miscible elements, thus resulting in alloy formation. A particularly interesting study would be the parallel observation of phase transformation and diffusion processes by combining GISAXS and WAXS analysis, which would provide information about the evolution of layer thickness and density, on the one hand, the phase composition on the other, and thus give a rounded picture of alloying dynamics.
3) Thin Film, All Solid-State Batteries: due to the combination of their high innovation potential and the relatively small amount of literature in this research area, much

interesting work remains to be carried out. As was shown in this thesis, understanding and optimising micro-structural-mechanical aspects of Li+ intercalation and de-intercalation are crucial for enhancing electrochemical battery performance. A significant step towards more reliable thin film batteries would be the application of results from the Cu/W nano-multilayers studied in the scope of this thesis. Careful design of the residual stress profiles within nano-multilayer batteries can be used to pre-strain the cathode and electrolyte layer and to avoid fracture and crack growth during charge and discharge. Introducing compressive residual stress in the solid electrolyte layer would for instance reduce the effect of interfacial crack formation during charge. Finally, a crucial understanding of the Lithium diffusion dynamics at the cathode-solid electrolyte interface needs to be developed. For this purpose, cryo-FIB can be employed to create a thin TEM lamella, which can be charged at the E01 beamline at Diamond Light Source to observe Lithium intercalation at lattice resolution *operando*.

References

[1] H. Frey, Applications and developments of thin film technology, in: Handb. Thin-Film Technol., Springer Berlin Heidelberg, 2015: pp. 1–3. doi:10.1007/978-3-642-05430-3_1.

[2] M. Sugiyama, T. Uemura, M. Kondo, M. Akiyama, N. Namba, S. Yoshimoto, Y. Noda, T. Araki, T. Sekitani, An ultraflexible organic differential amplifier for recording electrocardiograms, Nat. Electron. 2 (2019) 351–360. doi:10.1038/s41928-019-0283-5.

[3] EUV mirrors/X-ray mirrors | NTT-AT, (n.d.). https://www.ntt-at.com/product/multilayer/ (accessed January 23, 2021).

[4] New lithium thin-film battery - Alcom, (n.d.). https://alcom.be/shop/product-group/power-emc/new-lithium-thin-film-battery/ (accessed January 23, 2021).

[5] S. Melchoir-Bonnet, The Mirror: A History, Taylor & Francis, 2014.

[6] J.E. Greene, Tracing the recorded history of thin-film sputter deposition: From the 1800s to 2017, J. Vac. Sci. Technol. A Vacuum, Surfaces, Film. 35 (2017) 05C204. doi:10.1116/1.4998940.

[7] A.A. Griffith, The Phenomena of Rupture and Flow in Solids, (1920) 163–198. doi:10.1098/rspa.1952.0029.

[8] G.R. Irwin, Analysis of Stresses and Strains near the End of a Crack Traversing a Plate, J. Appl. Mech. ASME. E24 (1957) 351–369.

[9] A.M. Korsunsky, A Teaching Essay on Residual Stresses and Eigenstrains, Butterworth-Heinemann, 2017.

[10] N. Kaiser, Review of the fundamentals of thin-film growth, Appl. Opt. 41 (2002) 3053. doi:10.1364/ao.41.003053.

[11] M. Benelmekki, M. Benelmekki, Two-dimensional nanostructures, in: Nanomaterials, IOP Publishing, 2019. doi:10.1088/2053-2571/ab126dch5.

[12] F.C. Matacotta, G. Ottaviani, P.B. BARNA, M. ADAMIK, Growth Mechanisms of Polycrystalline Thin Films, Sci. Technol. Thin Film. (1995) 1–28. doi:10.1142/9789814261425_0001.

[13] B.E. Belkerk, S. Bensalem, A. Soussou, M. Carette, H. Al Brithen, M.A. Djouadi, Y. Scudeller, Substrate-dependent thermal conductivity of aluminum nitride thin-films processed at low temperature, Appl. Phys. Lett. 105 (2014) 221905. doi:10.1063/1.4903220.

[14] J. Martan, N. Semmar, C. Boulmer-Leborgne, P. Plantin, E. Le Menn, Thermal Characterization of Tungsten Thin Films by Pulsed Photothermal Radiometry, Nanoscale Microscale Thermophys. Eng. 10 (2006) 333–344. doi:10.1080/15567260601009189.

[15] C. Duquenne, Thermal conductivity of aluminium nitride thin films prepared by reactive magnetron sputtering, (2012). doi:10.1088/0022-3727/45/1/015301.

[16] L. Dong, G. Wei, T. Cheng, J. Tang, X. Ye, M. Hong, L. Hu, R. Yin, S. Zhao, G. Cai, Y. Shi, B. Pan, C. Jiang, F. Ren, Thermal Conductivity, Electrical Resistivity, and Microstructure of Cu/W Multilayered Nanofilms, ACS Appl. Mater. Interfaces. 12 (2020) 8886–8896. doi:10.1021/acsami.9b21182.

[17] A.M. Korsunsky, A Critical Discussion of the sin2ψ Stress Measurement Technique, Mater. Sci. Forum. 571–572 (2008) 219–224. doi:10.4028/www.scientific.net/MSF.571-572.219.

[18] J. Keckes, M. Bartosik, R. Daniel, C. Mitterer, G. Maier, W. Ecker, J. Vila-Comamala, C. David, S. Schoeder, M. Burghammer, X-ray nanodiffraction reveals strain and microstructure evolution in nanocrystalline thin films, Scr. Mater. 67 (2012) 748–751.

doi:10.1016/j.scriptamat.2012.07.034.
[19] R. Treml, D. Kozic, J. Zechner, X. Maeder, B. Sartory, H.-P. Gänser, R. Schöngrundner, J. Michler, R. Brunner, D. Kiener, High resolution determination of local residual stress gradients in single- and multilayer thin film systems, Acta Mater. 103 (2016) 616–623. doi:10.1016/j.actamat.2015.10.044.
[20] M. Sebastiani, K.E. Johanns, E.G. Herbert, G.M. Pharr, Measurement of fracture toughness by nanoindentation methods: Recent advances and future challenges, Curr. Opin. Solid State Mater. Sci. 19 (2015) 324–333. doi:10.1016/j.cossms.2015.04.003.
[21] C. Bundesmann, H. Neumann, Tutorial: The systematics of ion beam sputtering for deposition of thin films with tailored properties, J. Appl. Phys. 124 (2018) 231102. doi:10.1063/1.5054046.
[22] A. Tiwari, Handbook of antimicrobial coatings, Elsevier, 2017. doi:10.1016/C2016-0-01441-9.
[23] N.P. Barradas, N. Added, W.M. Arnoldbik, I. Bogdanović-Radović, W. Bohne, S. Cardoso, C. Danner, N. Dytlewski, P.P. Freitas, M. Jakšić, C. Jeynes, C. Krug, W.N. Lennard, S. Lindner, C. Linsmeier, Z. Medunić, P. Pelicon, R.P. Pezzi, C. Radtke, J. Ërhrich, T. Sajavaara, T.D.M. Salgado, F.C. Stedile, M.H. Tabacniks, I. Vickridge, A round robin characterisation of the thickness and composition of thin to ultra-thin AlNO films, Nucl. Instruments Methods Phys. Res. Sect. B Beam Interact. with Mater. Atoms. 227 (2005) 397–419. doi:10.1016/j.nimb.2004.08.021.
[24] A. De Bonis, R. Teghil, Ultra-short pulsed laser deposition of oxides, borides and carbides of transition elements, Coatings. 10 (2020) 501. doi:10.3390/COATINGS10050501.
[25] B.J. Inkson, 2 - Scanning electron microscopy (SEM) and transmission electron microscopy (TEM) for materials characterization, in: G. Hübschen, I. Altpeter, R. Tschuncky, H.-G. Herrmann (Eds.), Mater. Charact. Using Nondestruct. Eval. Methods, Woodhead Publishing, 2016: pp. 17–43. doi:https://doi.org/10.1016/B978-0-08-100040-3.00002-X.
[26] J. Gierak, Focused Ion Beam nano-patterning from traditional applications to single ion implantation perspectives, Nanofabrication. 1 (2014). doi:10.2478/nanofab-2014-0004.
[27] S.P. Lynch, Metallographic and fractographic techniques for characterising and understanding hydrogen-assisted cracking of metals, in: R.P. Gangloff, B.P. Somerday (Eds.), Gaseous Hydrog. Embrittlement Mater. Energy Technol., Woodhead Publishing, 2012: pp. 274–346. doi:https://doi.org/10.1533/9780857093899.2.274.
[28] A.J. Schwartz, M. Kumar, B.L. Adams, D.P. Field, Electron backscatter diffraction in materials science, Springer US, 2009. doi:10.1007/978-0-387-88136-2.
[29] M. Cotte, A. Genty-Vincent, K. Janssens, J. Susini, Applications of synchrotron X-ray nano-probes in the field of cultural heritage, Comptes Rendus Phys. 19 (2018) 575–588. doi:10.1016/j.crhy.2018.07.002.
[30] C. Stan, C. Beavers, M. Kunz, N. Tamura, X-Ray Diffraction under Extreme Conditions at the Advanced Light Source, Quantum Beam Sci. 2 (2018) 4. doi:10.3390/qubs2010004.
[31] Powder Diffraction for industry | Diamond Light Source - - Diamond Light Source, (n.d.). https://www.diamond.ac.uk/industry/Industry-News/Latest-News/Synchrotron-Industry-News-Powder-Diffraction.html (accessed November 11, 2020).
[32] J. Filik, A.W. Ashton, P.C.Y. Chang, P.A. Chater, S.J. Day, M. Drakopoulos, M.W. Gerring, M.L. Hart, O. V. Magdysyuk, S. Michalik, A. Smith, C.C. Tang, N.J. Terrill, M.T. Wharmby, H. Wilhelm, Processing two-dimensional X-ray diffraction and small-angle scattering data in DAWN 2, J. Appl. Crystallogr. 50 (2017) 959–966.

doi:10.1107/S1600576717004708.
[33] G. Santoro, S. Yu, Grazing Incidence Small Angle X-Ray Scattering as a Tool for In-Situ Time-Resolved Studies, X-Ray Scattering, Intech Open (2017). doi:10.5772/64877.
[34] G. Pospelov, W. Van Herck, J. Burle, J.M.C. Loaiza, C. Durniak, J.M. Fisher, M. Ganeva, D. Yurov, J. Wuttke, BornAgain: Software for simulating and fitting grazing-incidence small-angle scattering, J. Appl. Crystallogr. 53 (2020) 262–276. doi:10.1107/S1600576719016789.
[35] BornAgain — Software for simulating and fitting X-ray and neutron small-angle scattering at grazing incidence, (2020). https://www.bornagainproject.org.
[36] GISAXS Form Factors - Overview, (n.d.). https://www.bornagainproject.org/documentation/examples/embedded-particles/all-formfactors/ (accessed November 12, 2020).
[37] P. Li, A. Maiden, Multi-slice ptychographic tomography, Sci. Rep. 8 (2018) 1–10. doi:10.1038/s41598-018-20530-x.
[38] M. Marciszko, A. Baczmański, N. Zazi, J.P. Chopart, A. Lodini, K. Wierzbanowski, Stress in aluminium alloys measured using Göbel mirror as a primary beam optics of X-ray diffractometer, in: Mater. Sci. Forum, Trans Tech Publications Ltd, 2011: pp. 393–398. doi:10.4028/www.scientific.net/MSF.681.393.
[39] C. Mocuta, S. Stanescu, M. Gallard, A. Barbier, A. Dawiec, B. Kedjar, N. Leclercq, D. Thiaudiere, Fast X-ray reflectivity measurements using an X-ray pixel area detector at the DiffAbs beamline, Synchrotron SOLEIL, J. Synchrotron Radiat. 25 (2018) 204–213. doi:10.1107/S1600577517015703.
[40] M. Björck, G. Andersson, *GenX* : an extensible X-ray reflectivity refinement program utilizing differential evolution, J. Appl. Crystallogr. 40 (2007) 1174–1178. doi:10.1107/S0021889807045086.
[41] X-ray Reflectivity, (n.d.). http://physics.valpo.edu/staff/arichter/XRR.htm (accessed November 13, 2020).
[42] G. Bertuzzi, M. Cova, A. Benincasa, Experimental evaluation of residual stresses uncertainty in heavy section ductile iron castings with different surface treatments using the hole drilling technique, CastTec conference proceedings, Darmstadt (2016).
[43] C. Eberl, Digital Image Correlation and Tracking, MATLAB Cent. File Exch. (2020). https://www.mathworks.com/matlabcentral/fileexchange/12413-digital-image-correlation-and-tracking (accessed July 22, 2020).
[44] E. Salvati, L. Romano-Brandt, M.Z. Mughal, M. Sebastiani, A.M. Korsunsky, Generalised Residual Stress Depth Profiling at the Nanoscale using Focused Ion Beam Milling, J. Mech. Phys. Solids. (2019). doi:10.1016/J.JMPS.2019.01.007.
[45] Y. Kilinc, U. Unal, B.E. Alaca, Residual stress gradients in electroplated nickel thin films, Microelectron. Eng. 134 (2015) 60–67. doi:10.1016/j.mee.2015.01.042.
[46] L.R. Brandt, E. Salvati, C. Papadaki, H. Zhang, S. Ying, E. Le Bourhis, I. Dolbnya, T. Sui, A.M. Korsunsky, Probing the deformation and fracture properties of Cu/W nano-multilayers by in situ SEM and synchrotron XRD strain microscopy, Surf. Coat. Technol. 320 (2017) 158–167. doi:10.1016/j.surfcoat.2017.01.065.
[47] C. Wang, P. Brault, C. Zaepffel, J. Thiault, A. Pineau, T. Sauvage, Deposition and structure of W-Cu multilayer coatings by magnetron sputtering, J. Phys. D. Appl. Phys. 36 (2003) 2709–2713. doi:10.1088/0022-3727/36/21/018.
[48] S. Djaziri, D. Thiaudière, G. Geandier, P.-O. Renault, E. Le Bourhis, P. Goudeau, O. Castelnau, D. Faurie, Controlled biaxial deformation of nanostructured W/Cu thin films studied by X-ray diffraction, Surf. Coatings Technol. 205 (2010) 1420–1425. doi:10.1016/j.surfcoat.2010.08.118.

[49] B. Girault, P. Villain, E. Le Bourhis, P. Goudeau, P.O. Renault, X-ray diffraction analysis of the structure and residual stresses of W/Cu multilayers, Surf. Coatings Technol. 201 (2006) 4372–4376. doi:10.1016/j.surfcoat.2006.08.034.
[50] B. Tlili, C. Nouveau, G. Guillemot, A. Besnard, A. Barkaoui, Investigation of the Effect of Residual Stress Gradient on the Wear Behavior of PVD Thin Films, J. Mater. Eng. Perform. 27 (2018) 457–470. doi:10.1007/s11665-018-3132-1.
[51] J.A. Thornton, J. Tabock, D.W. Hoffman, Internal stresses in metallic films deposited by cylindrical magnetron sputtering, Thin Solid Films. 64 (1979) 111–119. doi:10.1016/0040-6090(79)90550-9.
[52] A.M. Engwall, Z. Rao, E. Chason, Origins of residual stress in thin films: Interaction between microstructure and growth kinetics, Mater. Des. 110 (2016) 616–623. doi:10.1016/j.matdes.2016.07.089.
[53] G. Abadias, E. Chason, J. Keckes, M. Sebastiani, G.B. Thompson, E. Barthel, G.L. Doll, C.E. Murray, C.H. Stoessel, L. Martinu, Review Article: Stress in thin films and coatings: Current status, challenges, and prospects, J. Vac. Sci. Technol. A Vacuum, Surfaces, Film. 36 (2018) 020801. doi:10.1116/1.5011790.
[54] A.J. Lunt, N. Baimpas, E. Salvati, I.P. Dolbnya, T. Sui, S. Ying, H. Zhang, A.K. Kleppe, J. Dluhoš, A.M. Korsunsky, A state-of-the-art review of micron-scale spatially resolved residual stress analysis by FIB-DIC ring-core milling and other techniques, J. Strain Anal. Eng. Des. 50 (2015) 426–444. doi:10.1177/0309324715596700.
[55] J. McCarthy, Z. Pei, M. Becker, D. Atteridge, FIB micromachined submicron thickness cantilevers for the study of thin film properties, Thin Solid Films. 358 (2000) 146–151. doi:10.1016/S0040-6090(99)00680-X.
[56] E. Salvati, A.M. Korsunsky, An analysis of macro- and micro-scale residual stresses of Type I, II and III using FIB-DIC micro-ring-core milling and crystal plasticity FE modelling, Int. J. Plast. 98 (2017) 123–138. doi:10.1016/j.ijplas.2017.07.004.
[57] M. Renzelli, M.Z. Mughal, M. Sebastiani, E. Bemporad, Design , fabrication and characterization of multilayer Cr-CrN thin coatings with tailored residual stress profiles, JMADE. 112 (2016) 162–171. doi:10.1016/j.matdes.2016.09.058.
[58] A.M. Korsunsky, E. Salvati, A.G.J. Lunt, T. Sui, M.Z. Mughal, R. Daniel, J. Keckes, E. Bemporad, M. Sebastiani, Nanoscale residual stress depth profiling by Focused Ion Beam milling and eigenstrain analysis, Mater. Des. 145 (2018) 55–64. doi:10.1016/j.matdes.2018.02.044.
[59] A. Zeilinger, J. Todt, C. Krywka, M. Müller, W. Ecker, B. Sartory, M. Meindlhumer, M. Stefenelli, R. Daniel, C. Mitterer, J. Keckes, In-situ Observation of Cross-Sectional Microstructural Changes and Stress Distributions in Fracturing TiN Thin Film during Nanoindentation, Sci. Rep. 6 (2016) 1–14. doi:10.1038/srep22670.
[60] M. Stefenelli, J. Todt, A. Riedl, W. Ecker, T. Müller, R. Daniel, M. Burghammer, J. Keckes, X-ray analysis of residual stress gradients in TiN coatings by a Laplace space approach and cross-sectional nanodiffraction: a critical comparison, J. Appl. Crystallogr. 46 (2013) 1378–1385. doi:10.1107/S0021889813019535.
[61] U. Selvadurai, W. Tillmann, G. Fischer, T. Sprute, The influence of multilayer design on residual stress gradients in Ti/TiAlN systems, Mater. Sci. Forum. 768–769 (2014) 264–271. doi:10.4028/www.scientific.net/MSF.768-769.264.
[62] E. Chason, J.W. Shin, S.J. Hearne, L.B. Freund, Kinetic model for dependence of thin film stress on growth rate, temperature, and microstructure, J. Appl. Phys. 111 (2012). doi:10.1063/1.4704683.
[63] F.M. D'Heurle, J.M. Harper, Note on the origin of intrinsic stresses in films deposited via evaporation and sputtering, Thin Solid Films. 171 (1989) 81–92. doi:10.1016/0040-6090(89)90035-7.

[64] Q. Wang, S. Kishimoto, Y. Tanaka, K. Naito, Fabrication of nanoscale speckle using broad ion beam milling on polymers for deformation analysis, Theor. Appl. Mech. Lett. 6 (2016) 157–161. doi:10.1016/J.TAML.2016.07.001.
[65] E. Salvati, T. Sui, A.J.G. Lunt, A.M. Korsunsky, The effect of eigenstrain induced by ion beam damage on the apparent strain relief in FIB-DIC residual stress evaluation, Mater. Des. 92 (2016) 649–658. doi:10.1016/j.matdes.2015.12.015.
[66] E. Salvati, L.R. Brandt, C. Papadaki, H. Zhang, S.M. Mousavi, D. Wermeille, A.M. Korsunsky, Nanoscale structural damage due to focused ion beam milling of silicon with Ga ions, Mater. Lett. 213 (2018) 346–349. doi:10.1016/j.matlet.2017.11.043.
[67] A.M. Korsunsky, J. Guénolé, E. Salvati, T. Sui, M. Mousavi, A. Prakash, E. Bitzek, Quantifying eigenstrain distributions induced by focused ion beam damage in silicon, Mater. Lett. 185 (2016) 47–49. doi:10.1016/j.matlet.2016.08.111.
[68] J. Guénolé, A. Prakash, E. Bitzek, Influence of intrinsic strain on irradiation induced damage: the role of threshold displacement and surface binding energies, Mater. Des. 111 (2016) 405–413. doi:10.1016/j.matdes.2016.08.077.
[69] M. Senn, Digital Image Correlation and Tracking, (2015). https://uk.mathworks.com/matlabcentral/fileexchange/50995-digital-image-correlation-and-tracking. (accessed: 5th May 2020).
[70] Material: Silicon (Si), bulk, (n.d.). https://www.memsnet.org/material/siliconsibulk/ (accessed October 19, 2018).
[71] A. Benediktovich, I. Feranchuk, A. Ulyanenkov, Theoretical Concepts of X-Ray Nanoscale Analysis, 2014. doi:10.1007/978-3-642-38177-5.
[72] G.S. Schajer, ed., Practical Residual Stress Measurement Methods, John Wiley & Sons, Ltd, Chichester, UK, 2013. doi:10.1002/9781118402832.
[73] A.M. Korsunsky, S. Cherian, R. Raiteri, R. Berger, On the micromechanics of micro-cantilever sensors: Property analysis and eigenstrain modeling, Sensors Actuators, A Phys. 139 (2007) 70–77. doi:10.1016/j.sna.2007.03.007.
[74] A.J.G. Lunt, N. Baimpas, E. Le Bourhis, A.M. Korsunsky, Materials and Design Cover Image: "Roman brick wall" cracking of a thin coating, Mater. Des. 88 (2015) 1210–1212. doi:10.1016/j.matdes.2015.08.139.
[75] A.P. McGuigan, G.A.D. Briggs, V.M. Burlakov, M. Yanaka, Y. Tsukahara, An elastic-plastic shear lag model for fracture of layered coatings, Thin Solid Films. 424 (2003) 219–223. doi:10.1016/S0040-6090(02)01124-0.
[76] M. Yanaka, Y. Tsukahara, N. Nakaso, N. Takeda, Cracking phenomena of brittle films in nanostructure composites analysed by a modified shear lag model with residual strain, J. Mater. Sci. 33 (1998) 2111–2119. doi:10.1023/A:1004371203514.
[77] H.L. Cox, The elasticity and strength of paper and other fibrous materials, Br. J. Appl. Phys. 3 (1952) 72–79. doi:10.1088/0508-3443/3/3/302.
[78] S. Frank, U.A. Handge, S. Olliges, R. Spolenak, The relationship between thin film fragmentation and buckle formation: Synchrotron-based in situ studies and two-dimensional stress analysis, Acta Mater. 57 (2009) 1442–1453. doi:10.1016/j.actamat.2008.11.023.
[79] F. Ahmed, K. Bayerlein, S.M. Rosiwal, M. Göken, K. Durst, Stress evolution and cracking of crystalline diamond thin films on ductile titanium substrate: Analysis by micro-Raman spectroscopy and analytical modelling, Acta Mater. 59 (2011) 5422–5433. doi:10.1016/j.actamat.2011.05.015.
[80] B. Girault, G. Geandier, D. Eyidi, P.O. Renault, E. Le Bourhis, P. Goudeau, Size effects on the mechanical behavior of nanometric W/Cu multilayers, Mater. Res. Soc. Symp. Proc. 1086 (2008) 73–79. doi:10.1557/proc-1086-u04-04.
[81] E. Salvati, M. Benedetti, T. Sui, A.M. Korsunsky, Residual stress measurement on shot

peened samples using FIB-DIC, in: Conf. Proc. Soc. Exp. Mech. Ser., Springer New York LLC, 2016: pp. 275–283. doi:10.1007/978-3-319-21765-9_33.
[82] A.M. Korsunsky, K.E. Wells, P.J. Withers, Mapping two-dimensional state of strain using synchroton X-ray diffraction, Scr. Mater. 39 (1998) 1705–1712. doi:10.1016/S1359-6462(98)00385-6.
[83] DuPont, DuPont Kapton HN, (2019) 2. https://www.dupont.com/content/dam/dupont/amer/us/en/products/ei-transformation/documents/DEC-Kapton-HN-datasheet.pdf (accessed July 27, 2020).
[84] H. Huang, F. Spaepen, Tensile testing of free-standing Cu, Ag and Al thin films and Ag/Cu multilayers, Acta Mater. 48 (2000) 3261–3269. doi:10.1016/S1359-6454(00)00128-2.
[85] G. Ouyang, C.X. Wang, G.W. Yang, Surface energy of nanostructural materials with negative curvature and related size effects, Chem. Rev. 109 (2009) 4221–4247. doi:10.1021/cr900055f.
[86] P. Villain, P. Goudeau, P.O. Renault, K.F. Badawi, Size effect on intragranular elastic constants in thin tungsten films, Appl. Phys. Lett. 81 (2002) 4365–4367. doi:10.1063/1.1527229.
[87] P. Goudeau, P. Villain, T. Girardeau, P.O. Renault, K.F. Badawi, Elastic constants investigation by X-ray diffraction of in situ deformed metallic multi-layers, Scr. Mater. 50 (2004) 723–727. doi:10.1016/j.scriptamat.2003.11.053.
[88] A. Hansen, P.C. Hemmer, S. Pradhan, The Fiber Bundle Model: Modeling Failure in Materials, wiley, 2015. doi:10.1002/9783527671960.
[89] S. Zhang, X. Zhang, Toughness evaluation of hard coatings and thin films, Thin Solid Films. 520 (2012) 2375–2389. doi:10.1016/j.tsf.2011.09.036.
[90] E. Hintsala, & D. Kiener, & J. Jackson, W.W. Gerberich, In-Situ Measurements of Free-Standing, Ultra-Thin Film Cracking in Bending, (2015). doi:10.1007/s11340-015-0069-2.
[91] G. Jaeger, I. Endler, M. Heilmaier, K. Bartsch, A. Leonhardt, New method of determining strength and fracture toughness of thin hard coatings, Thin Solid Films. 377–378 (2000) 382–388. doi:10.1016/S0040-6090(00)01312-2.
[92] Z. Chen, Z. Gan, Fracture toughness measurement of thin films on compliant substrate using controlled buckling test, Thin Solid Films. 515 (2007) 3305–3309. doi:10.1016/j.tsf.2006.01.044.
[93] Z. Chen, B. Cotterell, W. Wang, The fracture of brittle thin films on compliant substrates in flexible displays, Eng. Fract. Mech. 69 (2002) 597–603. doi:10.1016/S0013-7944(01)00104-7.
[94] A. Favache, C.H. Sacré, M. Coulombier, L. Libralesso, P. Guaino, J.P. Raskin, C. Bailly, B. Nysten, T. Pardoen, Fracture mechanics based analysis of the scratch resistance of thin brittle coatings on a soft interlayer, Wear. 330–331 (2015) 461–468. doi:10.1016/j.wear.2015.01.081.
[95] A.A. Voevodin, J.S. Zabinski, Supertough wear-resistant coatings with “chameleon” surface adaptation, Thin Solid Films. 370 (2000) 223–231. doi:10.1016/S0040-6090(00)00917-2.
[96] C.L. Li, J.P. Chu, J.W. Lee, Measuring notch toughness of thin film metallic glasses using focused ion beam-based microcantilever method: Comparison with Ti and TiN crystalline films, Mater. Sci. Eng. A. 698 (2017) 104–109. doi:10.1016/j.msea.2017.05.002.
[97] J. Ast, T. Przybilla, V. Maier, K. Durst, M. Göken, Microcantilever bending experiments in NiAl - Evaluation, size effects, and crack tip plasticity, J. Mater. Res. 29 (2014) 2129–2140. doi:10.1557/jmr.2014.240.

[98] E.I. Preiß, B. Merle, M. Göken, Understanding the extremely low fracture toughness of freestanding gold thin films by in-situ bulge testing in an AFM, Mater. Sci. Eng. A. 691 (2017) 218–225. doi:10.1016/j.msea.2017.03.037.
[99] T.Y. Tsui, Y.C. Joo, A new technique to measure through film thickness fracture toughness, Thin Solid Films. 401 (2001) 203–210. doi:10.1016/S0040-6090(01)01613-3.
[100] P. Jedrzejowski, J.E. Klemberg-Sapieha, L. Martinu, Relationship between the mechanical properties and the microstructure of nanocomposite TiN/SiN1.3 coatings prepared by low temperature plasma enhanced chemical vapor deposition, Thin Solid Films. 426 (2003) 150–159. doi:10.1016/S0040-6090(03)00028-2.
[101] E. Salvati, L.R. Brandt, C. Papadaki, H. Zhang, S.M. Mousavi, D. Wermeille, A.M. Korsunsky, Nanoscale structural damage due to focused ion beam milling of silicon with Ga ions, Mater. Lett. 213 (2018). doi:10.1016/j.matlet.2017.11.043.
[102] R. Bermejo, R. Danzer, High failure resistance layered ceramics using crack bifurcation and interface delamination as reinforcement mechanisms, Eng. Fract. Mech. 77 (2010) 2126–2135. doi:10.1016/j.engfracmech.2010.02.020.
[103] Y. Gao, T. Yang, J. Xue, S. Yan, S. Zhou, Y. Wang, D.T.K. Kwok, P.K. Chu, Y. Zhang, Radiation tolerance of Cu/W multilayered nanocomposites, J. Nucl. Mater. 413 (2011) 11–15. doi:10.1016/j.jnucmat.2011.03.030.
[104] H. Vogel, A better way to construct the sunflower head, Math. Biosci. 44 (1979) 179–189. doi:10.1016/0025-5564(79)90080-4.
[105] T.L. Anderson, Fracture Mechanics: Fundamentals and Applications, Fourth Edition, Fourth, CRC Press, 2017.
[106] L. Romano-Brandt, E. Salvati, E. Le Bourhis, T. Moxham, I.P. Dolbnya, A.M. Korsunsky, Nano-scale residual stress depth profiling in Cu/W nano-multilayers as a function of magnetron sputtering pressure, Surf. Coatings Technol. 381 (2020) 125142. doi:10.1016/j.surfcoat.2019.125142.
[107] H. Hirakata, O. Nishijima, N. Fukuhara, T. Kondo, A. Yonezu, K. Minoshima, Size effect on fracture toughness of freestanding copper nano-films, Mater. Sci. Eng. A. 528 (2011) 8120–8127. doi:10.1016/j.msea.2011.07.071.
[108] R.R. Keller, J.M. Phelps, D.T. Read, Tensile and fracture behavior of free-standing copper films, Mater. Sci. Eng. A. 214 (1996) 42–52. doi:10.1016/0921-5093(96)10253-7.
[109] J. Ast, M. Göken, K. Durst, Size-dependent fracture toughness of tungsten, Acta Mater. 138 (2017) 198–211. doi:10.1016/j.actamat.2017.07.030.
[110] J.Y. Zhang, G. Liu, X. Zhang, G.J. Zhang, J. Sun, E. Ma, A maximum in ductility and fracture toughness in nanostructured Cu/Cr multilayer films, Scr. Mater. 62 (2010) 333–336. doi:10.1016/j.scriptamat.2009.10.030.
[111] Y. Liu, I. Bhamji, P.J. Withers, D.E. Wolfe, A.T. Motta, M. Preuss, Evaluation of the interfacial shear strength and residual stress of TiAlN coating on ZIRLO™ fuel cladding using a modified shear-lag model approach, J. Nucl. Mater. 466 (2015) 718–727. doi:10.1016/j.jnucmat.2015.06.003.
[112] L. Vergani, Meccanica dei materiali, McGraw-Hill Companies, 2006.
[113] J.A. Thornton, D.W. Hoffman, Internal stresses in titanium, nickel, molybdenum, and tantalum films deposited by cylindrical magnetron sputtering, J. Vac. Sci. Technol. 14 (1977) 164–168. doi:10.1116/1.569113.
[114] H.Y. Liu, G.S. Tang, F. Zeng, F. Pan, Influence of sputtering parameters on structures and residual stress of AlN films deposited by DC reactive magnetron sputtering at room temperature, J. Cryst. Growth. 363 (2013) 80–85. doi:10.1016/j.jcrysgro.2012.10.008.

[115] Y.G. Shen, Y.W. Mai, Q.C. Zhang, D.R. McKenzie, W.D. McFall, W.E. McBride, Residual stress, microstructure, and structure of tungsten thin films deposited by magnetron sputtering, J. Appl. Phys. 87 (2000) 177–187. doi:10.1063/1.371841.
[116] T.J. Vink, W. Walrave, J.L.C. Daams, A.G. Dirks, M.A.J. Somers, K.J.A. Van Den Aker, Stress, strain, and microstructure in thin tungsten films deposited by dc magnetron sputtering, J. Appl. Phys. 74 (1993) 988–995. doi:10.1063/1.354842.
[117] K.Y. Chan, B.S. Teo, Effect of Ar pressure on grain size of magnetron sputter-deposited Cu thin films, IET Sci. Meas. Technol. 1 (2007) 87–90. doi:10.1049/iet-smt:20060110.
[118] W. Qin, L. Fu, J. Zhu, W. Yang, J. Sang, D. Li, L. Zhou, Electrical and thermal properties of Cu-Ta films prepared by magnetron sputtering, Appl. Surf. Sci. 443 (2018) 97–102. doi:10.1016/j.apsusc.2018.02.262.
[119] Y. Isosaki, Y. Yamashita, T. Yagi, J. Jia, N. Taketoshi, S. Nakamura, Y. Shigesato, Structure and thermophysical properties of GaN films deposited by reactive sputtering using a metal Ga target, J. Vac. Sci. Technol. A Vacuum, Surfaces, Film. 35 (2017) 041507. doi:10.1116/1.4985182.
[120] C. Linsmeier, M. Rieth, J. Aktaa, T. Chikada, A. Hoffmann, J. Hoffmann, A. Houben, H. Kurishita, X. Jin, M. Li, A. Litnovsky, S. Matsuo, A. Von Müller, V. Nikolic, T. Palacios, R. Pippan, D. Qu, J. Reiser, J. Riesch, T. Shikama, R. Stieglitz, T. Weber, S. Wurster, J.H. You, Z. Zhou, Development of advanced high heat flux and plasma-facing materials, Nucl. Fusion. 57 (2017) 092007. doi:10.1088/1741-4326/aa6f71.
[121] L. Romano Brandt, E. Salvati, E. Le Bourhis, A.M. Korsunsky, Mode I fracture toughness determination in Cu/W nano-multilayers on polymer substrate by SEM - Digital Image Correlation, J. Mech. Phys. Solids. 145 (2020) 104145. doi:10.1016/j.jmps.2020.104145.
[122] A. Reza, C.A. Dennett, M.P. Short, J. Waite, Y. Zayachuk, C.M. Magazzeni, S. Hills, F. Hofmann, Non-contact, non-destructive mapping of thermal diffusivity and surface acoustic wave speed using transient grating spectroscopy, Rev. Sci. Instrum. 91 (2020) 054902. doi:10.1063/5.0003742.
[123] O.W. Käding, H. Skurk, A.A. Maznev, E. Matthias, Transient thermal gratings at surfaces for thermal characterization of bulk materials and thin films, Appl. Phys. A Mater. Sci. Process. 61 (1995) 253–261. doi:10.1007/BF01538190.
[124] J.A. Johnson, A.A. Maznev, M.T. Bulsara, E.A. Fitzgerald, T.C. Harman, S. Calawa, C.J. Vinels, G. Turner, K.A. Nelson, Phase-controlled, heterodyne laser-induced transient grating measurements of thermal transport properties in opaque material, J. Appl. Phys. 111 (2012) 023503. doi:10.1063/1.3675467.
[125] C.A. Dennett, M.P. Short, Time-resolved, dual heterodyne phase collection transient grating spectroscopy, Appl. Phys. Lett. 110 (2017) 211106. doi:10.1063/1.4983716.
[126] F. Hofmann, M.P. Short, C.A. Dennett, Transient grating spectroscopy: An ultrarapid, nondestructive materials evaluation technique, MRS Bull. 44 (2019) 392–402. doi:10.1557/mrs.2019.104.
[127] Z.J. Radzimski, Directional copper deposition using dc magnetron self-sputtering, J. Vac. Sci. Technol. B Microelectron. Nanom. Struct. 16 (1998) 1102. doi:10.1116/1.590016.
[128] R.E. Somekh, The thermalization of energetic atoms during the sputtering process, J. Vac. Sci. Technol. A Vacuum, Surfaces, Film. 2 (1984) 1285–1291. doi:10.1116/1.572396.
[129] A.K. Bandyopadhyay, S.K. Sen, Calculation of Self-Interstitial Formation Energy (Both Split and Non-Split) in Noble Metals, Phys. Status Solidi. 157 (1990) 519–530. doi:10.1002/pssb.2221570204.

[130] I.M. Neklyudov, E. V Sadanov, G.D. Tolstolutskaja, V.A. Ksenofontov, T.I. Mazilova, I.M. Mikhailovskij, Interstitial atoms in tungsten: Interaction with free surface and in situ determination of formation energy, (n.d.). doi:10.1103/PhysRevB.78.115418.
[131] J. Dalla Torre, G.H. Gilmer, D.L. Windt, R. Kalyanaraman, F.H. Baumann, P.L. O'Sullivan, J. Sapjeta, T. Díaz de la Rubia, M. Djafari Rouhani, Microstructure of thin tantalum films sputtered onto inclined substrates: Experiments and atomistic simulations, J. Appl. Phys. 94 (2003) 263–271. doi:10.1063/1.1579112.
[132] R. Koch, Stress in Evaporated and Sputtered Thin Films - A Comparison, Surf. Coatings Technol. 204 (2010) 1973–1982. doi:10.1016/j.surfcoat.2009.09.047.
[133] R. Koch, The intrinsic stress of polycrystalline and epitaxial thin metal films, J. Phys. Condens. Matter. 6 (1994) 9519–9550. doi:10.1088/0953-8984/6/45/005.
[134] G. Abadias, W.P. Leroy, S. Mahieu, D. Depla, Influence of particle and energy flux on stress and texture development in magnetron sputtered TiN films, J. Phys. D. Appl. Phys. 46 (2013) 55301–55310. doi:10.1088/0022-3727/46/5/055301.
[135] S.C. Seel, C. V. Thompson, Tensile stress generation during island coalescence for variable island-substrate contact angle, J. Appl. Phys. 93 (2003) 9038–9042. doi:10.1063/1.1571964.
[136] P. Nath, K.L. Chopra, Thermal conductivity of copper films, Thin Solid Films. 20 (1974) 53–62. doi:10.1016/0040-6090(74)90033-9.
[137] Z. Zhou, C. Uher, A. Jewell, T. Caillat, Influence of point-defect scattering on the lattice thermal conductivity of solid solution Co(Sb1-xAsx)3, Phys. Rev. B - Condens. Matter Mater. Phys. 71 (2005) 235209. doi:10.1103/PhysRevB.71.235209.
[138] K.-M. Chang, T.-H. Yeh, I.-C. Deng, C.-W. Shih, Amorphouslike chemical vapor deposited tungsten diffusion barrier for copper metallization and effects of nitrogen addition, J. Appl. Phys. 82 (1997) 1469. doi:10.1063/1.365925.
[139] G. Ackland, Controlling radiation damage, Science (80-.). 327 (2010) 1587–1588. doi:10.1126/science.1188088.
[140] V.A. Turchenko, A. V. Trukhanov, I.A. Bobrikov, S. V. Trukhanov, A.M. Balagurov, Investigation of the crystal and magnetic structures of BaFe12 - xAlxO19 solid solutions (x = 0.1–1.2), Crystallogr. Reports. 60 (2015) 629–635. doi:10.1134/S1063774515030220.
[141] A.L. Kozlovskiy, I.E. Kenzhina, M. V. Zdorovets, FeCo– Fe2CoO4/Co3O4 nanocomposites: Phase transformations as a result of thermal annealing and practical application in catalysis, Ceram. Int. 46 (2020) 10262–10269. doi:10.1016/j.ceramint.2020.01.019.
[142] C. Cancellieri, F. Moszner, M. Chiodi, S. Yoon, J. Janczak-Rusch, L.P.H. Jeurgens, F. Moszner, The effect of thermal treatment on the stress state and evolving microstructure of Cu/W nano-multilayers, J. Appl. Phys. 120 (2016). doi:10.1063/1.4967992.
[143] A. V. Druzhinin, D. Ariosa, S. Siol, N. Ott, B.B. Straumal, J. Janczak-Rusch, L.P.H. Jeurgens, C. Cancellieri, Effect of the individual layer thickness on the transformation of Cu/W nano-multilayers into nanocomposites, Materialia. 7 (2019) 100400. doi:10.1016/j.mtla.2019.100400.
[144] F. Moszner, C. Cancellieri, M. Chiodi, S. Yoon, D. Ariosa, J. Janczak-Rusch, L.P.H. Jeurgens, Thermal stability of Cu/W nano-multilayers, Acta Mater. 107 (2016) 345–353. doi:10.1016/j.actamat.2016.02.003.
[145] A. V. Druzhinin, B. Rheingans, S. Siol, B.B. Straumal, J. Janczak-Rusch, L.P.H. Jeurgens, C. Cancellieri, Effect of internal stress on short-circuit diffusion in thin films and nanolaminates: Application to Cu/W nano-multilayers, Appl. Surf. Sci. 508 (2020) 145254. doi:10.1016/j.apsusc.2020.145254.

[146] R. Raghavan, J.M. Wheeler, D. Esqué-de los Ojos, K. Thomas, E. Almandoz, G.G. Fuentes, J. Michler, Mechanical behavior of Cu/TiN multilayers at ambient and elevated temperatures: Stress-assisted diffusion of Cu, Mater. Sci. Eng. A. 620 (2015) 375–382. doi:10.1016/j.msea.2014.10.023.
[147] J. Snel, M.A. Monclús, M. Castillo-Rodríguez, N. Mara, I.J. Beyerlein, J. Llorca, J.M. Molina-Aldareguía, Deformation Mechanism Map of Cu/Nb Nanoscale Metallic Multilayers as a Function of Temperature and Layer Thickness, JOM. 69 (2017) 2214–2226. doi:10.1007/s11837-017-2533-1.
[148] D.I. Tishkevich, S.S. Grabchikov, L.S. Tsybulskaya, V.S. Shendyukov, S.S. Perevoznikov, S. V. Trukhanov, E.L. Trukhanova, A. V. Trukhanov, D.A. Vinnik, Electrochemical deposition regimes and critical influence of organic additives on the structure of Bi films, J. Alloys Compd. 735 (2018) 1943–1948. doi:10.1016/j.jallcom.2017.11.329.
[149] D.I. Tishkevich, S.S. Grabchikov, S.B. Lastovskii, S. V. Trukhanov, T.I. Zubar, D.S. Vasin, A. V. Trukhanov, Correlation of the synthesis conditions and microstructure for Bi-based electron shields production, J. Alloys Compd. 749 (2018) 1036–1042. doi:10.1016/j.jallcom.2018.03.288.
[150] T.I. Zubar, V.M. Fedosyuk, S. V. Trukhanov, D.I. Tishkevich, D. Michels, D. Lyakhov, A. V. Trukhanov, Method of surface energy investigation by lateral AFM: application to control growth mechanism of nanostructured NiFe films, Sci. Rep. 10 (2020) 1–10. doi:10.1038/s41598-020-71416-w.
[151] T. Zubar, V. Fedosyuk, D. Tishkevich, O. Kanafyev, K. Astapovich, A. Kozlovskiy, M. Zdorovets, D. Vinnik, S. Gudkova, E. Kaniukov, A.S.B. Sombra, D. Zhou, R.B. Jotania, C. Singh, S. Trukhanov, A. Trukhanov, The Effect of Heat Treatment on the Microstructure and Mechanical Properties of 2D Nanostructured Au/NiFe System, Nanomaterials. 10 (2020) 1077. doi:10.3390/nano10061077.
[152] P. Müller-Buschbaum, Grazing incidence small-angle X-ray scattering: An advanced scattering technique for the investigation of nanostructured polymer films, Anal. Bioanal. Chem. 376 (2003) 3–10. doi:10.1007/s00216-003-1869-2.
[153] ProfilmOnline, (n.d.). https://www.profilmonline.com/ (accessed October 6, 2020).
[154] Z. Czigány, G. Radnóczi, Columnar growth structure and evolution of wavy interface morphology in amorphous and polycrystalline multilayered thin films, Thin Solid Films. 347 (1999) 133–145. doi:10.1016/S0040-6090(98)01760-X.
[155] L. Romano Brandt, A. Reza, E. Salvati, E. Le Bourhis, F. Hofmann, A.M. Korsunsky, Controlling Thermal Diffusivity, Residual Stress and Texture in W/Cu Nano-Multilayers by Magnetron Chamber Pressure Variation, SSRN Electron. J. (2020). doi:10.2139/ssrn.3708733.
[156] Y.N. Osetsky, D.J. Bacon, A. Serra, B.N. Singh, S.I. Golubov, One-dimensional atomic transport by clusters of self-interstitial atoms in iron and copper, Philos. Mag. 83 (2003) 61–91. doi:10.1080/0141861021000016793.
[157] C.M. Gilmore, J.A. Sprague, Molecular dynamics simulation of defect formation during energetic Cu deposition, Thin Solid Films. 419 (2002) 18–26. doi:10.1016/S0040-6090(02)00609-0.
[158] H. Windischmann, Intrinsic stress in sputter-deposited thin films, Criticul Rev. Solid State Und Mater. Sci. 17 (1992) 547–596. doi:10.1080/10408439208244586.
[159] D. Magnfält, G. Abadias, K. Sarakinos, Atom insertion into grain boundaries and stress generation in physically vapor deposited films, Appl. Phys. Lett. 103 (2013) 051910. doi:10.1063/1.4817669.
[160] B. Girault, Étude De L'Effet De Taille Et De Structure Sur L'Élasticité, Thesis. (2008).
[161] J. Yang, W. Deng, Q. Li, X. Li, A. Liang, Y. Su, S. Guan, J. Wang, D. He, Strength

enhancement of nanocrystalline tungsten under high pressure, Matter Radiat. Extrem. 5 (2020) 058401. doi:10.1063/5.0005395.
[162] F. Foote, E.R. Jette, The fundamental relation between lattice constants and density, Phys. Rev. 58 (1940) 81–86. doi:10.1103/PhysRev.58.81.
[163] E. Chason, T.M. Mayer, Thin film and surface characterization by specular X-ray reflectivity, Crit. Rev. Solid State Mater. Sci. 22 (1997) 1–67. doi:10.1080/10408439708241258.
[164] M. Bockstedte, A. Mattausch, O. Pankratov, Ab initio study of the annealing of vacancies and interstitials in cubic SiC: Vacancy-interstitial recombination and aggregation of carbon interstitials, Phys. Rev. B - Condens. Matter Mater. Phys. 69 (2004) 235202. doi:10.1103/PhysRevB.69.235202.
[165] G.J. Dienes, A.C. Damask, Kinetics of vacancy-interstitial annihilation. III. Interstitial migration to sinks, Phys. Rev. 128 (1962) 2542–2546. doi:10.1103/PhysRev.128.2542.
[166] J.H. Zhao, Y. Du, M. Morgen, P.S. Ho, Simultaneous measurement of Young's modulus, poisson ratio, and coefficient of thermal expansion of thin films on substrates, J. Appl. Phys. 87 (2000) 1575–1577. doi:10.1063/1.372054.
[167] A. Lahav, K.A. Grim, I.A. Blech, Measurement of thermal expansion coefficients of W, WSi, WN, and WSiN thin film metallizations, J. Appl. Phys. 67 (1990) 734–738. doi:10.1063/1.345779.
[168] J. Janczak-Rusch, M. Chiodi, C. Cancellieri, F. Moszner, R. Hauert, G. Pigozzi, L.P.H. Jeurgens, Structural evolution of Ag-Cu nano-alloys confined between AlN nano-layers upon fast heating, Phys. Chem. Chem. Phys. 17 (2015) 28228–28238. doi:10.1039/c5cp00782h.
[169] H. Jiang, W. Hua, N. Tian, A. Li, X. Li, Y. He, Z. Zhang, In situ GISAXS study on the temperature-dependent performance of multilayer monochromators from the liquid nitrogen cooling temperature to 600 °C, Appl. Surf. Sci. 508 (2020) 144838. doi:10.1016/j.apsusc.2019.144838.
[170] J. Horváth, R. Birringer, H. Gleiter, Diffusion in nanocrystalline material, Solid State Commun. 62 (1987) 319–322. doi:10.1016/0038-1098(87)90989-6.
[171] J.K. Solberg, The crystal structure of η-Cu3Si precipitates in silicon, Acta Crystallogr. Sect. A. 34 (1978) 684–698. doi:10.1107/S0567739478001448.
[172] N. Ponweiser, K.W. Richter, New investigation of phase equilibria in the system Al-Cu-Si, J. Alloys Compd. 512 (2012) 252–263. doi:10.1016/j.jallcom.2011.09.076.
[173] M. Seibt, M. Griess, A.A. Istratov, H. Hedemann, A. Sattler, W. Schröter, Formation and properties of copper silicide precipitates in silicon, Phys. Status Solidi Appl. Res. 166 (1998) 171–182. doi:10.1002/1521-396.
[174] M.M. Salem, L. V. Panina, E.L. Trukhanova, M.A. Darwish, A.T. Morchenko, T.I. Zubar, S. V. Trukhanov, A. V. Trukhanov, Structural, electric and magnetic properties of (BaFe11.9Al0.1O19)1-x - (BaTiO3)x composites, Compos. Part B Eng. 174 (2019) 107054. doi:10.1016/j.compositesb.2019.107054.
[175] A.L. Kozlovskiy, M. V. Zdorovets, The study of the structural characteristics and catalytic activity of Co/CoCo2O4 nanowires, Compos. Part B Eng. 191 (2020) 107968. doi:10.1016/j.compositesb.2020.107968.
[176] S. V. Trukhanov, I.O. Troyanchuk, N. V. Pushkarev, H. Szymczak, The influence of oxygen deficiency on the magnetic and electric properties of la0.70Ba0.30MnO3-γ (0 ≤ γ ≤ 0.30) manganite with a perovskite structure, J. Exp. Theor. Phys. 95 (2002) 308–315. doi:10.1134/1.1506439.
[177] M. V. Zdorovets, A.L. Kozlovskiy, The effect of lithium doping on the ferroelectric properties of LST ceramics, Ceram. Int. 46 (2020) 14548–14557. doi:10.1016/j.ceramint.2020.02.254.

[178] M.D. Radin, S. Hy, M. Sina, C. Fang, H. Liu, J. Vinckeviciute, M. Zhang, M.S. Whittingham, Y.S. Meng, A. Van der Ven, Narrowing the Gap between Theoretical and Practical Capacities in Li-Ion Layered Oxide Cathode Materials, Adv. Energy Mater. 7 (2017) 1–33. doi:10.1002/aenm.201602888.
[179] F. Schipper, E.M. Erickson, C. Erk, J.-Y. Shin, F.F. Chesneau, D. Aurbach, Review—Recent Advances and Remaining Challenges for Lithium Ion Battery Cathodes, J. Electrochem. Soc. 164 (2017) A6220–A6228. doi:10.1149/2.0351701jes.
[180] F. Friedrich, B. Strehle, A.T.S. Freiberg, K. Kleiner, S.J. Day, C. Erk, M. Piana, H.A. Gasteiger, Capacity fading mechanisms of NCM-811 cathodes in lithium-ion batteries studied by X-ray diffraction and other diagnostics, J. Electrochem. Soc. 166 (2019) A3760–A3774. doi:10.1149/2.0821915jes.
[181] J.V. Laveda, J.E. Low, F. Pagani, E. Stilp, S. Dilger, V. Baran, M. Heere, C. Battaglia, Stabilizing Capacity Retention in NMC811/Graphite Full Cells via TMSPi Electrolyte Additives, ACS Appl. Energy Mater. 2 (2019) 7036–7044. doi:10.1021/acsaem.9b00727.
[182] H. Zhou, F. Xin, B. Pei, M.S. Whittingham, What Limits the Capacity of Layered Oxide Cathodes in Lithium Batteries?, ACS Energy Lett. 4 (2019) 1902–1906. doi:10.1021/acsenergylett.9b01236.
[183] S. Xia, L. Mu, Z. Xu, J. Wang, C. Wei, L. Liu, P. Pianetta, K. Zhao, X. Yu, F. Lin, Y. Liu, Chemomechanical Interplay of Layered Cathode Materials undergoing Fast Charging in Lithium Batteries, Nano Energy. 53 (2018) 753–762. doi:10.1016/j.nanoen.2018.09.051.
[184] L. Mu, R. Lin, R. Xu, L. Han, S. Xia, D. Sokaras, J.D. Steiner, T.C. Weng, D. Nordlund, M.M. Doeff, Y. Liu, K. Zhao, H.L. Xin, F. Lin, Oxygen Release Induced Chemomechanical Breakdown of Layered Cathode Materials, Nano Lett. 18 (2018) 3241–3249. doi:10.1021/acs.nanolett.8b01036.
[185] Y. Yang, R. Xu, K. Zhang, S. Lee, L. Mu, P. Liu, C.K. Waters, S. Spence, Z. Xu, C. Wei, D.J. Kautz, Q. Yuan, Y. Dong, Y. Yu, X. Xiao, H. Lee, P. Pianetta, P. Cloetens, J. Lee, K. Zhao, F. Lin, Y. Liu, Quantification of Heterogeneous Degradation in Li-Ion Batteries, Adv. Energy Mater. 9 (2019) 1900674. doi:10.1002/aenm.201900674.
[186] B. Song, T. Sui, S. Ying, L. Li, L. Lu, A.M. Korsunsky, Nano-structural changes in Li-ion battery cathodes during cycling revealed by FIB-SEM serial sectioning tomography, J. Mater. Chem. A. 3 (2015) 18171–18179. doi:10.1039/C5TA04151A.
[187] J. Li, A.R. Cameron, H. Li, S. Glazier, D. Xiong, M. Chatzidakis, J. Allen, G.A. Botton, J.R. Dahn, Comparison of Single Crystal and Polycrystalline LiNi 0.5 Mn 0.3 Co 0.2 O 2 Positive Electrode Materials for High Voltage Li-Ion Cells , J. Electrochem. Soc. 164 (2017) A1534–A1544. doi:10.1149/2.0991707jes.
[188] G. Sun, T. Sui, B. Song, H. Zheng, L. Lu, A.M. Korsunsky, On the fragmentation of active material secondary particles in lithium ion battery cathodes induced by charge cycling, Extrem. Mech. Lett. 9 (2016) 449–458. doi:10.1016/J.EML.2016.03.018.
[189] A.M. Korsunsky, T. Sui, B. Song, Explicit formulae for the internal stress in spherical particles of active material within lithium ion battery cathodes during charging and discharging, Mater. Des. 69 (2015) 247–252. doi:10.1016/j.matdes.2014.12.058.
[190] J. Li, R. Shunmugasundaram, R. Doig, J.R. Dahn, In Situ X-ray Diffraction Study of Layered Li-Ni-Mn-Co Oxides: Effect of Particle Size and Structural Stability of Core-Shell Materials, Chem. Mater. 28 (2016) 162–171. doi:10.1021/acs.chemmater.5b03500.
[191] S.M. Bak, E. Hu, Y. Zhou, X. Yu, S.D. Senanayake, S.J. Cho, K.B. Kim, K.Y. Chung, X.Q. Yang, K.W. Nam, Structural changes and thermal stability of charged LiNixMnyCozO2 cathode materials studied by combined in situ time-resolved XRD

and mass spectroscopy, ACS Appl. Mater. Interfaces. 6 (2014) 22594–22601. doi:10.1021/am506712c.
[192] R. Jung, M. Metzger, F. Maglia, C. Stinner, H.A. Gasteiger, Oxygen Release and Its Effect on the Cycling Stability of LiNi $_x$ Mn $_y$ Co $_z$ O $_2$ (NMC) Cathode Materials for Li-Ion Batteries, J. Electrochem. Soc. 164 (2017) A1361–A1377. doi:10.1149/2.0021707jes.
[193] J. Li, L.E. Downie, L. Ma, W. Qiu, J.R. Dahn, Study of the Failure Mechanisms of LiNi 0.8 Mn 0.1 Co 0.1 O 2 Cathode Material for Lithium Ion Batteries , J. Electrochem. Soc. 162 (2015) A1401–A1408. doi:10.1149/2.1011507jes.
[194] R. Jung, M. Metzger, F. Maglia, C. Stinner, H.A. Gasteiger, Chemical versus electrochemical electrolyte oxidation on NMC111, NMC622, NMC811, LNMO, and conductive carbon, J. Phys. Chem. Lett. 8 (2017) 4820–4825. doi:10.1021/acs.jpclett.7b01927.
[195] T. Hatsukade, A. Schiele, P. Hartmann, T. Brezesinski, J. Janek, Origin of Carbon Dioxide Evolved during Cycling of Nickel-Rich Layered NCM Cathodes, ACS Appl. Mater. Interfaces. 10 (2018) 38892–38899. doi:10.1021/acsami.8b13158.
[196] Z. Xu, M.M. Rahman, L. Mu, Y. Liu, F. Lin, Chemomechanical behaviors of layered cathode materials in alkali metal ion batteries, J. Mater. Chem. A. 6 (2018) 21859–21884. doi:10.1039/C8TA06875E.
[197] H.H. Ryu, K.J. Park, C.S. Yoon, Y.K. Sun, Capacity fading of ni-rich li[Ni x Co y Mn 1-x-y]O 2 ($0.6 \leq x \leq 0.95$) Cathodes for High-Energy-Density Lithium-Ion Batteries: Bulk or Surface Degradation?, Chem. Mater. 30 (2018) 1155–1163. doi:10.1021/acs.chemmater.7b05269.
[198] W.H. Woodford, Y.-M. Chiang, W.C. Carter, “Electrochemical Shock” of Intercalation Electrodes: A Fracture Mechanics Analysis, J. Electrochem. Soc. 157 (2010) A1052. doi:10.1149/1.3464773.
[199] F. Xin, H. Zhou, X. Chen, M. Zuba, N. Chernova, G. Zhou, M.S. Whittingham, Li-Nb-O Coating/Substitution Enhances the Electrochemical Performance of the LiNi0.8Mn0.1Co0.1O2 (NMC 811) Cathode, ACS Appl. Mater. Interfaces. 11 (2019) 34889–34894. doi:10.1021/acsami.9b09696.
[200] X. Xu, L. Xiang, L. Wang, J. Jian, C. Du, X. He, H. Huo, X. Cheng, G. Yin, Progressive concentration gradient nickel-rich oxide cathode material for high-energy and long-life lithium-ion batteries, J. Mater. Chem. A. 7 (2019) 7728–7735. doi:10.1039/C9TA00224C.
[201] R. Chen, T. Zhao, X. Zhang, L. Li, F. Wu, Advanced cathode materials for lithium-ion batteries using nanoarchitectonics, Nanoscale Horizons. 1 (2016) 423–444. doi:10.1039/c6nh00016a.
[202] X. Xu, H. Huo, J. Jian, L. Wang, H. Zhu, S. Xu, X. He, G. Yin, C. Du, X. Sun, Radially Oriented Single-Crystal Primary Nanosheets Enable Ultrahigh Rate and Cycling Properties of LiNi0.8Co0.1 Mn0.1O2 Cathode Material for Lithium-Ion Batteries, Adv. Energy Mater. 9 (2019) 1803963. doi:10.1002/aenm.201803963.
[203] D.J. Miller, C. Proff, J.G. Wen, D.P. Abraham, J. Bareño, Observation of microstructural evolution in li battery cathode oxide particles by in situ electron microscopy, Adv. Energy Mater. 3 (2013) 1098–1103. doi:10.1002/aenm.201300015.
[204] J.Y. Huang, L. Zhong, C.M. Wang, J.P. Sullivan, W. Xu, L.Q. Zhang, S.X. Mao, N.S. Hudak, X.H. Liu, A. Subramanian, H. Fan, L. Qi, A. Kushima, J. Li, In situ observation of the electrochemical lithiation of a single SnO 2 nanowire electrode, Science (80-.). 330 (2010) 1515–1520. doi:10.1126/science.1195628.
[205] A. Demortiere, J. Ando, M. Bettge, V. De Andrade, K. Amine, D. Miller, Monitoring morphological evolution of Li-ion cathode secondary particles through In situ

FIB/SEM electrochemical experiment, in: Eur. Microsc. Congr. 2016 Proc., Wiley-VCH Verlag GmbH & Co. KGaA, 2016: pp. 293–295. doi:10.1002/9783527808465.emc2016.6960.
[206] C. Heubner, U. Langklotz, C. Lämmel, M. Schneider, A. Michaelis, Electrochemical single-particle measurements of electrode materials for Li-ion batteries: Possibilities, insights and implications for future development, Electrochim. Acta. 330 (2020). doi:10.1016/j.electacta.2019.135160.
[207] P.-C. Tsai, B. Wen, M. Wolfman, M.-J. Choe, M.S. Pan, L. Su, K. Thornton, J. Cabana, Y.-M. Chiang, Single-particle measurements of electrochemical kinetics in NMC and NCA cathodes for Li-ion batteries, Energy Environ. Sci. 11 (2018) 860–871. doi:10.1039/C8EE00001H.
[208] H. Munakata, B. Takemura, T. Saito, K. Kanamura, Evaluation of real performance of LiFePO 4 by using single particle technique, J. Power Sources. 217 (2012) 444–448. doi:10.1016/j.jpowsour.2012.06.037.
[209] I. Uchida, H. Fujiyoshi, S. Waki, Microvoltammetric studies on single particles of battery active materials, J. Power Sources. 68 (1997) 139–144.
[210] K. Dokko, M. Mohamedi, Y. Fujita, T. Itoh, M. Nishizawa, M. Umeda, I. Uchida, Kinetic Characterization of Single Particles of LiCoO[sub 2] by AC Impedance and Potential Step Methods, J. Electrochem. Soc. 148 (2001) A422. doi:10.1149/1.1359197.
[211] E.H.R. Tsai, J. Billaud, D.F. Sanchez, J. Ihli, M. Odstrčil, M. Holler, D. Grolimund, C. Villevieille, M. Guizar-Sicairos, Correlated X-Ray 3D Ptychography and Diffraction Microscopy Visualize Links between Morphology and Crystal Structure of Lithium-Rich Cathode Materials, IScience. 11 (2019) 356–365. doi:10.1016/j.isci.2018.12.028.
[212] R.F. Ziesche, T. Arlt, D.P. Finegan, T.M.M. Heenan, A. Tengattini, D. Baum, N. Kardjilov, H. Markötter, I. Manke, W. Kockelmann, D.J.L. Brett, P.R. Shearing, 4D imaging of lithium-batteries using correlative neutron and X-ray tomography with a virtual unrolling technique, Nat. Commun. 11 (2020) 1–11. doi:10.1038/s41467-019-13943-3.
[213] R. Xu, Y. Yang, F. Yin, P. Liu, P. Cloetens, Y. Liu, F. Lin, K. Zhao, Heterogeneous damage in Li-ion batteries: Experimental analysis and theoretical modeling, J. Mech. Phys. Solids. 129 (2019) 160–183. doi:10.1016/j.jmps.2019.05.003.
[214] T. Li, X.-Z. Yuan, L. Zhang, D. Song, K. Shi, C. Bock, Degradation Mechanisms and Mitigation Strategies of Nickel-Rich NMC-Based Lithium-Ion Batteries, Springer Singapore, 2020. doi:10.1007/s41918-019-00053-3.
[215] A.M. Maiden, J.M. Rodenburg, An improved ptychographical phase retrieval algorithm for diffractive imaging, Ultramicroscopy. 109 (2009) 1256–1262. doi:10.1016/j.ultramic.2009.05.012.
[216] R.R. Keller, R.H. Geiss, Transmission EBSD from 10 nm domains in a scanning electron microscope, J. Microsc. 245 (2012) 245–251. doi:10.1111/j.1365-2818.2011.03566.x.
[217] Q. Huang, Y.Y. Lee, B. Gurkan, Pyrrolidinium Ionic Liquid Electrolyte with Bis(trifluoromethylsulfonyl)imide and Bis(fluorosulfonyl)imide Anions: Lithium Solvation and Mobility, and Performance in Lithium Metal-Lithium Iron Phosphate Batteries, Ind. Eng. Chem. Res. 58 (2019) 22587–22597. doi:10.1021/acs.iecr.9b03202.
[218] H. Sun, K. Zhao, Electronic Structure and Comparative Properties of LiNi x Mn y Co z O 2 Cathode Materials , J. Phys. Chem. C. 121 (2017) 6002–6010. doi:10.1021/acs.jpcc.7b00810.

[219] E.J. Cheng, K. Hong, N.J. Taylor, H. Choe, J. Wolfenstine, J. Sakamoto, Mechanical and physical properties of LiNi0.33Mn0.33Co0.33O2 (NMC), J. Eur. Ceram. Soc. 37 (2017) 3213–3217. doi:10.1016/J.JEURCERAMSOC.2017.03.048.
[220] E. Zhao, L. Fang, M. Chen, D. Chen, Q. Huang, Z. Hu, Q.B. Yan, M. Wu, X. Xiao, New insight into Li/Ni disorder in layered cathode materials for lithium ion batteries: A joint study of neutron diffraction, electrochemical kinetic analysis and first-principles calculations, J. Mater. Chem. A. 5 (2017) 1679–1686. doi:10.1039/c6ta08448f.
[221] S. Hwang, S.Y. Kim, K.Y. Chung, E.A. Stach, S.M. Kim, W. Chang, Determination of the mechanism and extent of surface degradation in Ni-based cathode materials after repeated electrochemical cycling, APL Mater. 4 (2016) 096105. doi:10.1063/1.4963723.
[222] E. Salvati, A.M. Korsunsky, A simplified FEM eigenstrain residual stress reconstruction for surface treatments in arbitrary 3D geometries, Int. J. Mech. Sci. 138–139 (2018) 457–466. doi:10.1016/J.IJMECSCI.2018.02.016.
[223] D. Fraggedakis, N. Nadkarni, T. Gao, T. Zhou, Y. Zhang, Y. Han, R.M. Stephens, Y. Shao-Horn, M.Z. Bazant, A scaling law to determine phase morphologies during ion intercalation, Energy Environ. Sci. 13 (2020) 2142. doi:10.1039/d0ee00653j.
[224] M. Dachyar, T.Y.M. Zagloel, L.R. Saragih, Knowledge growth and development: internet of things (IoT) research, 2006–2018, Heliyon. 5 (2019) e02264. doi:10.1016/j.heliyon.2019.e02264.
[225] M. Zulqarnain, S. Stanzione, G. Rathinavel, S. Smout, M. Willegems, K. Myny, E. Cantatore, A flexible ECG patch compatible with NFC RF communication, Npj Flex. Electron. 4 (2020) 1–8. doi:10.1038/s41528-020-0077-x.
[226] Y. Jin, G. Chen, K. Lao, S. Li, Y. Lu, Y. Gan, Z. Li, J. Hu, J. Huang, J. Wen, H. Deng, M. Yang, Z. Chen, X. Hu, B. Liang, J. Luo, Identifying human body states by using a flexible integrated sensor, Npj Flex. Electron. 4 (2020) 1–8. doi:10.1038/s41528-020-00090-9.
[227] D. Ruzmetov, V.P. Oleshko, P.M. Haney, H.J. Lezec, K. Karki, K.H. Baloch, A.K. Agrawal, A. V. Davydov, S. Krylyuk, Y. Liu, J. Huang, M. Tanase, J. Cumings, A.A. Talin, Electrolyte stability determines scaling limits for solid-state 3D Li ion batteries, Nano Lett. 12 (2012) 505–511. doi:10.1021/nl204047z.
[228] Y. Liu, Y. Zhu, Y. Cui, Challenges and opportunities towards fast-charging battery materials, Nat. Energy. 4 (2019) 540–550. doi:10.1038/s41560-019-0405-3.
[229] A. Tomaszewska, Z. Chu, X. Feng, S. O'Kane, X. Liu, J. Chen, C. Ji, E. Endler, R. Li, L. Liu, Y. Li, S. Zheng, S. Vetterlein, M. Gao, J. Du, M. Parkes, M. Ouyang, M. Marinescu, G. Offer, B. Wu, Lithium-ion battery fast charging: A review, ETransportation. 1 (2019) 100011. doi:10.1016/j.etran.2019.100011.
[230] E. Quartarone, P. Mustarelli, Review—Emerging Trends in the Design of Electrolytes for Lithium and Post-Lithium Batteries, J. Electrochem. Soc. 167 (2020) 050508. doi:10.1149/1945-7111/ab63c4.
[231] R. Schmuch, R. Wagner, G. Hörpel, T. Placke, M. Winter, Performance and cost of materials for lithium-based rechargeable automotive batteries, Nat. Energy. 3 (2018) 267–278. doi:10.1038/s41560-018-0107-2.
[232] L. Romano Brandt, J.-J. Marie, T. Moxham, D.P. Förstermann, E. Salvati, C. Besnard, C. Papadaki, Z. Wang, P.G. Bruce, A.M. Korsunsky, Synchrotron X-ray quantitative evaluation of transient deformation and damage phenomena in a single nickel-rich cathode particle, Energy Environ. Sci. (2020) 3556–3566. doi:10.1039/d0ee02290j.
[233] U.H. Kim, G.T. Park, B.K. Son, G.W. Nam, J. Liu, L.Y. Kuo, P. Kaghazchi, C.S. Yoon, Y.K. Sun, Heuristic solution for achieving long-term cycle stability for Ni-rich

layered cathodes at full depth of discharge, Nat. Energy. 5 (2020) 860–869. doi:10.1038/s41560-020-00693-6.
[234] H. Kawasoko, S. Shiraki, T. Suzuki, R. Shimizu, T. Hitosugi, Extremely Low Resistance of Li 3 PO 4 Electrolyte/Li(Ni 0.5 Mn 1.5)O 4 Electrode Interfaces, ACS Appl. Mater. Interfaces. 10 (2018) 27498–27502. doi:10.1021/acsami.8b08506.
[235] Q. Zhao, S. Stalin, C.Z. Zhao, L.A. Archer, Designing solid-state electrolytes for safe, energy-dense batteries, Nat. Rev. Mater. 5 (2020) 229–252. doi:10.1038/s41578-019-0165-5.
[236] K. Nishio, N. Nakamura, K. Horiba, M. Kitamura, H. Kumigashira, R. Shimizu, T. Hitosugi, Impact of the Crystal Orientation of Positive Electrodes on the Interface Resistance across a Solid Electrolyte and Electrode, ACS Appl. Energy Mater. 3 (2020) 6416–6421. doi:10.1021/acsaem.0c00644.
[237] K. Simon, L. Porz, T. Swamy, Y.M. Chiang, A. Slocum, Low-profile self-sealing sample transfer flexure box, Rev. Sci. Instrum. 88 (2017). doi:10.1063/1.4997952.
[238] Gatan Microscopy Suite Software | Gatan, Inc., (n.d.). https://www.gatan.com/products/tem-analysis/gatan-microscopy-suite-software (accessed November 23, 2020).
[239] CrystalMaker: Overview, (n.d.). http://crystalmaker.com/crystalmaker/index.html (accessed November 23, 2020).
[240] A.M. James, MacMillan's chemical and physical data, Biochem. Educ. 21 (1993) 109–110. doi:10.1016/0307-4412(93)90067-a.
[241] O.S. Bondareva, M.A. Simonov, N. V Belov, The crystal structure of the synthetic analogue of the lithiophospate Li3 P O4 -gamma, Dokl. Akad. Nauk SSSR. 240 (1978) 75–77.
[242] W.H. Baur, Solid solutions between octahedral and terahedral olivine types in Li-Zn-germanates, Inorg. Nucl. Chem. Lett. 16 (1980) 525–527.
[243] B. Wang, B.C. Chakoumakos, B.C. Sales, B.S. Kwak, J.B. Bates, Synthesis, crystal structure, and ionic conductivity of a polycrystalline lithium phosphorus oxynitride with the gamma-Li3 P O4 structure, J. Solid State Chem. 115 (1995) 313–323.
[244] O. V Yakubovich, V.S. Urusov, Electron distribution in lithiophosphatite: Crystallochemical features of orthophasphates with hexagonal close packing, Kristallografiya. 42 (1997) 301–308.
[245] J. Zemann, Die Kristallstruktur von Lithiumphosphat, Li3 P O4, Acta Crystallogr. 13 (1960) 863–867.
[246] Masys, V. Jonauskas, Elastic properties of rhombohedral, cubic, and monoclinic phases of LaNiO3 by first principles calculations, Comput. Mater. Sci. 108 (2015) 153–159. doi:10.1016/j.commatsci.2015.06.034.
[247] mp-5229: SrTiO3 (cubic, Pm-3m, 221), (n.d.). https://www.materialsproject.org/materials/mp-5229/ (accessed November 28, 2020).
[248] X.L. Wang, K. An, L. Cai, Z. Feng, S.E. Nagler, C. Daniel, K.J. Rhodes, A.D. Stoica, H.D. Skorpenske, C. Liang, W. Zhang, J. Kim, Y. Qi, S.J. Harris, Visualizing the chemistry and structure dynamics in lithium-ion batteries by in-situ neutron diffraction, Sci. Rep. 2 (2012) 1–7. doi:10.1038/srep00747.